Luminescence Dating of Past Seismic and Tectonic Events: Methodological Aspects and Applications

A thesis submitted to

THE GUJARAT UNIVERSITY,
AHMEDABAD

for the award of the degree of

DOCTOR OF PHILOSOPHY

in

PHYSICS

By

ANIL KUMAR TYAGI

Under the supervision of

Prof. Ashok K. Singhvi
Physical Research Laboratory
Ahmedabad

Year of submission: 2014

CERTIFICATE

CERTIFIED that the work incorporated in the thesis "**Luminescence Dating of Past Seismic and Tectonic Events: Methodological Aspects and Applications**" submitted by Shri **ANIL KUMAR TYAGI** was carried out by the candidate under my supervision/guidance. To the best of my knowledge: (i) the candidate has not submitted the same research work to any other institution for any degree/diploma, Associateship, Fellowship or other similar titles (ii) the thesis submitted is a record of original research work done by the student during the period of study under my supervision, and (iii) the thesis represents independent research work on the part of the student.

_____

(Guide)

Prof. Ashok Kumar Singhvi

Physical Research Laboratory

Ahmedabad 380 009

Gujarat, India

Place: Ahmedabad Date:

DECLARATION

I declare that the thesis entitled "**Luminescence Dating of Past Seismic and Tectonic Events: Methodological Aspects and Applications**" submitted by me for the degree of Doctor of Philosophy is the record of research work carried out by me during the period from 2006 to 2014 under the guidance of **Prof. Ashok Kumar Singhvi** and has not formed the basis for the award of any degree, diploma, associateship, fellowship, titles in this or any other University or other institution of higher learning.

I further declare that the material obtained from other sources has been duly acknowledged in the thesis. I shall be solely responsible for any plagiarism or other irregularities, if noticed in the thesis.

_____

(Signature of the Candidate) Date:

Anil Kumar Tyagi

Dedicated to

My

Late Parents

Abstract

Climate and tectonics are important processes that sculpt the surface of Earth and control other geomorphic and sediment transport processes. Therefore understanding of timing and amplitude of the past seismic and tectonic history of area during the geological past is needed to inform the planning of built and other infrastructures. This calls for the development of long series of patterns and nature of release of stress as earthquakes. This thesis examined three possibilities to reconstruct the timing of the past earthquakes using both theoretical calculations from first principles and their field/laboratory validations in respect of the use of luminescence dating technique that enabled dating of the most recent thermal or optical exposure of natural minerals constituting the sediment. The three possible archives of the chronology of past earth quakes are the sand dikes, the fault gouges and tectonically sculpted landforms.

Earlier studies on sand dikes (Porat et al., 2007) indicated a reduced luminescence signal in dikes compared to host, despite the absence of any obvious possibility of thermal or daylight bleaching. Following recent preliminary works (Singh et al., 2009), this thesis examined in detail the aspect of flash heating of sediment in sand dike due to grain friction using first principles and inferred that heating up to few hundred degrees could occur. The critical parameters were the sediment viscosity, width of the dike and injection velocity. Effect of these parameters on rise in temperature was examined. Flash heating was invoked as it reconciled with thermal zeroing of luminescence signal. This was validated by luminescence dating and analysis of luminescence properties of the sand dike and host samples from North−East (Assam). The studies suggested the resetting of luminescence due to viscous heating during the injection of the sand dikes. The experimental validation included the estimation of extent of heating in dike samples by laboratory measurement. For this the sensitivity of 110 °C TL peak of quartz was used.

The second possibility of dating past earthquakes/tectonic event was via the dating of pulverized rock material during the movement along a fault viz. the fault gouge. The heat excursion due to slip was simulated along with the heat dissipation and it was seen that

sufficient heat to reset luminescence would be generated for slip of about 15 cm and if dated can provide a direct age estimate of the past seismic activity.

The third possibility of dating tectonic events was via the dating of fault scarp and river channels affected by the earthquake in the Great Rann of Kachhchh, Western India.

The principal conclusion of the thesis is that flash heating under suitable conditions can result in the zeroing of luminescence. Thermal zeroing of luminescence can result in resting of signal in dike and gouge material. These make therefore luminescence dating an attractive option for the dating of past earth quakes and tectonic events.

The catastrophic earthquakes in the rocks lead to the formation of the gouge material. The extent of heating in the fault gouge material was estimated by theoretical calculations and validated with the experiments in laboratory. Attempt was also made to understand the effect of stress on the quartz grains. Quartz grains were stressed by dropping different mass from different heights and luminescence from these stressed grains were recorded. The results presented in Chapter 5, show the pattern of reduction in luminescence due to the applied stress on the samples.

The luminescence studies were also made using standard laboratory protocols on the dike, fault gouge and fault scarp samples to estimate the time of tectonic events. The results from the fault scarp and truncated river channels from Western India are presented in Chapter 6.

Based on the studies on sand dike samples four earthquake events of M >6 and M >7 were identified in North-East, further the fault gouge samples suggested two earthquakes in Sikkim-Darjeeling Himalaya. Results of fault scarp samples suggested that the present form of Allah bund scarp was an outcome of two major earthquakes in the area. These events were 1819 earthquake and another tectonic event between 1.4−2 ka.

Acknowledgements

Many years of my work at PRL with help, support, suggestions, discussions and encouragement of people, enabled me to complete the work presented in this thesis. After having so many years of love with all PRL and my family members it is time to express my gratitude to all of them.

I would first like to thank my supervisor Prof. Ashok Kumar Singhvi, his guidance, enthusiasm, commitment and integral view made it possible to complete this work. His ideas and commitment of working will inspire me to do always a better work in science and in personal life. He guided me as a supervisor in the lab and advised as a father in taking personal decisions. I am glad to be his student and overwhelmed in expressing my gratitude to him. I am thankful to Aunty ji for giving love and affection like mother, which reduced the overload of work at lab.

Present thesis would not have been possible without the understanding of geological process, which were explained and discussed by Juyal sir with me. He made me to understand all those things which I might not have been thorough otherwise. His style of working on war front in lab made me a quick and systematic worker in the lab. I am thankful to Juyal sir and bhabhi ji for their love and care which they provide and made homely environment for me whenever I was with them.

I would also like express my gratitude to Prof. R. N. Singh for his guidance and discussion on theoretical part of my work. I am thankful to Prof. M. D. Shastry for various discussions during his visits in PRL.

I am thankful to my seniors Nagar, Madhav, Bhavesh and Morthekai for their valuable inputs, suggestions on time to time basis. They helped in early days of my research work in gaining insights of many physical processes. I am thankful to Nagar for explaining things at lab. Special thanks to Nagar for his support and advice like an elder brother who is your supervisor. Madhav and Bhavesh bhai introduced me with Matlab and encouraged to use it at all possible places even for small calculations which helped me in the later part of work.

I am thankful to my lab mates Naveen and Rabiul for helping me as and when needed and for all fruitful discussions with them. I am thankful to Vaidehi, Pinkky, Komal, Nikita and Haresh for making my stay in the lab comfortable in later days of my work.

I would like to thank Dr. Devender Kumar from NGRI Hyderabad, who helped me to undertake the filed in the North-East (Assam). His efforts made it possible to identify the dikes in the area which otherwise would not have been possible for me. He made me to understand how to search for a dike in the field.

I am grateful to Prof. M. M. Sarin, Prof. S. V. S. Murty, Prof. J. N. Goswami, Prof. Ramesh, Dr. J. S. Ray, Dr. S. K. Singh, Dr. D. Banerjee, Prof A. Jayaraman, Dr. Angom, Prof. Shyamlal, Dr. Jitesh Bhatt and Dr. P. Sharma for their valuable suggestions during my seminars and reviews at PRL.

Many thanks to Jigar bhai, Mishra ji and Alok bhai in computer lab for their help in setting up things during course work and afterwards as well. I am thankful to people at workshop, library, canteen, admin, stores and purchase for providing their help and support as and when needed. I am greatly thankful to Mr. Rajesh Kaila for immediate help at workshop for making sampling pipes. Thanks to Vishnu bhai and Ubale ji for their help in making small instruments which I used in lab. I am thankful to Vaghela bhai and Bhavsar bhai for providing distilled water for our laboratory use.

I am thankful to Dr. Anil Shukla, Dr. Ravi Bhushan, and Dr. M. G. Yadava for their guidance and support at various stages.

I would like to thank my PRL batch mates Naveen Gandhi, Sumita Kedia, Aswini, Gyan, Rahman, Kirpa, Sanjeev, Ram, Bhavik, Vishal, Manan, Harindar Pal, Sumanta, Brajesh, Jeetu, Shuchita and Arvind Singh for giving cheerful company at PRL. I am also thankful to Neeraj, Saxena and Manan for the cheerful moments at tea time during writing of thesis at PRL in later days.

I am thankful to Dr. Shishir Deshpande and Dr. Vinay Kumar at ITER-India, IPR for their help and support to allow me to complete this work.

I am thankful to PRL for providing me opportunity to work at Luminescence lab during my stay as a research scholar in the early stage of my research carrier, and providing necessary help and support as a guest after I left from PRL.

I feel a deep sense of gratitude for my late parents it was their effort which led to me to reach at PRL, and to my brother Arvind and my bhabhi Neeraj who guided and encouraged me after I lost my parents. I am thankful to my mother in law and father in law, who made it possible to feel me that I am always with my parents and supporting me throughout my work at PRL. I am thankful to my sisters Bebi, Babli, Anita, Abha and sister in law Deepa, for their love and care. I am thankful to Dipen bhai who encouraged, advised and helped me at various levels in personal life.

Finally this thesis would not have been possible without the support from my best friend and best half, my wife Sejal. The time dedicated to work in lab was stolen from what I would have spent with my wife and daughter Soumya. They allowed me to spend quality time on this work without complain. One single smile on their face refreshed me at reaching home and gave sense of happiness.

Thesis Contents

CHAPTER 1 INTRODUCTION 1

1.1 MOTIVATION AND BACKGROUND 1

1.2 CHRONOMETRIC METHODS FOR FAULT GOUGES AND SAND DIKES 3

1.2.1 Cosmogenic radionuclide method 3

1.2.2 Radiocarbon dating method 4

1.2.3 Fission track dating analysis 6

1.2.4 Fault scarp diffusion 7

1.2.5 U/Th dating 8

1.2.6 K−Ar dating 9

1.2.7 Electron Spin Resonance (ESR) Dating 10

1.2.8 Soil chronosequence method 12

1.3 LUMINESCENCE 13

1.3.1 Basic principles 13

1.3.2 Thermoluminescence (TL) 15

1.3.3 Optically Stimulated Luminescence (OSL) 15

1.3.4 Luminescence dating 16

1.3.5 Age determination (Age equation) 20

1.3.6 Evaluation of D_e 21

1.3.7 Dose rate 21

1.4 OBJECTIVES AND SCOPE OF THE THESIS 21

1.5 CHAPTER−WISE DETAILS 22

CHAPTER 2 EXPERIMENTAL PROCEDURES AND PROTOCOLS 24

2.1 INTRODUCTION 24

2.2 SAMPLE COLLECTION AND PREPARATION METHODS 24

2.2.1 Fine Grain Method 25

2.2.2 Coarse Grain Method 25

2.3 MEASUREMENT OF TL AND OSL: INSTRUMENT 26

2.3.1 Detection Unit (TL OSL Reader) 26

2.3.2 Stimulation Unit 28

2.3.3 Irradiation Unit 30

2.3.3.1 Risø TL/OSL Reader 30

2.4 MEASUREMENT OF NATURAL DOSE RATE 32

2.4.1 Measurement of Uranium (U−234) and Thorium (Th−237) Concentration *36*
2.4.2 Measurement of Potassium (K−40) Concentration *36*
2.4.3 Measurement of Cosmic Ray Dose Rate *37*
2.4.4 Moisture content *37*
2.4.5 Alpha efficiency 'a' value *38*
2.5 EQUIVALENT DOSE ($\mathbf{D_e}$) 38
2.5.1 Multiple Aliquot Additive Dose Method (MAAD) *39*
2.5.2 Normalization methods *40*
2.5.3 Single Aliquot Regenerative Protocol (SAR) *42*
2.5.4 Natural Correction Factor (NCF) *42*
2.6 THE NATURE OF DISTRIBUTION IN D_E WITH IN A SAMPLE 46
2.6.1 Radial plot *46*
2.6.2 Probability Density Plots *46*
2.7 ESTIMATION OF ERRORS IN TL/OSL MEASUREMENT 47
CHAPTER 3 RESETTING OF LUMINESCENCE IN SAND DIKES **48**
3.1 INTRODUCTION 48
3.2 MECHANISM OF DIKE FORMATION 49
3.3 RESETTING OF LUMINESCENCE 52
3.3.1 Equation for Heat Dissipation in a fluid *52*
3.3.2 Viscous Heating in Sand Dikes *54*
3.3.3 Rise in temperature during injection of a sand dike *54*
3.4 DISCUSSION 58
CHAPTER 4 LUMINESCENCE STUDIES OF SAND DIKES **60**
4.1 INTRODUCTION 60
4.2 STUDY AREA 61
4.3 LUMINESCENCE STUDIES OF SAND DIKES 62
4.3.1 Extent of heating *64*
4.3.2 Age Estimation *65*
4.4 DISCUSSION 87
4.5 CONCLUSION 89
APPENDIX 91
CHAPTER 5 RESETTING OF LUMINESCENCE IN FAULT GOUGES **106**
5.1 INTRODUCTION 106

5.2 FAULT GOUGE 107
5.3 RESETTING OF LUMINESCENCE IN FAULT GOUGE 107
5.4 AMPLITUDE RISE OF TEMPERATURE IN FAULT GOUGE DUE TO FRICTIONAL HEATING 110
5.4.1 Mathematical model *110*
5.4.2 Temperature during nucleation phase ($0 \leq t \leq t_1$) *114*
5.4.3 Temperature during constant velocity phase ($t_1 \leq t \leq t_2$) *114*
5.4.4 Temperature during deceleration phase ($t_2 \leq t \leq t_3$) *115*
5.4.5 Temperature after rupturing is stopped ($t > t_3$) *117*
5.4.6 Temperature profiles during faulting *117*
5.5 LUMINESCENCE STUDIES OF FAULT GOUGE SAMPLES 120
5.5.1 Predose effect in quartz *120*
5.5.2 Estimation of rise in temperature during faulting *121*
5.5.3 Equivalent Dose and Age Estimation *122*
5.5.1 Athermal Fading *122*
5.6 EFFECT OF STRESS ON QUARTZ 122
5.6.1 Effect of stress on OSL of quartz *125*
5.6.2 Effect of cumulative stress and variable stress on natural quartz *128*
5.7 RESULTS AND DISCUSSION 131

CHAPTER 6 LUMINESCENCE STUDIES OF TECTONIC EVENTS IN WESTERN INDIA 133

6.1 INTRODUCTION 133
6.2 STUDY AREA 134
6.2.1 Bet sequences *135*
6.2.2 Rann Sequences *139*
6.3 EVIDENCE OF PAST SEISMIC EVENTS 140
6.4 LUMINESCENCE STUDIES OF RANN SAMPLES 142
6.5 DISCUSSION 146
6.6 CONCLUSIONS 150

CHAPTER 7 CONCLUSIONS AND FUTURE OUTLOOK 152

7.1 CONCLUSIONS 152
7.2 FUTURE WORK 155

REFERENCES 159

List of Figures

Chapter 1: Introduction

Figure 1.1: Schematic diagram showing (a) fault gouge and (b) sand dike 2

Figure 1.2: Splitting of the energy levels in a magnetic field (Zeeman splitting) 12

Figure 1.3: Mechanism of luminescence a)ionization and trapping of electrons and holes at localized energy states, b)trapping depends upon the amount of trapping energy (separation from conduction band or valence band for electron or hole respectively) and c) release of light in the form of luminescence after external stimulation like heat or light (after Aitken, 1985) 14

Figure 1.4: Natural TL glow curves for (a) feldspar (PCMA−11 from Gish Fault) and (b) quartz (BB−1 from Bedabari site) 15

Figure 1.5: Shine down curves for (a) PCMA-11, feldspar from Gish fault (IRSL stimulation) and (b) KKT-16, quartz from Kakoti site (BLSL stimulation) 16

Chapter 2: Experimental procedures and protocols

Figure 2.1: PMT response curve of quantum efficiency vs. wavelength. (Bøtter−Jensen et al., 2003a) 27

Figure 2.2: (a) Stimulation spectra of IR− LED and the filter combinations used to detect the luminescence in blue region and (b) Stimulation spectra of Blue LED and the filter combinations used to detect the luminescence in UV region 29

Figure 2.3: (a) Schematic of TL/OSL Reader, (b) detailed schematic of illumination and detection unit from (after Bøtter−Jensen et al., 2003b) 31

Figure 2.4: Decay schemes of the Uranium series, (a) Uranium−235 and (b) Uranium−238 33

Figure 2.5: Decay schemes of the radioactive series, (a) Thorium−232, and (b) Potassium−40 and Rubidium−87 34

Figure 2.6: Ranges of ionizing radiations in natural environment 35

Figure 2.7: Multiple Aliquot Additive Dose (MAAD) method schematic 41

Figure 2.8: Single aliquot regeneration method, sensitivity corrected luminescence is plotted against the incremental doses (R_1, R_2, R_3….). D_e is measured by interpolating the (L_N/T_N) on to the dose axis (Murray and Wintle, 2000) 43

Figure 2.9: NCF correction factor model after (Singhvi et al., 2011) 44

Figure 2.10: (a) Histogram for the sample JR−4 (Jira village), (b) Radial plot of JR−4. Shaded region is the band of 2σ on the y−axis and (c) Probability density plot for the same sample 45

Chapter 3: Resetting of Luminescence in Sand Dikes

Figure 3.1: schematic representation of upward flow of dike and b) dialation profile of dike (after Levi et al., 2008) 50

Figure 3.2: Temperature rise during injection of dike 56

Figure 3.3: Schematic of rise in temperature and its dependence on channel flow. Maximum channel flow of the injected material will be at the center of the dike, and will therefore result into the maximum viscous heating of the material. The flow velocity at the edge of the dike will be minimum and thus may lead to partial resetting of the luminescence in the material near to edge of the dike 58

Chapter 4: Luminescence Studies of Sand Dikes

Figure 4.1: Location map of the study area. The sites Bedabari, Beltaghat are close to the Krishnai river and Jira is near the Mora Krishna river

(dead river). The other sites Kakoti and Namgon are close to the Kopili River (modified after Sukhija et al., 1999).....63

Figure 4.2: Flow chart for the measurement protocol for the monitoring of 110 ℃ TL peak of quartz (Step wise heating).....64

Figure 4.3: (a) Sensitivity change in 110 °C peak of quartz from dike and host samples for Bedabari and (b) Beltaghat sites.....66

Figure 4.4: (a) Sensitivity change in 110 °C peak of quartz from dike and host samples for Jira and (b) Kakoti sites.....67

Figure 4.5: Effect of preheat on higher temperature TL peak for samples from (a) Beltaghat site and (b) Kakoti site 68

Figure 4.6: Natural (N) and Natural + laboratory beta dose (β) curves for dike and host samples (a), (b) fromKakoti site and (c), (d) from Bedabari site. Also shown is the ratio of N/(N+β). The plateau level towards the higher temperature side (starting from 350 °C) shows the stability of the TL signal.....70

Figure 4.7: Dose recovery of samples KKT-10 and KKT-16 for Kakoti site (a, c); natural shine down curve for same samples (b,d), the growth curves for these samples are shown in the inset of figures (b) and (d).....71

Figure 4.8: Preheat Plateau for Samples (a) KKT-1 and (b) KKT-17 collected from Kakoti site. 72

Figure 4.9: TL glow curves (natural and dosed) for dike and host samples (a), (b) Bedabari site; (c), (d) Kakoti site; (e), (f) Jira site. 73

Figure 4.10: SAR regeneration curves for samples (a) KKT-16, (b) KKT-17, (c) NG-3 and (d) NG-7 constructed using the NCF protocol as discussed in chapter-2; SAR regeneration curves for samples (e) BG-2 and (f) BG-4.....75

Figure 4.11: Histogram showing comparisons of D_e distribution with NCF protocol (a), (c) and without NCF protocol (b) and (d) for samples KKT-1 and KKT-14 76

Figure 4.12: (a, c and e) shows the radial plot of D_e obtained for samples BB−1, BG−2 and BG−4 and (b, d and f) shows the dose distribution for these samples 77

Figure 4.13: (a, c and e) shows the radial plot of D_e obtained for samples JR−3, JR−4 and JR−7 and (b, d and f) shows the dose distribution for these samples 78

Figure 4.14: (a, c and e) shows the radial plot of D_e obtained for samples KKT−1, KKT−8 and KKT−14 and (b, d and f) shows the dose distribution for these samples 79

Figure 4.15: (a, c and e) shows the radial plot of D_e obtained for samples KKT−16, KKT−17 and NG−7 and (b, d and f) shows the dose distribution for these samples 80

Figure 4.16: Estimation of the minimum magnitude of earthquake resulting paleoliquefaction at the study area by plotting the distances of liquefaction sites from epicenters on the global data curve of Obermeier (1996). The location of the Bedabari, Beltaghat, and Jira sites (lower black rectangle) and for Kakoti and Namgaon sites (upper black rectangle) are plotted considering that the earthquake epicenter which produced liquefaction either occurred: within a radius of 35 km and 150 km (distance between 1987 Shillong Plateau earthquake epicenter and the sites). The magnitude of the earthquake(s) estimated based on these two scenarios ranges between M6 and M7.5 respectively. 88

Figure 4.17: Field Photograph of dike in Beltaghat site-1 93

Figure 4.18: Stratigraphy of the Beltaghat site, ages obtained for samples are shown adjacent to the samples marked 94

Figure 4.19: Field photograph of dike from Beltaghat site-2 95

Figure 4.20: Stratigraphy of the Beltaghat site, ages obtained for samples are shown adjacent to the samples marked 95

Figure 4.21: Field photograph of dike from Bedabari site 96

Figure 4.22: Stratigraphy of Bedabari site, ages obtained for samples are shown adjacent to sampling mark 97

Figure 4.23: Field photograph of dike from Jira site 98

Figure 4.24: Stratigraphy of Jira site, ages obtained for samples are shown adjacent to sampling mark 99

Figure 4.25: Field photograph of dike from Namgaon site 100

Figure 4.26: Stratigraphy of Namgaon site, ages obtained for samples are shown adjacent to sampling mark 101

Figure 4.27: Field photograph of dike from Kakoti site-1 102

Figure 4.28: Stratigraphy of Kakoti site-1, ages obtained for samples are shown adjacent to sampling mark 103

Figure 4.29: Field photograph of dike from Kakoti site-2 104

Figure 4.30: Stratigraphy of Kakoti site-2, ages obtained for samples are shown adjacent to sampling mark 105

Chapter 5: Resetting of Luminescence in Fault Gouges

Figure 5.1: Schematic for resetting due to mechanical stress. Smaller grain (in center) will have larger level of resetting as compared to larger grains (after Lee and Schwarcz, 1994). 109

Figure 5.2: Schematic representation of earthquake event. The event is divided into three phases i.e. nucleation, constant velocity and deceleration phase. 111

Figure 5.3: Schematic of heat generation during faulting event. The fault plane is at z=0, which is indicated as source and at z= ∞ is a sink indicating that the heat flux is zero at sink 112

Figure 5.4: Effect of slip distance (slip velocity) on temperature rise during rupture at 1mm and 5mm away from the fault plane for depth of 1km (λ=0.6, $\boldsymbol{\mu}$=0.6, κ =1e-6, K=2.5 and $\boldsymbol{\rho}$=2800) 118

Figure 5.5: Effect of pore pressure on rise in temperature during rupture at a depth of 1km (d=10cm, μ=0.6, κ=1e-6, K=2.5 and **ρ**=2800) 118

Figure 5.6: Effect of friction coefficient on rise in temperature during rupture at a depth of 1km (d=10cm, λ =0.6 κ=1e-6, K=2.5 and **ρ**=2800) 119

Figure 5.7: Effect of thermal conductance on rise in temperature during rupture at a depth of 1km (d=10cm, μ =0.6, λ =0.6, κ =1e-6 and **ρ**=2800) 119

Figure 5.8: Flow chart for the measurement protocol for the monitoring of 110 ℃ TL peak of quartz 121

Figure 5.9: (a), (c) and (e) normalized glow curves for PCMA-8, 9 and 10; (b), (d) and (f) ratio of N/(N+β) showing the stability of the TL signal for same samples and (g) natural TL glow curves for the same samples 123

Figure 5.10: Equivalent dose plateau for samples (a) PCMA-8, (b) PCMA-10, (c) PCMA-12 and (d) PCMA-13 124

Figure 5.11: Change in sensitivity of 110 ℃ TL peak for samples PCMA-9, PCMA-11 (fault gouge) and for PCMA-14 (host) 125

Figure 5.12: Measurement protocol to see the effect of stress on 110 °C peak and OSL 127

Figure 5.13: TL 110 °C response before and after stress 127

Figure 5.14: OSL normalized to first run 128

Figure 5.15:-Protocol to see the effect of cumulative and variable stress on quartz 110 °C peak 128

Figure 5.16: Stress induced 110 °C TL peak 129

Figure 5.17: Response of 325 ºC peak after stress 129

Figure 5.18: Measurement protocol to see the effect of same amount of stress due to repeated cycles 130

Figure 5.19: effect on grain size on TL counts integrated over temperature range 220–400°C.....130

Chapter 6: Luminescence studies of Tectonic Events in western India

Figure 6.1: (a) Map showing the location of the study area, NPF—Nagar Parker Fault, KMF—Kachchh Mainland Fault (after Biswas, 1987). (b) Geomorphological map of the area (after Rajendran and Rajendran, 2001; Merh, 2005).....136

Figure 6.2: Stratigraphy and optical chronology of the shallow sedimentary sequences investigated in the present study. (1) Allah Bund (Rann sediment), (2) Rann sediment (incised channel), (3) Nara River bank, (4) Nara River Bed, (5) Karim Shahi (Bet sediment), (6) Karim Shahi (Archaeological mound) and (7) Rann sediment (at Shakti Bet). Radiocarbon ages are shown in italic bold font. Dashed upward arrow indicates land movement, whereas the downward arrow indicates river incision. 137

Figure 6.3: Drainage pattern in the vicinity of Allah Bund. Western segment shows higher density of embryonic streams (W) compared to the Eastern segment (E). Channels show a preferential south west side trend. 141

Figure 6.4: Preheat plateau test for samples (a) KSTL-2 and (b) ABTL-1.....143

Figure 6.5: Dose Recovery test for 10 discs of sample (a) KSTL-1 and (c) KSTL-2, SAR Growth curve and Shine down curve for sample (b) KSTL-1 and (d) KSTL-2 144

Figure 6.6: (a), (c), (e) and (g) shows radial plots for the samples ABTL-1, ABTL-2, KSTL-2 and ABP-1 and (b), (d), (f) and (h) showing the histograms of these samples. Total number of discs (n) shown on the upper right corner of the figures.....145

Figure 6.7: (a) Marginal lowering of the sea between 5 and 3 ka caused by low energy environment around Shakti Bet and the river activity was limited to the north-eastern fringes. Surface expression of

the Allah Bund Fault Scarp (ABFS) may have appeared at this time. Human settlement probably also came around this period. (b) Fluvial system began to weaken along with withdrawal of marginally high sea; first major earthquake probably caused initiation of Allah Bund Fault during 2.2 and 1.4 ka. (c) Weakening of fluvial regime continued, development of Allah Bund scarp and submergence of Sindri after 1819 earthquake to achieve present land form.....151

List of Tables

Chapter 1: Introduction

Table1.1: Dating methods for seismic and tectonic events (after Noller et al., 2000).....5

Chapter 2: Experimental procedures and protocols

Table 2.1:Single aliquot regenerative protocol (Murray and Wintle, 2000).....44

Chapter 3: Resetting of Luminescence in Sand Dikes

Table 3.1: Soil Profile Type Classifications reproduced from International Building code Council (2009).....55

Table 3.2: Rise in temperature for a combination of different channel velocity and dike width, for kinematic viscosity 1 m^2/s and injection time 1 second.....57

Chapter 4: Luminescence Studies of Sand Dikes

Table 4.1:List of major earthquakes in North East India.....62

Table 4.2: Comparison of SAR D_e with NCF correction and without NCF correction.....81

Table 4.3: Details of samples, depth, type, radioactivity data, water content, De and calculated Ages.....82

Chapter 5: Resetting of Luminescence in Fault Gouges

Table 5.1: Details of samples, measured D_e, radioactivity data, alpha efficiency fading factor, assumed water content and TL ages.....126

Chapter 6: Luminescence studies of Tectonic Events in western India

Table 6.1: Equivalent dose (De), Dose Rate and ages obtained on the western Great Rann sediments.....148

Chapter 1

Introduction

1.1 Motivation and Background

Tectonics and seismicity arise from complex motion of plates and consequent generation and release of internal and external stresses on various spatial and temporal scales. These play an important role in transforming and creating new landscapes and affect the life and landscapes on the earth. Evaluation of seismic hazards on the earth therefore becomes necessary to better inform the development of survival strategies and, this call for reconstruction of the timing and amplitude of past tectonic/seismic events as also of understanding of the stresses and rock structure underneath. Dating of seismic/tectonic events is an essential part of the paleoseismology. It provides an estimate of the fault activity, associated deformations, rate of fault slip, and rate of earthquake recurrence. For dating of fault activity one need to 1) identify the fault related features (e.g. fault gouge, liquefaction

features, fault scarp, river terraces etc), 2) assign a date to these features using suitable geochronological methods (Burbank and Anderson, 2009)

Reconstruction of history of earth evolution process is challenging. Several methods and techniques have been and are being developed. These methods can be divided in to two categories 1) relative dating methods and 2) absolute dating methods (Table 1). Some of these methods are summarized in section 1.2. Ideally the technique best suited to reconstruct past seismic/tectonic events are the ones that use materials/landscape feature that were created in direct response to past tectonic /seismic events. This thesis explores the use of luminescence dating in the reconstruction of the dating of past seismic events and examines the prospect of dating of fault gouges, sand dikes, fault scarp and sediments of truncated river channels and follows from previous such attempts by Ikeya et al. (1982), Singhvi et al. (1994), Banerjee (1996), Banerjee et al. (1999), for Fault Gouge and Porat et al. (2007), Mahan and Crone (2008) for Sand Dikes.

The identification of a geomorphic marker related (directly or indirectly) to the tectonic activity is an essential part to have correct estimation of time of the tectonic activity. The best suitable geomorphic markers which can be used to reconstruct the past seismic history such as river terraces, Fault scarp, Fault Gouge and Sand Dikes are a consequence of tectonic activity and provide a suitable means to understand the seismic history of the area.

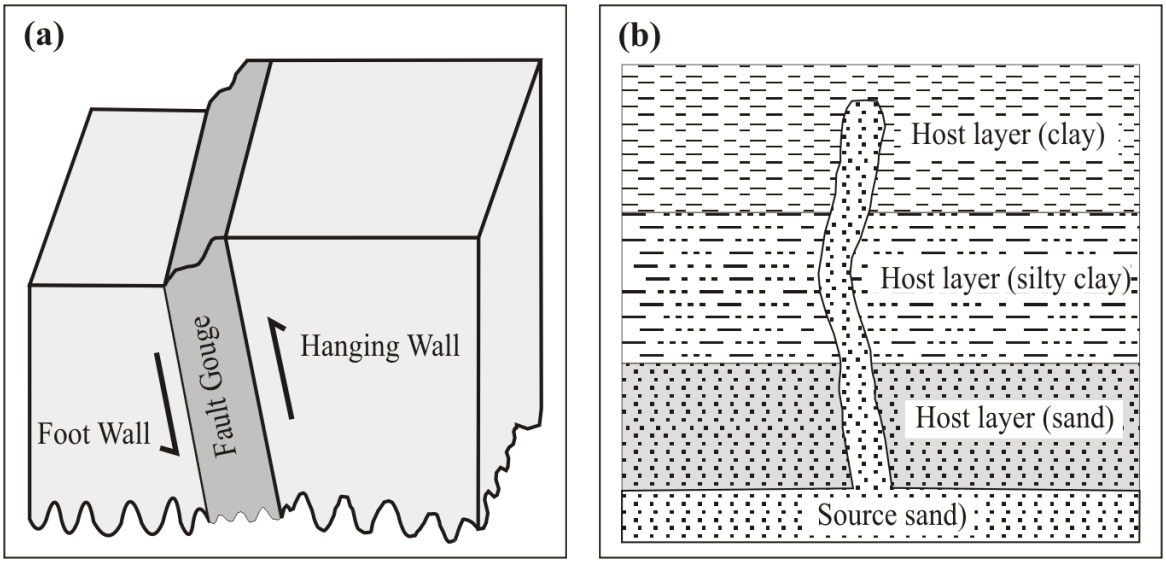

Figure 1.1: Schematic diagram showing (a) fault gouge and (b) sand dike

When the two blocks of rock slide each other a fine powdery material is generated (May or may not be recrystallized depending upon the frictional temperature generated during faulting event), the material generated is called as fault gouge. The fault gouge is usually composed of detrital minerals and secondary authigenic clay minerals. Particularly, illite forms due to retrograde hydration reactions (Zwingmann and Mancktelow, 2004).

When earthquake takes place shock waves are generated, these waves travel through the earth's crust. Due to the hydrostatic pressure some of the base material is injected into the layers overlying the base material. During this process the water act as lubricant, the injected material is called dike. Figure 1.1 shows the schematic diagram of fault gouge and sand dike.

1.2 Chronometric methods for Fault Gouges and Sand dikes

The methods for estimating the timing of earthquakes can be classified as direct and indirect dating methods. The direct dating methods use the features which are directly associated with the event, like fault gouge, injection dikes, sand blows, surfaces exposed by faulting. In case of indirect methods associated features like fault scarp, river terraces, colluvium wedge etc are used. The other indirect methods which were used in past includes relationships between the displaced and un−displaced layer associated with the fault (Yamazaki et al., 1984), surface texture analysis of quartz grains (Kanaori et al., 1978; Kanaori, 1983). Some of these chronometric methods are discussed in following sections

1.2.1 Cosmogenic radionuclide method

Cosmogenic radionuclides are produced by nuclear spallation reactions in the rocks, due to exposure to cosmic ray neutrons and muons at the surface of the earth (lal and Arnold, 1985). Materials ranging in age from few hundred years to tens of million years can be dated using this method. Presently commonly used nuclides are ^{10}Be, ^{14}C, ^{26}Al, ^{36}Cl, ^{3}He, ^{21}Ne and stable noble gases. In most of the case the used target is quartz which contains Si and O, and product are ^{10}Be, ^{26}Al and ^{36}Cl, the production of a radionuclide by nuclear reaction is given by following equation

$$P = \frac{R}{\lambda}[1 - \exp(-\lambda t)] \qquad (1.1)$$

The Cosmogenic Radionuclide Method (CRN) has been applied on fault scarp and exposed fault rock surfaces. When the faulting takes place one of the blocks is uplifted, and the uplifted surface gets exposed to cosmic rays. On exposed surface a buildup of cosmic ray induced radionuclides takes place and concentration gives an estimate of age of fault movement. The method was used for the dating of fault scarp along the Hebgen Lake fault zone (Zreda and Noller, 1998). The ^{36}Cl ages from the bedrock and fault scarp indicated that the earthquakes were occurred at 0.4, 1.7, 2.6, 7.0, 20.3, and 23.8 ka. Phillips et al. (2003) applied the CRN on alluvial fault scarp of Canyon fault in central New Mexico. The CRN ages on the alluvial fault scarp accounted for degraded fault scarp profile in the Canyon fault suggested the rupture event during 79−108 ka and 5−46 ka. Palumbo et al. (2004) and Schlagenhauf et al. (2011) used the method to estimate the movement along Magnola fault in Central Italy, and suggested occurrence of at least five events at 4.8, 6.7, 7.4, 10.5 and 12.0 ka with slips varying from 275 to 155 cm along Magnola fault. Schlagenhauf et al. (2011) using CRN dating suggested the 9 large earthquakes occurrence along the Magnola fault in two 5–6 ka long cycles.

Where P is number of atoms of the unstable product nuclide, R is production rate of the product nuclide by the nuclear Reaction and λ is decay constant of the unstable product nuclide.

1.2.2 Radiocarbon dating method

The method of radiocarbon dating relies on the principal that the carbon (organic matter) is widely distributed over the earth, and cycled through many carbon reservoirs. Various geological processes including the volcanic activities, deposition of carbon in sediments etc., involves the carbon cycle (Craig, 1953; Craig, 1957). Carbon has three isotopes ^{12}C, ^{13}C and ^{14}C. Among these ^{14}C is radioactive with half−life of 5730 years while other two are stable. In the upper atmosphere the radioactive carbon isotope is produced by the cosmic ray spallation on ^{14}N, subsequently oxidized to $^{14}CO_2$ and distributed to earth's atmosphere (Taylor, 1985). Most of this CO_2 is absorbed by the ocean, leaving a small percentage for the terrestrial biosphere. The metabolic processes maintain the activity of ^{14}C in living organisms with the atmosphere. Once the metabolic processes cease (due to death of the organism, plant, human or animal) the decay of radioactive carbon isotope starts. Measuring the activity

Table1.1: Dating methods for seismic and tectonic events (after Noller et al., 2000)

Method	**Dating Range**	**Material/Proxies used**
(a) Relative Dating methods		
Soils and Soil−profile development	10−500 ka	Boulders, changes in soil properties due to weathering, redistribution of minerals
Scarp morphology	2−20 ka	Changes in scarp profile due to surface processes
Rock and mineral weather	0.1−400 ka	Boulders, alteration of rock and minerals due to exposure to weathering
(b) Absolute Dating methods		
Cosmogenic Radionuclide	~years to 10Ma	Quartz, olivene
Radiocarbon	50 years to 50 ka	Wood, shell, organic tissues
Fission Track	>2 ka	apatite, mica, sphene, zircon, volcanic glass
K−Ar dating	>20 ka	K−bearing silicates
U Series	0.1 ka to 50 ka	Sedimentary materials, carbonate (corals and speleothems)
Electron Spin Resonance	1 ka to >100 Ma	Enamel, bone, calcite, gypsum
Luminescence (TL/OSL)	~30 years to ~500 ka	Quartz, feldspar

of residual ^{14}C in the dead organism the age of sample can be estimated. The conventional age calculation equation (Stuiver and Polach, 1977) is given by

$$t = 8033 \log_e \left(\frac{CPM_{sample}}{CPM_{STD}} \right) \tag{1.2}$$

Where CPM_{sample} is the activity (counts per minute) for sample and CPM_{STD} is the activity for the standard. In the recent past the new improved method uses the isotope fractionation method and the equation 1.2 is modified to

$$t = 8033 \log_e \left(1 + \frac{D^{14}C}{1000} \right) \tag{1.3}$$

With $D^{14}C$ representing the normalized value of $d^{14}C$ and,

$$d^{14}C = \left(\frac{CPM_{sample}}{CPM_{STD}} - 1 \right) 1000 \quad {}^{0}/_{00} \tag{1.4}$$

The dating range of this method is from 50 years to 50000 years beyond which limitation of measurement techniques make it difficult to measure the concentration. Radiocarbon dating method was applied to determine the recurrence of earthquakes due to the movement along San Andreas fault California (Berger and Kaufman, 1980). The wood, charcoal and other organic materials associated with earthquake induced geomorphic features (e.g. sand dike) or broken stem of tree were used previously for radiocarbon dating to estimate the occurrence of earthquakes (Tuttle and Seeber, 1991; Bull, 1996; Sukhija et al., 1999; Tuttle et al., 2000).

1.2.3 Fission track dating analysis

The Fission Track Dating (FTD) method was introduced by Price and Walker (1963), afterwards the method was applied to variety of minerals e.g. mica, glass, calcite, zircon, horneblende, sphene and apatite. The method is based on the fact that the heavy charged particles from radioactive nuclides such as Uranium, while pass through the insulating material could leave the trails of the radiation damage. These tracks are called fission tracks. Each fission event produces single track as the two fragments fly in opposite directions and produce line defect in the crystal. These tracks can be seen by high resolution optical

microscope after etching the sample to stabilize the tracks (Young, 1958; Silk and Barnes, 1959; Price and Walker, 1962). The concentration of the natural ^{238}U in the sample can be estimated by counting number of tracks for natural collected sample and compared with the tracks due to irradiation of sample by ^{238}U in laboratory (Price and Walker, 1963; Naeser, 1967). The age equation and age of the sample is given by

$$t = \frac{1}{\lambda_D} \log_e \left(1 + \frac{\lambda_D \varphi \sigma I}{\lambda_f} \frac{\rho_s}{\rho_i} \right) \tag{1.5}$$

where λ_D is total decay constant for ^{238}U, λ_f is spontaneous fission decay constant of ^{238}U, I is isotopic ratio ^{235}U / ^{238}U , σ is thermal neutron cross section for ^{235}U , φ is thermal neutron fluence, ρ_s is spontaneous track density =number of spontaneous tracks/ area of sample and ρ_i is induced track density =number of induced tracks/ area of sample. Seward and Mancktelow (1994) used the FTD of apatite and zircon from the Simplon fault zone in the Simplon Alps. The FTD of apatite and zircons separated from the pseudotachylyte layer and from the borehole samples from Nojima fault Japan gave the initiation of the Nojima fault at ~60 Ma (Murakami and Tagami, 2004; Yamada et al., 2007).

1.2.4 Fault scarp diffusion

In this method, the age of a fault are derived by fitting the scarp profiles to the synthetic profiles generated using a diffusion equation or alternatively by classification using linear discriminant function (Mayer, 1984). In this method scrap degradation is expressed as a continuity equation for conservation of mass with sediment transport model (Bucknam and Anderson, 1979; Hanks et al., 1984; Nash, 1984). The age estimates are obtained by solving diffusion equation

$$\frac{\partial u}{\partial t} = K \frac{\partial}{\partial x} \left[F \left(\frac{\partial u}{\partial x} \right) \right] \tag{1.6}$$

Where u is the elevation, x is the horizontal distance, t is time, F is the function of slope representing the transport of the material at any time and at any point along the profile.

Diffusion coefficient K is estimated by comparing the morphology of fault scarp with the morphology of scarps of known age. The diffusion equation (1.6) has been solved

analytically (Hanks et al., 1984) and numerically using linear and nonlinear method to estimate the time of fault scarp formation (Andrews and Bucknam, 1987; Mattson and Bruhn, 2001). Pearthree and Calvo (1987) used the scarp diffusion method and estimated ages of faulted and unfaulted surfaces or about 100 ka for the most recent surface−rupture event. This method has been used to estimate the age of fault scarp formed due to repeated slip events along the San Andreas fault (Arrowsmith et al., 1998), scarp in Arava Valley along the Dead Sea, Israel (Enzel et al., 1996), fault scarp created due to surface−rupturing earthquakes along the Wasatch Fault Zone (Mattson and Bruhn, 2001).

1.2.5 U/Th dating

Uranium/Thorium or Uranium series dating is based on the detection the activities of ^{234}U decaying to ^{230}Th products in the decay chain of ^{238}U. The method can only be used if secular equilibrium has been established in the parent and daughter decay. When water seeps through the ground it dissolves some uranium but no thorium, as a result during evaporation of water. At the time of mineral formation the Uranium is trapped and starts decaying to produce the thorium. The elemental fractionation is a result of the different geochemical behavior of U and Th. U mainly exists in two oxidation states in nature ($U^{4+}$and U^{6+}), and at the Earth's surface it is dominant in its soluble U^{6+} form. It is soluble as uranyl ion $(UO_2)^{2+}$ in various uranyl carbonate forms (Ivanovich and Harmon, 1992)

For U/Th dating, the initial ratio of $\left(^{230}Th/^{238}U\right)$ at the time of sample formation must be known or calculated. With time, ^{230}Th accumulates in the sample through radiometric decay. The sample age is based on the difference between the initial ratio of $\left(^{230}Th/^{238}U\right)$ and the one in the sample being dated. The method assumes that the sample does not exchange ^{230}Th or ^{234}U with the environment (i.e., it is a closed system.) The method can be used for samples that can retain U and Th, such as carbonate sediments, bones and teeth. Ages between 1000 and 300,000 years have been reported.

Taking the assumption that the decay system remains closed after the deposition of U and Th, the development of $\left(^{234}U/^{238}U\right)$ and $\left(^{230}Th/^{238}U\right)$ is described by equations (Ivanovich and Harmon, 1992) below

$$\left(\frac{^{234}U}{^{238}Th}\right)(t) = \left(\left(\frac{^{234}U}{^{238}Th}\right)_{initial} - 1\right)e^{-\lambda_{234}t} + 1 \qquad (1.7)$$

$$\left(\frac{^{230}Th}{^{238}U}\right)(t) = \left(1-e^{-\lambda_{230}t}\right) + \left(\left(\frac{^{230}U}{^{238}U}\right)(t) - 1\right)\frac{\lambda_{230}}{\lambda_{230}-\lambda_{234}}\left(1 - e^{-(\lambda_{230} - \lambda_{234})t}\right) \qquad (1.8)$$

Where $\left(^{234}U/^{238}U\right)_{initial}$ is the initial $\left(^{234}U/^{238}U\right)$ ratio, λ_i are the decay constants for ^{230}Th and ^{234}U, respectively.

The method has been used to constrain the tectonic activities along various faults (Uysal et al., 2007; Nuriel et al., 2012; Saillard et al., 2012). Paleoseismic events using mollusk from seismically uplifted beaches in Persian Gulf gave age range 11.3−2 ka (Ivanovich et al., 1983). U/Th ages from Grotta del Cervo Italy, suggested the seismic activity in the periods 350−150 ka, 110−90 ka, 40−30 ka and <5 ka (Postpischl et al., 1991). Flotte et al., (2001) and Verhaert et al., (2004) used this method on post−tectonic flowstones on fault planes and syn−tectonic calcite mixed with brecciated limestones. Some other studies have utilized the U−series dating technique to date displaced and damaged cave deposits to constrain the recurrence patterns of paleoseismic events (Pons−Branchu et al., 2004; Kagan et al., 2005). Speleothems from preseismic and postseismic depostis from Soreq and Har−Tuv caves, located near Dead Sea Transform in Israel were dated by U/Th dating (Kagan et al., 2005). Eighteen earthquake events were identified in the Dead Sea Transform and a recurrence interval of 10 ka was estimated during 185 ka period. Uysal et al. (2007) used U/Th dating method to date travertine deposits precipitated in co−seismic extensional fissures along a fault in Western Turkey, and suggested the initiation of formation of fissures ranging from 24.6 ± 0.2 ka to 121.0 ± 2.0 ka. Recently travertine deposits in North Anatolian Fault Zone, Turkey were dated by Temiz et al. (2013), using U/Th method. The estimated age of these travertine deposits were 52,649 ± 8040 years and 96,308 ± 17,674 years, and between 17,962 ± 1671 years and 133,463 ± 76,882 years.

1.2.6 K−Ar dating

The K−Ar system has been used for the dating of lavas and was developed in 1950s. Potassium has three natural occurring isotopes ^{41}K, ^{39}K and ^{40}K, former two are stable whereas Potassium−40 is radioactive and decays with a half−life of 1.25 billion years. ^{40}K

decays to ^{40}Ar and ^{40}Ca in a ratio of ~11 to ~89. Chemically potassium is reactive metal whereas argon is an inert gas meaning while mineral formation potassium will be trapped and argon will escape. Argon is found in Earth's atmosphere to about 1 percent. So assuming that no air gets into a mineral grain when it first forms, it has zero argon content i.e. a fresh mineral grain has its K−Ar "clock" set at zero. The K−Ar method works by counting these radiogenic ^{40}Ar atoms trapped inside minerals. The age equation for K−Ar method is

$$t = \frac{1}{\lambda}\left(\frac{^{40}Ar^{*}}{^{40}K}\left(\frac{\lambda}{\lambda_e}\right) - 1\right) \qquad (1.9)$$

Where λ is total decay constant of ^{40}K, λ_e is the decay constant of ^{40}K to ^{40}Ar, $^{40}Ar^{*}$ is the argon produced by decay of ^{40}K.

With an assumption of having illite formation *insitu,* the method was first applied by Lyons and Jonathan (1971) to determine the absolute timing of fault activities. Illite separated from the fault gouge was used. A discrepancy was observed in expected and measured age by K−Ar method and attributed to the loss of radiogenic argon from the fault gouge. Illite separated from fault gouge has been used as the test object for isotopic dating (K−Ar) and to analyze the characteristics of fault activities (Yurtmen et al., 2002; Zwingmann and Mancktelow, 2004; Uysal et al., 2006; Sasseville et al., 2008; Zwingmann et al., 2010; Tu et al., 2012).

1.2.7 Electron Spin Resonance (ESR) Dating

Electron Spin Resonance (also called as Electron Paramagnetic Resonance, EPR) involves the measurements of paramagnetic ions in a sample. ESR is a non−destructive method for measuring the concentration of paramagnetic species (centers) and free radicals in liquids and solids. Some of these centers are inducted by exposure to radiation and the concentration of such centers in a sample is a measure of the total radiation dose to which the sample was exposed. The age can be calculated from geological dose by estimating the annual dose of the natural radiation from the content of natural radioactive elements (^{238}U, ^{232}Th, ^{40}K, and cosmic rays).

Observation of ESR is based on the fact that a charged particle spins around its axis and acts like a tiny bar magnet. In a magnetic field, the degeneracy of a particular energy state that depends on the value of m_l (magnetic quantum number) as well as of total quantum

number (n), is broken and lead to the Zeeman splitting. Under a magnetic field H, spin states of a paramagnetic system are quantized in directions parallel and antiparallel to the field resulting in a splitting of the energy levels, so that the interaction of magnetic moment with magnetic field gives rise to an additional energy contribution E, $\Delta E = -\mu . H$ or

$$\Delta E = -\mu_{s,z} H = -g\beta m_s H \qquad (1.10)$$

Where g is known as g factor, β is the Bohr magnetron, m_s is the spin quantum number of electron. The value of E corresponding to the two possible states is shown in Figure 1.2. The population in the two energy states is governed by the Maxwell Boltzmann law and it is possible to excite charges from lower energy state to the upper, by supplying external energy in the microwave region such that the relation (1.11) is satisfied,

$$\Delta E = h\nu = g\,\beta\,H \qquad (1.11)$$

This is the fundamental equation of ESR and represents the resonance condition. Here ν is the frequency of electromagnetic radiation. The age equation is given by

$$Age(T) = \frac{D_e}{\dot{D}} \qquad (1.12)$$

Where in equation(1.12), D_e is the equivalent dose and $\dot{D}$ is the dose rate at which dose has been accumulated in the sample.

Ikeya et al. (1982) reported the first ESR date by using quartz grains from Atotsugawa fault gouge. The fault gouge was dated to 65 ka. Fukuchi et al. (1986) used different ESR centers to date the movement along Itoigawa−Shizuoka Tectonic line and Minobu fault in Japan. The fault movement range was estimated to be from 0.30 Ma to 0.55 Ma. Buhay et al. (1988) used the plateau ESR ages for finer grain size and suggested the movement along San Jacinto Fault around 75 ka. In similar approach Lee and Schwarcz (1994) used different ESR centers and age plateau for different grain sizes to date the fault gouge along the San Gabriel fault zone. The results from their study suggested the tectonic activity along the San Gabriel fault zone during 339−440 ka (Limerock fault), 230−611 ka (Barrel Spring fault), 344−666 ka (Santa Clara fault), 352−984 (Bear Divide fault) and 221−504 ka (San Gabriel fault).

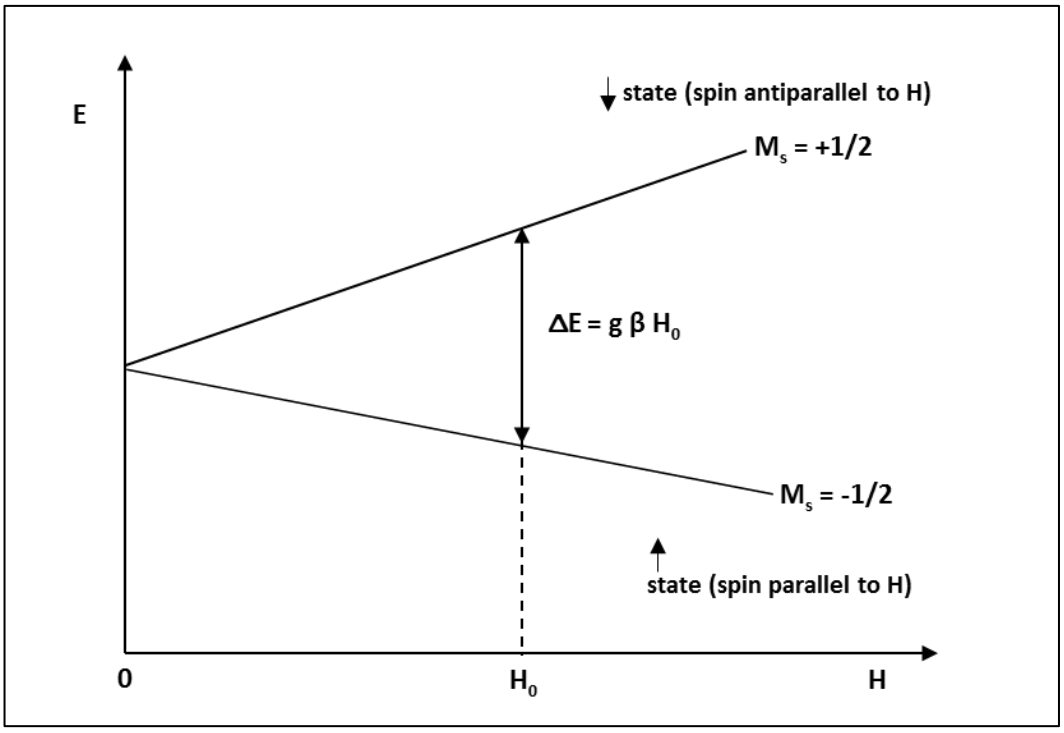

Figure 1.2: Splitting of the energy levels in a magnetic field (Zeeman splitting)

The ESR dating has been used to date the events like mineralization, thermal annealing, geological faults and optical bleaching (Grun and Invernati, 1985; Ikeya, 1993; Grun, 2006). The ESR dates on fault gouge from Palghat gap shear zone Kerala, India suggested that fault at Desamangalam was active during the mid−Quaternary period ~ 430 ka (Gundu Rao et al., 2002). ESR dating of intrafault gypsum from Katrol hill range, India suggested the uplift during late quaternary period (~70 ka) (Mathew et al., 2004). ESR dating of calcareous fault gouge from Ushikubi fault in Japan using SO_3^- center showed the latest movement along the fault at around 1.9 ka (Fantong et al., 2013).

1.2.8 Soil chronosequence method

The soils of deposits or surfaces that have been deformed or are related to tectonics, have been successfully used to date neotectonic events (Birkeland, 1984; Amit et al., 1996; McCalpin and Berry, 1996).

A chronosequence is defined as “A sequence of soils developed on similar parent materials and relief under the influence of constant or ineffectively varying climate and biotic factors, whose differences can thus be ascribed to the lapse of differing increments of time

since the initiation of soil formation" (Stevens and Walker, 1970). In the method the soil chronosequence of faulted area are compared to independent age estimates of similar soil chronosequence of nearby region and thus time for tectonic events are constrained, (McCalpin and Berry, 1996).

Buried soils developed on colluvial and fluvial sediments were dated using thermoluminescence (Forman et al., 1988) in Utah and Colorado from Wasatch fault zone America. The ages obtained on the buried soils were 0.5 ± 0.1 ka and 2.7 ± 0.4 ka. The thermoluminescence method was used to date the paleoearthquakes by Forman et al. (1989), Forman et al. (1991) and McCalpin and Forman (1991). Forman et al. (1991) identified three faulting events which occurred during 4.5−3.5 ka, 3.2−2.5 ka and 1.4−1.0 ka. The TL ages obtained were in good agreement with radiocarbon ages from the site. Porat et al. (1996) using Infrared stimulated luminescence on soil samples and correlating these with the geomorphic features suggested that Arava valley has faced three tectonic events at 34.8 ka, 18.1 ka and 2 ka. Fault gouge from South−Central Kumaun Himalaya was dated by infrared stimulated luminescence of feldspar mineral (Singhvi et al., 1994; Banerjee, 1996). Optically stimulated luminescence method was sued to date alluvial gravels and colluvial deposits from Sabzevar thrust fault in northeastern Iran (Fattahi et al., 2006). Rodríguez−Pascua et al. (2012) using radiocarbon dating of the soil samples from a trench, lacustrine cores and archaeoseismic records suggested three events along the Pozohondo fault in South East Spain. These events were dated to < 26,000 years BP, 8000 BP and centuries I−VI AD.

1.3 Luminescence

1.3.1 Basic principles

When an insulating material, like mineral is exposed to ionizing radiation a tiny fraction of energy is stored in the form of trapped charges at defect sites in the lattice. The residence time of these charges ranges from a second or less to millions of years. The storage of these charges is cumulative with radiation dose and this makes the possible use of luminescence a tool for radiation dosimetry and geological chronometry. The mechanism of luminescence can be understood with band theory of solids. (Aitken, 1985; Chen and McKeever, 1997; McKeever and Chen, 1997; Bøtter−Jensen et al., 2003c). Irradiation by ionizing radiation caused excitation of electrons in the valence band to the conduction band and some of these

get trapped at lattice defects that result in localized energy states (Figure 1.3a and b). The stored charges can be released by external stimulus (thermal, optical, mechanical etc.) and some of these released charges radiatively recombine to emit light (Figure 1.3c). Generally two variants used for external stimulation are thermal stimulation and optical stimulation and both variants are used. The light intensity after the stimulation is proportional to the trapped charges and hence proportional to the radiation dose.

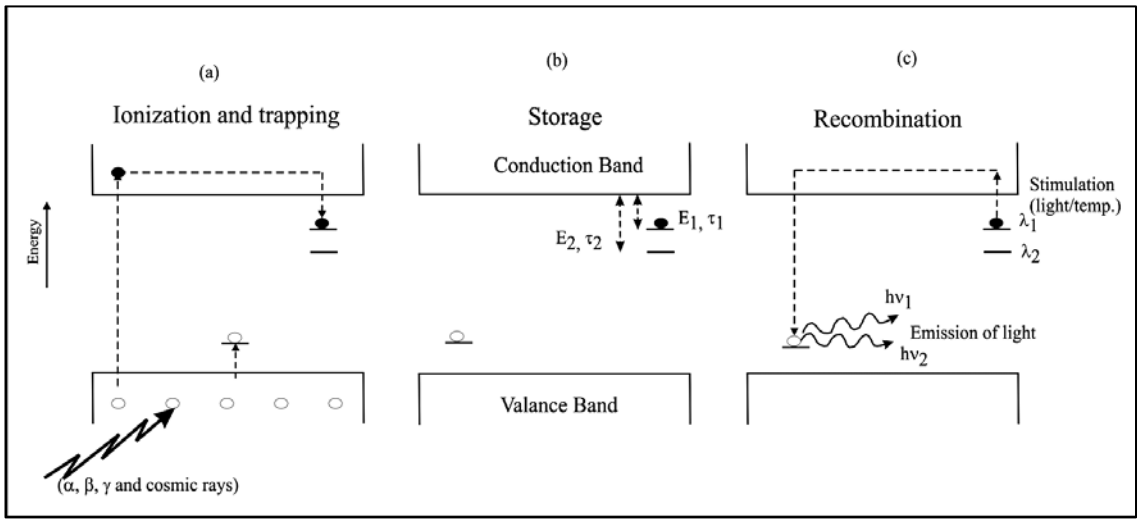

Figure 1.3: Mechanism of luminescence a)ionization and trapping of electrons and holes at localized energy states, b)trapping depends upon the amount of trapping energy (separation from conduction band or valence band for electron or hole respectively) and c) release of light in the form of luminescence after external stimulation like heat or light (after Aitken, 1985)

The life time of these trapped charges is decided by the charge environment at its trapping site i.e. binding energy of trapped charge, called as trap depth. The life time of a trap can be expressed as,

$$\tau = s^{-1} \exp(E / kT) \qquad (1.13)$$

where s is the frequency factor, E is the trap depth, k is the Boltzmann's constant and T is the ambient temperature. The trap depth typically ranges between 0.5−2.0 eV, giving life time ranging from $1-10^{15}$ s for very shallow traps to very deep traps (Singhvi and Wagner, 1986).

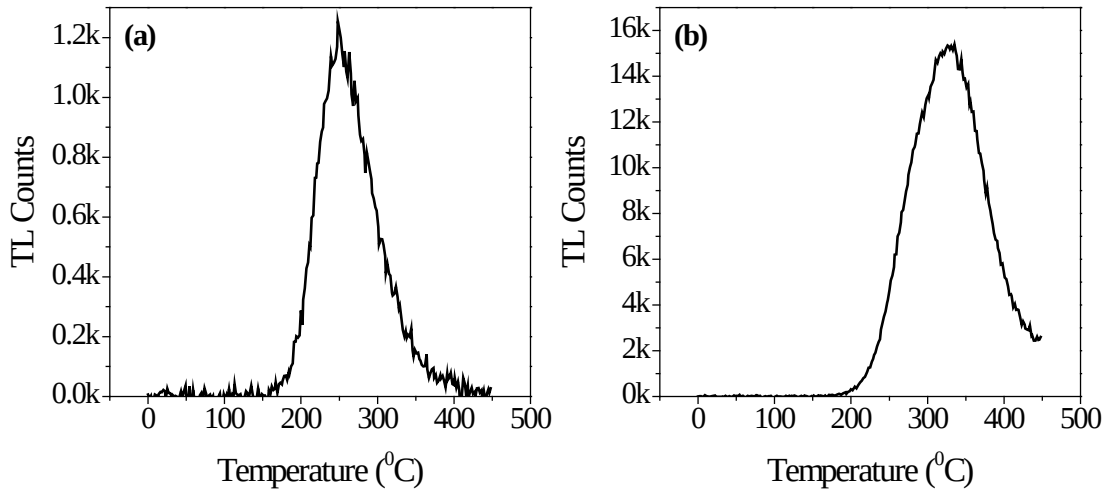

Figure 1.4: Natural TL glow curves for (a) feldspar (PCMA−11 from Gish Fault) and (b) quartz (BB−1 from Bedabari site)

1.3.2 Thermoluminescence (TL)

In thermally stimulated luminescence measurements eviction of charges occurs as the temperature of sample is increased in a controlled manner and one observes a series of peaks in luminescence emission, termed as glow peaks and glow curves. At higher temperatures the incandescence takes over. The basic concepts were developed by Randall and Wilkins (1945) and later by Garlick and Gibson (1948). Levy (1974) provide a summary of the basics of physical processes leading to thermoluminescence. The details of thermoluminescence process can be found in McKeever (1985) and Aitken (1985). A typical glow curve for feldspar and quartz are shown in Figure 1.4, and the shape can change depending on the spectral window in which the emission is recorded.

1.3.3 Optically Stimulated Luminescence (OSL)

In OSL the luminescence is recorded under constant wave stimulation and the signal is in the form of decay curve known as shine down curve. In the recent past OSL was preferably used over TL due to advantages like probing of single type traps, absence of interference from black body radiation, thereby improving the signal to noise ratio to be large, absence of phase change due to heating etc. Based on the wavelength of the optical stimulation source the OSL is termed as IRSL (InfraRed Stimulated Luminescence), BLSL (Blue Light

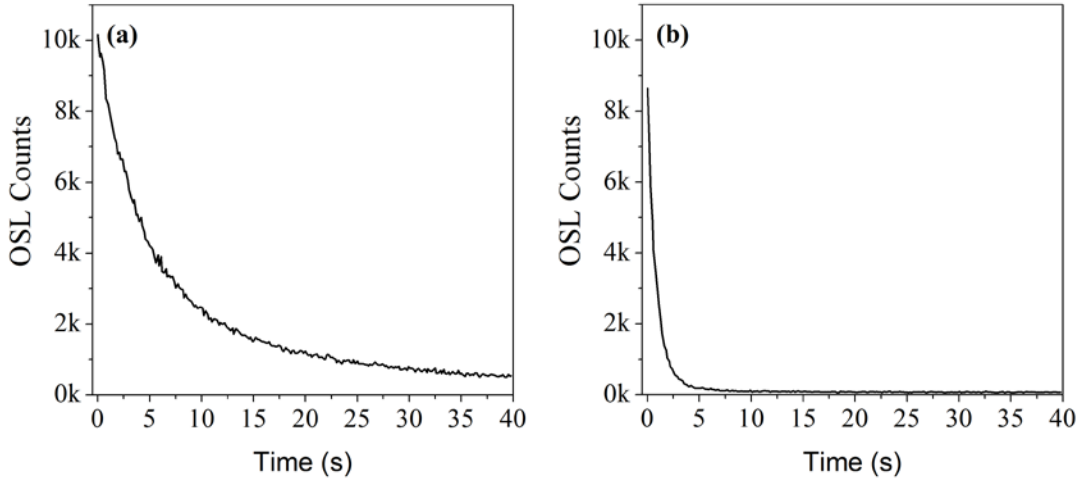

Figure 1.5: Shine down curves for (a) PCMA-11, feldspar from Gish fault (IRSL stimulation) and (b) KKT-16, quartz from Kakoti site (BLSL stimulation)

Stimulated Luminescence) etc. Whereas based on the stimulating power it is termed as continuous wave OSL (CW−OSL), linear modulated OSL (LMOSL) or pulsed OSL (Bøtter−Jensen et al., 2003c). Figure 1.5 shows the IRSL and OSL shine down curves for feldspar and quartz samples collected from Gish fault zone and Kakoti site (sand dike).

The CW OSL from quartz and feldspar can be expressed as the sum of exponentials (Bailey et al., 1997; Bluszcz and Adamiec, 2006; Li and Li, 2006) and are termed as the components of OSL decay. Murari (2008) suggested that the blue stimulated luminescence can be expressed as sum of exponentials,

$$I_{OSL} = \sum_{k} a_k e^{-\lambda_k t} \tag{1.14}$$

where a_k is the amplitude of k^{th} component and λ_k is the product of photon flux and photo−ionization cross−section (decay constant). In general up to three components have been reported in quartz OSL but in some cases it can even be seven. For feldspars generally three components are inferred (Kitis et al., 2002; Tsukamoto et al., 2006).

1.3.4 Luminescence dating

In essence luminescence dating (LD) is dosimetry of natural environment. The

early attempts to use luminescence method in estimating the exposure of radiation towards natural mineral and their TL properties was done by Daniels and his coworkers in early 1940s. Later attempts were made to use the method in ceramics, personal dosimetry, archaeology and earth sciences (Aitken et al., 1964; Aitken et al., 1968; Bortolot et al., 1973; McKeever, 1985; Singhvi and Wagner, 1986)

In luminescence dating the radiation dose acquired by a natural mineral is measured as the intensity of stimulated luminescence and this with appropriate calibration for luminescence sensitivity is converted to radiation dose units. The measurement of elemental abundance of naturally occurring radioactive nuclides (e.g. U−238, U−235, Th−232 and K−40) enables in computation of annual dose rate and the ratio of (acquired radiation dose and dose rate) these two provide the age.

The events dated by the method are the events that erase the geological luminescence to zero or a near zero value. On burial the accumulation of luminescence is reinitiated due to irradiation of ambient radioactivity. The event which can be dated by luminescence technique are, i) the most recent daylight exposure of the minerals in the sediment, ii) heating event and iii) authigenic precipitation event i.e. mineral formation (Singhvi and Wagner, 1986).

The luminescence signal from a mineral, exposed to natural ionizing radiation, is proportional to concentration of the trapped electron in a particular trap. The electron population in the trapping center is proportional to time of irradiation. Thus, naturally available ubiquitous minerals can be used as thermoluminescent dosimeters, with the constraints,

I. the number of trap sites in the mineral are sufficiently large (to avoid saturation of luminescent signal)
II. the life time of the trapped electrons is higher than the event duration, (to have sufficient time for the storage of luminescence signal)
III. the system is closed, implies there should not be any means to leak the trapped electron or there is no change in the natural dose rate. In any case if there was any leakage, or change a proper correction for that should be applied
IV. and most importantly when the event starts, the trapped electron population, related to “that” signal, must be zeroed (resetting of luminescence signal)

Most commonly used and available natural dosimeters which satisfy above constraints are quartz and feldspar.

1.3.4.1 Quartz

Quartz is the most widely used dating chronometer due to its robustness against weathering and the long terms stability of its luminescence signal. Several authors (McKeever, 1985; Franklin et al., 1995; Krbetschek et al., 1997; Bøtter−Jensen et al., 2003a) reported the TL glow peaks and emission spectrum of quartz. Quartz has TL peaks at 95–110°C, 150–180°C, 200–220°C, 325°C and 375°C with trap depth 0.84 eV to 1.66 eV and life time 0.13×10^{-3} year to $\geq 10^{8}$ year (Aitken, 1985). Three main TL emission bands of quartz used for dating applications are 360–440 nm (UV−blue), 460–500 nm (blue−green) and at 600–650 nm (orange−red). The OSL spectra of quartz with 647 nm stimulation suggest, the presence of single emission band centered at 365 nm (Huntley et al., 1996). The OSL of quartz is correlated with 325°C TL peak (Smith et al., 1990; Kitis et al., 2010).

The difficulty with quartz however has been its lower saturation in respect of luminescence intensity with radiation dose. In normal radiation environments, this low saturation dose limits its application to 100 ka and thereabouts, however using isolation of components higher ages have also been reported (Pawley et al., 2010; Zander and Hilgers, 2013).

1.3.4.2 Feldspar

Most natural feldspars belong to the K−Na−Ca ternary diagram and have a general formula $K_xNa_yCa_{1-(x+y)}Al_{2-(x+y)}Si_{2+(x+y)}O_8$ (Krbetschek et al., 1997). In general feldspars have an ordered structure at low temperature and disorder structure at high temperature. At high temperature, all feldspar can form mixed crystals because of larger lattice parameters. Most feldspar classified in three groups, (i) sodium feldspars, (ii) potassium feldspars and (iii) calcium feldspars. Feldspar has TL peaks at 120°C, 250°C and 330°C with trap depth 0.76 eV to 1.68 eV and corresponding life time of the trapped electron ranges from 0.16×10^{-3} year to 9.2×10^{9} years (Aitken, 1985; Stricertsson, 1985; Mejdahl, 1989).The TL emission from feldspars comprises emissions at 280 nm, 340 nm, 380−400 nm, 550 nm and 730 nm (Townsend et al., 1993; Rendell et al., 1995). The IR stimulation using diodes (centered emission at 880 nm) of K feldspar showed two emission band from 300−350 nm and

centered at ~410 nm (Huntley et al., 1991). A correlation between the TL and IRSL was suggested, implying that the same recombination centers are being used by the two processes

The OSL stimulation of feldspar measured at 3.1 eV (300 nm) show emission bands centered at ~2.05 eV (600 nm), ~1.45 eV (855 nm) (Hütt et al., 1988). It was found that the 600−620 nm emission can be bleached by visible and IR stimulation. Jungner and Huntley (1991) using 633 nm He−Ne laser stimulated the K feldspar from Finland and observed that the stimulated emissions show band at 340 nm, strong emission at 400 nm and little emission at 300 and 500 nm wavelengths.

Most of the feldspar used in the natural dosimetry has been reported to be more sensitive and have higher saturation dose limits as compared to quartz, making them suitable for dating the older events. Wintle (1973)reported that the ages obtained from the feldspar were underestimated and attributed this as athermal or anomalous fading. The occurrence of anomalous fading in IRSL signal of feldspar has been also reported by several workers (Wintle, 1977; Spooner, 1992; Spooner, 1994; Lamothe and Auclair, 1999; Huntley and Lamothe, 2001) and models have been proposed for the fading mechanism (Aitken, 1985; Visocekas, 1985; Templer, 1986). The fading has been explained by quantum mechanical tunneling (Poolton et al., 2002a; Poolton et al., 2002b; Li and Li, 2008) described by a power law decay (Delbecq et al., 1974; Huntley, 2006).

Recent work using elevated temperature (290 °C) IRSL, after IR bleaching of the sample and known as post−IR IRSL ($pIRIR_{290}$) of K feldspar suggested less fading of the luminescence signal (Jain and Ankjærgaard, 2011; Thiel et al., 2011; Thomsen et al., 2011; Buylaert et al., 2012). Jain and Ankjærgaard (2011) using the time resolved OSL (TR−OSL) attempted to understand decay of feldspar signal due to tunneling. The various luminescence phenomena in feldspar such as luminescence efficiency, thermal partitioning of charge in different energy states and the recombination routes were successfully explained by using single trap model by them. The detail work by Sohbati et al. (2013) on the IRSL stimulation of Na−rich feldspar using IR stimulation at 50 °C, pIRIR stimulation at 290 °C in yellow and blue emission suggested that the $pIRIR_{290}$ in yellow emission is relatively stable, and when corrected for fading provided a good agreement with known ages.

1.3.5 Age determination (Age equation)

The estimation of radiation exposure of mineral in the natural environment and the rate at which exposure took place, the ratio of these two provide the luminescence age of the mineral. The total absorbed dose is estimated by calibration experiments which provide the laboratory beta dose that gives the same luminescence as given by a natural sample. This dose is termed as the paleodose or the equivalent beta dose (D_e). The time (age) since the last exposure to heat or light might have happened can be given by

$$\text{Age}(T) = \frac{\text{Luminescence acquired (L)}}{\text{Rate of Luminescence}} = \frac{\text{Luminescence acquired (L)}}{(\text{Luminescence}/\text{year})} \tag{1.15}$$

$$= \frac{\text{Luminescence acquired (L)}}{(\text{Luminescence}/\text{radiation dose}) \text{ x } (\text{radiation dose}/\text{year})} \tag{1.16}$$

$$= \frac{L}{(L/d)\times(d/t)} \tag{1.17}$$

$$T = \frac{L}{\sum_i \chi_i D_i} \tag{1.18}$$

where, i =α,β,γ and c (cosmic rays), χ = Luminescence sensitivity luminescence/radiation dose) and D = dose rate (radiation dose/year).

The linear energy transfer (LET) of alpha is higher than that of beta and gamma on account of higher charge and mass. This leads to a higher ionization density along the α–tracks and leads to charge saturation effects such that charge produced exceeds the trap available. Thus a major fraction of charge produced is not utilized to increase the level of luminescence. Consequently the efficiency of luminescence production per Gy of dose is reduced. Beta, gamma and cosmic rays have low LET and hence the luminescence production is higher. Thus,

$$\chi_\alpha \neq \chi_\beta = \chi_\gamma = \chi_c \tag{1.19}$$

With the above equality the age equation can be modified to,

$$T = \frac{P}{a D_\alpha + D_\beta + D_\gamma + D_c} \qquad (1.20)$$

Where, $a = \chi_\alpha / \chi_\beta$ is the alpha efficiency factor and $P = L/\chi_\beta$ is the laboratory dose (from a calibrated source) that produces the same level of luminescence in sample as by the natural dose rate and known as paleodose (P) or equivalent dose (De).

1.3.6 Evaluation of D_e

The basic principle is to compare natural luminescence with the luminescence induced by artificial (laboratory) irradiation. Two analytical methods, multiple aliquot additive dose method (MAAD) and single aliquot regeneration (SAR) method have been used widely. Methods for measurement of De are given in Chapter 2.

1.3.7 Dose rate

The amount of nuclear (ionizing) radiation delivered per unit time to a material is called dose rate and for dating application is usually expressed as Gy/ka. The dose rate is estimated by measuring concentration of natural radioactive elements (U, Th, and K). U and Th concentration can be measured using thick source ZnS (Ag) alpha counting whereas ^{40}K is estimated by gamma spectrometry. Cosmic rays contribution is computed using the latitude, longitude, altitude and the average burial depth and equations as suggested by Prescott and Hutton (1994). Details of dose rate calculations are discussed in Chapter 2.

1.4 Objectives and scope of the Thesis

The present thesis explored the application of luminescence dating for the dating of seismic events. The main objective of the thesis is to ascertain that the zeroing of luminescence signal occurs during the seismic events. For this the three types of markers were used 1) sand dikes, 2) fault gouge and 3) river terraces and truncated river channels.

Sand dikes are the direct outcome of seismic events and are of potential to provide the timing of the event. However a big difficulty is to make prediction, if the zeroing of signal happened. This concern has been addressed in the present work and calculations are being reported. Experimental work on the sand dike has been done and the dike samples were collected from North east India.

Similarly for the fault gouge the resetting of signal has been discussed and results from North east India have been presented.

The samples from Great Rann of Kutch were collected for paleaochannels and based on the luminescence studies an attempt was done to reconstruct the past seismic history of the region.

1.5 Chapter−wise details

Chapter 1: Introduction

This chapter describes the motivation of work and a brief description of dating methods used to date seismic and tectonic events. The basic principles and methodology of Luminescence dating is discussed in detail. A discussion on the minerals used for luminescence dating and nature of their signal is also presented.

Chapter 2: Experimental procedures and protocols

In this chapter details about the instruments used for the measurements in luminescence dating are discussed. This include, selection of luminescence emission using different optical filters and detection of light along with sample preparation methods and different measurement protocols used to estimate radiation dose.

Chapter 3: Resetting of Luminescence in Sand Dikes

This chapter discusses the resetting of luminescence signal due to viscous heating of dike material. The mathematical model has been discussed and calculations for rise in temperature during injection of dike have been described.

Chapter 4: Luminescence studies of Sand Dikes

This chapter discusses the results of luminescence studies carried out for samples, collected from different sand dikes from the north east India.

Chapter 5: Resetting of Luminescence in Fault Gouges

In this chapter a review of earlier work is given for the resetting of luminescence signal in fault gouge material. The calculations have been made to show that there is a rise in temperature during the rock rupture due to transient heating. This chapter also describes the results of luminescence studies carried out on samples collected from Sikkim Himalaya (North East India).

Chapter 6: Luminescence studies of tectonic events in Western India

In this chapter the luminescence studies performed on the samples from Great Rann of Kachchh and a model for the landscape evolution during the last 5 ka have been presented.

Chapter 7: Conclusions and Summary

This chapter summarizes the results obtained from the present study and also gives the future outlook.

Chapter 2

Experimental procedures and protocols

2.1 Introduction

This chapter presents a general discussion of methods and protocols used in the thesis along with a description of instruments used. The discussion includes sample collection and preparation, measurement techniques, analysis protocols and related aspects.

2.2 Sample collection and preparation methods

After freshly exposing the section the samples were collected in specially designed cylindrical tubes (~20 cm long and 2.5 cm diameter) made of aluminum or galvanized iron (Chandel et al., 2006). Due care was taken during the collection to ensure that the sample did not get any exposure to daylight. In the laboratory, the sample tubes were opened under subdued red light conditions and the outer ~ 5 cm from both sides of the tube were used for

the dose rate estimation. Central 10 cm portion was chemically processed for luminescence analysis. The laboratory equivalent dose (D_e) were estimated either using fine grain fraction (poly mineral) or coarse grain fraction (quartz). The grain size was chosen considering the availability of fraction and mean grain size. A brief description of fine grain and coarse grain method is given in section 2.2.1 and section 2.2.2

2.2.1 Fine Grain Method

The fine grain method was developed by (Zimmerman, 1971a). In this method fine grain fraction (4−11 μm) are extracted after treating the naturally collected sample with 1N HCl and 30% H_2O_2 to remove carbonates and organic matter respectively. This is followed by a de−flocculation treatment in 0.01N sodium oxalate solution. The de−flocculation helps to remove the clay size fraction. Multiple cycles of these steps are needed and at each step the samples were kept in ultrasonic bath to facilitate desegregation. Finally, the fine grain fraction is extracted by Stokes' settling method by suspending the sample in 6 cm column of alcohol for 1.5 minutes (to remove >11 μm) and for 15 minutes (to remove < 4 μm grain size). The 4−11 μm fraction is re−suspended in alcohol and equal volume of ~1 ml is pipetted onto 9.65 mm diameter aluminum discs kept in glass vials of ~1 cm diameter. These vials were then dried at temperature < 50 °C for about 16 hours. Since it is physically difficult to extract either quartz or feldspar from this grain size the luminescence signal is cumulative for polymineralic assemblages, where the signal is mostly dominated by K−feldspar on account of its significantly higher luminescence sensitivity. The use of fine grain luminescence implies the use of full age equation and the need to determine the alpha efficiency. This implies additional measurements using a vacuum alpha irradiation. Despite the tedium of additional measurements, the alpha dose dilutes the uncertainty due to environmental dose.

2.2.2 Coarse Grain Method

The method proposed by Ichikawa (1965) was further developed by Fleming (Fleming, 1970; Fleming, 1979). The chemical pretreatments here comprise treatment by 1N HCl and 30% H_2O_2 as for the fine grain method. After the removal of carbonate and organic matter the sample is dried at temperature < 50 °C and sieved to obtain the desired grain size. The quartz and feldspar separation is done either by density separation method using sodium

polytungstate (ρ = 2.58 gm/cm^3) where quartz (ρ = 2.65 gm/cm^3) sinks and feldspar (ρ = 2.56 gm/cm^3) floats; or by magnetic separation (Porat, 2006) using a Frantz Magnetic Separator (Model LB−1 of S. G. Frantz Company Inc.). The quartz fraction after separation is etched by 40% HF for 80 minutes (equivalent to removal of 15−20 μm alpha skin) followed by 12N HCl treatment for 30 minutes to dissolve the fluorides and oven dried at temperature < 50 °C for final measurement. Etched, cleaned and dried grains were deposited on stainless steel discs of diameter 9.65 mm using silicon oil (silkospray^{TM}). The advantage of using quartz is that it has no internal radioactivity and does not suffer athermal fading of its luminescence signal but the tradeoff is its lower saturation range. On the other hand the feldspar luminescence provides a possibility of both higher and lower dating range due to high sensitivity and saturation dose but has the difficulty associated with athermal fading.

2.3 Measurement of TL and OSL: Instrument

In the present work for the measurement of luminescence, two instruments Risø TL/OSL reader (Bøtter−Jensen et al., 2000) and Daybreak 2200 Reader (Bortolot, 2000) were used. A typical TL/OSL reader is an assembly of following units

1. A detection unit (assembly of photomultiplier tube and detection filters)
2. Stimulation unit (for TL/OSL measurements)
3. Irradiation unit (for administrating laboratory dose)
4. A system controller for interface and readout system

2.3.1 Detection Unit (TL OSL Reader)

The detection unit is the assembly of photomultiplier tube (PMT) and combination of filters placed in its front. The filters enable the selection of the desired band of emission and detection (normally UV 370 ± 30 nm for Quartz OSL AND TL) and 470 ± 30 nm for Feldspar (Feldspar IRSL and TL).

2.3.1.1 Photomultiplier Tube (PMT)

To detect the luminescence signal from quartz/feldspar minerals, a bi−alkali type PMT (EMI 9235 QA) is used. The maximum detection efficiency of this type of PMT is ~ 380 nm

(Figure 2.1), which makes it possible to detect the entire luminescence signal from quartz or feldspar grains in Ultraviolet (UV) to Blue region. For bright samples the photon counts were kept < 5×10^5 count/second (to avoid pileup effects) by employing either neutral density filter or by keeping low power of stimulation source. The sample to PMT cathode distance in the Risø TL/OSL luminescence reader is 55 mm, giving a detection solid angle of approximately 0.4 steradians (Bøtter−Jensen et al., 2000; Bøtter−Jensen et al., 2003a).

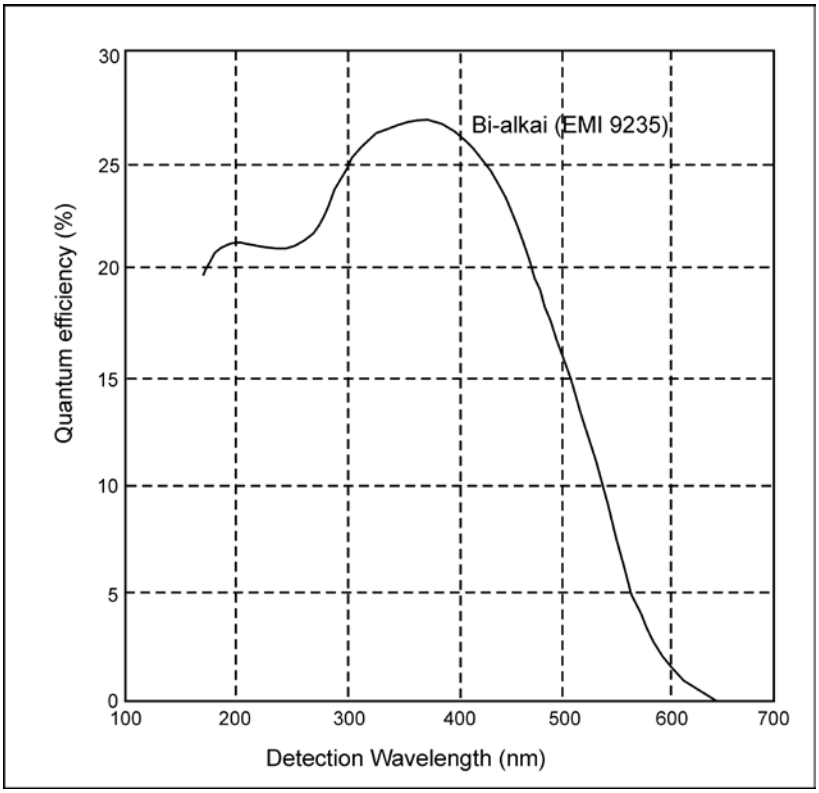

Figure 2.1: PMT response curve of quantum efficiency vs. wavelength. (Bøtter−Jensen et al., 2003a)

2.3.1.2 Filters

The emission of luminescence from minerals, like quartz and feldspar, ranges in the entire visible region of electromagnetic spectrum, more specifically UV to near Infrared (IR) range, after stimulation. The samples are stimulated using Light Emitting Diodes (LEDs) or lasers, in general blue (470 ± 30) nm for quartz and 890 ± 80 nm IR for feldspar. The main objectives of using a filter combination are (a) to avoid interference from stimulation source, (b) to isolate the desired emission band and (c) to reduce the blackbody radiation. To detect

emission from quartz samples during OSL measurement a 7.5 mm thick Hoya U−340 (330 ± 35 nm) filter was used. The emission from feldspar is around 410 nm (Krbetschek et al., 1997), for which the blue emission was selected using Corning CS 7−59 (390 ± 60 nm) filter along with a combination of BG−39 (320−650 nm) filter to cut the IR. The transmission spectra of these filter is shown in Figure 2.2.

2.3.2 Stimulation Unit

A luminescence sample can be stimulated either by heat (Thermal Stimulation) or light (Optical Stimulation). The Risø TL/OSL and Daybreak 2200 Reader both have heating and optical stimulation units suitable for quartz and feldspar minerals.

2.3.2.1 Thermal Stimulation

A linear heating is obtained by placing the sample on a low−mass heater strip made of a Nickel and Kanthal (a high resistance alloy). The heater strip is shaped with a depression to provide good heat transmission to the sample and to lift sample disc securely into the measurement position. The desired temperature is obtained by feeding a controlled current through the heating element. A good control on the temperature of heater strip is obtained by mounting a Cromel−Alumel (Cr/Al) thermocouple underneath the heater strip which provides feedback to controller for controlling the temperature. The heating system is able to heat samples to 700 °C, at linear heating rates from 0.1 to 10 °C/s with step of 0.1 °C/s. The heating strip is constantly purged by nitrogen gas which not only prevents the heating system from oxidation at high temperatures but also helps in conduction of heat to the sample from the heater plate to the grains and quenches spurious non radiative luminescence. In Risø reader the precession of the temperature control is < ±4°C and the error in reproducibility of heating rate is < 1%.

2.3.2.2 Optical Stimulation

For stimulation of quartz and feldspar samples blue and IR LEDs were used respectively. Infrared (IR) stimulation in the region 800−900 nm can stimulate luminescence from most feldspars (Hütt et al., 1988), but not from quartz at room temperature. For the stimulation of

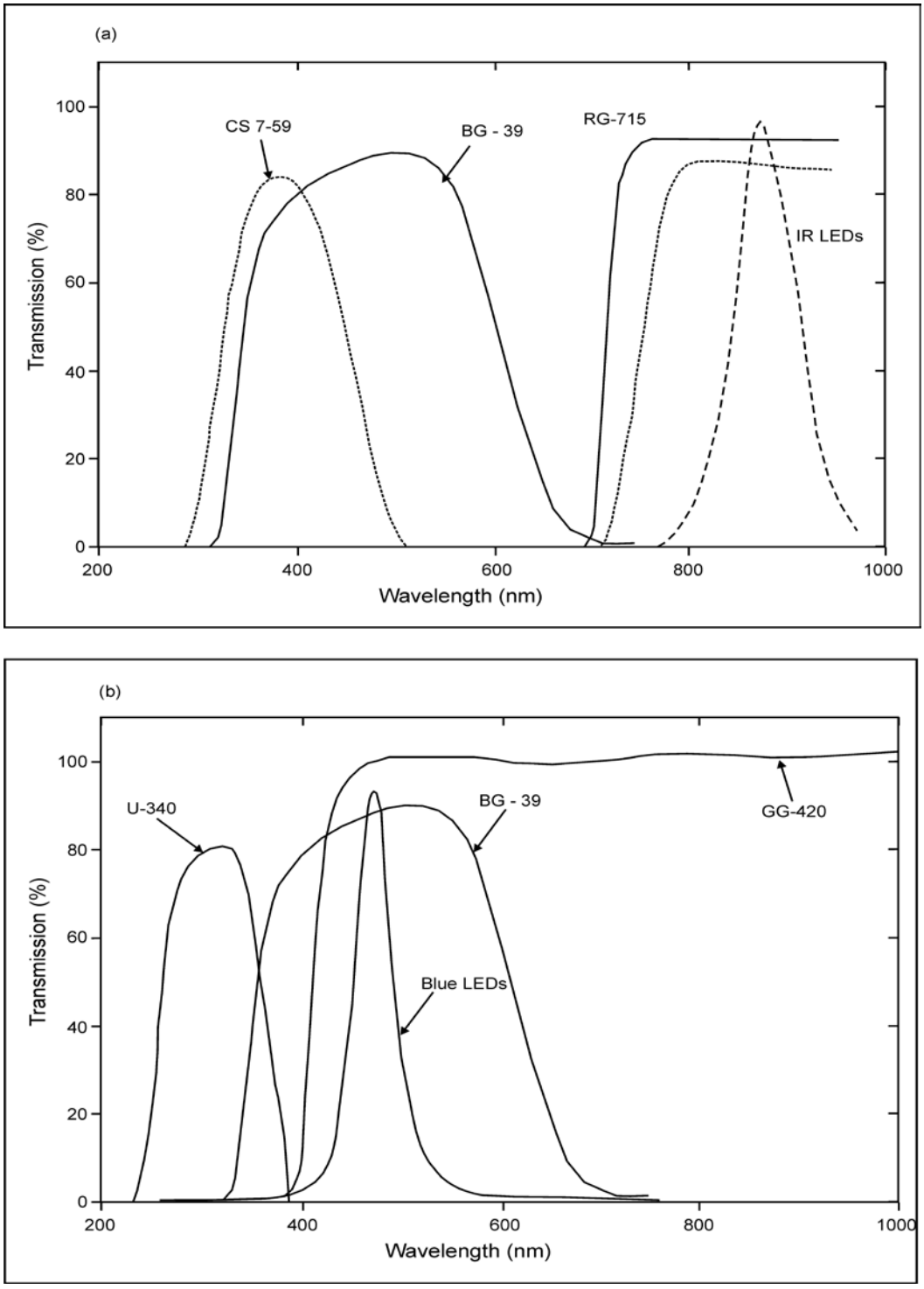

Figure 2.2: (a) Stimulation spectra of IR− LED and the filter combinations used to detect the luminescence in blue region and (b) Stimulation spectra of Blue LED and the filter combinations used to detect the luminescence in UV region

a single grain quartz sample, a green laser at 532 nm was used. The optical arrangement of Risø and Daybreak TL/OSL reader are as follows

Risø TL/OSL reader: In this system, an array of 28 blue LEDs is used. The LEDs are arranged in 4 clusters each containing seven of them. The emission wavelength of these LEDs is 470 ± 20 nm (Bøtter-Jensen et al., 2003). A long pass green filter (Schott GG−420) is incorporated in front of each blue LED cluster to minimize the amount of tail end of directly scattered blue light into the detection window (center at 330 nm). The distance between stimulation source and sample is ~20 mm. The maximum total power from 28 blue LEDs is 80 mW/cm2 at the sample position (Bøtter-Jensen et al., 2003). The IR LEDs, arranged in three clusters each containing seven individual LEDs, emits at 870 ± 40 nm. The maximum power is ~145 mW/cm^2 at the sample position (Bøtter-Jensen et al., 2003). Basic component of OSL detection system is shown in Figure 2.3.

The luminescence from single grains is achieved by stimulating grains kept in rhodium plated aluminum disc containing 100 cylindrical holes with 300 µm diameter and 300 µm depth, arranged in the form of a 10 by 10 array with 600 µm spacing between hole centers. The individual grains are stimulated by using a 10 mW

Nd:YVO_4 solid state laser beam, emitting at 532 nm focused at a spot <20 µm in diameter with maximum energy fluence rate at the sample of ~50 W/cm^2. The laser spot is steered by orthogonal mirrors attached to two programmed high precision motors.

Daybreak TL/OSL reader: The daybreak system has 20 blue LEDs, arranged in two parallel rows each containing 10 LEDs, emitting light at 470 ± 30 nm with maximum power 60 mW/cm^2 at sample position. For IR excitation, 10 LEDs arranged in two rows each containing 5 of them are used with the peak wavelength at 880 nm and the maximum power delivered to the sample position is 50 mW/cm^2 (Bortolot, 2000).

2.3.3 Irradiation Unit

2.3.3.1 Risø TL/OSL Reader

Most experiments were carried out on a Risø TL/OSL TL/DA−15 which has a mounted beta irradiator (^{90}Sr/^{90}Y beta source) on the top of the system as shown in Figure 2.3a. The distance between the radiation source and the sample is 5 mm. The calibration of the source

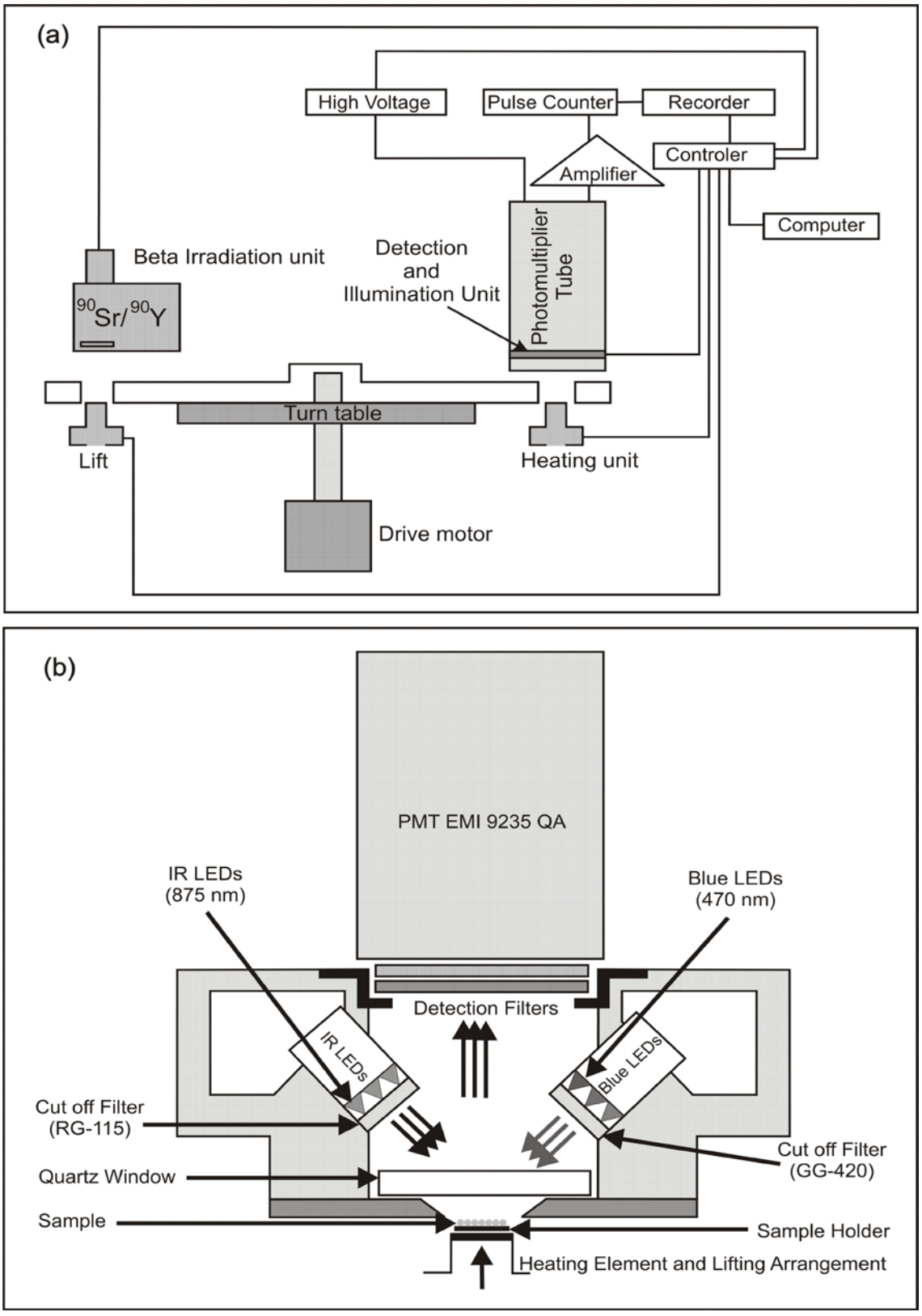

Figure 2.3: (a) Schematic of TL/OSL Reader, (b) detailed schematic of illumination and detection unit from (after Bøtter−Jensen et al., 2003b)

on the system using calibration quartz supplied by Risø yielded the beta source strength to be 3.29 Gy/min.

2.3.3.2 Daybreak TL/OSL Reader

Daybreak−2200 TL−OSL reader has the beta irradiator with source strength of 0.9 Gy/min as calibrated on March, 2012. The distance between the irradiation source and sample is 15 mm. In few cases the beta irradiations were performed using a 20 slots beta irradiator manufactured by Daybreak−Nuclear and medical systems. The calibration of Daybreak beta irradiator gave a dose rate of 0.061 Gy/sec and 0.041 Gy/sec for Quartz (90−150 μm) and fine grains (4−11 μm), respectively.

For alpha efficiency calculation a six seater alpha irradiator with ^{241}Am source in vacuum was used (Singhvi and Aitken, 1978). ^{241}Am decays with a half−life of 432.6 years emitting alpha particles of several energies ranging from 4.76 MeV to 5.54 MeV. However, most dominant decay is through 5.48 MeV (85% probability) and 5.44 MeV (13% probability) α particle (www.nndc.bnl.gov data). This isotope is commercially available in form of 1 μm thick layer backed with 200 μm silver foil and front face protected by 2 μm thick gold−palladium alloy protective covering.

2.4 Measurement of Natural Dose Rate

The age estimation of natural samples requires the estimation of natural dose rate that results in luminescence buildup. Environmental dose rate is the rate at which energy is deposited in the sediment from the ambient nuclear radiation flux. Major contributors to environmental dose rate are Uranium (^{238}U, ^{235}U), Thorium (^{232}Th) and Potassium (^{40}K). The decay schemes for these radioactive isotopes are shown in Figure 2.4 and Figure 2.5. Given the large decay time (~Billon years) of these radionuclides the activity of these radionuclides over a Million year time scales can reasonably be assumed as constant. However in the case of samples with interaction with water there is a reasonable chance of the parent/daughter being unsupported and in such case the dose rate becomes time dependent. In this case the present activity is used to calculate the evolution of dose rate with

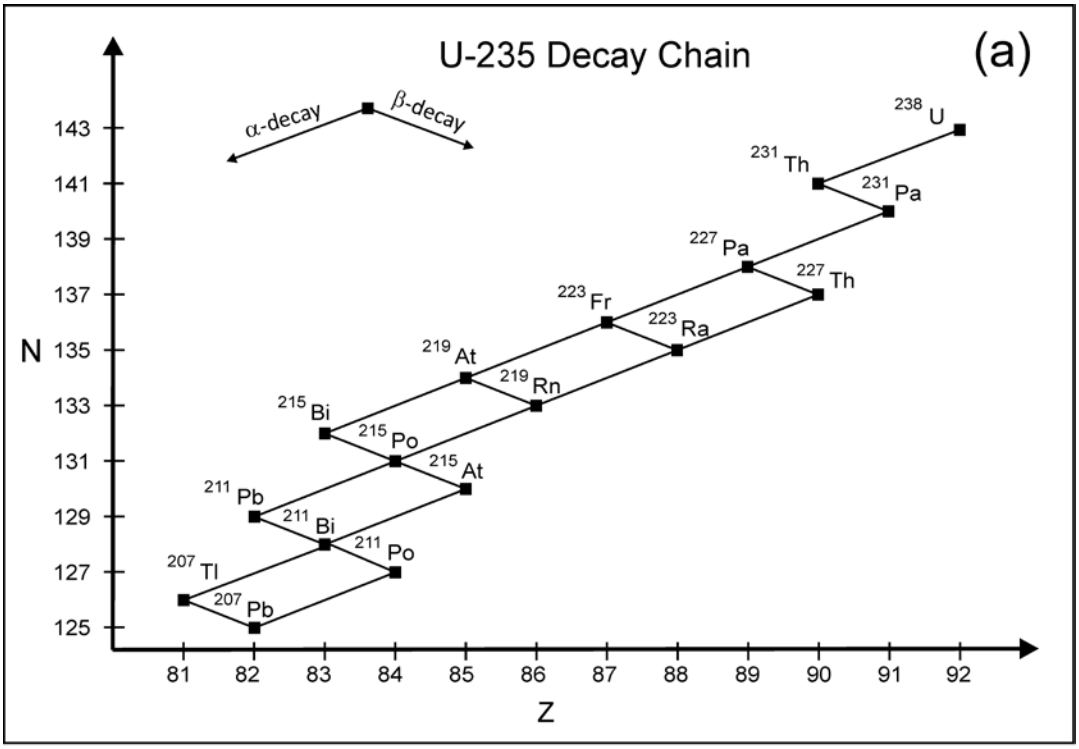

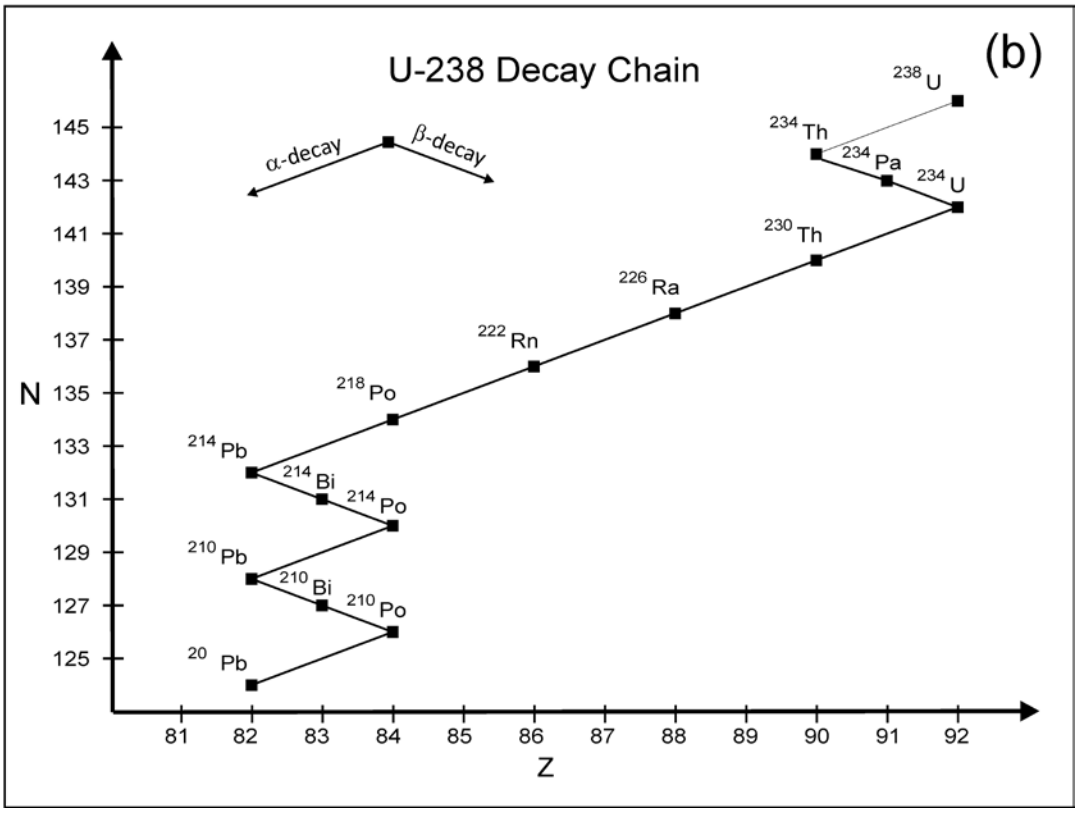

Figure 2.4: Decay schemes of the Uranium series, (a) Uranium−235 and (b) Uranium−238

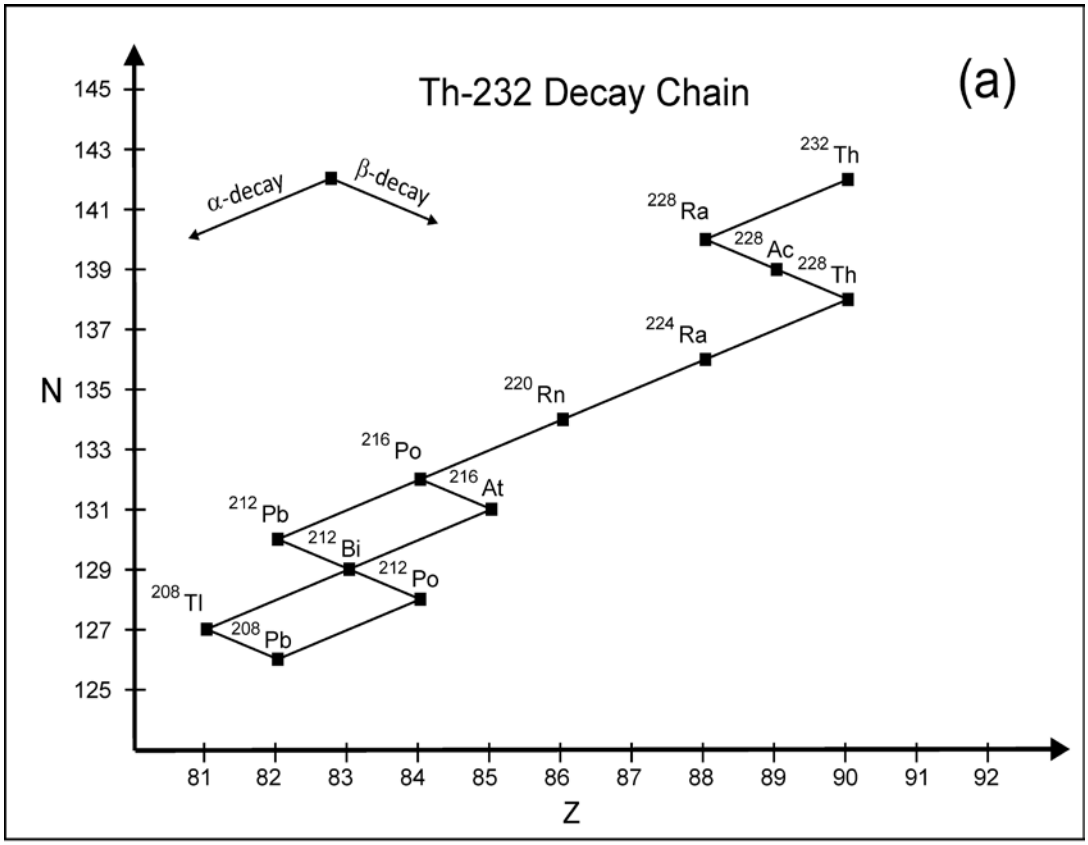

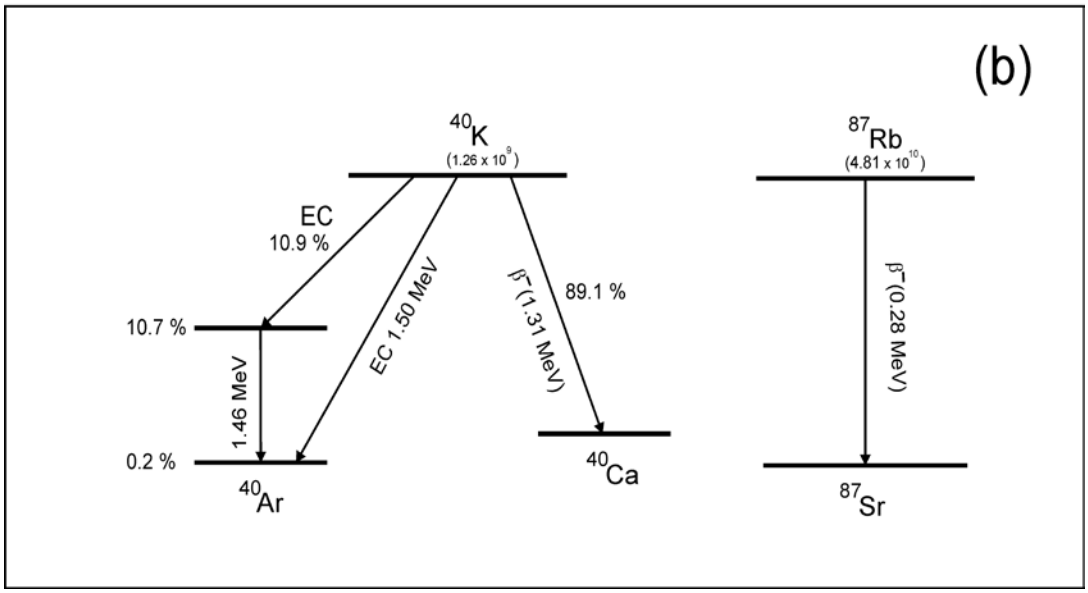

Figure 2.5: Decay schemes of the radioactive series, (a) Thorium−232, and (b) Potassium−40 and Rubidium−87

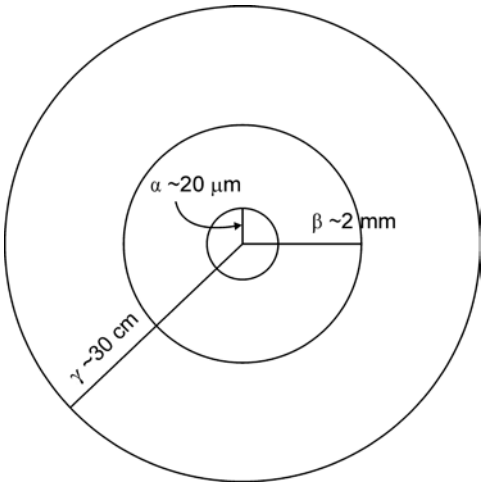

Figure 2.6: Ranges of ionizing radiations in natural environment

time and this is folded in with the total dose to compute the age. The radiation from these isotopes is in the form of α, β particles and γ rays (Figure 2.6). Also a small (< 2%) but finite contribution (Mejdahl, 1987) from rubidium (^{87}Rb) and secondary cosmic rays mesons, electrons and gamma rays also contributes to the annual dose rate . The natural dose delivered to sample arises both from the radioactivity within the individual grain and the radioactivity in the surrounding matrix. Internal dose rate is ~ few % for coarse grains (>100 μm) of feldspars (Mejdahl, 1987) but is absent in quartz grains due to its being devoid of any internal radioactivity. The concentrations of U, Th and K in the sample can be determined by many experimental techniques such as thick source alpha counters, gamma ray spectrometry using germanium detector and thallium activated Sodium Iodide (NaI) scintillation spectrometer.

The annual dose can be calculated using the conversion factors by (Adamiec and Aitken, 1998) taking into account the matrix, its grain size distribution, the distribution of radioactivity and the fraction that is being used. In present study thick source alpha counting technique was used.

In scintillation counters ionizing particles produce scintillation corresponding to each decay of parent to daughter nucleus. The scintillation are then detected and amplified by PMT and counted using electronic counting unit. The techniques for the measurement of different radioactivity concentration are briefly discussed in next section

2.4.1 Measurement of Uranium (U−238) and Thorium (Th−232) Concentration

The estimation of concentration of U and Th were done by thick source α pair counting technique (Aitken, 1985; Appendix J)

In thick source alpha counting the sample is powdered to less than 10 μm size and typically an alpha thick layer (>20 μm) of powdered sample is spread uniformly on a 42 mm diameter ZnS(Ag) scintillation screen, positioned in a sealed perspex holder. The detector gives total number of alpha counts due to both U and Th, slow pair counts for $^{232}\mathrm{Th}$ decay series $^{220}\mathrm{Rn} \rightarrow {}^{216}\mathrm{Po}$ ($T_{1/2}$ = 0.15 s) and fast pair counts for $^{235}\mathrm{U}$ decay series $^{219}\mathrm{Rn} \rightarrow {}^{215}\mathrm{Po}$ ($T_{1/2}$ = 0.0018 s). The concentrations of U and Th are proportional to count rate and the relationship between count rate and the concentrations of U and Th for the particular geometry is discussed in Aitken,1985. In this calculation, it is assumed that the decay series of U and Th are in equilibrium. However, disequilibrium may take place mainly due to loss of Rn ($T_{1/2}$ =3.83 days) from U−238 decay series. Such cases can be tested using hyper pure Germanium (HPGe) detector by measuring γ rays from different members of the decay chain. The discrepancy in U concentrations, calculated from the characteristics gamma ray, emitted from different radioisotopes before and after Rn of the decay chain decides the disequilibrium phenomenon. For the present work all samples showed equilibrium.

2.4.2 Measurement of Potassium (K−40) Concentration

To estimate the concentration of Potassium in sediments γ counting is done by using NaI(Tl) as scintillator. In this the gamma ray photons emitted by sediment is compared with a known standard and concentration is found by comparing the count rate of the two.

In gamma spectrometry a 3″×3″ well type thallium (Tl) activated sodium iodide crystal and lithium doped hyper pure germanium crystal were used to measure the K concentration in the sample. To measure $^{40}\mathrm{K}$ concentration, the Compton subtracted photo peak corresponding to 1.46 MeV gamma photon emissions were used. The background subtracted photo peak is then compared with KCl standards with known $^{40}\mathrm{K}$ concentration. To ensure identical geometry for sample and standard a Perspex spacer was used. To reduce the

background ~6″ lead shield was used. The resolution of the NaI detector was 4 keV whereas HPGe detector had resolution of 0.25 keV.

2.4.3 Measurement of Cosmic Ray Dose Rate

Cosmic rays consist of the charged particles which get deflected by earth's magnetic field. In earth's equatorial region cosmic ray flux is minimum, where magnetic field lines are perpendicular to the direction of the charged particle, and in the polar region it is maximum, where magnetic field lines are nearly parallel to the direction of the charged particle. Very high energetic particle (>GeV) can enter into the earth atmosphere. Most of the cosmic rays are absorbed by the earth's atmosphere. However the secondary particles mainly muons contribute to the natural dose rate. These particles show a dependency on altitude and geographical latitude due to earth magnetic field. The cosmic dose rate was calculated as a function of altitude and latitude using equations as suggested by Prescott and Hutton (1994).

2.4.4 Moisture content

The presence of water in the void spaces affects the dose rate significantly. The water in voids does not carry any radioactivity but attenuates the radiation dose from the radioactivity in the sediment. Therefore, a correction to the dose rate estimation is made to estimate the dose rate correctly. This is calculated considering saturation water content (W) measured in laboratory and expressed as

$$\mathrm{W}=\frac{\text{weight of water}}{\text{weight of dry sample}} \qquad (2.1)$$

W and a factor F which is the average soil water content as a fraction of this saturation water content W is used for the dose rate estimation. It is generally considered to be (0.8 ± 0.2)W. Using these two factors and the nuclear tables the α, β and γ dose rates are corrected as suggested by Zimmerman (1971a) and the dose rates used were calculated as

$$\dot{D}_{\alpha} = \frac{\dot{D}_{\alpha\ \mathrm{dry}}}{1 + 1.50 \times \mathrm{W} \times \mathrm{F}} \qquad (2.2)$$

$$\dot{D}_{\beta} = \frac{\dot{D}_{\beta\ \mathrm{dry}}}{1 + 1.25 \times \mathrm{W} \times \mathrm{F}} \tag{2.3}$$

$$\dot{D}_{\gamma} = \frac{\dot{D}_{\gamma\ \mathrm{dry}}}{1 + 1.14 \times \mathrm{W}_1 \times \mathrm{F}} \tag{2.4}$$

W refers to sample and W_1 to soil.

2.4.5 Alpha efficiency 'a' value

The luminescence efficiency of alpha particles is less as compared to beta and gamma. This occurs due to local charge saturation effects and high linear energy transfer by alpha particles as compared to beta and gamma ray. The alpha efficiency factor 'a' can be determined by the formula suggested by Aitken and Bowman (1975)

$$\mathrm{a} = \frac{\beta}{13 \times \mathrm{s} \times \mathrm{y}} \tag{2.5}$$

Where, S ($\mu m^{-2} min^{-1}$), is the strength of alpha source and β, is the beta dose (Gy) which induces the same amount of luminescence as y minutes of alpha dose. There are other formalisms for 'a' value estimation but overall these provide similar results (Bowman and Huntley, 1984).

2.5 Equivalent Dose (D_e)

An important component of the luminescence dating is the estimation of equivalent dose D_e. The equivalent dose D_e is the amount of laboratory beta or gamma dose that produces the same amount of luminescence signal, as given by the natural sample or as received by the sample due to irradiation in the environment. Aitken (1985) summarizes several protocols devised to estimate D_e. These protocols take into account the changes in sensitivity (Luminescence per unit dose per unit mass) during various readout cycles. These measurement protocol include, Multiple Aliquot Additive Dose abbreviated as MAAD, (Aitken, 1985) and Single Aliquot Additive dose abbreviated as SAAD, (Stokes et al., 2000; Wallinga et al., 2000; Zhao et al., 2003; Vandenberghe et al., 2004). In these protocols,

incremental beta doses are given in addition to natural dose to a set of identical discs and a dose versus luminescence growth curve is constructed. The D_e estimate is made by extrapolating the growth curve on negative x axis (dose axis). Depending on the sample requirement several other protocols like, Australian slide method (Prescott et al., 1993), photo transferred thremoluminescence abbreviated as PTTL, (Murray, 1996), thermally transferred OSL (TTOSL) by, Wang et al., (2007), Post IR IRSL (Buylaert et al., 2009) etc. have been developed to make the age determination more robust. In these measurements different normalization criterion are applied to make the luminescence signal and sample or aliquot independent. Some of these are weight normalization, zero glow normalization, second glow normalization and short shine normalization. Aitken (1985) provide a good over view and assessment of the normalization methods. All these protocols applied to samples provide a better estimation of equivalent dose. However single aliquot protocol (Murray and Wintle, 2000) is now the most widely and routinely used protocol.

Equivalent dose measurement methods can be broadly classified into two categories, viz the additive dose method and the regenerative dose method, which are described here.

2.5.1 Multiple Aliquot Additive Dose Method (MAAD)

This method was first developed for the Thermoluminescence dating of archeological pottery (Aitken, 1985). This method uses several identical aliquots of same sample. In order to obtain appropriate D_e, aliquots are divided into several groups, the very first group is used for the measurement of natural luminescence (i.e. sample as received) and other groups are given increasing laboratory dose (e.g. β_1, β_2, β_3….. β_N) over and above the natural signal. The luminescence signal thus obtained is plotted against the applied dose and a growth curve is reconstructed. The equivalent dose is obtained by extrapolation of the growth−curve to zero luminescence intensity (Figure 2.7), and the distance of this intersection point to the origin is equal to the D_e. This method assumes that all aliquots have identical radiation history and that the radiation response of the sample. This method while ensures against sensitivity changes, requires a priori assessment of the nature of the growth curve. Further in MAAD, growth curve is extrapolated on to the x−axis; hence the result depends quite significantly on the choice of the mathematical function used (linear, exponential or polynomial). In addition to this, problem arises when the extrapolation is to be made over a large dose−span, where

the growth is non−linear and/or there is a large scatter between the data points. As the construction of growth curves involves a large number of aliquots, appropriate normalization (discussed in section 2.5.2) is needed. Monte−Carlo simulations by Felix and Singhvi (1997) provide practical guidelines for construction of growth curves and extrapolations.

2.5.2 Normalization methods

For D_e measurement in laboratory using MAAD or SAR protocol, the assumption of identical environment and dose rate is not completely fulfilled. For example in MAAD protocol, the amount of sample number of bright grain in every disc may not same and different irradiations are given to different set of discs before the luminescence measurement which will cause difference in luminescence sensitivity. Similarly in SAR protocol, same disc is being repeatedly used and in each cycle irradiation (variable), preheat and luminescence measurement are done which will also cause different luminescence sensitivity at different cycle whereas all these protocol aim to measure the luminescence to construct dose response curve under identical sensitivity condition. In order to circumvent this problem, several normalization methods have been proposed (Aitken, 1985; Jain et al., 2003). The most common methods employed are;

2.5.2.1 Weight normalization

In this method aliquots are normalized by weight of sample and assume that either all grains have identical luminescence output or in every disc, number of effective bright grains is equal. Given that individual grains have variable luminescence sensitivity and that in general less than few percent of the grains provide a major fraction of luminescence of an aliquot, weight normalization often results in a scatter of ~10% or more (Aitken, 1985; Jain et al., 2003).

2.5.2.2 Zero glow normalization

This method was used initially for TL MAAD protocol (Aitken et al., 1979). A small test dose on natural sample is given and luminescence output corresponding to 110 °C TL peak which is absent in natural sample due to its short life (of about few hours) is used for the normalization of high temperature peak. A correlation between 110 °C TL peak and OSL in

quartz (Stoneham and Stokes, 1991) led to the potential of this method (Stokes, 1994). In the present work this method has been used in SAR protocol to correct for the change in the

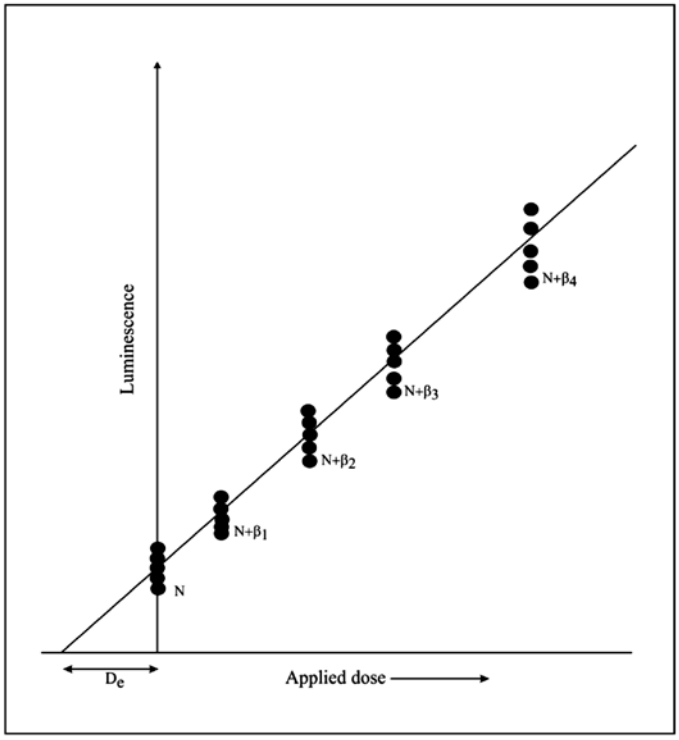

Figure 2.7: Multiple Aliquot Additive Dose (MAAD) method schematic

natural sensitivity during first read out of OSL (Singhvi et al., 2011) and is termed as Natural Correction Factor (NCF).

2.5.2.3 Short shine normalization

In this method a very short period (0.1 s) OSL signal is recorded before the measurement (~40 s recording of OSL). The short pulse deplete the signal by <1%. This method assumes that the luminescence sensitivity of first 0.1 s and rest of the OSL decay curve are correlated. This method is also used for multiple aliquot where short shine of natural sample take care the sample amount and the sensitivity. The applicability of this method is limited in very young or dim samples with low natural light levels.

2.5.2.4 Post normalization

This method is widely used in SAR protocol (Murray and Wintle, 2000). After each luminescence measurement a small test dose is given to the samples and then luminescence due to test dose is measured. The test dose signal at each cycle is the measure of sensitivity at each cycle. In the present work, mostly this normalization procedure was used.

2.5.3 Single Aliquot Regenerative Protocol (SAR)

The SAR protocol by Murray and Roberts (1997) and by Murray and Wintle (2000) suggested the single aliquot regeneration procedure for OSL signals. In this method each disc (single aliquot) or each grain (single grain) provides one equivalent dose. This method improves the dose precision by combining measurements of several discs or grains and provides statistical firmness.

In SAR method D_e is estimated on a single aliquot by recording its natural luminescence and then a regeneration growth curve generated by giving incremental beta dose. The intensity of natural sample is then read on the regenerated growth curve to obtain D_e as shown in Figure 2.8. In this method choice of signal and pretreatment to get that signal are important. At each stage a sensitivity measurement is included to ensure that any lab induced sensitivity is corrected for. For example OSL−SAR in quartz a preheat of 160−300°C is given to remove the unstable trapped electrons, which has lifetime less than or nearly same of age of the sample and first ~0−0.8 second of OSL signal is used for D_e estimation (Murray and Wintle, 2000). The natural and regenerative OSL measurements are carried out at 125 °C in order to keep the 110 °C trap empty during the OSL stimulation (Murray and Wintle, 2000). Table 1 gives the details of SAR protocol, which was used. The specific details of the protocols, used for different samples will be described in the corresponding section.

2.5.4 Natural Correction Factor (NCF)

During the measurement of OSL in SAR protocol the changes in the sensitivity occurring in each regeneration cycle are taken care off by normalizing the signal with successive test dose OSL. Normalization in SAR protocol holds good if any OSL measurement and consecutive test dose OSL are measured under identical sensitivity condition or same factor of sensitivity change takes place during these two consecutive measurements for each cycle.

But natural OSL is measured in laboratory sensitivity condition whereas immediate test dose OSL is measured under laboratory condition. The conventional SAR protocol (Murray and Wintle, 2000) has in−built

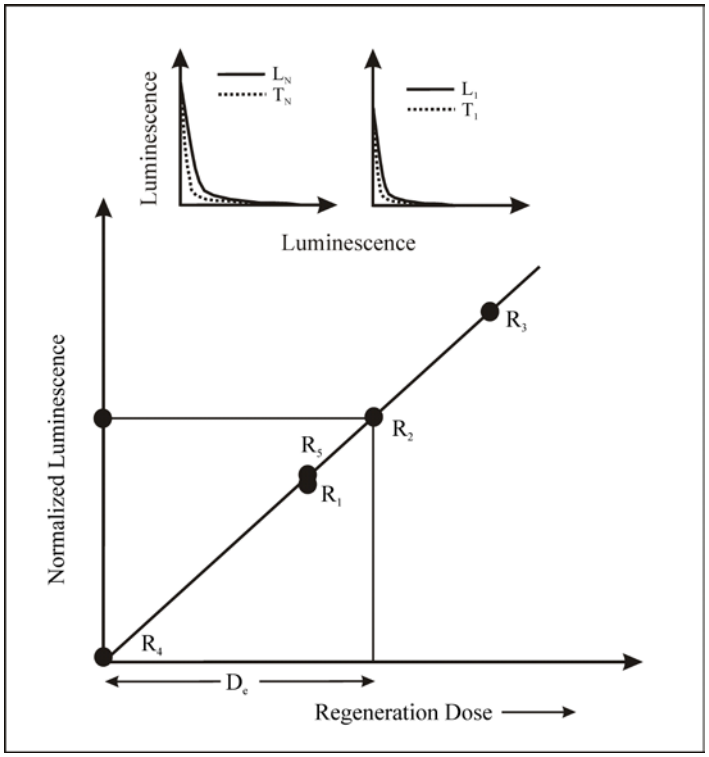

Figure 2.8: Single aliquot regeneration method, sensitivity corrected luminescence is plotted against the incremental doses (R_1, R_2, R_3….). D_e is measured by interpolating the (L_N/T_N) on to the dose axis (Murray and Wintle, 2000)

assumption of no change in sensitivity during natural OSL readout. However during the measurement of natural OSL (first OSL measurement), sensitivity change can happen (Singhvi et al., 2008).

To overcome this problem (Singhvi et al., 2010), introduced a modified SAR (NCF−SAR) protocol. In this protocol the additional steps are, before and after the natural OSL measurement a test dose TL up to 200°C is measured and the ratio of these two TL peak (after/before) is then multiplied with the natural point (L_N/T_N) and the modified sensitivity corrected natural point is the interpolated on the regeneration growth curve. The detail of the protocol is discussed by Singhvi et al. (2011).

Table 2.1:Single aliquot regenerative protocol (Murray and Wintle, 2000)

Step	Treatment	Observation
1	Preheat (160−300 °C) / 10 (s)	
2	OSL (Natural)	L_N
3	Test dose	
4	Cut heat (160 °C) / 10 (s)	
5	Test dose OSL	T_N
6	Illumination (240−280 °C) / 100 (s)	
7	Regeneration dose (R_1)	
8	Preheat (160−300 °C) / 10 (s)	
9	OSL (R_1)	L_1
10	Test dose	
11	Cut heat (160 °C) / 10 (s)	
12	Test dose OSL	T_1
13	Illumination (240−280 °C) / 100 (s)	
14	Go to step−7 and repeat it for R_2, R_3……	

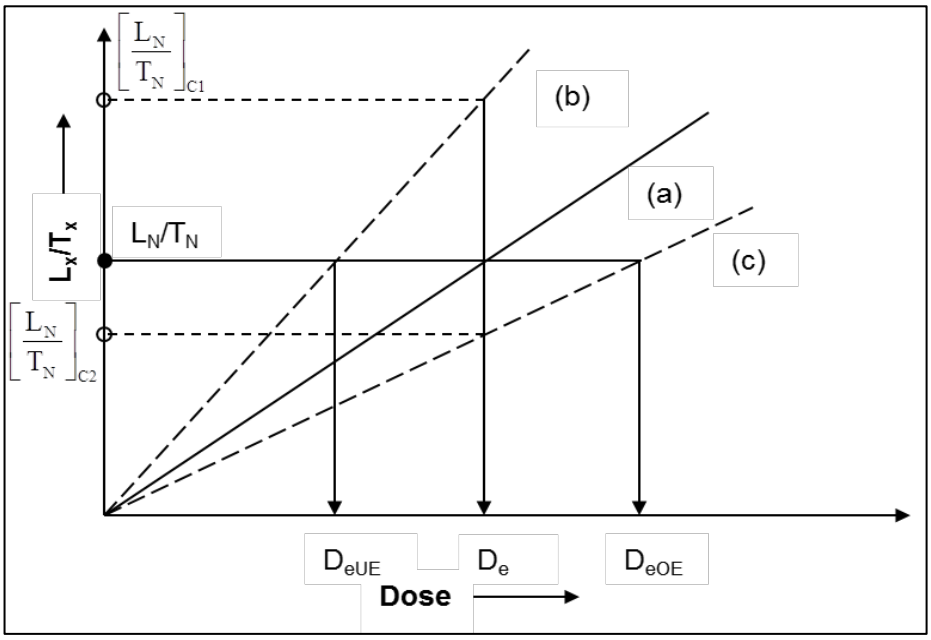

Figure 2.9: NCF correction factor model after (Singhvi et al., 2011)

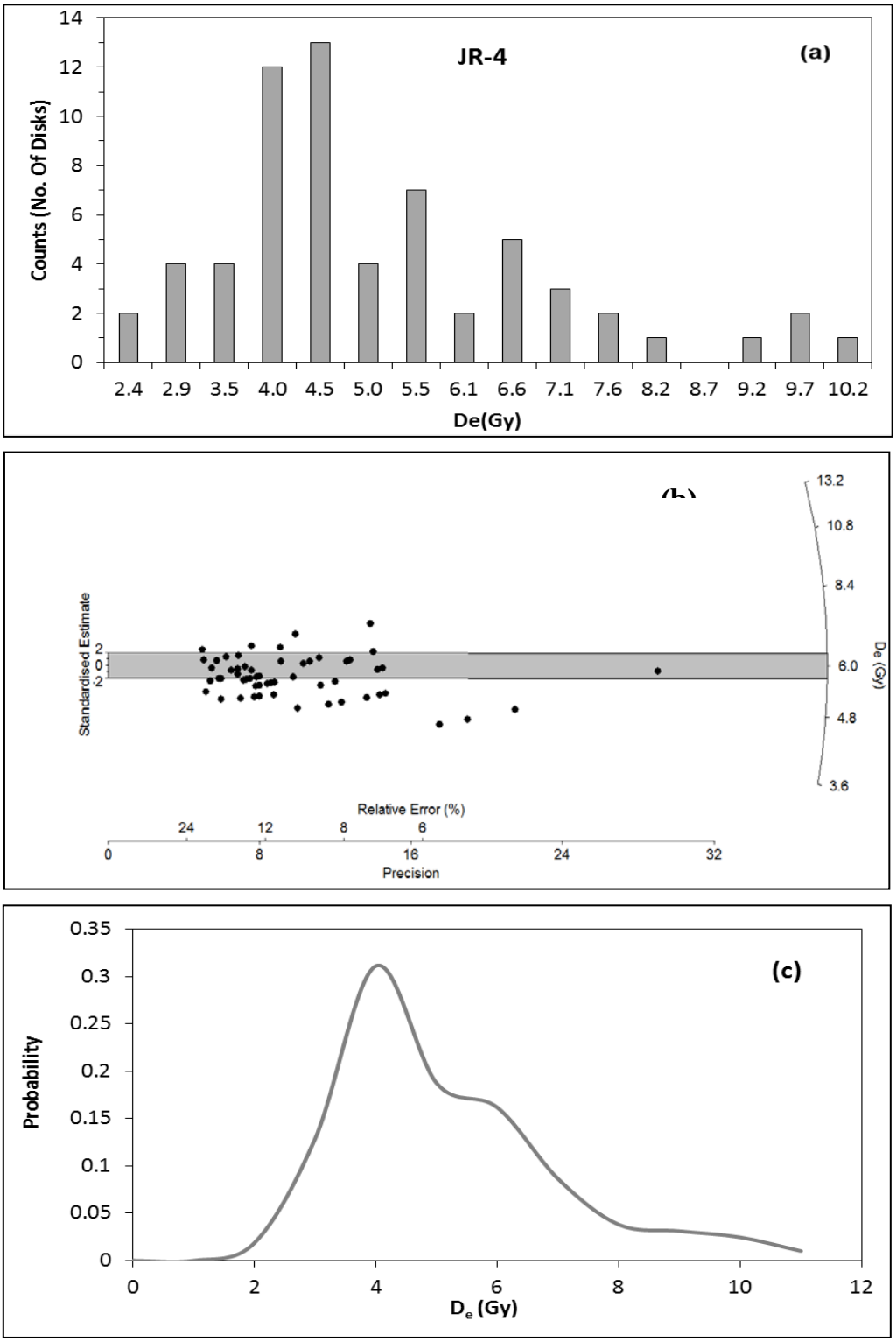

Figure 2.10: (a) Histogram for the sample JR−4 (Jira village), (b) Radial plot of JR−4. Shaded region is the band of 2σ on the y−axis and (c) Probability density plot for the same sample

2.6 The nature of Distribution in D_e with in a sample

When the SAR protocol is repeated for number of aliquots for single event, each aliquot provide a D_e value which is slightly different from other, resulting into the distribution of D_e. There could be several causes for this distribution of D_e for a single event e.g. partial resetting of the luminescence signal, heterogeneous distribution ^{40}K hotspot within the matrix (Mayya et al., 2006) or because of experimental variation. To have the knowledge of degree of scattering in D_e values, a pictorial representation is necessary. Several methods have been proposed in order to visualize the distribution, as follows.

2.6.1 Radial plot

A radial plot is a graphical representation of D_e values (Galbraith, 1988; Galbraith, 1990), especially for comparing several estimates which have different precision.

Figure 2.10b shows the radial plot of the same sample. The X−axis represents the precision, expressed in relative error (%). The Y−axis is the standardized estimates of D_e, which is,

$$\frac{\log(D_e - w')}{E'} \tag{2.1}$$

where, w' is weighted average of all the aliquots, and E' is the standard error of $\log D_e$. Equivalent doses are statistically consistent at the 2σ level are easily recognized, as these fall within the shaded band.

2.6.2 Probability Density Plots

In this a Gaussian can be simulated for Each D_e value with an error associated with it as standard deviation. For N number of D_e will N Gaussian are simulated. The average Gaussian is constructed and represented as probability density plot (Figure 2.10c). Recent work by Chauhan and Singhvi (2011) suggested that the dose visualization methods such as radial plot and histograms may not be sufficient to draw inferences on the proper causes for the distribution in the paleodose and few other checks might be helpful. They suggested using the ratio (R) of maximum to minimum paleodose to account for the beta heterogeneity due to radioactive potassium in the sediment matrix as an additional proxy. A ratio $R \geq 10$ would

then imply sources of paleodose distribution (such as poor bleaching) other than the K heterogeneity, and a ratio less than 10 would imply well bleaching of the sample and mean D_e would give the correct age of the event. The minimum number of aliquots required for the estimation of D_e will also depend on the amount of radioactive potassium in the sediment matrix. As suggested for K = 3%, minimum 24 aliquots would be needed to have a dose within ± 5% range of the actual value.

2.7 Estimation of errors in TL/OSL measurement

The errors in a luminescence age can be divided into two groups as in other standard cases, a) random errors and b) systematic errors. Random errors are those that comprise error in estimation of D_e, error in a−value, error in spectrometric measurement, in the computation of the annual dose and arise due to statistical fluctuation in photon counting, scintillation counting etc. Systematic errors are those that comprise error in the calibration of the alpha and beta source, error in calibration of alpha and gamma counters, parameters used in converting the U and Th concentration to dose rate, error in water content etc. The error estimation in the present case was based on the calculation proposed by Aitken (1985) and Murray and Olley (2002) . The error quoted in TL/OSL ages are normally at 1 sigma level.

Chapter 3

Resetting of Luminescence in Sand Dikes

3.1 Introduction

Injection dikes have been seen in a wide range of geological settings, and are consequence of injection of host material through the overlying sediment layers due to pressure difference induced by the passage of Rayleigh waves, produced by earthquakes. Earthquakes of magnitude M > 5 can produce liquefaction (Atkinson, 1984; Allen, 1986; McCalpin, 1996; Galli, 2000; Castilla and Audemard, 2007) and can result in the form of sand dikes few tens of mm to meter height. Even though their final forms are similar at different locations, there are uncertainties about their formation and associated processes (Aspler and Donaldson, 1985).

In terms of their chronology, isolated attempts have been made to date these injected dikes using luminescence dating technique (Porat et al., 2007; Mahan and Crone, 2008).

Porat et al. (2007) used OSL to differentiate between depositional and injection dikes and found that the ages in case of injection dikes were lower compared to the source layer suggesting that the dike injection event caused some reduction of luminescence. The age for source layer was 33.9 ± 2.0 ka and that of injected material ranged from 12.1 ± 1.1 ka to 13.5 ± 1.1 ka. This significant difference is possible only if these sand dikes have been exposed to sun light or have undergone heating to reset the TL/OSL clocks. There is no evidence that injected materials have been exposed to sunlight as they reside in subsurface. Besides, absence of evidences of mineralogical changes in the injected material due to an extended thermal regime and lowering of the luminescence signal lead us to postulate possible flash type heating which would rest the TL/OSL clock during the injection of the dike (Singh et al., 2009). This concept proposed that viscous flash heating during the injection of sand dikes results in resetting of luminescence signal to yield the results as obtained by Porat et al. (2007). Following the initial work of (Singh et al., 2009), we considered the possibility of heating during the injection process on account of injection speed and friction between sediment grains leading to viscous heating. In the geological literature, viscous heating has been invoked to explain a wide variety of geological processes, such as mantle convection models, lithospheric delamination, plateau uplift, subduction, continental collision, shear zones, and microstructure (Ranalli, 1995; Schubert et al., 2001). The role of frictional heating, also termed as viscous dissipation has been used to define the total heat budget required for the metamorphism process beneath the earth surface (Graham and England, 1976; England and Thompson, 1984; Burg and Gerya, 2005). Burg and Gerya (2005) have recently discussed the role of viscous heating in the modeling of metamorphism of collisional orogens in Central Alps. In this chapter an attempt has been made to estimate the temperature rise in liquefaction process due to the viscous heating of sand material.

3.2 Mechanism of Dike Formation

Vertical injection of a fluid requires high pressure difference and a medium to act as lubricant. These requirements are fulfilled when a sandy layer with sufficient pore water is sandwiched in two layers of high cohesiveness layers of clay. When a cyclic stress during earthquakes is applied to such a system, the water mixed sand layer intrudes into the clay layer and forms sand dike (Seed, 1979; McCalpin, 1996). Shearing stress increases the pore-

water pressure and this result into the liquefaction (Mohindra and Bagati, 1996; Moretti, 2000; Rodríguez−Pascua et al., 2000). Thus a dike can be considered an example of a natural hydraulic fracture (Lorenz et al., 1991; Cosgrove, 2001). The intruded material is locked into the fractured zone after the dissipation of excess pressure. The process of dike formation can be explained in three steps: (1) a build-up of an excess fluid pressure in a sand body; (2) failure of the seal i.e. fracturing of upper clay layer; (3) subsequent fluidization of the unconsolidated sand and injection into host sediments (Jolly and Lonergan, 2002). Two models for the injection dikes have been proposed viz., a) channel flow model and b) crack dilation due to injection of material (Levi et al., 2008). In the channel flow model, the dike is injected due to the pressure gradient (higher pressure at the source layer and lower pressure towards surface). As shown in Figure 3.1 this can be represented by following equation

$$\frac{dP}{dx} = \frac{(P_{out} - P_{in})}{2l} + (\rho_f - \rho_r)g \qquad (3.1)$$

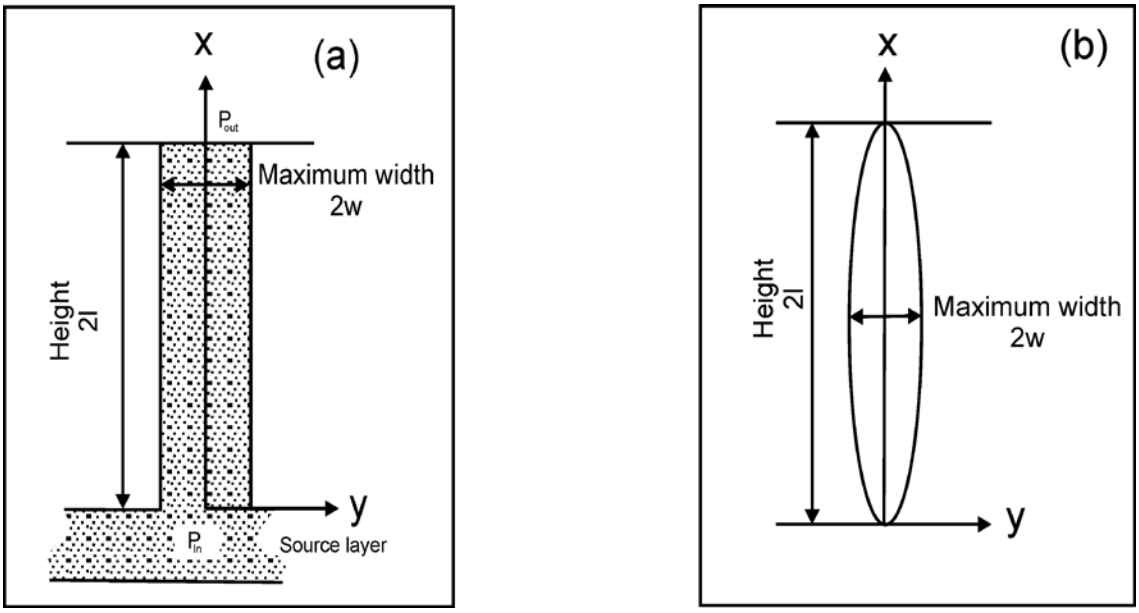

Figure 3.1: schematic representation of upward flow of dike and b) dialation profile of dike (after Levi et al., 2008)

Where 2l is the dike height, ρ_r is the density of host material and ρ_f is the fluid density i.e. density of material injected as dike, P_{in} is the pressure at source layer and P_{out} is the

pressure at $x = 2l$. For the dikes which are exposed at the surface, P_{out} is same as the atmospheric pressure and it will be the lowest magnitude of the pressure.

Equation (3.1) with appropriate boundary (Levi et al., 2008) can be solved to obtain the pressure at the source layer to be

$$P_{in} = \frac{0.0791 R_e^{1.75} \nu^3 \rho_f l}{4w^3} + 2(\rho_f - \rho_r)lg + P_{out} \qquad (3.2)$$

In above equation P_{in} is the pressure at source layer, P_{out} is the pressure at the depth where dike terminates, Re is the Reynolds number, w is the half width of the dike, ρ_r, ρ_f are the density of host material and the fluid, 2l is the height of the dike and g is acceleration due to gravity.

The channel flow model assumes the source layer as the pressure reservoir. This means for the injection of the material through the overlying layers sufficient pressure is available. This assumption leads limitation on the P_{out}. The magnitude of P_{out} will increase in proportion to the mixture viscosity, and will decrease in proportion to the channel width. For example if the channel width $w_1 > w_2$ then the P_{out} corresponding to width w_1 will be less for the same amount of the pressure at the source layer.

In the dike dilation profile a correlation between opening profiles and existing pressure gradient was assumed, just before the injection process ceased. This model takes into consideration that a fracture was already in existence and the only pressure difference was needed was for the injection of the material. With this assumption the pressure gradient in the model was assumed to be comparable to the fluid pressure in the dikes.

Based on this the estimation of driving pressure and the injection velocities were done. For channel flow model, the injection velocity estimates were made for different dike widths and for kinematic viscosities 3×10^{-3} and 15×10^{-3}. The injection velocities found to be varying from 0.2 to ~ 250 m/s and the corresponding pressure at source layers varied from ~0.2 to ~65 MPa. The estimates show injection velocity of ~10m/s with injection time of 0.1 to 2 seconds for a dike of height of ~18 m, with driving pressure 1 MPa.

3.3 Resetting of luminescence

In luminescence dating, the dated events are the most recent heating or most recent light exposure. Therefore, for a robust age estimate of dike formation event, it is necessary to ascertain that the luminescence signal is either reduced to zero or near zero level during the injection of dike.

Based on the comparison of luminescence ages from filled dike, injection dike and host rocks Porat et al. (2007) proposed the possibility of resetting of OSL signal in dikes. The Resetting of luminescence signal during dike formation has not been explored as yet. Eddingsaas and Suslick (2006) suggested that a shock wave that accelerate the micrometer-sized particles to high velocities leads to the interparticle collisions and create similar effect as mechanoluminescence and can reset the luminescence signal. In sand dike formation the injected material also faces the cyclic stress which may result in collision of quartz grains and thereby reducing the luminescence (Levi et al., 2008).

We have analyzed an alternative way of thermal resetting via the effect of viscous heating of the sediment grain during dike injection and, extended the initial concepts of Singh et al. (2009) and then examined these via field studies (discussed in Chapter 4)

3.3.1 Equation for Heat Dissipation in a fluid

When stress is applied to a fluid the dissipation of shear strain due to the viscosity of fluid takes place which causes the local viscous heating of the fluid material (Singh et al., 2009). This process has been observed in various areas of science and engineering. When a deviatoric stress is applied to a fluid the fluid parcel is distorted and strain is generated. The strain rates are a measure of how fast the three components of velocity change in each direction. The strain rate tensor of a fluid parcel under the influence of deviatoric stress is given by

$$e_{ij} \equiv \frac{1}{2}\left(\frac{\partial u_i}{\partial x_j} + \frac{\partial u_j}{\partial x_i} \right) \tag{3.3}$$

Where u_i and u_j are the velocity components and x_i, x_j are position coordinates of the point under observation in fluid parcel. For an isotropic Newtonian fluid the relation between deviatoric stress and strain rate tensor can be give as

$$\tau_{ij} = 2\mu e_{ij} + \lambda e_{kk}\delta ij \tag{3.4}$$

Where δ_{ij} is the Kronecker delta, δ_{ij} is 0 if $i \neq j$ and 1 if $i=j$, μ is dynamic viscosity, λ is second viscosity. The second viscosity is small in most of fluids and can be considered as zero (Rosenhead, 1954).

The deviatoric stress is a second rank tensor and the average of normal deviatoric stress on three mutual perpendicular planes in the fluid is the average of the diagonal elements of the stress tensor therefore from equation (3.4) we have,

$$\frac{\tau_{ii}}{3} = \frac{1}{3}\left(2\mu e_{ii} + \lambda 3 e_{ii}\right) = \left(\frac{2}{3}\mu + \lambda\right)e_{ii} = k_B e_{ii} \tag{3.5}$$

Here k_B is the bulk viscosity and is a measure of compression or dissipation due to applied stress. Inserting equation (3.5) in equation (3.4) and substituting the value of e_{ij} from equation (3.3) leads to,

$$\tau_{ij} = 2\mu e_{ij} + \left(k_B - \frac{2}{3}\mu\right)e_{kk}\delta_{ij} = \mu\left(\frac{\partial u_i}{\partial x_j} + \frac{\partial u_j}{\partial x_i}\right) + \left(k_B - \frac{2}{3}\mu\right)\frac{\partial u_k}{\partial x_k}\delta_{ij} \tag{3.6}$$

Equation (3.6) is the general form of deviatoric stress for a fluid under consideration. The viscous dissipation of energy (viscous heat) due to the deviatoric stress is,

$$\phi \equiv \tau_{ij}\frac{\partial u_i}{\partial x_j} \tag{3.7}$$

Therefore the heat dissipated for a Newtonian[1] fluid can be obtained by substituting equation (3.6) into equation (3.7) and is

[1] A fluid for which viscous stresses that arise from its flow, at every point, are proportional to the rate of change of its deformation over time

$$\phi = 2\mu\left\{\frac{1}{2}\left(\frac{\partial u_i}{\partial x_j}+\frac{\partial u_j}{\partial x_i}\right)-\frac{1}{3}\left(\frac{\partial u_k}{\partial x_k}\right)\delta_{ij}\right\}^2 + k_B\left(\frac{\partial u_i}{\partial x_i}\right)^2 \tag{3.8}$$

This is general expression for viscous heating assuming the medium as incompressible and homogeneous fluid with constant density, specific heat and thermal conductivity (Schubert et al., 2001).

3.3.2 Viscous Heating in Sand Dikes

Viscous heating due to the applied stress on a fluid is given by equation (3.8). For an incompressible fluid flowing in vertical direction, the boundary conditions are

$$\frac{\partial u_i}{\partial x_i} = 0, \frac{\partial u_j}{\partial x_i} = 0 \tag{3.9}$$

with these boundary conditions equation (3.8) yields

$$\Phi = \frac{\mu}{2}\left(\frac{\partial u_i}{\partial x_j}\right)^2 = \frac{\mu}{2}\left(\frac{\partial u}{\partial y}\right)^2 \tag{3.10}$$

Where u is vertical velocity and y is horizontal coordinate. For a simple Poiseuille flow with central velocity as u_{max} , and adopting model Fujii and Uyeda (1974) for infinitely long tubes for thermal point of view we have

$$\Phi = \frac{\mu}{2}\left(\frac{u_{\max}}{w}\right)^2 \tag{3.11}$$

Where w is the half width of the dike. Equation (3.11) is the total heat generated due to viscous heating during the injection of the dike.

3.3.3 Rise in temperature during injection of a sand dike

The general heat conduction equation is

$$\rho c\frac{\partial T}{\partial t} = K\frac{\partial^2 T}{\partial x^2} + \Phi \tag{3.12}$$

Where ρ, c and K are density, heat capacity and thermal conductivity of fluid (sand dike), t is time and x is spatial coordinate perpendicular direction of injection of sand dike. The rise in temperature during injection of dike can be obtained by solving equation (3.12).

In order to calculate the local temperature it is assumed that the heat generated by the viscous heating, will not be dissipated far away from the heat source (as the sand is not a good conductor of heat). We thus can drop the first term in right hand side of equation (3.12) and the rise in the temperature is given by

$$\rho c \frac{dT}{dt} = \Phi \tag{3.13}$$

Substituting the value of Φ from equation (3.11), rise in temperature ∇T is

$$\nabla T = \frac{\frac{\mu}{2}\left(u_{\max} / w\right)^2}{\rho c} \nabla t = \frac{\nu (u_{\max} / w)^2}{2c} \nabla t \tag{3.14}$$

$\nu (= \mu / \rho)$ is the kinematic viscosity in above equation.

Table 3.1: Soil Profile Type Classifications reproduced from International Building code Council (2009)

Soil Profile Type	**Soil Profile Name**	**Average Shear-Wave Velocity to 30-m depth (V_s)**
A	Hard Rock	Vs > 1524
B	Rock	762 <Vs< 1524
C	Very dense soil and soft rock	366 < Vs< 762
D	Stiff soil profile	183 < Vs< 366
E	Soft soil profile	Vs < 183

Maximum channel velocity i.e. $u_{\max}$ for sand dikes generated by fracturing is about half of the Rayleigh wave velocity (Freund, 1998). The Rayleigh wave velocity is equal to 0.92 of the shear wave velocity. Shear wave velocity, V_s is of the order of 1500 m/s in hard rock and 760 m/s in compact soil layer as determined by seismological investigation (Table 3.1).

Taking the boundary limit value for soil profile type C and D the shear wave velocity 366 m/s would result into 168 m/s of channel velocity. We shall consider a channel velocity

towards lower side 50 m/ss. Heat capacity c can be estimated by combining the heat capacity of sand and water and the porosity. Taking the heat capacity of sand as 800 J/Kg-K and heat capacity of water as 4180 J/Kg-K, we get the heat capacity of the sand dike for 30% porosity as 1814 J/Kg K.

Levi et al. (2008) estimated the value of kinematic viscosity as $(0.3-1.5)\times10^{-04}$ m^2s^{-1}. However if material is injected at depth, it would be desirable to use the values of kinematic viscosity under confining pressure.

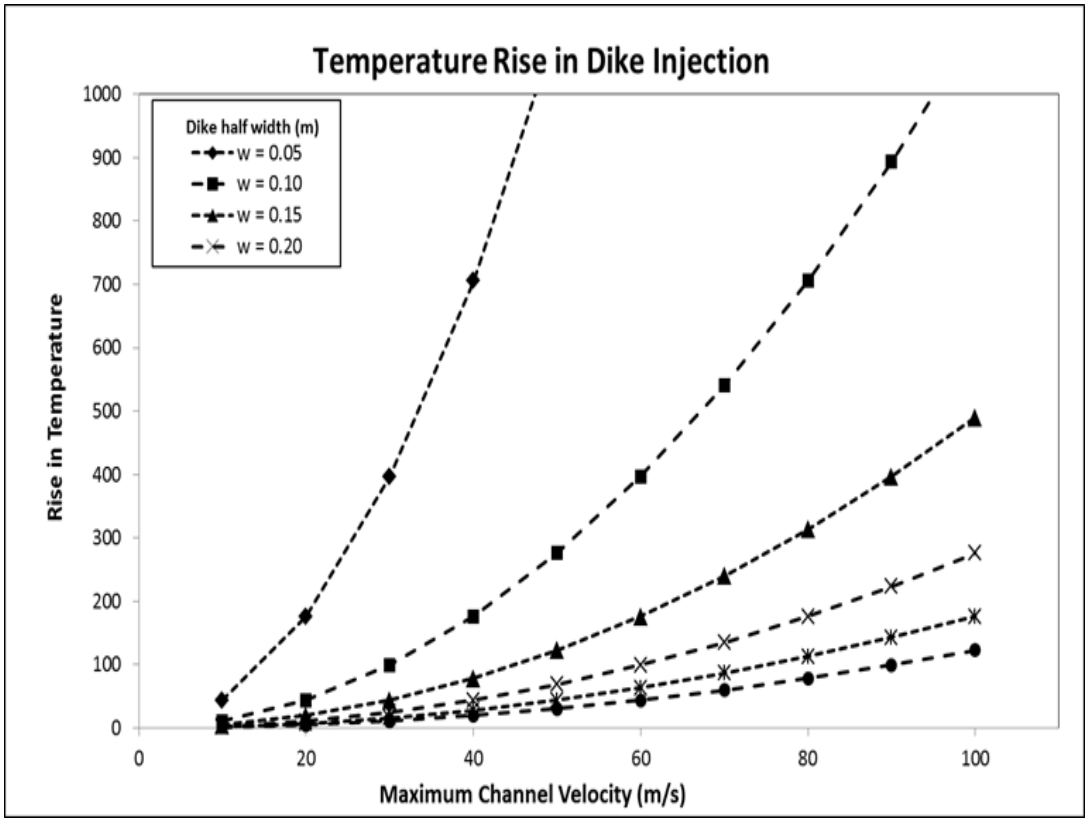

Figure 3.2: Temperature rise during injection of dike

The experimental measurement of the kinematic viscosity was done by Kawamura et al. (2002). Their laboratory experiments simulated the liquefaction under confined pressure. The dynamic viscosity for various confining pressures and as a function of time since liquefaction starts, were measured experimentally. Based on their experimental results we have considered a lower value of kinematic viscosity as 1.0 m^2s^{-1}. The other input parameters are

dike width $2w = 0.05m$ and injection time $\nabla t = 0.4s$. The rise in temperature from equation (3.14) is

$$\nabla T = \sim 440\,\mathrm{K} \qquad (3.15)$$

Table 3.2: Rise in temperature for a combination of different channel velocity and dike width, for kinematic viscosity 1 m^2/s and injection time 1 second

Max. Channel Velocity (m/s)	**Dike width (m)**					
	0.05	**0.10**	**0.15**	**0.20**	**0.25**	**0.30**
10	**44**	**11**	**5**	**3**	**2**	**1**
20	**176**	**44**	**20**	**11**	**7**	**5**
30	**397**	**99**	**44**	**25**	**16**	**11**
40	**706**	**176**	**78**	**44**	**28**	**20**
50	**1103**	**276**	**123**	**69**	**44**	**31**
60	**1588**	**397**	**176**	**99**	**64**	**44**
70	**2161**	**540**	**240**	**135**	**86**	**60**
80	**2822**	**706**	**314**	**176**	**113**	**78**
90	**3572**	**893**	**397**	**223**	**143**	**99**
100	**4410**	**1103**	**490**	**276**	**176**	**123**

Which implies the final temperature after the injection will be ~470 °C when the background temperature of the material before injection is 30 °C. Table 3.2 shows the estimated rise in temperature for various channel velocity and dikes of different widths. We have considered m2/s and injection time of 1 second.

3.4 Discussion

In present study we considered the likely role of viscous heating in resetting TL clocks of sand dikes material emplaced by earthquakes. The most crucial considerations are the velocity of dike emplacement and the viscosity of the sand dike materials. Sub-surface sand mobilization studies show that the viscosity would depend on confining pressures and also on time scale at which liquefaction takes place. Figure 3.2 shows the estimated rise in temperature during the injection of dike of different width and velocities, using the proposed model of viscous heating. It is evident from the Figure 3.2 that a temperature of 450 °C could be achieved under confining pressure for a value of kinematic viscosity of 1 m^2/s.

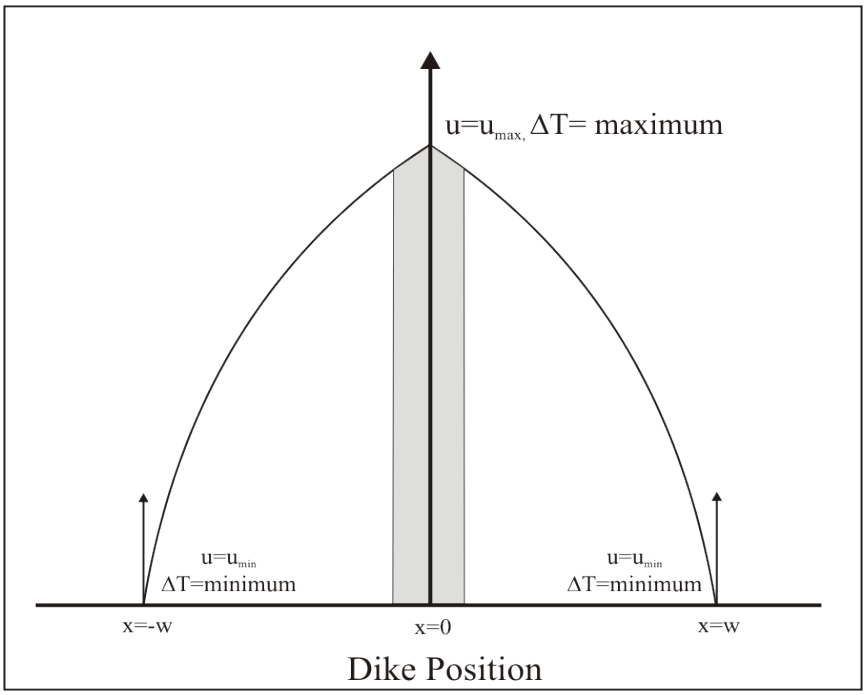

Figure 3.3: Schematic of rise in temperature and its dependence on channel flow. Maximum channel flow of the injected material will be at the center of the dike, and will therefore result into the maximum viscous heating of the material. The flow velocity at the edge of the dike will be minimum and thus may lead to partial resetting of the luminescence in the material near to edge of the dike

Kawamura et al. (2002) suggested that the value of kinematic viscosity is ~14 m^2/s for confining pressure as low as 0.05 MPa. This suggests that heating of up to 450 °C is possible in the dike of size several tens of cm. Such a rise in temperature will reset the TL clocks of the quartz grains. In our present model we have not considered the effect of transfer of heat energy away from the heat generation point.

In the present model a linear channel flow of dike injection was used, assuming the maximum channel flow at the center of the dike and minimum at the edge. As shown in Figure 3.3 the maximum amplitude rise during the injection of dike is at the center of the dike (gray color shaded zone), as the injection velocity at the edge is minimum the rise in temperature would be less. In view of this sample for the luminescence measurements have been collected from the best possible proximity of the center of the dike, where probability of resetting of signal is higher.

We have shown by taking conservative values of the parameters occurring in viscous heating that temperatures rise would be sufficient to reset the TL clocks of quartz grains during the formation of sand dikes. It is also suggested that the samples for the luminescence measurements should be collected from the center of the dike where probability of resetting of luminescence signal will be more.

Chapter 4

Luminescence Studies of Sand Dikes

4.1 Introduction

Northeast India is seismically one of the six most active regions of the world and is placed in zone 5 falling in the highest seismic zone in India (BIS, 2002). The North-Eastern region of India is bounded by Himalayan mountain belt in the North, the

Indo-Myanmar Range limits the East and the mighty Brahmaputra forms the Assam plain. The region has experienced several earthquakes (M >7) during the last hundred years as shown in Table 4.1 (Tiwari, 2002). The high seismicity in the region is attributed to the collision tectonics, between the Indian plate and the Eurasian plate in the north and subduction tectonics along the Indo-Myanmar range (IMR) in the east (Dewey and Bird, 1970; Molnar and Tapponnier, 1975; Molnar and Tapponnier, 1977; Rao and Kumar, 1997).

Major faults which remained active in the North-East region as reported by the Geological survey of India (Report, 2009) are, the basement faults consisting of E-W Dauki Fault along southern margin of the Shillong plateau NW-SE fault to the west of Shillong plateau, the Mikir Hills; NE-SW belt of imbricate thrusts over the northern part of Naga-Patkai range, the E-W and NE-SW frontal Himalayan thrust belt, the NW-SE Mishmi Thrust along Lohit foot-hills over the N-E Himalayan syntaxis, probable north-easterly extension of NE-SW Calcutta-Mymensing gravity high to the south of the North Cachar Hills through Cachar district.

Towards understanding the seismicity of North-East India region several workers used the liquefaction features associated with the earthquake events (e. g. Sukhija et al., 1999; Sukhija et al., 2000; Thomas et al., 2007b; Reddy et al., 2009).

In the present study the attempt was made to understand the applicability of luminescence dating to the liquefaction features (sand dikes). The samples were collected with the help of Dr. Devender Kumar from National Geophysical Research Laboratory, Hyderabad.

4.2 Study Area

The study area is located in Upper Assam, Northeast India. The samples were collected for the sand dikes from five sites namely Bedabari (26° 00’ 32.1”N, 90° 39’ 20.7”E), Belta Ghat (26° 00’ 16.5”N, 90° 39’ 7.1”E), Jira (25° 57’ 37.2”N, 90° 38’ 21.6”E), Nam Gaon (26° 13’ 10.6”N, 92° 26’ 57.4”E) and Kakoti (26° 12’ 14.2”N, 92° 31’ 48.8”E). The map of the study area is shown in Figure 4.1. The shallow water table in the region and ongoing tectonics leads to the deformation of soft sediments giving rise to the variety of sand dikes. Non availability of surface trace of the faults in the area makes it important to use the paleoliquefaction features (sand dikes) to reconstruct the past seismic history. Several sand dikes as well as multiple sand dikes were reported to be seen in the area after 1897 earthquake (Oldham, 1899; Sukhija et al., 1999). The reported thickness and height of the sand dikes in the area was up to 30 cm and >1 m. In few cases the sand water was ejected to the height of 3-5m (Sukhija et al., 1999). Similar observation of liquefactions were reported by Reddy et al. (2009) in connection with 1905 Assam earthquake.

Table 4.1:List of major earthquakes in North East India

Place	**Year**	**Magnitude**
Cachar	March 21, 1869	7.8
Shillong plateau	June 12, 1897	8.7
Sibsagar	August 31, 1906	7
Myanmar	December 12, 1908	7.5
Srimangal	July 8, 1918	7.6
SW Assam	September 9, 1923	7.1
Dhubri	July 2, 1930	7.1
Assam	January 27, 1931	7.6
Nagaland	1932	7
N-E Assam	October 23, 1943	7.2
Arunachal	July 7, 1947	7.5
Upper Assam	July 29, 1949	7.6
Upper Assam	August 15, 1950	8.7
Patkai Range, Arunachal	1950	7
Manipur-Burma border	1954	7.4
Darjeeling	1959	7.5
Indo-Myanmar border	August 6, 1988	7.5

4.3 Luminescence Studies of Sand dikes

In the present work the quartz extracted from a suit of 47 samples collected from sand dikes, source sand and host layers were analyzed by using the OSL method. The samples were tested for the dose recovery and preheat plateau to check the suitability of the SAR/NCF SAR protocol. Figure 4.9 shows the TL glow curves of quartz extracted from dike and host from Bedabari, Kakoti and Jira sites. A distinct peak at 300°C was observed for all samples along with a peak at 325 °C in all samples except for Bedabari site, in which the peak intensity is low and was overshadowed by the 300 °C peak. After giving 65.8 Gy beta dose in laboratory three peaks were observed in the same samples. The peaks were centered at 240 °C, 300 °C and 325 °C. The OSL response of the quartz is correlated with the 325 °C TL peak. The stability of higher temperature peak in range 200−450 °C, was tested by plotting

the ratio of N/ (N+β) with respect to the stimulation temperature. It is evident from Figure 4.6 that the TL signal of these samples is stable in temperature range350−450 °C showing a plateau in this temperature range.

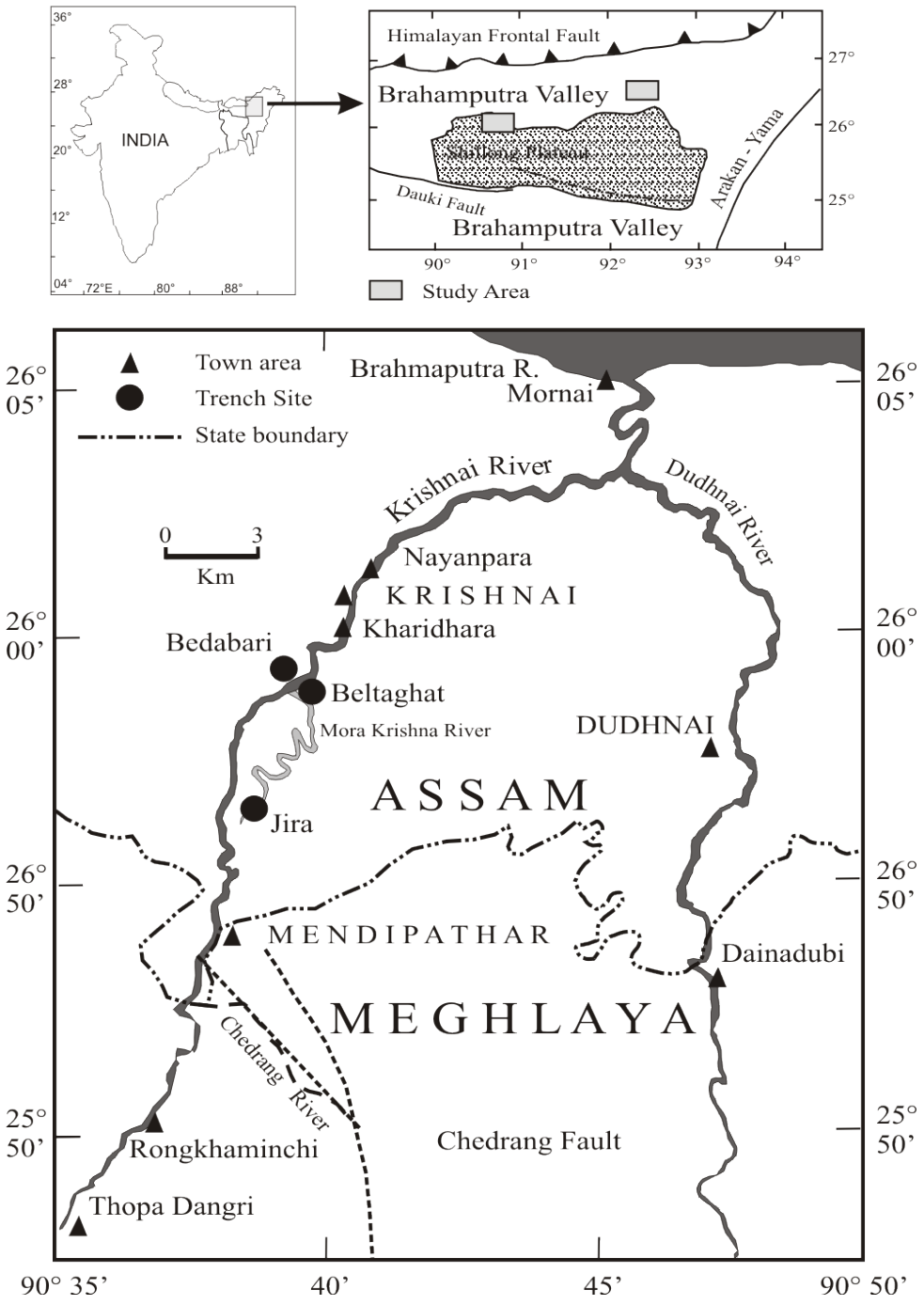

Figure 4.1: Location map of the study area. The sites Bedabari, Beltaghat are close to the Krishnai river and Jira is near the Mora Krishna river (dead river). The other sites Kakoti and Namgon are close to the Kopili River (modified after Sukhija et al., 1999)

4.3.1 Extent of heating

The extent of thermal resetting in the dike samples was tested by using the step wise heating method. It was observed that the 110 °C TL peak of quartz is sensitized after the repeated cycle of irradiation and heat (Zimmerman, 1971b; Rink et al., 1999). The protocol used for this experiment is shown in Figure 4.2. The TD response of TL 110 °C peak for dike and host layer samples from Bedabari site is shown in Figure 4.3a.

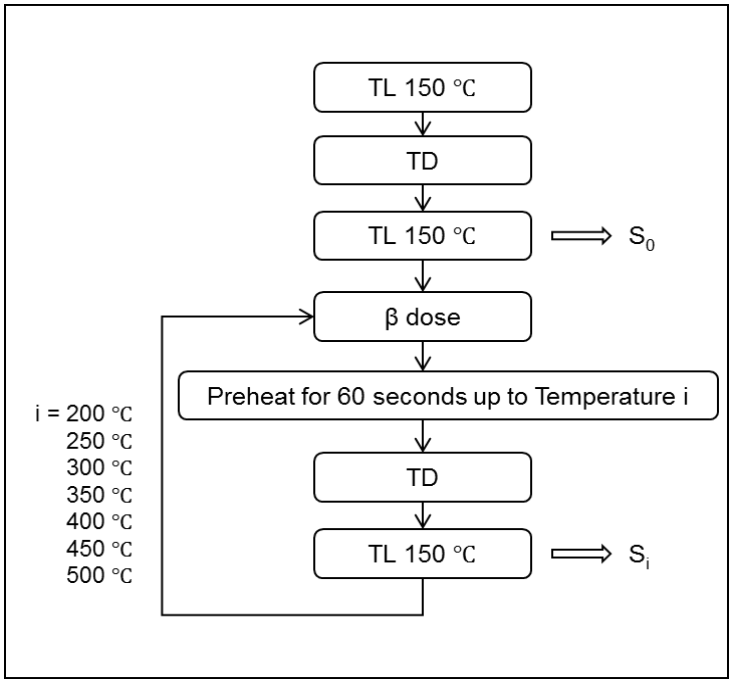

Figure 4.2: Flow chart for the measurement protocol for the monitoring of 110 °C TL peak of quartz (Step wise heating).

It was observed that the sensitization in the dike sample is more as compared to the host layer samples.The normalized TL response of 110 °C peak after The TL sensitivity change in step-wise heating method for sand dike and host layer samples collected from sites Bedabari, Beltaghat, Jira and Kakoti are shown in Figure 4.3(a), (b), Figure 4.4(a) and (b). Rink et al. (1999) used the stepwise heating experiment on quartz samples to see the change in sensitivity of the 110 °C peak of quartz and to estimate the extent of heating in quartz samples based on the laboratory preheat experiments. It was observed that the sensitivity of 110 °C quartz peak does not show any significant change in the sensitivity if the preheat temperature is less than the temperature already experienced by the sample. After that the

significant increase in the TD response of TL 110 °C peak was observed. In present case the sensitivity of 110 °C TL peak does not show any significant change up to preheat cycle of 300 °C (Figure 4.3). For Bedabari site it was observed that the increase in sensitivity started in temperature range 350-400 °C suggesting that the dike samples have faced heating between 350-400 °C. Similarly for the Beltaghat the TL sensitivity started increasing in a temperature range 350-400 °C. This suggested that the dike samples from the Beltaghat site also have faced heating at least up to 350 °C.

TL sensitivity of dike samples was found to be increasing significantly in temperature ranges 350-400 °C for the samples collected from Jira, Namgaon and Kakoti site. In all cases it was observed that the TL sensitivity after preheat temperature of 300 °C, became twice of the sensitivity at first preheat cycle and seven to ten times after preheat of 350 °C. These observations suggested us to infer that in present case all dike samples have at least experienced heating up to 350 °C. As discussed in Chapter 3, the only possibility of this heating in case of sand dike is viscous heating which might led the temperature to increase >350 °C and will result in the resetting of the luminescence signal in sand dikes. In another experiment to find the extent of possible heating of dike sample a preheat experiment was done for host layer samples. In this experiment the sample from the host layer was preheated at different temperature (200, 300 and 350 °C) for 10 second and the TL response of higher temperature peak (300-400 °C) was recorded. The results obtained are shown in Figure 4.5. It was observed that preheat of 250 °C reduce the level of natural luminescence in host layer sample equivalent to the natural luminescence signal in dike. This indicated that in dike samples the heating was > 250 °C (Figure 4.5a) .For the samples collected from Kakoti sites, it was observed that the >300 °C temperature is required to bring the natural luminescence from host sample to the natural luminescence equivalent in dike samples (Figure 4.5b).

4.3.2 Age Estimation

The typical OSL decay curves, growth curves and dose recovery curves for two of the representative samples from Kakoti site are shown in Figure 4.7 (a), (b), (c) and (d). The dose recovery of all samples was within ±10%. Figure 4.8 shows the preheat plateau for samples KKT-1 and KKT-17, the stable value of D_e was observed for preheat temperature ranging

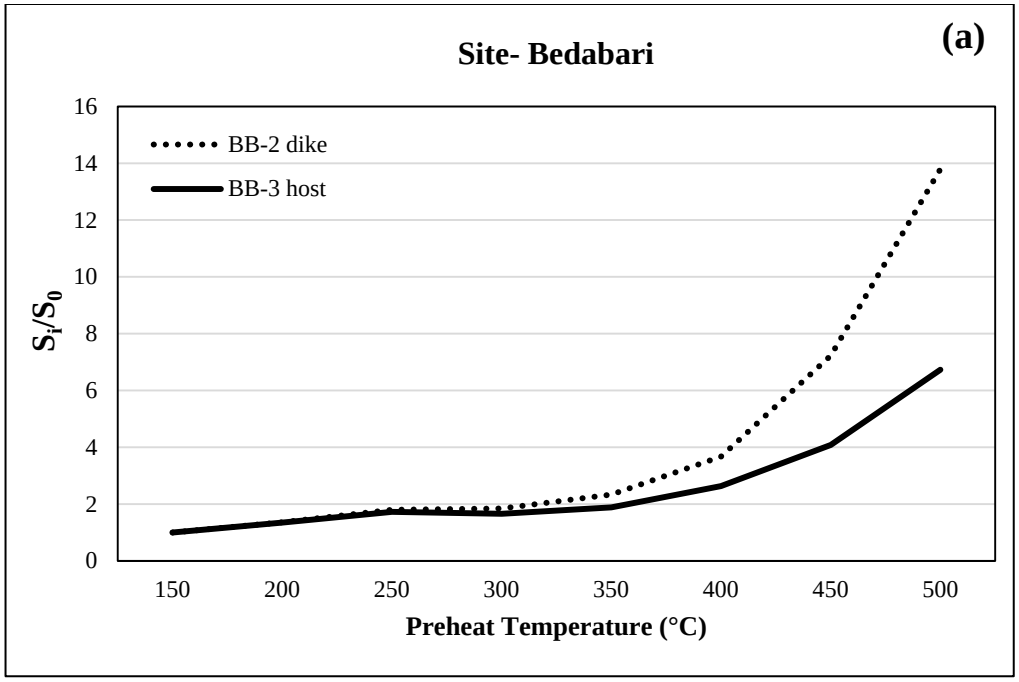

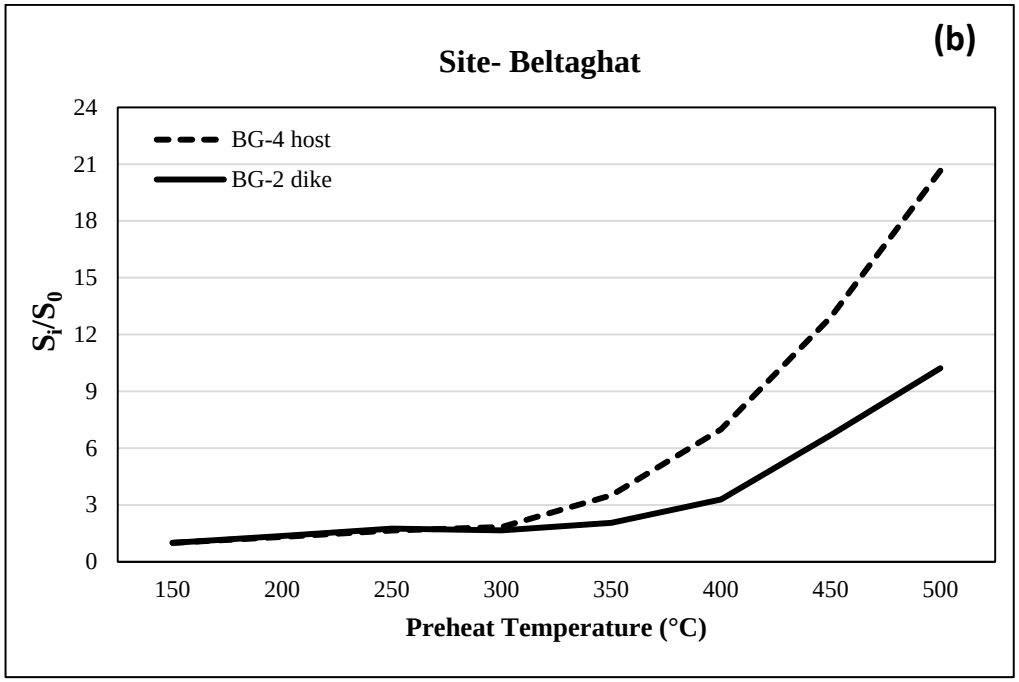

Figure 4.3: (a) Sensitivity change in 110 °C peak of quartz from dike and host samples for Bedabari and (b) Beltaghat sites

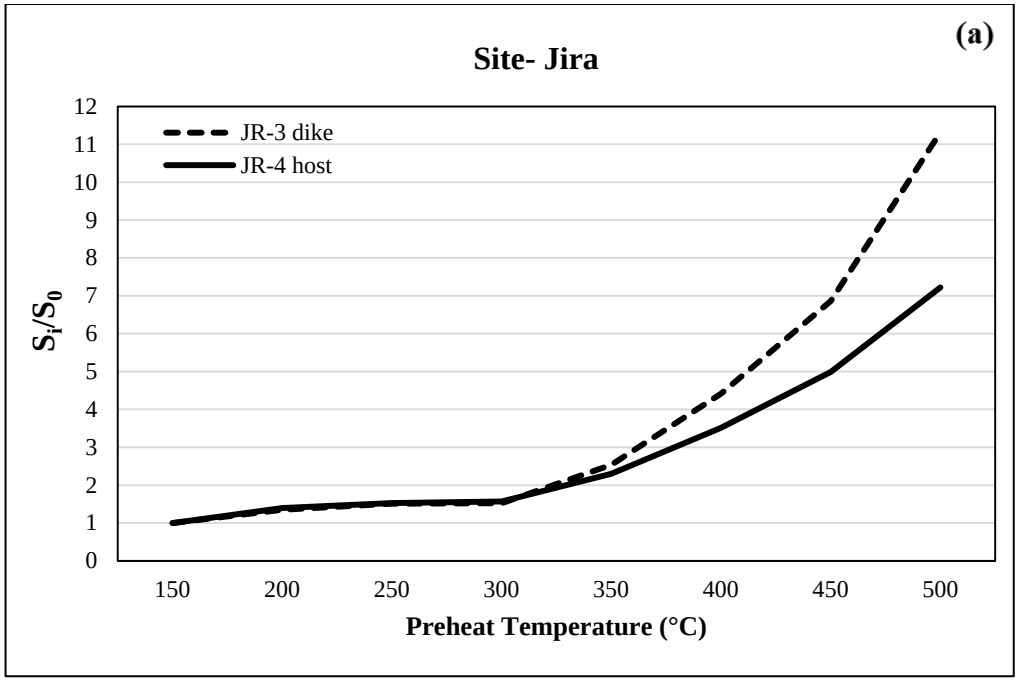

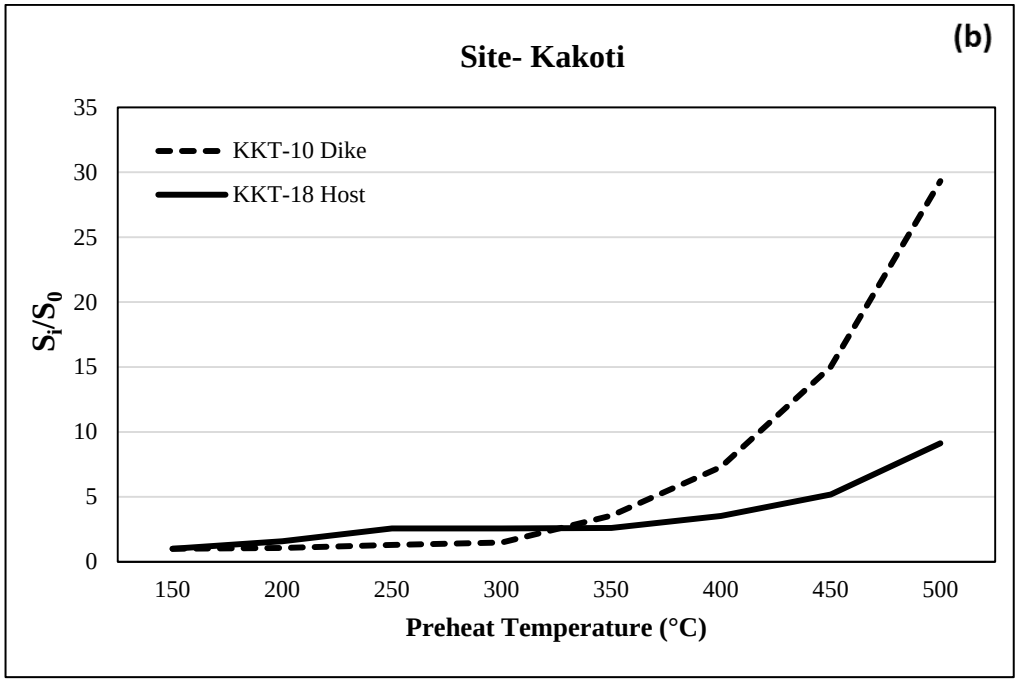

Figure 4.4: (a) Sensitivity change in 110 °C peak of quartz from dike and host samples for Jira and (b) Kakoti sites

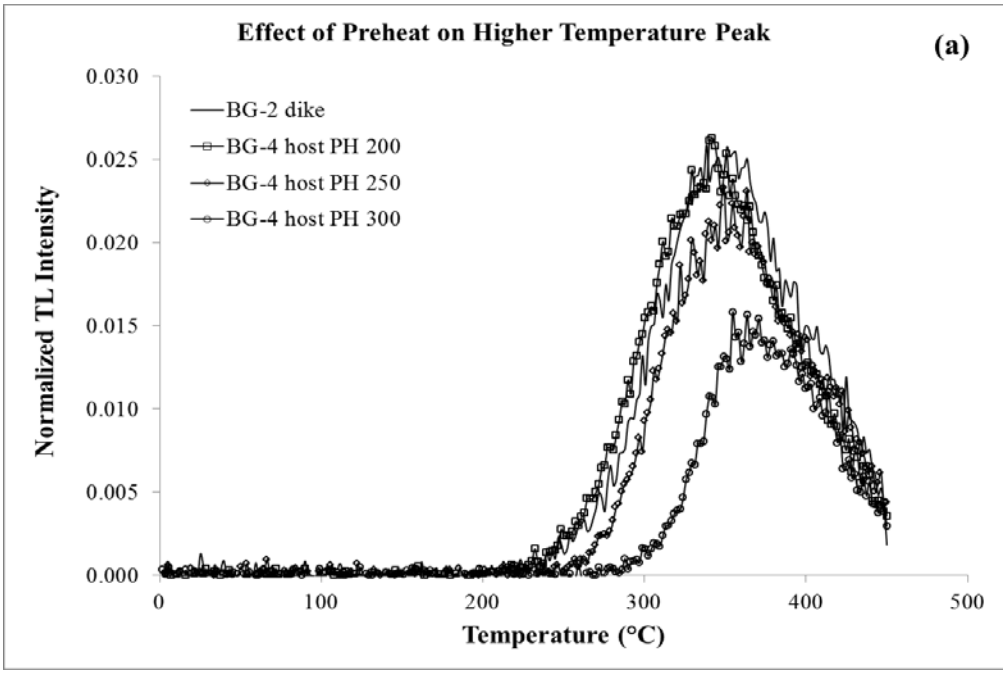

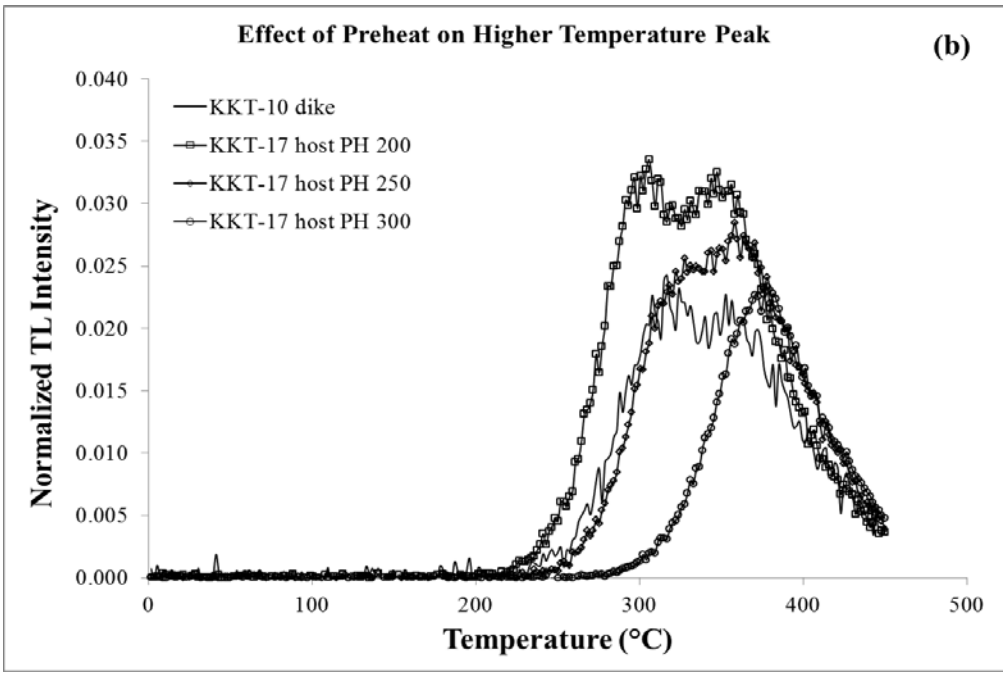

Figure 4.5: Effect of preheat on higher temperature TL peak for samples from (a) Beltaghat site and (b) Kakoti site

from 200-260 °C. Typical SAR growth curves of quartz extracted for KKT−16, KKT−17, NG-3, NG-7, BG2 and BG-4 are shown in Figure 4.10(a-f). The regeneration curves were constructed using the standard protocols SAR and NCF-SAR as discussed in chapter-2. A comparison of NCF corrected D_e (Mean and Minimum+2σ) and without NCF correction is shown in

Table 4.2. The D_e values without NCF correction show a larger distribution as compared to those obtained after NCF correction. Figure 4.11 shows the comparison of D_e distribution (histogram) for samples KKT-1 and KKT-14 with NCF correction and without NCF correction.

The distribution in the D_e values after NCF correction indicates the extent of partial resetting of luminescence signal during the resetting event. All samples were examined for the dose distribution by using the radial plots and histograms. The histograms for the samples were constructed using the bin size from the median of the errors of the doses. Typical radial plots and corresponding histograms for few samples are shown (Figure 4.12 to Figure 4.15). In view of the partial resetting of luminescence signal the ages were computed by using the minimum+2σ values (in most of the cases the least 10% and minimum+2σ values were similar or within the error range of each other).The details of the radioactivity data, water content, SAR ages obtained are shown in Table 4.1. A short discussion on the luminescence ages obtained for the samples collected from the different sites is given below

1. Bedabari

At Bedabari site two dikes (height ~1.5 m and width 15 cm, 5 cm) were found. The ages obtained for dike samples are 787 ± 121 years, 935 ± 113 years and for host layers are 787 ± 104 years, 1104 ± 127years.

2. Beltaghat

At Beltaghat two sites (150 meter away from each other) were explored for the sand dikes. At the first site, a dike of height about 3.5 m, bottom width about 25 cm was seen. Five samples were collected from this location (two from dike, one from bottom of the dike, one from source and one from host layer). The ages obtained for dike samples are 846 ± 147, 928 ± 116 and 903 ± 141 years, and for host layer and source layer are 1060 ± 158, 1178 ± 149 years respectively.

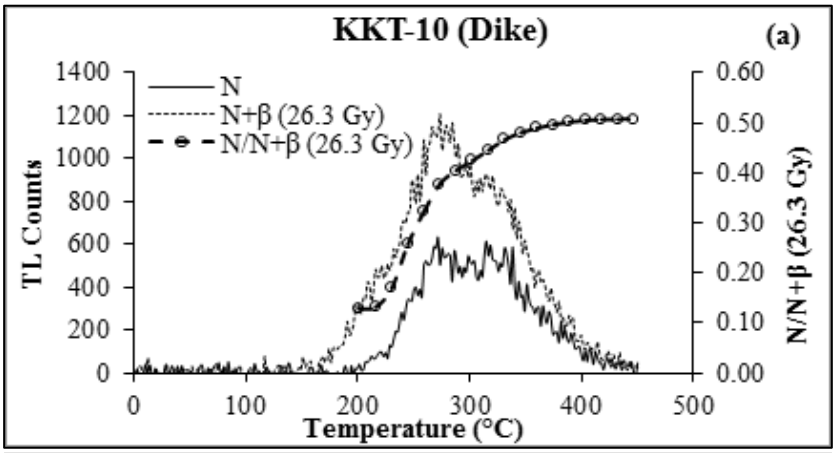
KKT-10 (Dike)
(a)
N
N+β (26.3 Gy)
N/N+β (26.3 Gy)
TL Counts
N/N+β (26.3 Gy)
Temperature (°C)

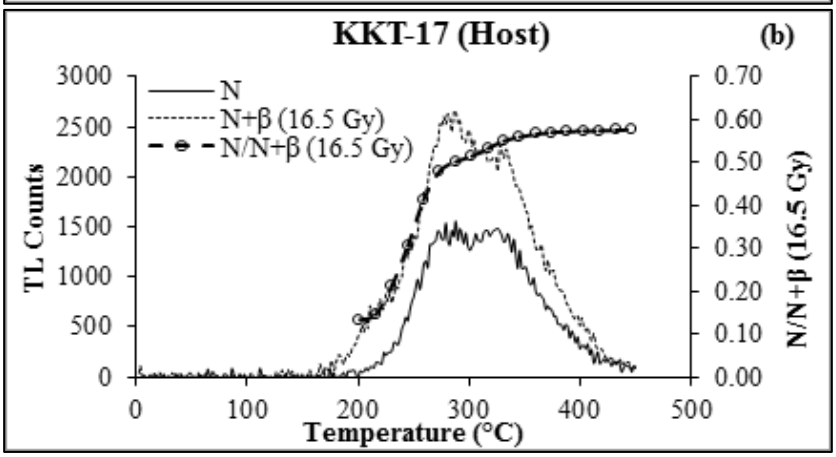
KKT-17 (Host)
(b)
N
N+β (16.5 Gy)
N/N+β (16.5 Gy)
TL Counts
N/N+β (16.5 Gy)
Temperature (°C)

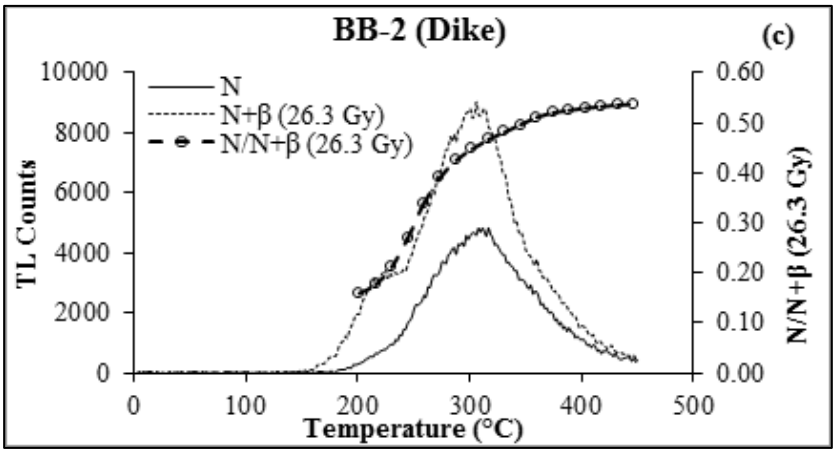
BB-2 (Dike)
(c)
N
N+β (26.3 Gy)
N/N+β (26.3 Gy)
TL Counts
N/N+β (26.3 Gy)
Temperature (°C)

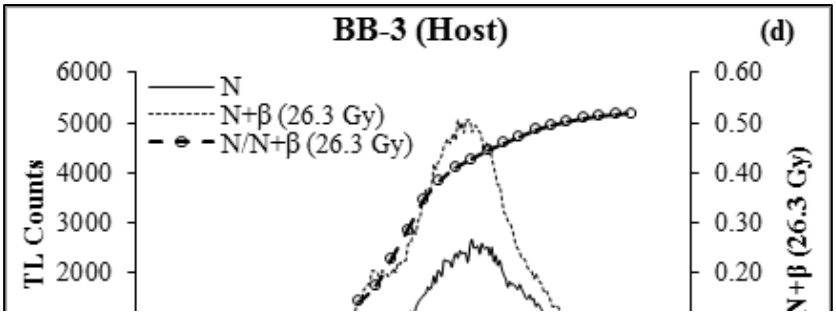
BB-3 (Host)
(d)
N
N+β (26.3 Gy)
N/N+β (26.3 Gy)
TL Counts

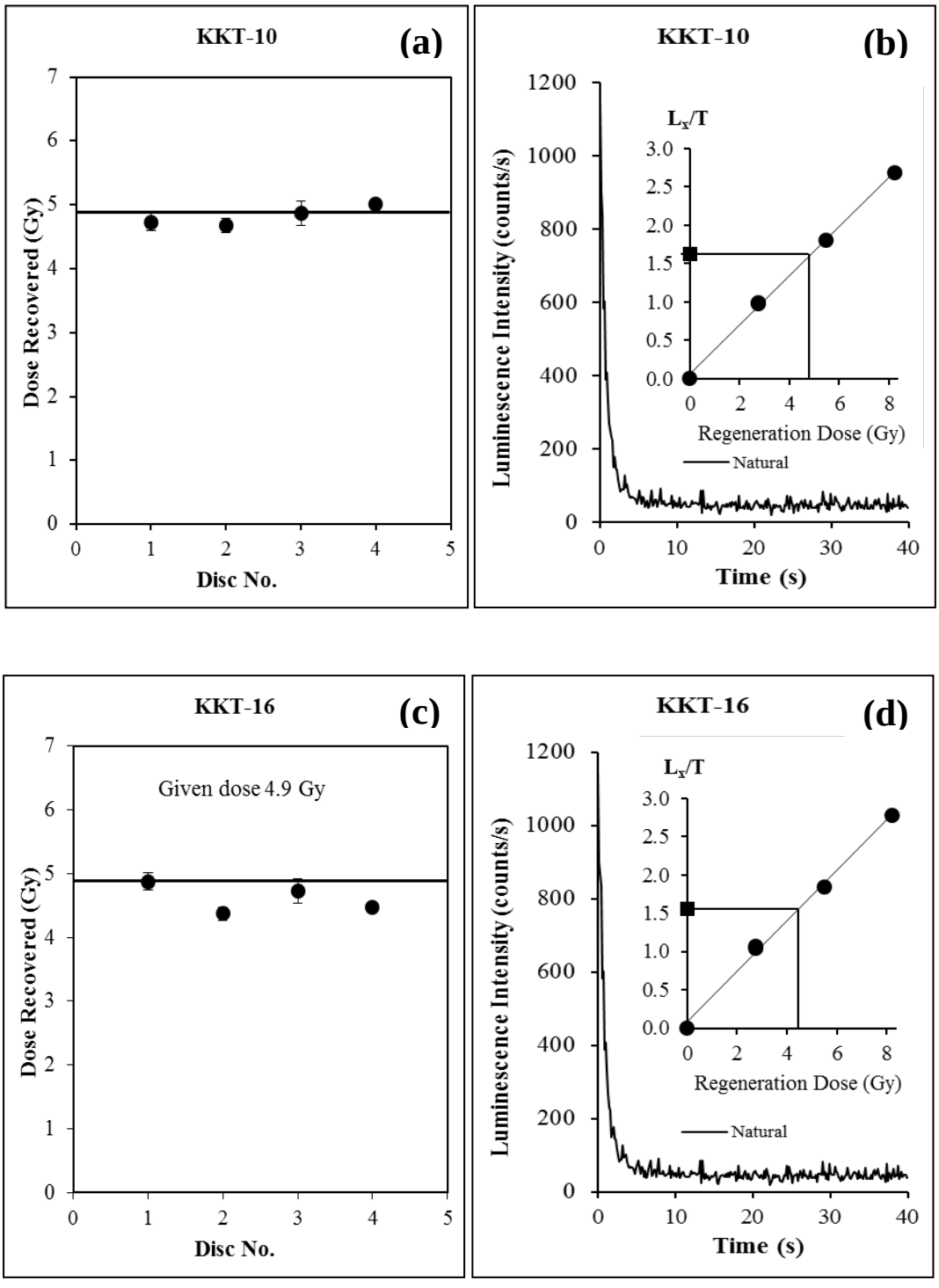

Figure 4.7: Dose recovery of samples KKT-10 and KKT-16 for Kakoti site (a, c); natural shine down curve for same samples (b,d), the growth curves for these samples are shown in the inset of figures (b) and (d).

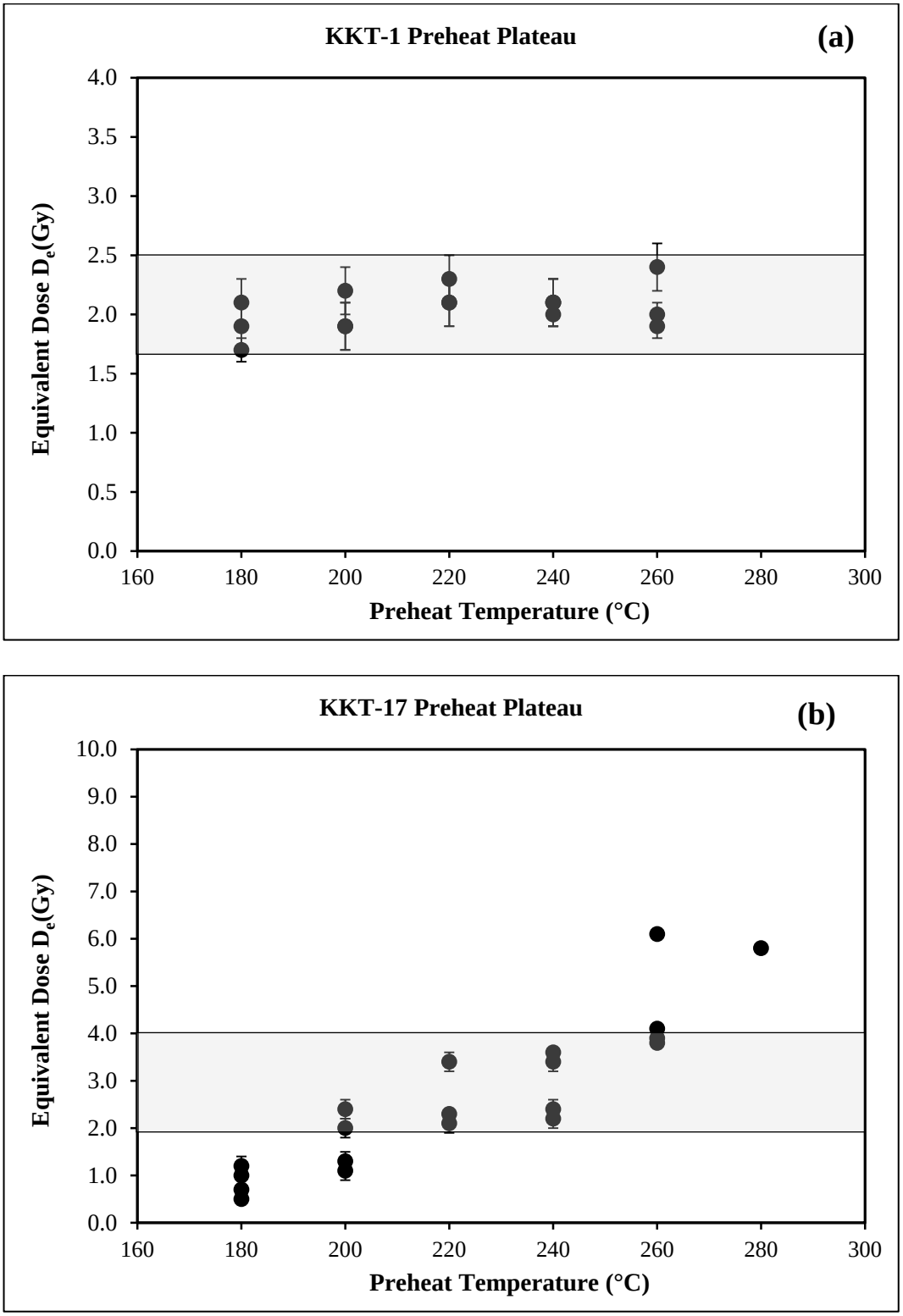

Figure 4.8: Preheat Plateau for Samples (a) KKT-1 and (b) KKT-17 collected from Kakoti site.

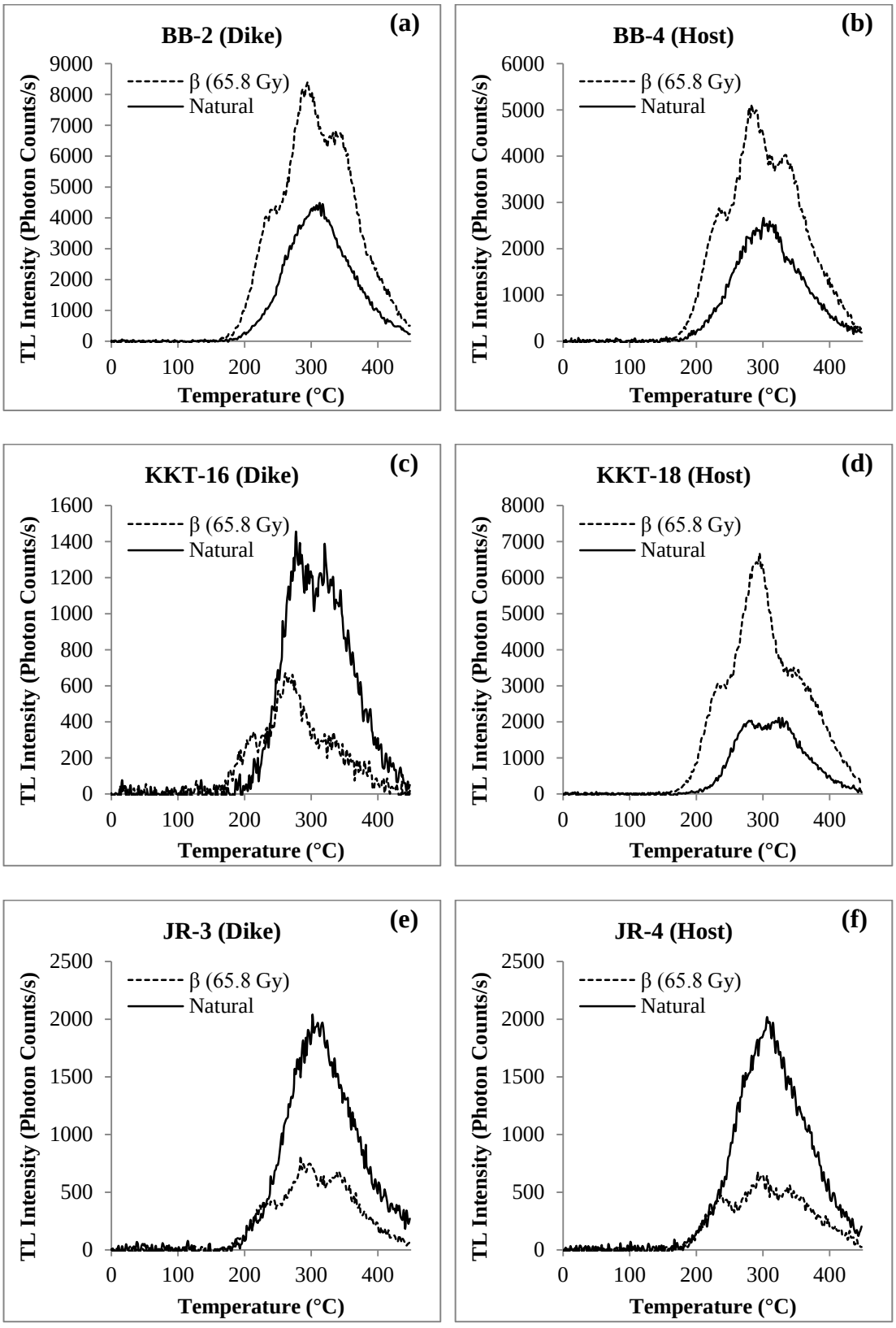

Figure 4.9: TL glow curves (natural and dosed) for dike and host samples (a), (b) Bedabari site; (c), (d) Kakoti site; (e), (f) Jira site.

From the nearby site another dike was also found, where sand was intruded in to the sand layer. Seven samples were collected from this location. Being a narrow dike, sometimes it was difficult to sample exactly from the dike and host layer and in that case sample from the dike/source or dike/host boundary was taken. This helped us in understanding the horizontal resetting pattern in dikes. The dike samples from this location gave age of 526 ± 69 years. The ages obtained for other samples are 1557 ± 219, 1023 ± 134 and 1128 ± 154 years for host layers; 641 ± 88 years for host/dike boundary and 921 ± 159, 943 ± 146 years for source/dike boundary.

3. Jira

At Jira a dike of height ~1.5 m and width 13 cm was found. Four samples were collected from this site are, two for dike, one for host and one for source layer. The dike samples from this site were dated to 600 ± 79, 677 ± 181 years; source layer sample was dated to 553 ± 84 years and the host sample was dated to 911 ± 115 years.

4. Kakoti

At Kakoti two sites were explored (within 200 meter of each other). A dike of height 3.1 m and width ~ 50 cm was found, which was having another branch of about same width. Total eight samples from this location were collected (two dike samples, three host layer samples and three source layer samples). The dike samples from this location were dated to 111 ± 12, 594 ± 90 years. Host layer samples were dated to 1521 ± 243, 1022 ± 161, 772 ± 107 years. The source layer samples were dated to 658 ± 95, 249 ± 40 and 512 ± 74 years. From another nearby location dikes with multiple branching were found. The total height of these dikes were 5.5 m and the widths varied from 5 cm to ~15 cm. Total eleven samples were collected from this site. The six dike samples were dated to 256 ± 35, 359 ± 57, 477 ± 67, 306 ± 37, 202 ± 24, 250 ± 34 years. The host layer samples were dated to 530 ± 74, 444 ± 91years. The source samples were dated to762 ± 128 and 177 ± 24 years. The sample from sand layer exposed at surface was dated to 305 ± 37years.

5. Namgaon

At Namgaon a dike of height ~1.6 m and width ~56 cm was found. Total eight samples (three dike samples, four host layer samples, and one source layer sample) were collected.

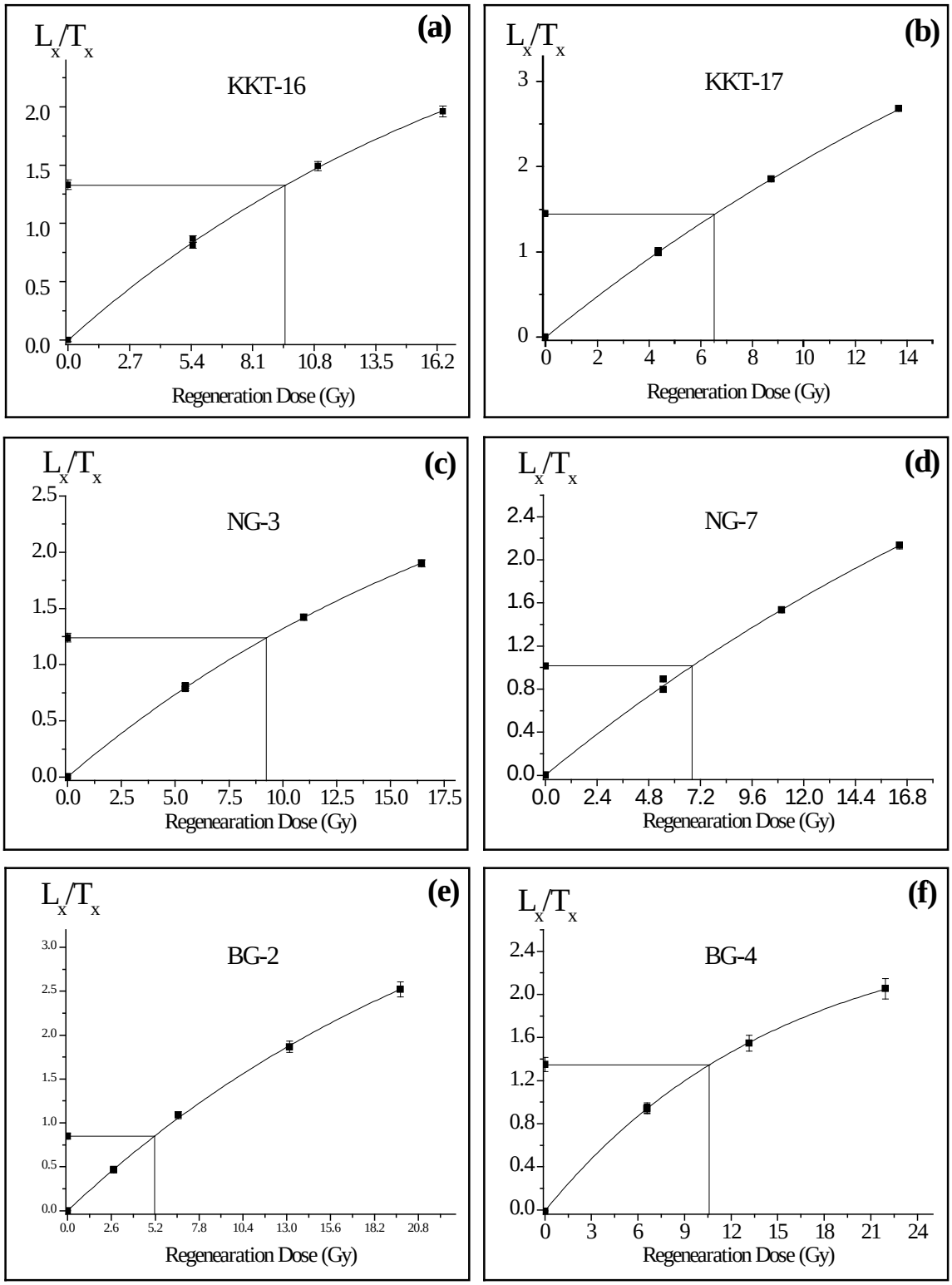

Figure 4.10: SAR regeneration curves for samples (a) KKT-16, (b) KKT-17, (c) NG-3 and (d) NG-7 constructed using the NCF protocol as discussed in chapter-2; SAR regeneration curves for samples (e) BG-2 and (f) BG-4

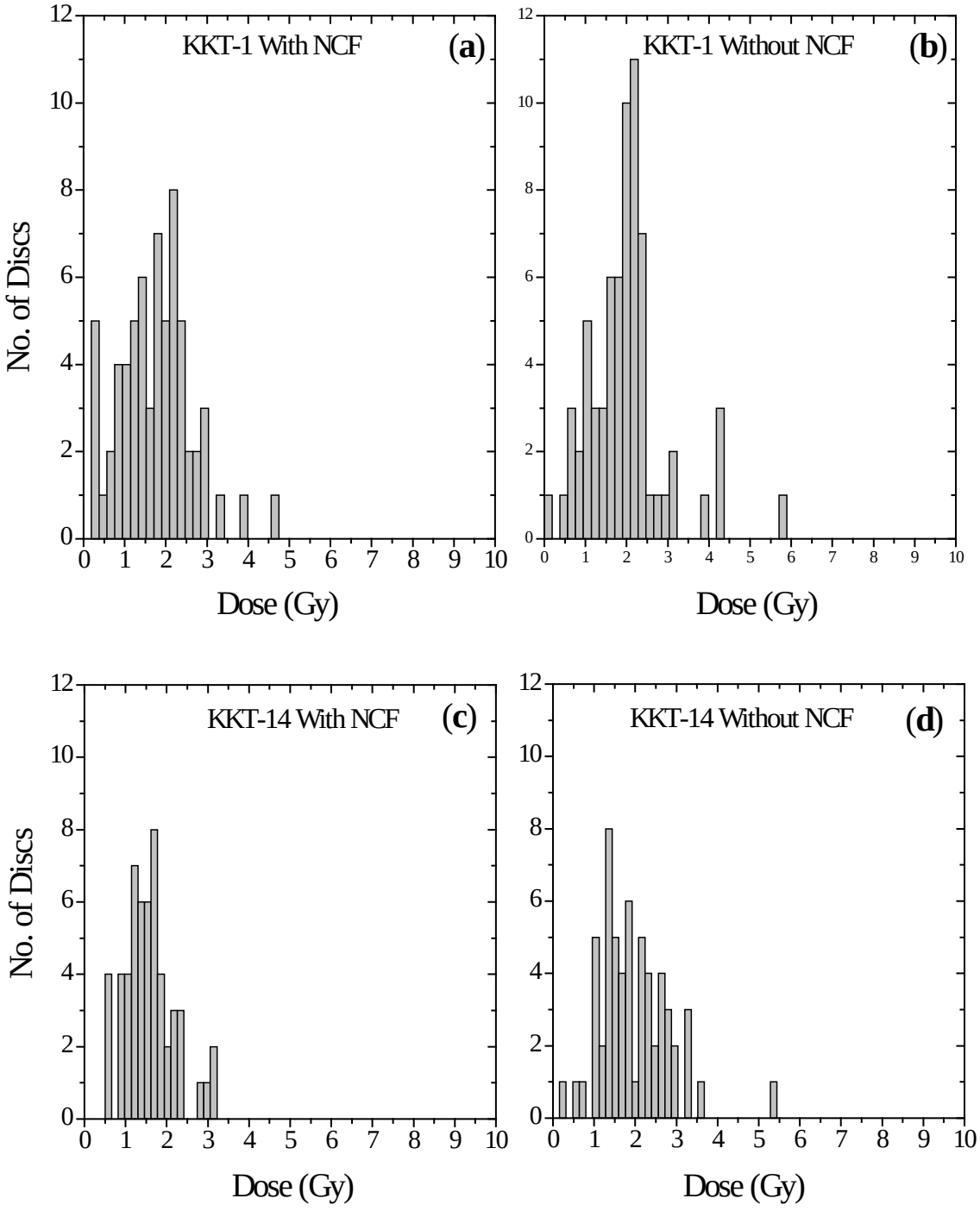

Figure 4.11: Histogram showing comparisons of D_e distribution with NCF protocol (a), (c) and without NCF protocol (b) and (d) for samples KKT-1 and KKT-14

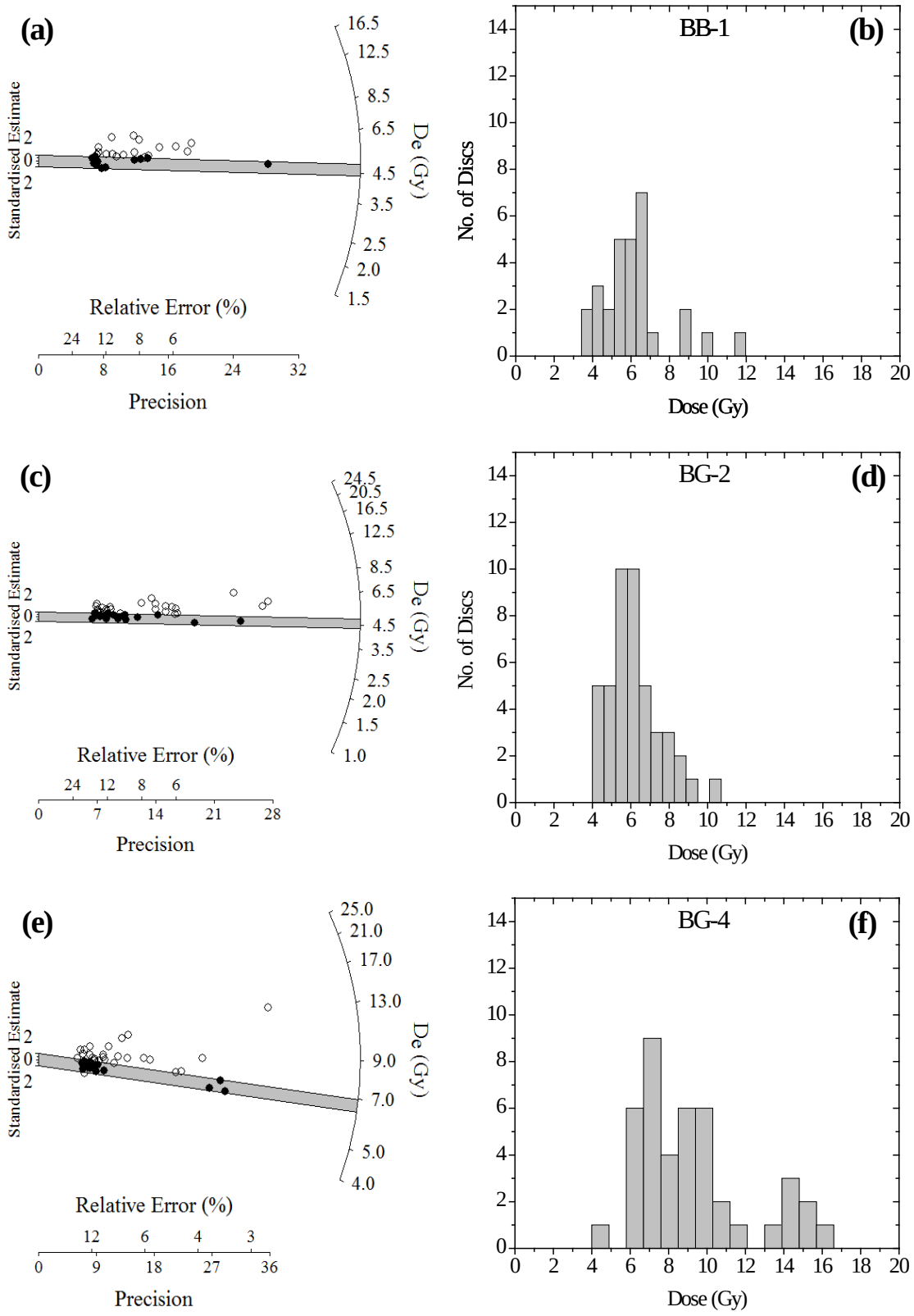

Figure 4.12: (a, c and e) shows the radial plot of D_e obtained for samples BB−1, BG−2 and BG−4 and (b, d and f) shows the dose distribution for these samples

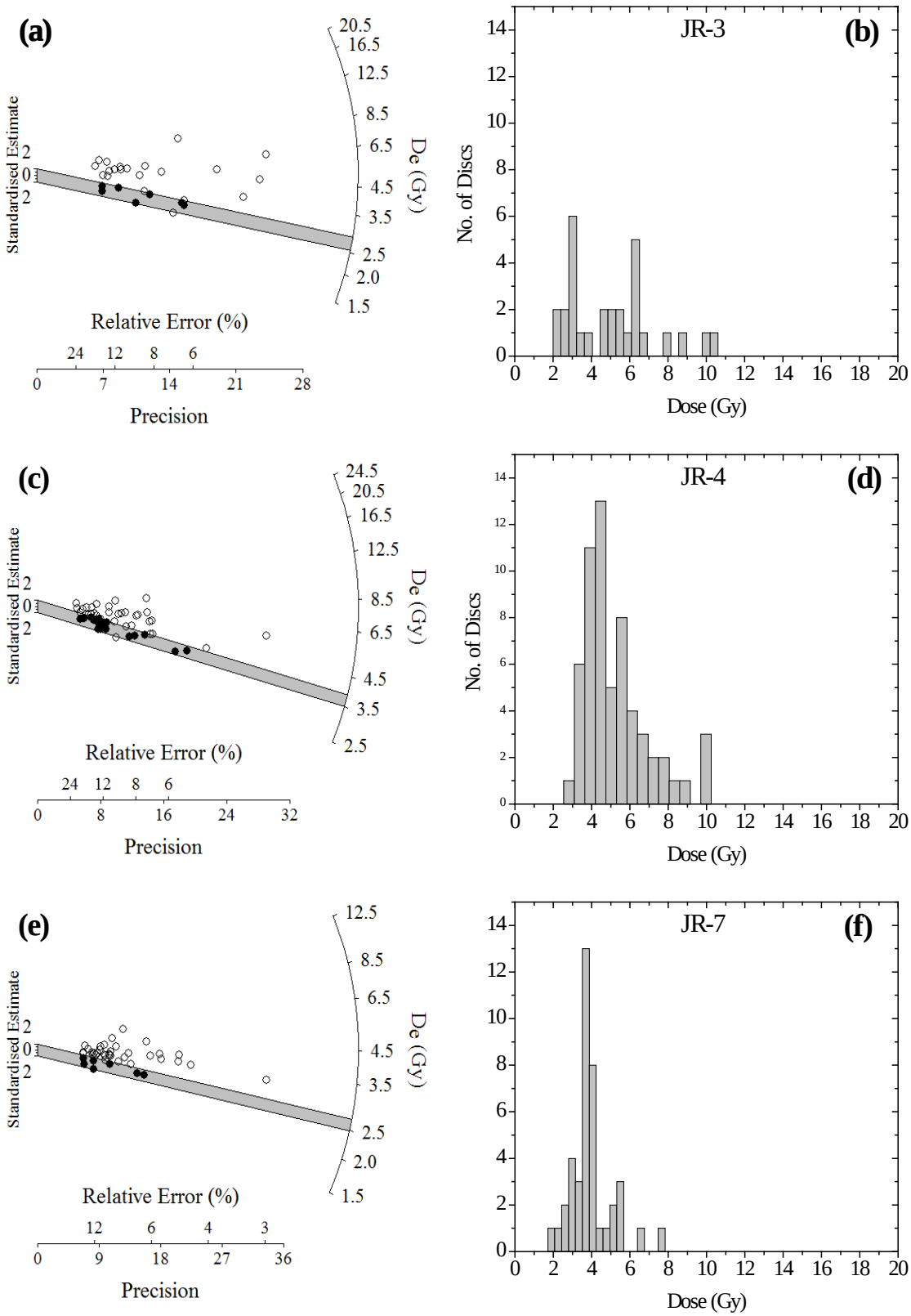

Figure 4.13: (a, c and e) shows the radial plot of D_e obtained for samples JR−3, JR−4 and JR−7 and (b, d and f) shows the dose distribution for these samples

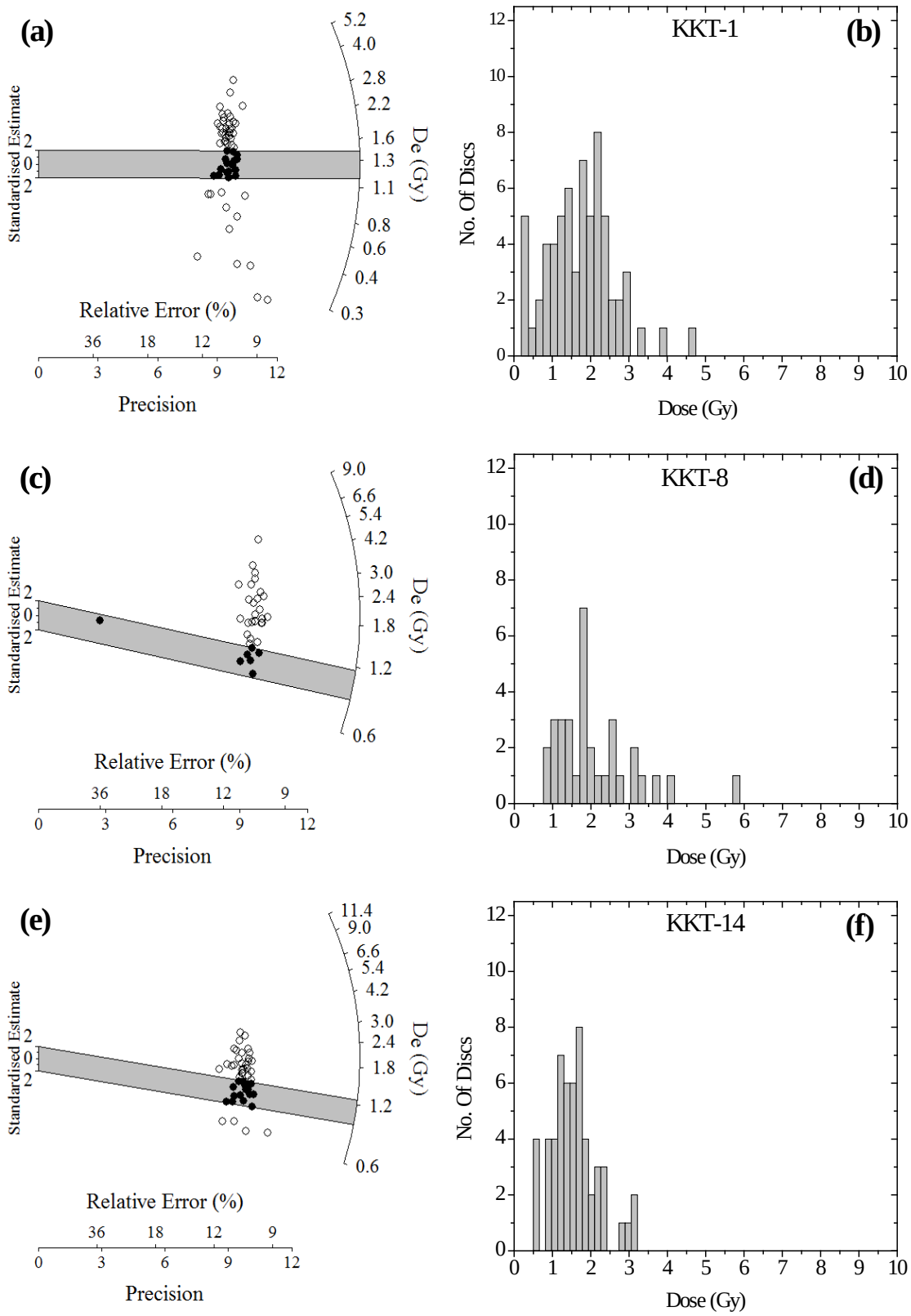

Figure 4.14: (a, c and e) shows the radial plot of D_e obtained for samples KKT−1, KKT−8 and KKT−14 and (b, d and f) shows the dose distribution for these samples

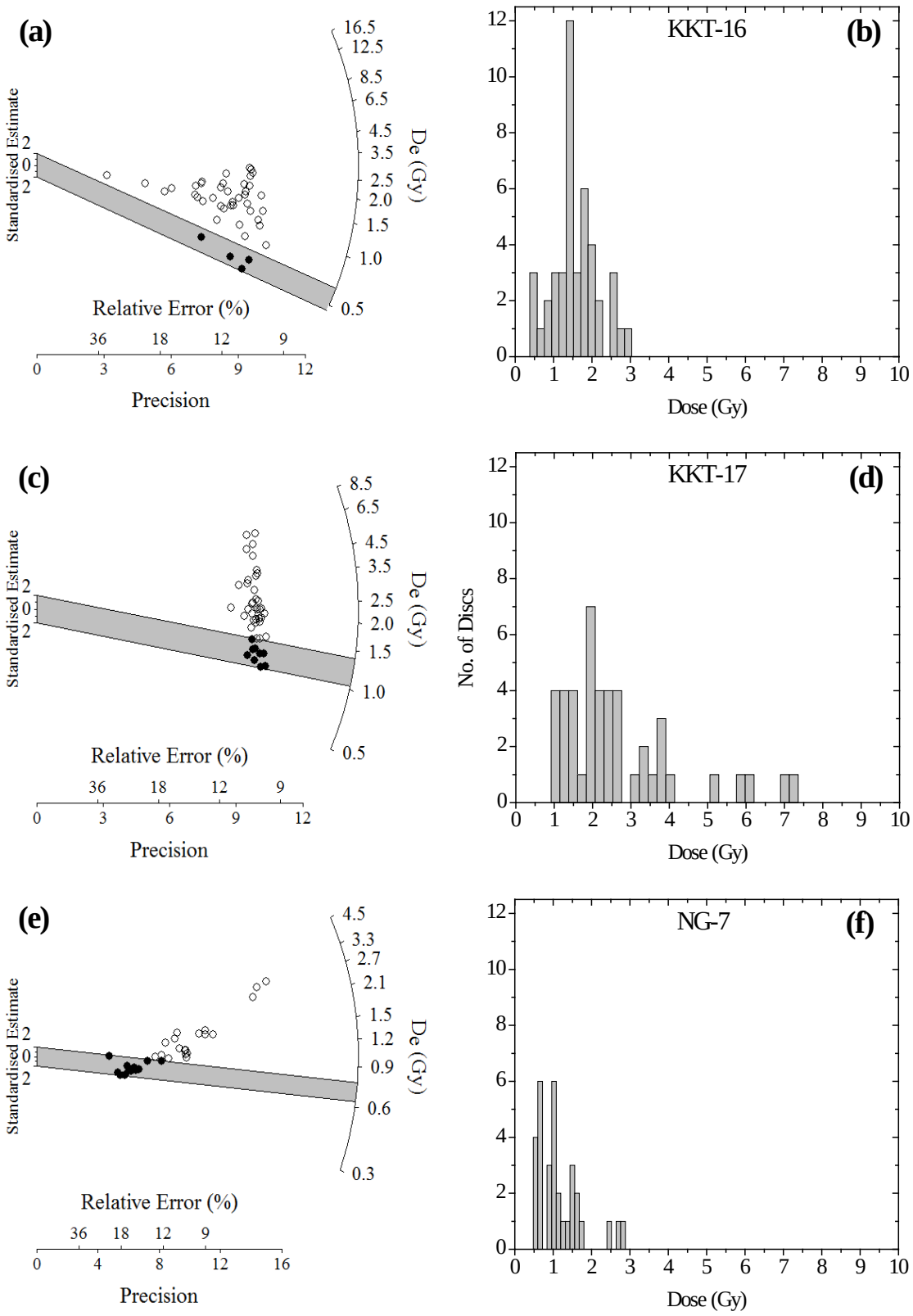

Figure 4.15: (a, c and e) shows the radial plot of D_e obtained for samples KKT−16, KKT−17 and NG−7 and (b, d and f) shows the dose distribution for these samples

Table 4.2: Comparison of SAR D_e with NCF correction and without NCF correction

Sample	D_e with NCF Correction		D_e without NCF Correction		% Variation from NCF D_e	
	Mean	Min+2σ	Mean	Min+2σ	Mean	Min+2σ
KKT-1	1.74 ± 0.11	0.23 ± 0.02	2.00 ± 0.12	2 ± 0.12	15	36
KKT-2	2.21 ± 0.19	0.96 ± 0.1	2.45 ± 0.18	2.45 ± 0.18	11	60
KKT-3	4.69 ± 0.19	2.94 ± 0.31	4.56 ± 0.16	4.56 ± 0.16	3	4
KKT-4	2.9 ± 0.14	1.97 ± 0.2	3.29 ± 0.18	3.29 ± 0.18	14	4
KKT-5	2.71 ± 0.13	1.63 ± 0.18	2.68 ± 0.12	2.68 ± 0.12	1	82
KKT-6	1.76 ± 0.12	0.91 ± 0.09	2.17 ± 0.21	2.17 ± 0.21	24	70
KKT-7	1.32 ± 0.11	0.59 ± 0.07	1.83 ± 0.18	1.83 ± 0.18	39	69
KKT-8	2.11 ± 0.19	0.9 ± 0.1	2.31 ± 0.19	2.31 ± 0.19	10	32
KKT-10	1.58 ± 0.15	0.55 ± 0.06	2.26 ± 0.13	2.26 ± 0.13	43	53
KKT-12	1.72 ± 0.2	0.85 ± 0.09	2.13 ± 0.22	2.13 ± 0.22	24	54
KKT-14	1.59 ± 0.08	0.62 ± 0.06	2.58 ± 0.13	2.58 ± 0.13	62	62
KKT-16	1.57 ± 0.09	0.52 ± 0.06	1.89 ± 0.11	1.89 ± 0.11	21	78
KKT-17	2.66 ± 0.23	1.1 ± 0.11	3.65 ± 0.34	3.65 ± 0.34	38	27
KKT-18	2.2 ± 0.14	1.05 ± 0.19	3.02 ± 0.16	3.02 ± 0.16	38	32
KKT-20	1.45 ± 0.13	0.43 ± 0.04	2.28 ± 0.29	2.28 ± 0.29	57	89
NG-1	1.26 ± 0.14	0.22 ± 0.03	1.16 ± 0.11	1.16 ± 0.11	8	69
NG-2	1.39 ± 0.17	0.29 ± 0.03	1.43 ± 0.17	1.43 ± 0.17	3	13
NG-3	1.08 ± 0.15	0.29 ± 0.03	1.53 ± 0.22	1.53 ± 0.22	42	18
NG-4	1.24 ± 0.17	0.45 ± 0.06	1.28 ± 0.17	1.28 ± 0.17	3	73
NG-5	0.86 ± 0.1	0.24 ± 0.02	1.12 ± 0.25	1.12 ± 0.25	30	41
NG-6	1.26 ± 0.2	0.3 ± 0.03	1.77 ± 0.25	1.77 ± 0.25	40	27
NG-7	1.17 ± 0.11	0.58 ± 0.1	1.3 ± 0.11	1.3 ± 0.11	11	43
NG-8	0.88 ± 0.1	0.16 ± 0.02	0.92 ± 0.09	0.92 ± 0.09	4	57

Table 4.3: Details of samples, depth, type, radioactivity data, water content, De and calculated Ages

U (ppm)	**Th (ppm)**	**K (%)**	**CR (Gy/ka)**	**Water (%)**
6.2 ± 0.2	20.6 ± 0.7	3.4 ± 0.1	179.9 ± 9	15 ± 5
3.8 ± 0	12.8 ± 0.2	3.2 ± 0.1	178.3 ± 8.9	15 ± 5
9.9 ± 0.2	33.1 ± 0.7	2.5 ± 0.1	167.4 ± 8.4	20 ± 5
13.3 ± 0.1	44.4 ± 0.4	3.7 ± 0.1	168.1 ± 8.4	20 ± 5
6.3 ± 0.2	20.9 ± 0.7	3.5 ± 0.1	180 ± 9	20 ± 5
3 ± 0	10.1 ± 0.1	3 ± 0.1	173.2 ± 8.7	15 ± 5
6.3 ± 0.2	20.9 ± 0.7	1.6 ± 0.1	165.5 ± 8.3	15 ± 5
9.5 ± 0.1	31.7 ± 0.4	2.4 ± 0.1	169 ± 8.5	20 ± 5
5.4 ± 0.1	17.9 ± 0.3	3.1 ± 0.1	160.8 ± 8	20 ± 5
9.7 ± 0.2	32.3 ± 0.6	2.4 ± 0.2	150.5 ± 7.5	15 ± 5

Table 4.3 Continued

S. No.	Sample	Type	Depth	U (ppm)	Th (ppm)	K (%)	CR
11	BG-7	host	4.62	2.4 ± 0.1	7.9 ± 0.2	2 ± 0.1	14
12	BG-8	host	4.70	5.9 ± 0.2	19.6 ± 0.5	2.2 ± 0.1	148
13	BG-9	host/dike boundary	4.72	10.4 ± 0.3	34.9 ± 0.9	1.9 ± 0.1	148
14	BG-10	source/dike boundary	4.94	3.3 ± 0.1	10.9 ± 0.3	1.5 ± 0.1	146
15	BG-11	source/dike boundary	5.10	2.1 ± 0	6.9 ± 0.2	3.1 ± 0.1	146
16	BG-12	host	4.90	5.3 ± 0	17.8 ± 0.1	1.8 ± 0.1	145
17	JR-3	dike	1.15	3.7 ± 0	12.3 ± 0.2	3 ± 0.1	18
18	JR-4	host	1.18	10.2 ± 0.3	34 ± 0.9	3.1 ± 0.1	181
19	JR-5	dike	1.54	3.4 ± 0	11.4 ± 0.1	2 ± 0.1	177
20	JR-7	source	1.94	4.6 ± 0.1	15.2 ± 0.2	2.9 ± 0.1	172

Table 4.3 Continued

S. No.	Sample	Type	Depth	U (ppm)	Th (ppm)	K (%)	C
21	KKT-1	dike	0.63	2.1 ± 0.1	7 ± 0.2	1.4 ± 0.1	1
22	KKT-2	dike	1.46	2.6 ± 0.1	8.6 ± 0.2	0.7 ± 0.1	1
23	KKT-3	host	1.62	12.9 ± 0.4	43.2 ± 1.3	1.6 ± 0.1	1
24	KKT-4	host	2.02	3.7 ± 0.1	12.3 ± 0.4	0.7 ± 0.1	1
25	KKT-5	host	2.17	4.1 ± 0.1	13.7 ± 0.4	0.7 ± 0.1	1
26	KKT-6	source	2.50	2.2 ± 0.1	7.3 ± 0.2	0.7 ± 0.1	1
27	KKT-7	source	2.86	4 ± 0.1	13.2 ± 0.3	1.2 ± 0.1	1
28	KKT-8	source	3.10	1.8 ± 0	5.9 ± 0.1	1.4 ± 0.1	
29	KKT-10	dike	2.20	2.4 ± 0	8.1 ± 0.1	1.3 ± 0.1	1
30	KKT-11	dike	3.50	2.8 ± 0.1	9.3 ± 0.3	0.6 ± 0.1	1

Table 4.3 Continued

U (ppm)	Th (ppm)	K (%)	CR (Gy/ka)	Water (%)
1.5 ± 0	5 ± 0.1	0.6 ± 0.1	146.8 ± 7.3	20 ± 5
1.2 ± 0	4.1 ± 0.1	0.5 ± 0.1	172 ± 8.6	15 ± 5
3.2 ± 0.1	10.5 ± 0.3	0.9 ± 0.1	161.5 ± 8.1	15 ± 5
1.3 ± 0	4.2 ± 0.1	0.5 ± 0.1	152.6 ± 7.6	15 ± 5
2.6 ± 0	8.6 ± 0.1	1.2 ± 0.1	174.3 ± 8.7	15 ± 5
2.2 ± 0	7.4 ± 0.1	1.6 ± 0.1	160.2 ± 8	20 ± 5
2.8 ± 0.1	9.2 ± 0.3	1.8 ± 0.1	156.8 ± 7.8	20 ± 5
1.5 ± 0	5.2 ± 0.1	1.3 ± 0.1	145.3 ± 7.3	20 ± 5

Table 4.3 Continued

Type	**Depth**	**U (ppm)**	**Th (ppm)**	**K (%)**	**CR (Gy/ka)**	**Water (%)**	**D_e**
dike xposed surface at the ime of event	0.60	1.7 ± 0	5.7 ± 0.1	0.8 ± 0.1	194.3 ± 9.7	15 ± 5	0.4 ± 0
host	0.30	4.5 ± 0.1	14.9 ± 0.5	2.4 ± 0.1	193 ± 9.7	20 ± 5	0.2 ± 0
dike	0.60	3.3 ± 0.1	10.9 ± 0.2	0.9 ± 0.1	189.8 ± 9.5	15 ± 5	0.3 ± 0
host	0.72	3.2 ± 0	10.8 ± 0.1	2.3 ± 0.1	188.1 ± 9.4	20 ± 5	0.3 ± 0
dike	1.00	3.2 ± 0.1	10.7 ± 0.3	1.3 ± 0.1	184.2 ± 9.2	15 ± 5	0.4 ± 0.1
dike	1.35	4.6 ± 0.1	15.2 ± 0.2	1.1 ± 0.1	179.7 ± 9	20 ± 5	0.2 ± 0
ource	1.70	2.8 ± 0.1	9.4 ± 0.2	1.2 ± 0.1	175.4 ± 8.8	20 ± 5	0.3 ± 0
host	0.51	5.6 ± 0.1	18.7 ± 0.2	2.2 ± 0.1	191.1 ± 9.6	20 ± 5	0.6 ± 0.1
host	1.47	3.8 ± 0.1	12.6 ± 0.2	1.1 ± 0.1	178.2 ± 8.9	20 ± 5	0.3 ± 0

The ages obtained are 135 ± 17, 193 ± 32, 96 ± 13 year for dike samples; 153 ± 22 years for source layer sample; 60 ± 9, 98 ± 13, 160 ± 32 and 141 ± 23 years for host layer samples.

4.4 Discussion

The luminescence studies of sand dike samples collected from the North-East India suggested the resetting of luminescence signal during the injection of dikes. While for some cases the ages obtained from the dike sample and host layers were found to be within errors for others a discernible difference was seen. In all dike samples it was found that the samples show an increasing trend from top to bottom. The samples from the top of the dike gave minimum ages. As identified by At Kakoti site a layer of same material as of sand dike was found below 30 cm from the present day surface. A sand blow was found at the Kakoti site which gave a greater

opportunity to ascertain the resetting of luminescence signal during the injection of the dike. At this site the source sand from ~ 5 m below the present day surface was found to be intruded in the form of dike ~ 5m. The dike was truncated ~ 30 cm below at the present day surface. At this depth the dike was found in contact with a sand layer of (about 5−10 cm in thickness) same material as of the sand. This suggested that the source sand was blown (sand blow) up to the surface at the time of earthquake. Thus the material of this sand blow was exposed to sunlight and most likely led to the zeroing of the luminescence of the quartz grains of the material. The sample collected from this sand blow layer gave age of 305±37 years, and the samples from the dike which were connected to this layer were dated to 256±35 years, 359±57 years, 477±67 years and 306±37 years. These ages from the exposed sand at surface and those of the dikes are in good agreement of each other indicating a resetting of the luminescence signal in the dike material. As the dike material itself was not exposed to the sunlight the possible mechanism which might have caused the luminescence signal to zero in the dike sample is the viscous heating as discussed in chapter-3.

Based on the study performed on the sand dike samples we suggest multiple tectonic events in this area. The ages on the sand dikes suggested tectonic events at around 300 years, 500 years and 1 ka. Earlier work by Sukhija et al. (1999) and Reddy et al. (2009) based on the radiocarbon dating resulted in similar ages from Beltaghat, Bedabari and Jira sites. Their

results were based on the radiocarbon ages from the charcoal, wood, tree trunk affected by the tectonic events.

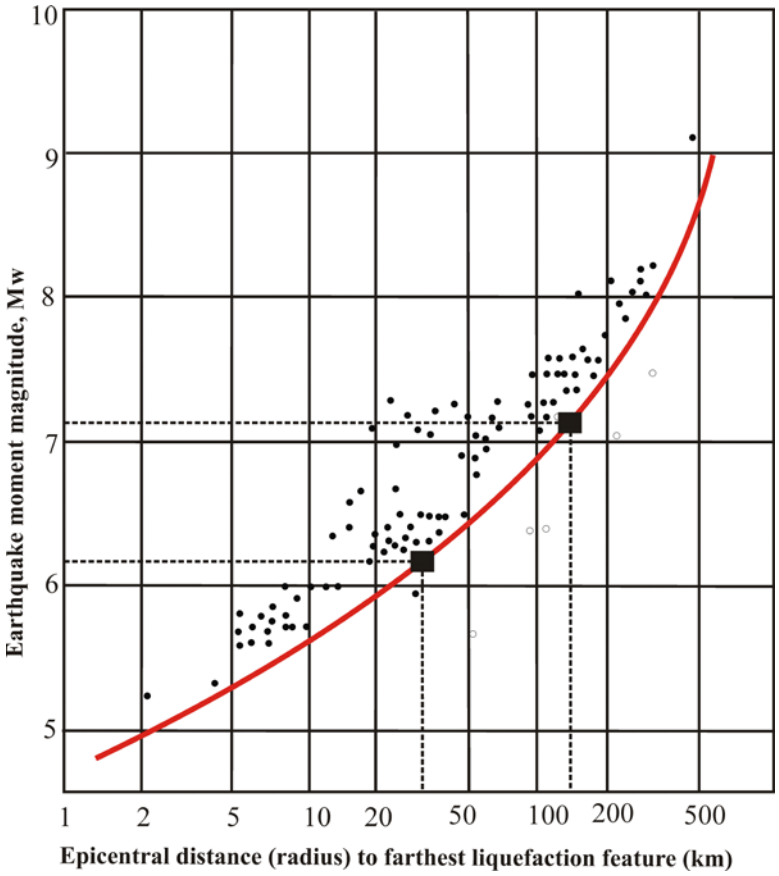

Figure 4.16: Estimation of the minimum magnitude of earthquake resulting paleoliquefaction at the study area by plotting the distances of liquefaction sites from epicenters on the global data curve of Obermeier (1996). The location of the Bedabari, Beltaghat, and Jira sites (lower black rectangle) and for Kakoti and Namgaon sites (upper black rectangle) are plotted considering that the earthquake epicenter which produced liquefaction either occurred: within a radius of 35 km and 150 km (distance between 1987 Shillong Plateau earthquake epicenter and the sites). The magnitude of the earthquake(s) estimated based on these two scenarios ranges between M6 and M7.5 respectively.

Liquefaction have been reported widely for magnitudes M >5 (Allen, 1986; McCalpin, 1996; Galli, 2000). The earthquakes of magnitude 6-6.5 are frequent in Shillong Plateau, however does not results into the liquefaction (Sukhija et al., 1999). This implies that the liquefaction features in this area due to prehistoric earthquakes were of at least M ≥6.5. Considering that shilling plateau is tectonically active, and was active in the past as well, it is reasonable to correlate the formation of sand dikes explored in the study area with the

earthquakes that was occurred in 1897 having an epicenter at 26°N 91°E. The distance of the study sites from this location is about 35 km (Bedabari, Beltaghat, and Jira sites), and about 150 km (Namgaon and Kakoti sites). In order to find the possible magnitude of earthquake events we used the global data of earthquake magnitude vs epicentral distances from Obermeier (1996). The global data has been generated based on the maximum distance of liquefaction seen from the epicenter. In our case when the distance of the location for Belataghat and Kakoti site was plotted on the global data taking the epicenter same as of 1897 earthquake of Shillong plateau. It was found that the liquefaction features near at the Bedabari and nearby sites have been generated by at least an earthquake of $M > 6$, and earthquake of magnitude $M > 7$ might have caused the formation of sand dikes in the Kakoti and Namgaon sites.

4.5 Conclusion

The important outcome of the present work on luminescence studies of sand dikes samples suggested that the resetting in quartz is possible due to rise in temperature caused by viscous heating during the injection of the dike. Also it was observed that the dikes of narrow width have more difference in ages from host layer as compared to the broader dikes. For example the dike at the Namgaon site is of width ~ 50 cm and for this site the ages obtained for dike and host samples are in ranges 90−190 and 60−160 years respectively. For Kakoti site the dikes are of narrow size and the ages obtained from the dike and that from the exposed material at surface were in agreement showing a resetting in dike.

The possibility of resetting of luminescence is more in narrow dikes, and to find better age estimate dikes of narrow width should be used. The samples should be collected from the center of the dikes, where extent of viscous heating will be high. For example the samples collected from the source/dike boundary or host/dike boundary have higher ages as compared to the dike ages at Beltaghat site where dike was formed due to intrusion of sand into sand layer. As suggested in chapter-3 the channel flow velocity during the injection of the dike will be higher in the central part and therefore the probability of thermal resetting of luminescence signal will be higher at the center. The results obtained from the Beltaghat site supports this view.

The dike ages from various sites in the present study falls near three time periods i.e. 300 years, 500 years and 1 ka. The events dated by luminescence are the last heating or sun light exposure. In the present case as discussed the resetting of luminescence in the dike was due to the viscous heating caused by the earthquakes in the area. This suggested that the area have faced four earthquakes of magnitude between M 6 to M 7.5 at around 111, 300 years, 500 year and 1 ka. At Kakoti site the multiple injected dikes and branching of dike suggested that these dikes might be due to more than one earthquake in this area. These events might have occurred at 111 years and 500 years before. The first event of 111 years before might be during 1905 Assam earthquake

Appendix

Stratigraphy

The samples were collected from the North-East India, Assam state. A field trip was organized in collaboration with Dr. Devender Kumar from National Geophysical Research Institute. An extensive field survey was done by covering and area 150 km towards east and west of Guwahati. Given below are the details of the sampling sites

A.1 Beltaghat

The Beltaghat (26° 0’ 16.5” N 90° 39’ 7.1” E) site is located near the Krishnai river (Mora meaning dead in local language). Being closure to the river this site made favorable conditions for the formation of sand dikes during seismic events. From bottom upward sequence started with 25 cm thick layer of medium to coarse light brown sand with some (source unexposed). Overlying to this was a 40 cm thick layer of medium grain light brown sand of. A sand dike was intruded into 250 cm thick layer of brown clay. The actual source of the sand dike material was unexposed.

Five samples were collected from this site from a depth of 1.3 m, 1.9 m, 2.3 m, 2.6 m and 3.1 m (Figure 4.18)

Another sand dike (sand intruded in sand) was also found at about 150 m away from this site Figure 4.20. From this location seven samples were collected for dike, host layer, source layer and boundary layers of dike/host and dike/source from depth of 4.4 m, 4.6 m, 4.7 m, 4.7, 4.9 m, 5.1 m and 4.90 m. The ages obtained for these samples are shown in Figure 4.20 along with their location.

A.2 Bedabari

Bedabari site (26° 0’ 32.1” N 90° 39’ 20.7” E) is also located near to the Mora Krishnai river. At this site the bottom upward sequence started with 140 cm thick graded brown sand with fining upward sequence. Overlying to this was a 100 cm thick layer of modern clay. Two sand dikes of light brown sand were intruded into the host layer. The source layer of the dikes was not exposed.

Five samples from depths 1.0 m 1.3 m, 1.4 cm, 2.3 m and 2.4 m were collected from this site. One sample was discarded on site due to clay contamination.

A.3 Jira

At Jira site (25° 57’ 37.2” N 90° 38’ 21.6” E) the bottom upward sequence of sedimentation is as follows. A 34 cm thick layer of silty clay was seen at the bottom; over this layer was a clay layer of thickness 100 cm. The top of the dike was covered with 73 cm thick modern clay.

Four samples were collected from this site from depths 85 cm, 115 cm, 154 cm and 190 cm. the ages obtained along with the sample marker are shown in Figure 4.24.

A.4 Namgaon

Eight samples were collected from Namgaon site (26° 13’ 10.6” N 92° 26’ 57.4” E). A thick layer of black clay of thickness 28 cm started the bottom sequence. This was followed by a layer of fine grain sand of thickness 82 cm, after which a layer of light gray sand of layer thickness 45 cm was seen. The sequence ended with a clay layer of thickness ~20cm.

The samples were collected from depth of 38 cm, 51 cm, 60 cm, 72 cm, 100 cm, 135 cm, 147 cm and 170 cm. The ages obtained on these samples are shown in Figure 4.26.

A.5 Kakoti

At Kakoti (26° 12’ 14.2” N 92° 31’ 48.8” E) two sites were explored for dikes. The bottom upward sequence at this site started with a 20 cm thick light gray sand. The was overlain by 44 cm thick light brown sand, followed by 19 cm thick black clay. This was followed by a layer of thickness 9 cm of dark brown sand, followed by 13 cm thick light gray clay, followed by thin layer (5 cm thick) of light brown sand, followed by 32 cm thick light brown clay. The sequence ended with a clay layer of thickness 140 cm.

Eight samples were collected from this site; the ages obtained from this site are shown in Figure 4.28.

About 200 m away from this site multiple sand dikes were seen with branching. 11 samples collected from this site from different depth (Table 4.3). The sequence of sedimentation at this site from bottom upward started with a source sand brown to yellow in color the completed source layer was not exposed. Overlying this was 45 cm dark gray sticky

Figure 4.17: Field Photograph of dike in Beltaghat site-1

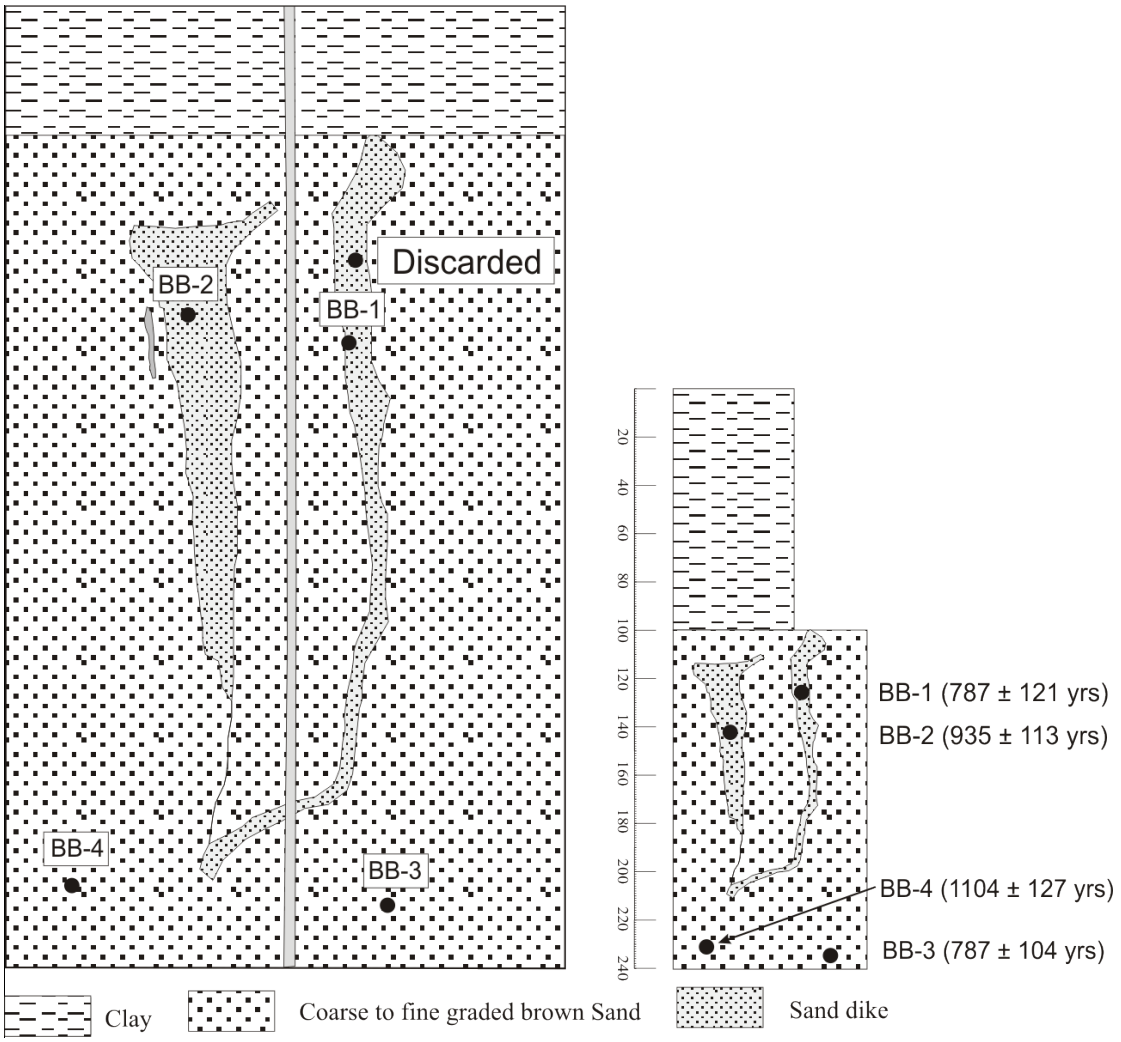

Figure 4.18: Stratigraphy of the Beltaghat site, ages obtained for samples are shown adjacent to the samples marked

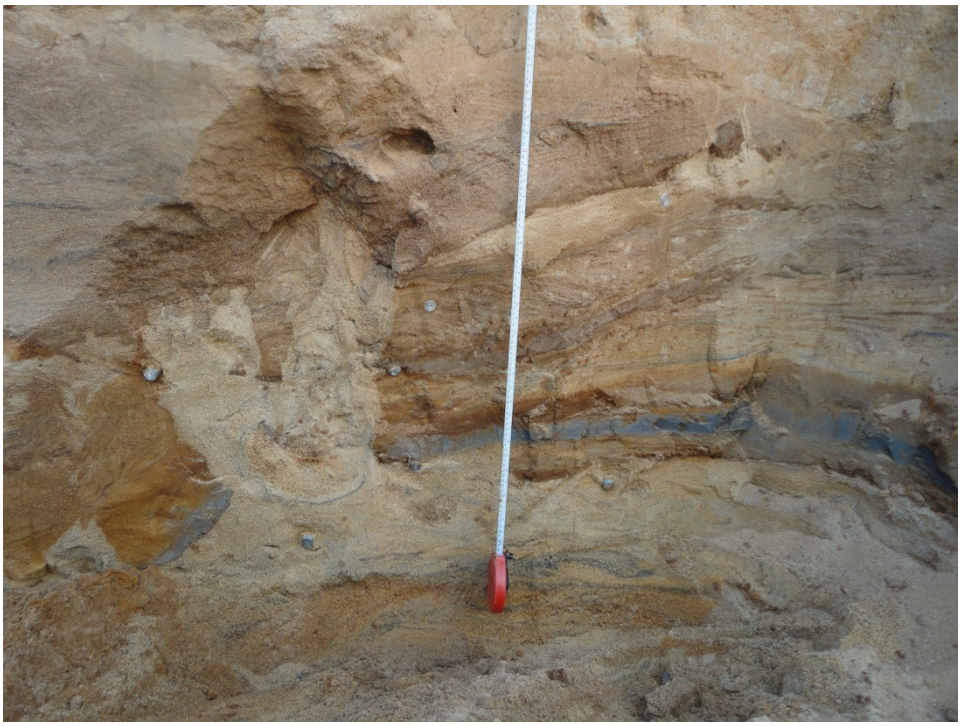

Figure 4.19: Field photograph of dike from Beltaghat site-2

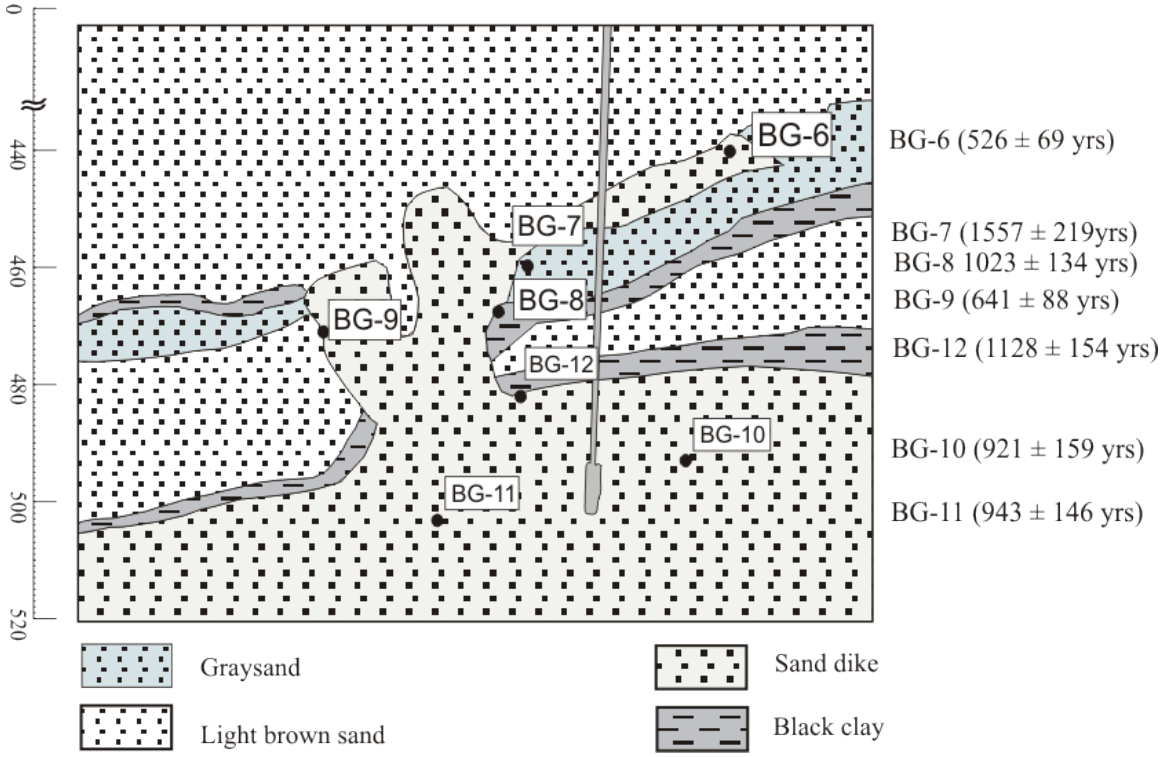

Figure 4.20: Stratigraphy of the Beltaghat site, ages obtained for samples are shown adjacent to the samples marked

Figure 4.21: Field photograph of dike from Bedabari site

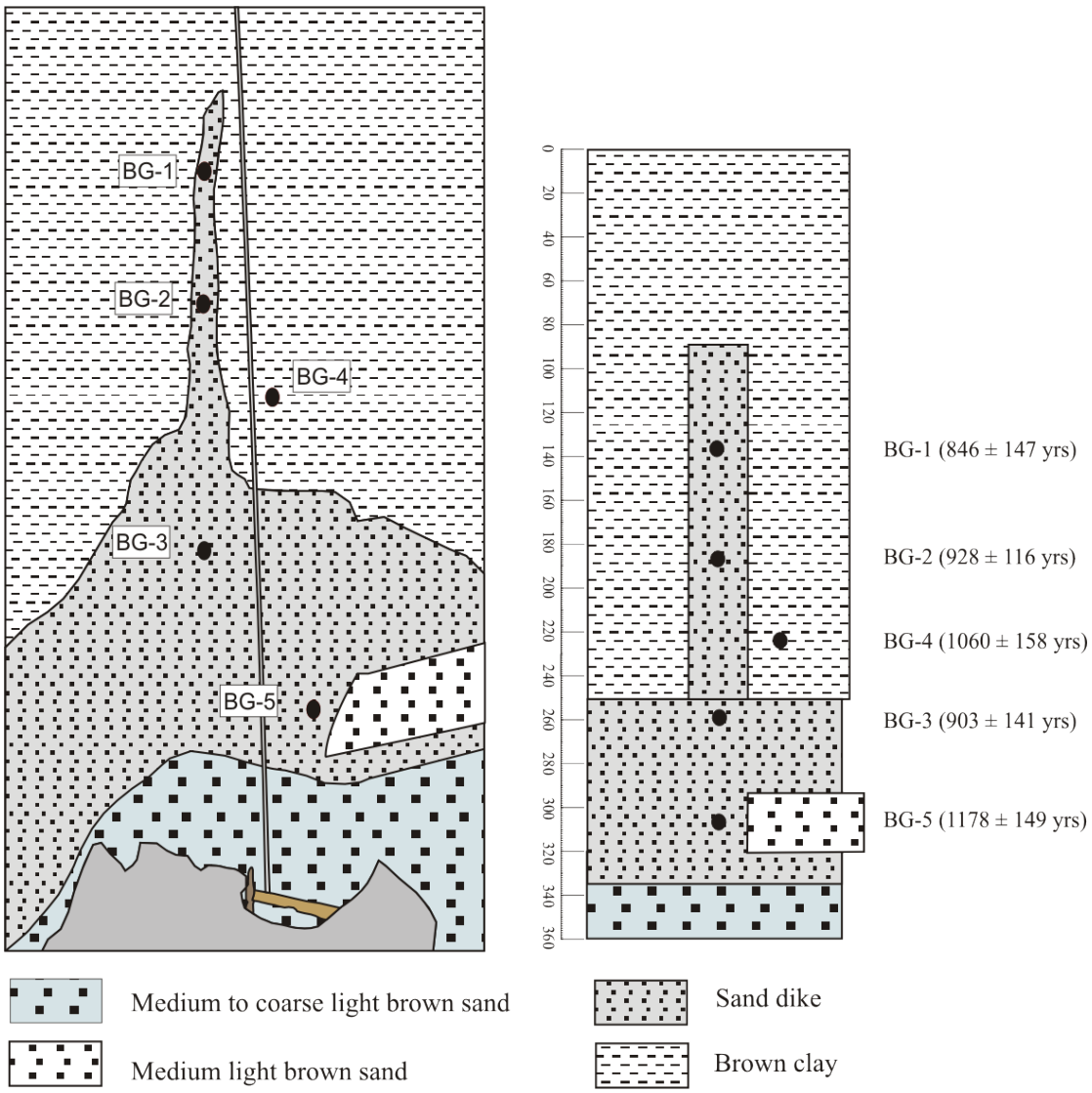

Figure 4.22: Stratigraphy of Bedabari site, ages obtained for samples are shown adjacent to sampling mark

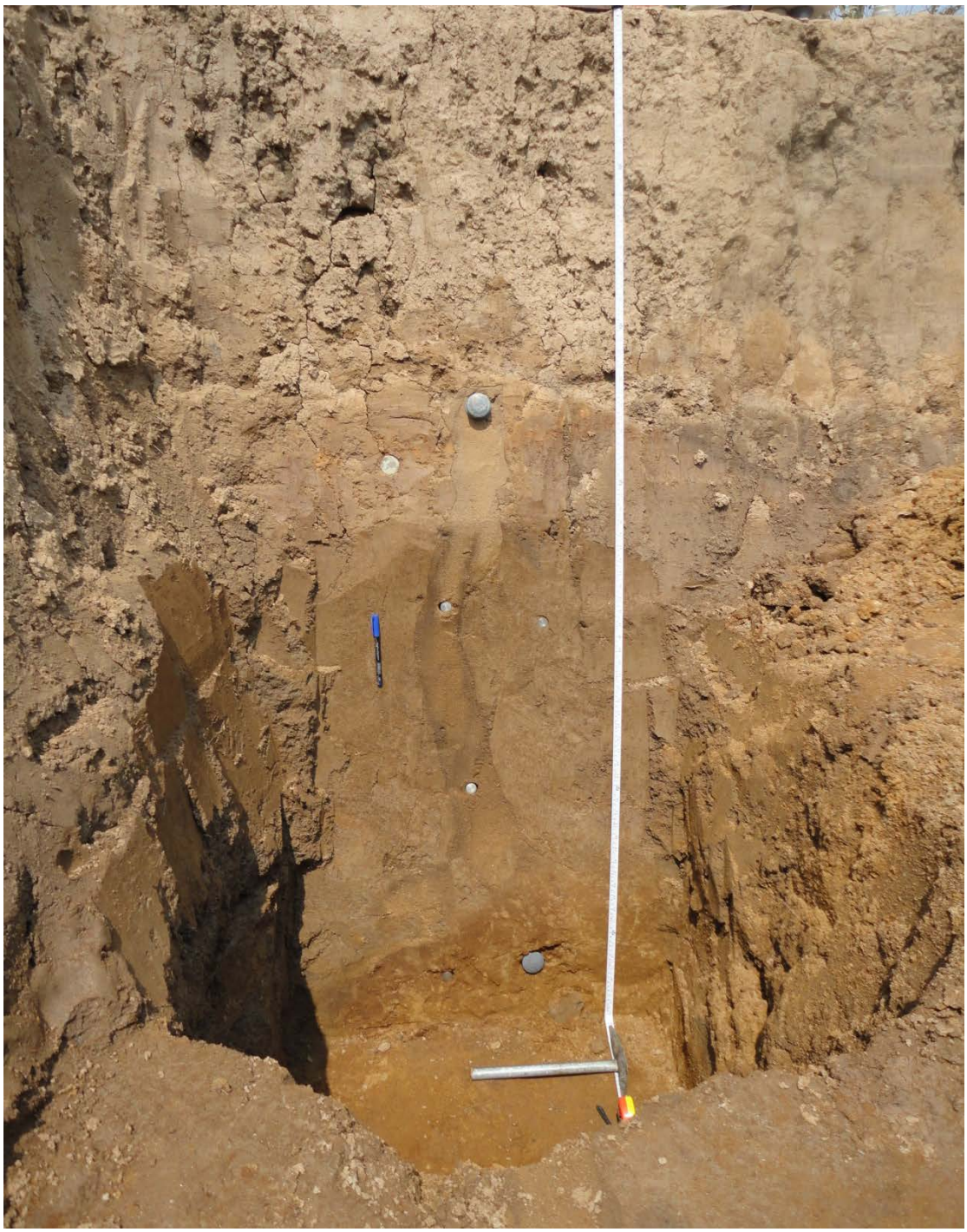

Figure 4.23: Field photograph of dike from Jira site

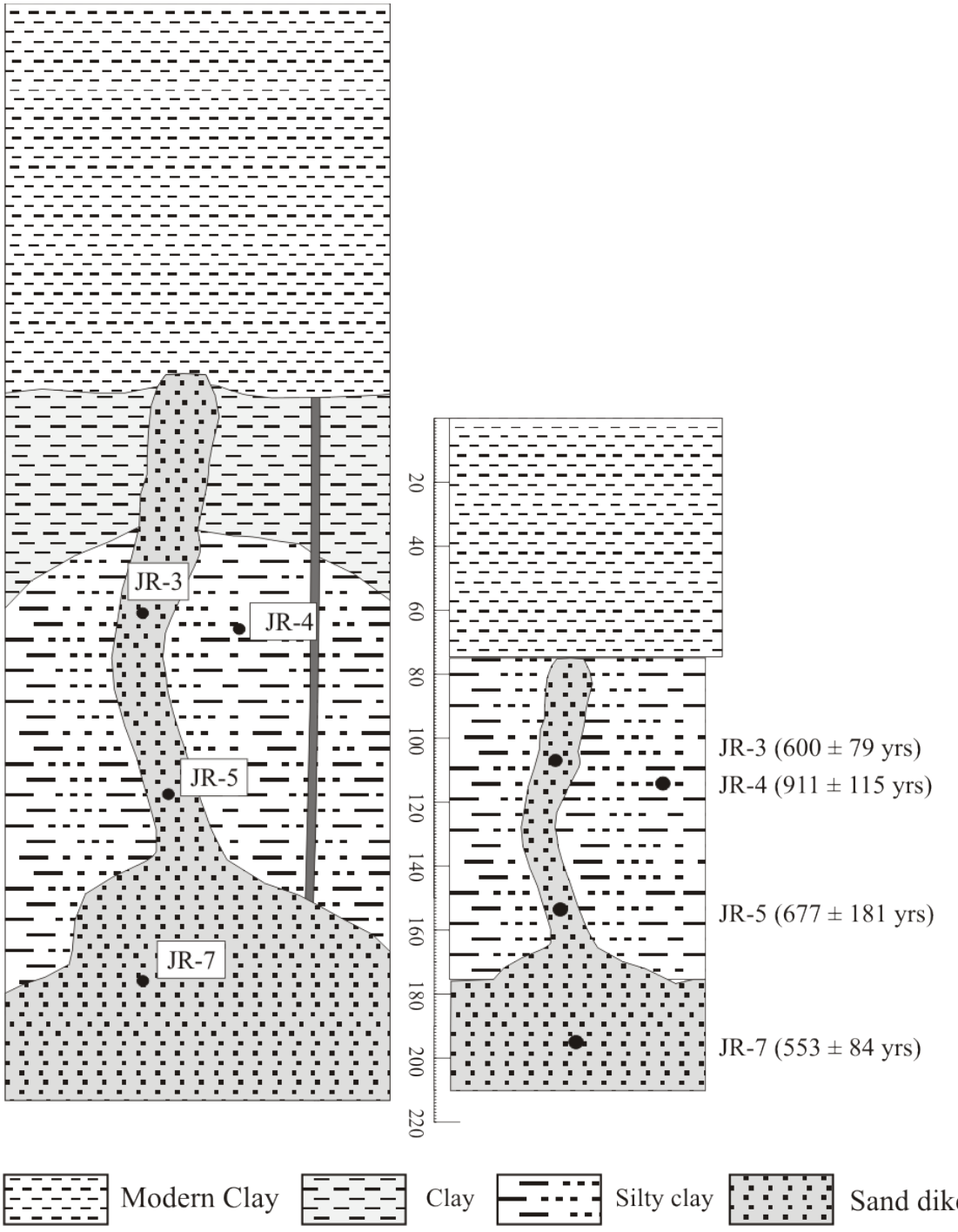

Figure 4.24: Stratigraphy of Jira site, ages obtained for samples are shown adjacent to sampling mark

Figure 4.25: Field photograph of dike from Namgaon site

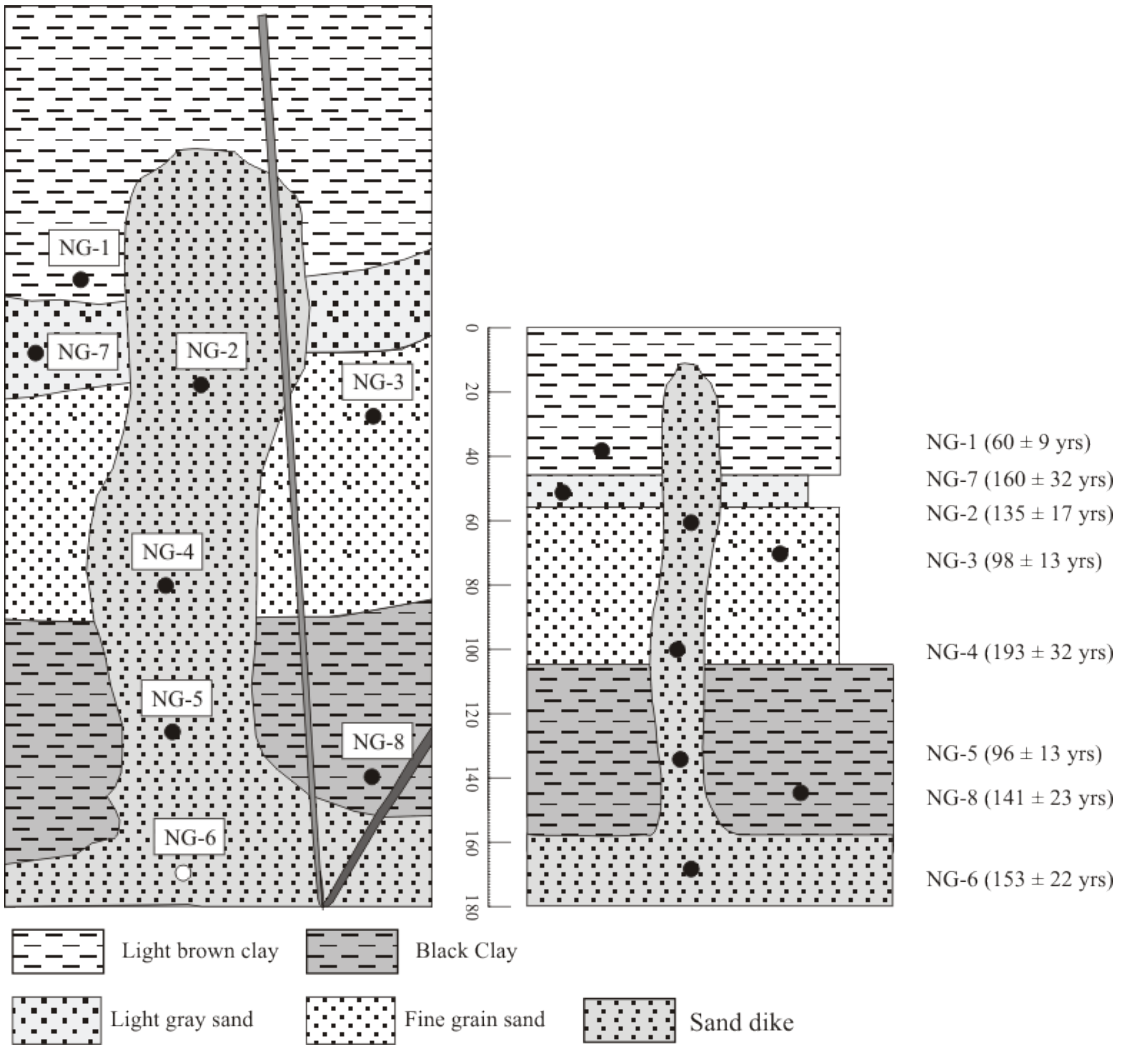

Figure 4.26: Stratigraphy of Namgaon site, ages obtained for samples are shown adjacent to sampling mark

Figure 4.27: Field photograph of dike from Kakoti site-1

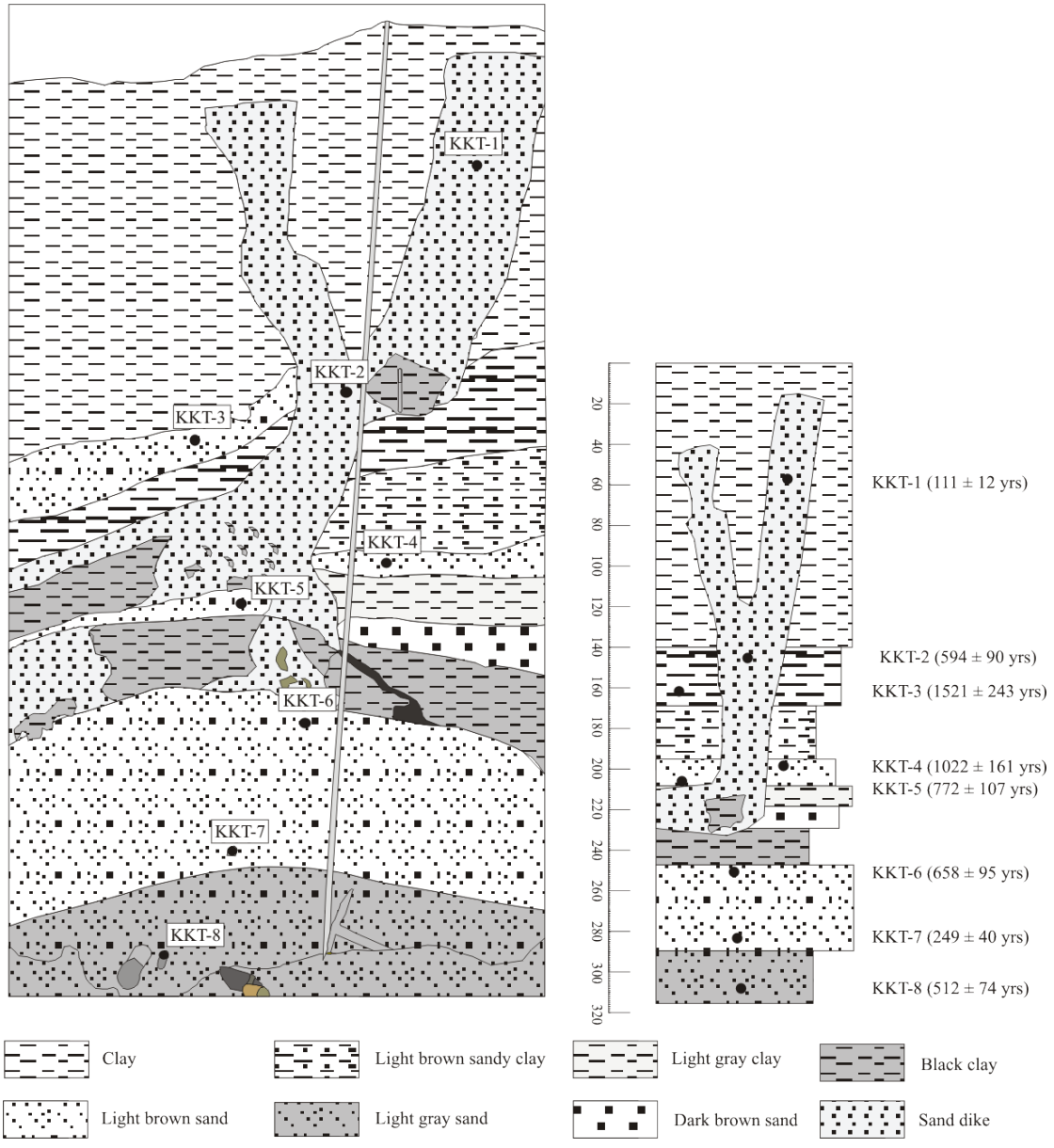

Figure 4.28: Stratigraphy of Kakoti site-1, ages obtained for samples are shown adjacent to sampling mark

Figure 4.29: Field photograph of dike from Kakoti site-2

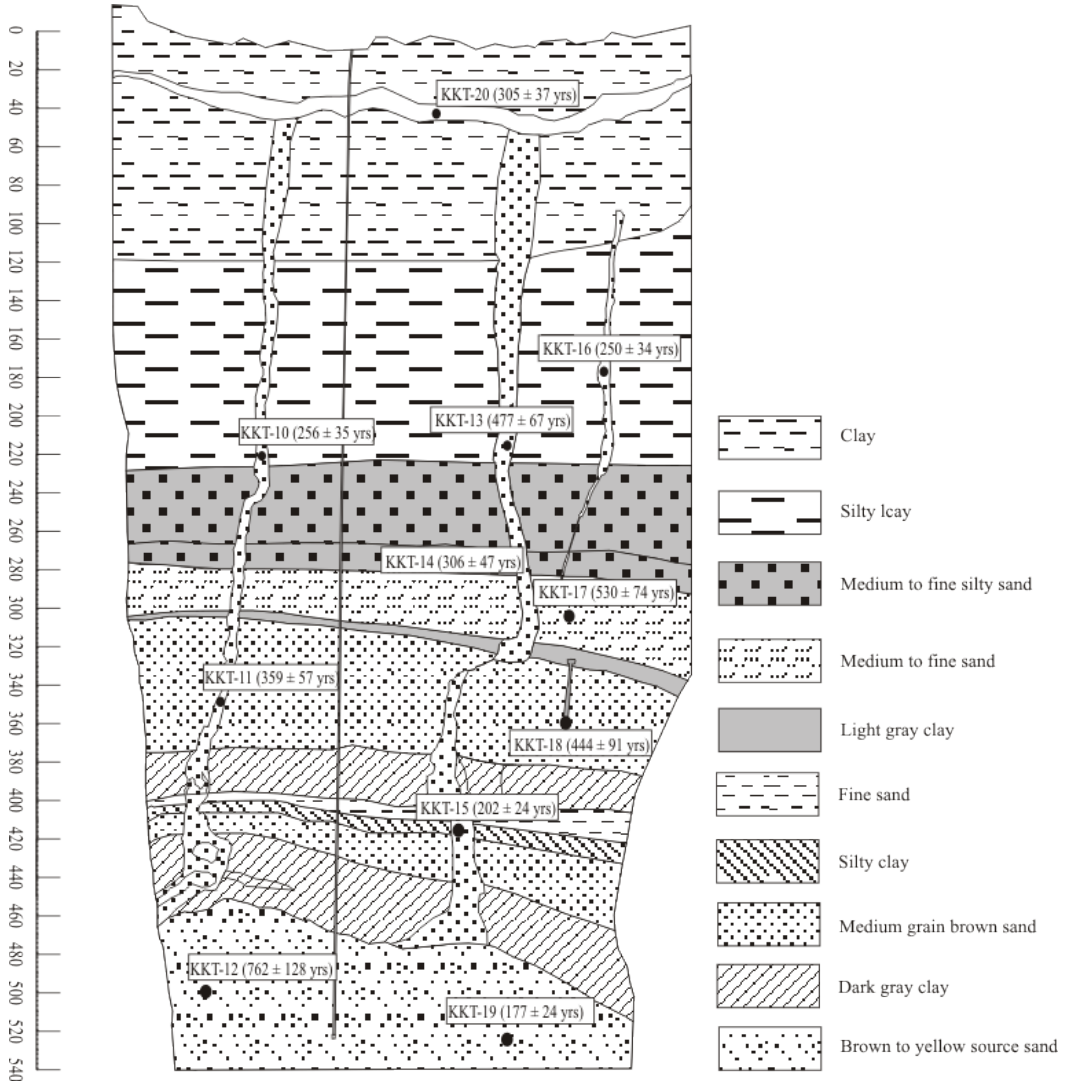

Figure 4.30: Stratigraphy of Kakoti site-2, ages obtained for samples are shown adjacent to sampling mark

clay, followed by 40 cm thick brown sand of medium grain size. A 10 cm thick silty clay followed the sequence in upward direction, overlying this was a layer of 15 cm thick fine sand, followed by 15 cm thick dark gray sticky clay, a 45 cm thick layer of medium grain brown sand continued the sequence of sedimentation. Overlying this sand layer was 5 cm thick light gray clay, followed by 50 cm thick layer of medium to fine sand, continued in upward direction by a 60 cm thick layer of medium to fine silty sand. This layer was underlain by 110 cm thick layer of silty clay. The sequence was terminated by 30 cm clay layer which was overriding the 5-10 cm thick sand layer of dike material. Figure 4.1shows the ages obtained for this site.

Chapter 5

Resetting of Luminescence in Fault Gouges

5.1 Introduction

The Himalayan arc (Himalayan frontal thrust, main boundary thrust and main central thrust) represents a zone of strong seismic activity in the north and North−East region of India. This region has faced several major earthquakes in the last century (of magnitude > 7, Table 4.1). These earthquakes claimed lives of several thousand people, caused large damage and pose great threat to the population in the area (Bilham et al., 2001). Therefore, it becomes important to understand the mechanisms responsible for producing such catastrophic earthquakes and their repeat frequency. This is possible if one understand the past behavior of seismicity in the areas to predict their future behavior (Crone, 1987).

To understand the seismic history of Sikkim-Darjeeling Himalaya, luminescence studies were made on fault gouge samples.

5.2 Fault Gouge

A geological fault is a fracture or zone of weakness in a volume of rock along which relative movement of block of different rock mass occurred due to applied stress. When the two blocks of rock slide in opposite direction at the fracture zone, the surfaces are damaged and erosion takes place, this process is known as wear. Under brittle condition and due to the hardness contrast between the blocks a powdery material is formed and is known as fault gouge (Scholz, 1987). The gouge material may or may not be recrystallized depending upon the frictional heat generated at the fault plane. The fault gouge comprises of detrital minerals and secondary authigenic clay minerals, particularly Illite forms deposited by later processes (Zwingmann and Mancktelow, 2004). Most of the earthquakes are caused by slip along pre-existing faults and of interest is to understand the nature and style of stress accumulation, stress release and its periodicity/recurrence rate if any. The work by Ikeya et al. (1982) to date the fault using Electron Spin Resonance opened up the possibility to develop the thermoluminescence method for dating of fault gouges (Singhvi et al., 1994; Banerjee, 1996). The first attempt to date paleoearthquakes using TL method was made by Forman et al. (1988) on samples collected by excavating a trench in the study area.

5.3 Resetting of luminescence in Fault Gouge

The dating of fault gouge using ESR or Luminescence is based on the assumption of resetting of signal to zero or near zero level during the rupture event. Several workers have investigated the zeroing of ESR signal based on the burial depth and the amount of displacement during the fault movement (e.g. Ariyama, 1985), use of different ESR (E', Al, OHC, GE) centers in quartz from injected veins in at the time of faulting (Fukuchi et al., 1985; Fukuchi et al., 1986), age plateau method for different grain size (Buhay et al., 1988; Lee and Schwarcz, 1994), use of isochrones age method for different grain sizes (Ikeya et al., 1995).

The resetting of ESR signal in fault gouge was attributed to the hydrostatic stress and to localized heating (Ikeya et al., 1982; Miki and Ikeya, 1982). Laboratory experiments to understand the effect of fracturing, crushing and grinding of quartz grains suggest that ESR signal associated with E' and OHC centers decreases with applied stress and reduces to zero

at differential stress of 700 MPa (Tanaka and Shidahara, 1985). The decrease in signal is faster in larger grains as compared to smaller size grains (Tanaka and Shidahara, 1985; Fukuchi et al., 1986). Ariyama (1985) reported a resetting of E' and Ge centers at a minimum pressure of 2 MPa at a minimum displacement of 20 cm. Annealing experiments made by Fukuchi et al. (1986) showed that Al and E' centers are completely reset at 400 ℃ while OHC and Ge centers reset beyond 400 ℃. Fukuchi (1992) attempted to find the resetting condition for ESR signal by thermal conduction on frictional heat as proposed by McKenzie and Brune (1972) combining with the decay curves of ESR signal. They concluded that ESR signal can never be reset under normal stress less than 6.8 MPa at a displacement of 1m. Also for ESR measurement on fault gouge material samples should be collected at least from a depth of 200 m or below, from the surface. The shearing experiments suggest that resetting of ESR signal is possible for a normal stress of 4 MPa. Also the ages obtained using finer grain sizes (< 100 μm) are closely related to the fault movement. The movement on Nojima fault during 1995 earthquake in Japan provided opportunity to study the resetting of ESR signal in quartz. Fukuchi and Imai (1998) studied the resetting of E' center as a result of movement on Nojima fault and did not find the resetting of ESR signal associated with E' center.

Theoretical studies have also been made to understand the resetting of ESR and Luminescence signals. McKenzie and Brune (1972) estimated the rise in temperature as a result of frictional heating and suggested that ~1000 ℃ temperature could be achieved during rupture of rocks during earthquakes. This was useful in explaining the presence of glassy material and pseudotachylyte as reported by several workers (Scott and Drever, 1953; Sibson, 1975; Sibson, 1977).

Studies of friction induced thermoluminescence (triboluminescence) have been reported by Suzuki and Kennedy (1991). The luminescence sensitivity of gouge material is found to be higher as compared to host rock material. The grain size dependence of fault gouge age and also the effect of mechanical stress on luminescence (mechanoluminescence) from gouge and host material studies show that the grain size < 200 μm can be used for dating of fault gouges (Singhvi et al., 1994; Banerjee et al., 1999).

Banerjee (1996) used the crystallinity of Illite group minerals and chlorite peak ratio method to estimate the extent of heating in fault gouge material. However due to the masking of the XRD peaks in the clay minerals by muscovite and kaolinite peaks the results were not

very promising. In another attempt to see the effect of mechanical stress on the luminescence of fault gouge and host rock samples, Banerjee (1996) performed the mechanoluminescence (ML) studies. The samples from fault gouge and host rock were stressed by dropping a fixed mass from different heights resulting in variable mechanical stress applied to the samples. The ML intensity of the samples was recorded by a PMT placed below the sample mount. It was found that the ML intensity of host rock was five times higher as compared to the fault gouge material. When the stress on the samples was applied repeatedly, the ML intensity from host rock or fault gouge material appear only in first two or three cycles after which ML from the sample was not seen. Based on their results they inferred that earthquakes of M >6 might cause the resetting of luminescence in fault gouge material.

The zeroing of ESR and luminescence signal due to mechanical stress is caused by localization of stress near the zone of weakness in the grains i.e. defect sites and consequent development of micro cracks in the grains. At grain boundary due to frictional sliding the stress concentrated around the defects leads to the breaking of the bonds which results in detrapping of the electrons from their sites (Lee and Schwarcz, 1994). The migrated charges released then recombine with the holes and thus reset the ESR centers to zero or near zero level. The effect of stress will be strongest at the grain-grain contact and thus resetting will be higher for smaller grain size Figure 5.1.

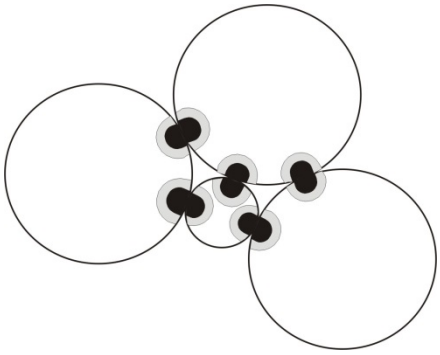

Figure 5.1: Schematic for resetting due to mechanical stress. Smaller grain (in center) will have larger level of resetting as compared to larger grains (after Lee and Schwarcz, 1994).

The milling experiment by Takeuchi (2006) to see the effect of stress on surface resetting of luminescence suggest that only 500 nm outer surface is reset due to the applied stress, and therefore finer grain size is suitable for dating of fault gouge using luminescence. The crushing experiment using hand crushing, automatic grinder and pellet die press does not

show clear signature of resetting of luminescence in quartz grains (Toyoda et al., 2000). Recent studies by Rink et al. (1999) and Toyoda et al. (2000) suggest that the luminescence sensitivity of quartz grains increases after the crushing.

5.4 Amplitude rise of temperature in fault gouge due to frictional Heating

In case of fault gouge material the zeroing occurs by heat generated during slip of blocks of rock. In order to decipher the temperature conditions at faulting events thermal modeling of such event is needed (Fukuchi, 1989; Caggianelli et al., 2005). In this regard the transient thermal modeling of earthquake faults considering appropriate slip rates, conductivities and pressure conditions would enable to construct the temperature profiles as a function of space and time. With these temperature profile and considering general order of kinetics of trapped charges in luminescent minerals, the extent of resetting by fault event can be studied. A preliminary work in this direction was done by Murari et al. (2009). Such studies have yet not been fully explored and would provide a prime opportunity to study the applicability of OSL to the fault activities. In present case we have extend the work by Murari et al. (2009).

5.4.1 Mathematical model

Several models to estimate the amplitude rise in temperature during earthquake frictional sliding, exist (e.g. McKenzie and Brune, 1972; Lachenbruch, 1980). The rupture event along a fault and the evolution of slip can be described and studied in three phases 1) nucleation phase, 2) a phase of maximum and constant slip velocity and 3) deceleration phase. These phases are shown in Figure 5.1. In the nucleation phase there is stress buildup which is locked at the fault plane. When the stress is increased to the brittle fracture limit of the rock the fracture is initiated. During this phase, the velocity of the fault plane rapidly changes from zero to a maximum limit that is determined by the fracture limit of the rock material. This phase is of short time and also results into the frictional heating.

During the rupture the blocks slide on each other and the materials on the surfaces of the contact are crushed. The blocks move with a constant velocity and the stress energy is used in crushing and heating of the material due to friction.

As the stress energy decreases a limit comes when the slip of blocks starts slowing down i.e. the deceleration phase. During this the heat is generated due to friction at the surfaces of

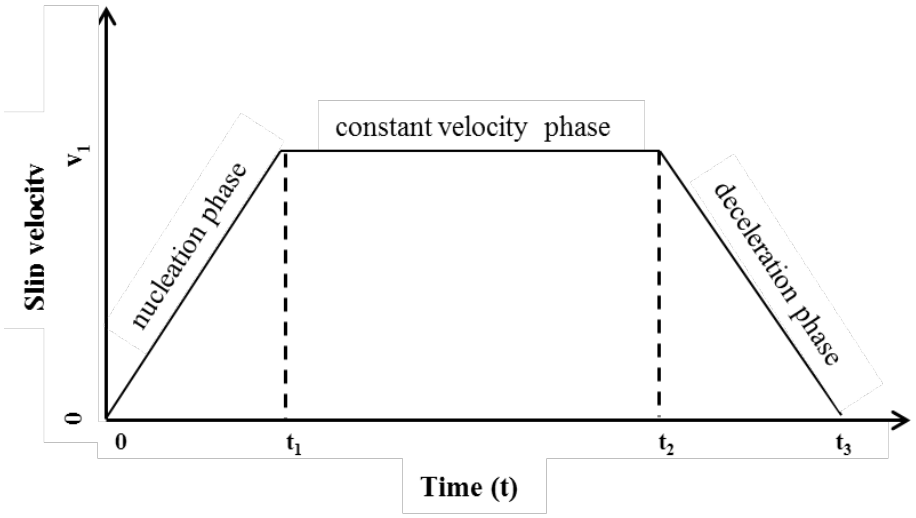

Figure 5.2: Schematic representation of earthquake event. The event is divided into three phases i.e. nucleation, constant velocity and deceleration phase.

contact. This phase is characterized by a progressive decrease of slip velocity until movement of blocks stop (Swanson, 1992).

For the simplicity of the calculations the fault plane is assumed to be aligned with z=0 plane. If a_1 and a_2 are the acceleration and deceleration during nucleation phase and deceleration phase then during the rupture in three phases the velocity can be represented as

$$\begin{aligned} \mathrm{v} &= a_1 t && 0 \le t \le t_1 && (a) \\ \mathrm{v} &= \mathrm{v}_1 && t_1 \le t \le t_2 && (b) \\ \mathrm{v} &= \mathrm{v}_1 - a_2 t && t_2 \le t \le t_3 && (c) \end{aligned} \qquad (5.1)$$

The heat flux due to frictional sliding generated at z=0 plane will diffuse in both x and y direction. Considering the fault plane lying in x-y plane, the heat flux at any time t and at a distance z from origin can be found by solving the 1D heat flux diffusion equation

$$\eta \frac{\partial^2 f}{\partial z^2} = \frac{\partial f}{\partial t} \qquad (5.2)$$

In equation (5.2) η is the thermal diffusivity of medium, z is the distance from the fault plane and t is the time. The temperature $\Theta(z,t)$ and heat flux are related to each other by following equation

$$f = -K\frac{\partial \Theta(z,t)}{\partial z} \tag{5.3}$$

In case of rock rupture since the temperature far from the fault plane is zero, it is reasonable to take the boundary condition $\Theta \to 0 \, as \, z \to \infty$. Therefore using this boundary condition, the temperature Θ can be obtained by integrating equation (5.3) and is given by

$$\Theta = -\frac{1}{K}\int_z^\infty f(z,t)dz \tag{5.4}$$

Now taking into account the symmetry of the generation of heat (heat is generated at z=0 plane), it can be considered that the heat source is a line source at z=0.

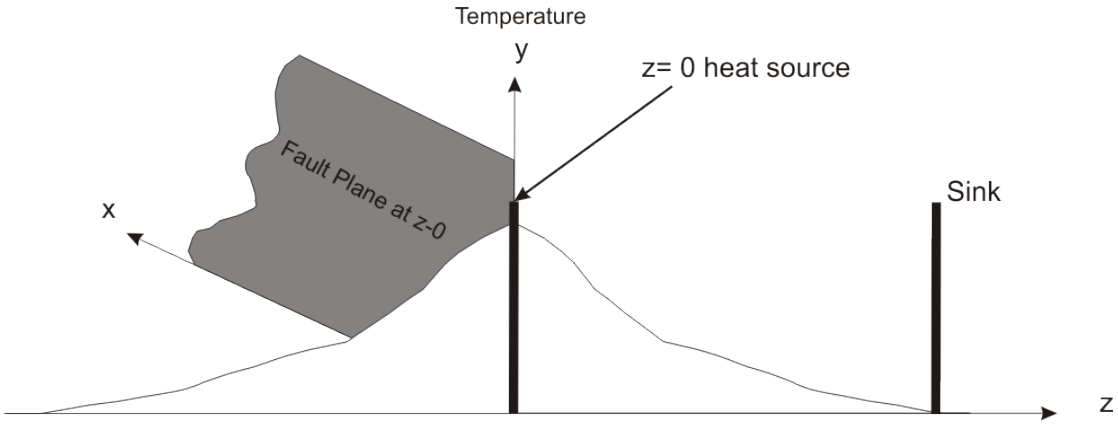

Figure 5.3: Schematic of heat generation during faulting event. The fault plane is at z=0, which is indicated as source and at z= ∞ is a sink indicating that the heat flux is zero at sink

Figure 5.3 shows the schematic of the situation at the time of faulting. Since the fault plane is considered at z=0 axis, it works as a source of heat flux. Far from the fault plane the heat flux is zero indicating a sink. The heat diffusion equation in this case can be solved by considering the two doublet of heat source (sink is also a negative source) using the method suggested by Carslaw and Jaeger (1959). The heat flux due to a continuous doublet of strength f (z,t') at the point z', in the case of linear flow, is given by

$$f(z,t) = \frac{(z-z')}{4\sqrt{\pi\kappa^3}}\int_0^t \frac{f(z',t')}{(t-t')^{3/2}}\exp\left(\frac{-(z-z')^2}{4\kappa(t-t')}\right)dt' \tag{5.5}$$

Substituting $z - z' = 2\kappa^{1/2}(t - t')^{1/2}\alpha$, equation (5.5) can be rewritten as

$$f(z,t) = \frac{2}{K\sqrt{\pi}} \int_{z-z'/2\sqrt{(\kappa t)}}^{\infty} e^{-\alpha^2} f\left(z', t - \frac{(z-z')^2}{4\kappa\alpha^2}\right) d\alpha \qquad \text{for } z > z' \qquad (5.6)$$

In our case z'=0 therefore

$$f(z,t) = \frac{2}{K\sqrt{\pi}} \int_{z/2\sqrt{(\kappa t)}}^{\infty} e^{-\alpha^2} f\left(z = 0, t - \frac{z^2}{4\kappa\alpha^2}\right) d\alpha \qquad (5.7)$$

During the rupture due to frictional sliding the heat flux generated is given by

$$f(z = 0, t) = \tau_f \mathrm{v}(t) \qquad (5.8)$$

Here τ_f is the shear stress and v is the slip velocity (Sibson, 1975). The shear stress τ_f is given by

$$\tau_f = \mu_d(\sigma_n - p) \qquad (5.9)$$

In equation (5.9), μ_d is the dynamic friction coefficient σ_n is the normal stress (equal to the overburden of the overlying material) and p is the pore pressure. If the rupture takes place at a depth H, and the material density is ρ, acceleration due to gravity is g, then $\sigma_n = \rho g H$. Defining $\lambda = p/(\rho g H)$ the shear stress is $\tau_f = \mu_d \rho \mathrm{gH}(1-\lambda)$. λ is a factor which is governed by the pore pressure of the overlying material. The heat flux f(z,t) generated during these phase can be represented as

$$f(z = 0, t) = \tau_f a_1 t \qquad 0 \le t \le t_1 \qquad (5.10)$$

$$f(z = 0, t) = \tau_f a_1 t_1 \qquad t_1 \le t \le t_2 \qquad (5.11)$$

$$f(z = 0, t) = \tau_f \{a_1 t_1 - a_2 (t - t_2)\} \qquad t_2 \le t \le t_3 \qquad (5.12)$$

Here f(z=0,t) is the heat flux generated at fault plane located at z=0 axis and at time t.

5.4.2 Temperature during nucleation phase ($0 \leq t \leq t_1$)

The rise in temperature during nucleation phase is obtained by substituting equation (5.10) into equation (5.7)

$$\begin{aligned} f_1(z,t) &= \frac{2}{\sqrt{\pi}} \int_{z/2\sqrt{(\kappa t)}}^{\infty} \tau_f a_1 \left(t - \frac{z^2}{4\kappa\alpha^2} \right) e^{-\alpha^2} d\alpha \\ &= \left[qt + \frac{qz^2}{2\kappa} \right] erfc\left(\frac{z}{\sqrt{4\kappa t}} \right) - qz\sqrt{\frac{t}{\kappa\pi}} \exp\left(-\frac{z^2}{4\kappa t} \right) \end{aligned} \tag{5.13}$$

Where $q = \mu_d \rho \, \mathrm{gH}(1-\lambda) a_1$ and $erfc\left(z/\sqrt{4\kappa t} \right)$ is the complementary error function and is given by

$$erfc(x) = 1 - erf(x) = \frac{2}{\sqrt{\pi}} \int_x^{\infty} e^{-\alpha^2} d\alpha$$

Therefore rise in temperature during nucleation phase is given by substituting equation (5.13) into equation (5.4) and is given by

$$\Theta_1(z,t) = \frac{1}{K} \int_z^{\infty} \left[\left\{ qt + \frac{qz^2}{2\kappa} \right\} erfc\left(\frac{z}{\sqrt{4\kappa t}} \right) - qz\sqrt{\frac{t}{\kappa\pi}} \exp\left(-\frac{z^2}{4\kappa t} \right) \right] dz$$

$$\begin{aligned} &= \frac{1}{K} \left[qt \left\{ -zerfc\left(\frac{z}{\sqrt{4\kappa t}} \right) + 2\sqrt{\frac{\kappa t}{\pi}} \exp\left(-\frac{z^2}{4\kappa t} \right) \right\} \right. \\ &+ \frac{q}{2\kappa} \left\{ -\frac{z^3}{3} erfc\left(\frac{z}{\sqrt{4\kappa t}} \right) + \frac{1}{3\sqrt{\pi\kappa t}} \left\{ 2\kappa t z^2 \exp\left(-\frac{z^2}{4\kappa t} \right) \right. \right. \\ &\left. \left. \left. + 8\kappa^2 t^2 \exp\left(-\frac{z^2}{4\kappa t} \right) \right\} \right\} - q\sqrt{\frac{t}{\kappa\pi}} \left(2\kappa t \exp\left(-\frac{z^2}{4\kappa t} \right) \right) \right] \end{aligned} \tag{5.14}$$

5.4.3 Temperature during constant velocity phase ($t_1 \leq t \leq t_2$)

The amount of heat flux generated during this phase can be obtained by substituting equation (5.11) into equation (5.7) and is given by

$$f_2(z,t) = \frac{2}{\sqrt{\pi}} \int_{z/2\sqrt{(\kappa t)}}^{\infty} \mu_d \rho g H (1-\lambda) a_1 t_1 f\left(z = 0, t - \frac{z^2}{4\kappa\alpha^2}\right) e^{-\alpha^2} d\alpha$$

$$\begin{aligned}
&= \frac{2}{\sqrt{\pi}} \int_{z/2\sqrt{(\kappa t)}}^{\infty} q t_1 f\left(z = 0, t - \frac{z^2}{4\kappa\alpha^2}\right) e^{-\alpha^2} d\alpha \\
&= \frac{2}{\sqrt{\pi}} \left[\int_{z/2\sqrt{(\kappa t)}}^{z/2\sqrt{(\kappa t_1)}} q t_1 e^{-\alpha^2} d\alpha + \int_{z/2\sqrt{(\kappa t_1)}}^{\infty} f\left(z = 0, t - \frac{z^2}{4\kappa\alpha^2}\right) e^{-\alpha^2} d\alpha \right] \\
&= \frac{2}{\sqrt{\pi}} \int_{z/2\sqrt{(\kappa t)}}^{z/2\sqrt{(\kappa t_1)}} q t_1 e^{-\alpha^2} d\alpha + f_1(z,t_1) \\
&= \mathrm{q t_1} \left[erfc\left(\frac{z}{\sqrt{4\kappa t}}\right) - erfc\left(\frac{z}{\sqrt{4\kappa t_1}}\right) \right] + f_1(z,t_1)
\end{aligned} \tag{5.15}$$

Using above expression for heat flux in equation (5.4) will give the rise in temperature during phase of constant slipping velocity. There the rise in temperature during this phase is

$$\begin{aligned}
\Theta_2(\mathrm{z,t}) &= \frac{1}{K} \int_z^{\infty} \left[q t_1 \left\{ erfc\left(\frac{z}{\sqrt{4\kappa t}}\right) - erfc\left(\frac{z}{\sqrt{4\kappa t_1}}\right) \right\} + f_1(\mathrm{z,t_1}) \right] \\
&= \Theta_1(\mathrm{z,t_1}) + \frac{q t_1}{K} \left[-z erfc\left(\frac{z}{\sqrt{4\kappa t}}\right) + 2\sqrt{\frac{\kappa t}{\pi}} \exp\left(-\frac{z^2}{4\kappa t}\right) \right. \\
&\qquad \left. + z erfc\left(\frac{z}{\sqrt{4\kappa t_1}}\right) - 2\sqrt{\frac{\kappa t_1}{\pi}} \exp\left(-\frac{z^2}{4\kappa t_1}\right) \right]
\end{aligned} \tag{5.16}$$

5.4.4 Temperature during deceleration phase ($t_2 \leq t \leq t_3$)

The heat flux generated during this phase can be obtained by substituting equation (5.12) into equation (5.7) and is given by

$$f_3(z,t) = \frac{2}{\sqrt{\pi}} \int_{z/2\sqrt{\kappa t}}^{z/2\sqrt{\kappa t}} \left[\tau_f a_1 t_1 - \tau_f a_2 \left(t - \frac{z^2}{4\kappa t}\right) \right] e^{-\alpha^2} d\alpha + f_2(\mathrm{z,t_2})$$

$$= \left[erfc\left(\frac{z}{\sqrt{4\kappa t}}\right) - erfc\left(\frac{z}{\sqrt{4\kappa t_2}}\right)\right] \times \left[\left(\tau_f a_1 t_1 - \tau_f a_2 t\right) - \tau_f a_2 \frac{z^2}{2\kappa}\right] + \tau_f a_2 z\left[-\sqrt{\frac{t_2}{\kappa\pi}}\exp\left(-\frac{z^2}{4\kappa t_2}\right) + \sqrt{\frac{t}{\kappa\pi}}\exp\left(-\frac{z^2}{4\kappa t}\right)\right] + f_2(z,t_2) \quad (5.17)$$

The rise in temperature due to the heat flux given in equation (5.17) is obtained by substituting this into equation (5.4) and is given by

$$\Theta_3(z,t) = \frac{1}{K}\int_z^\infty \left[\left\{erfc\left(\frac{z}{\sqrt{4\kappa t}}\right) - erfc\left(\frac{z}{\sqrt{4\kappa t_2}}\right)\right\} \times \left\{\tau_f a_1 t_1 - \tau_f a_2\left(t - t_2\right) - \tau_f a_2 \frac{z^2}{2\kappa}\right\} + \tau_f a_2 z\left\{-\sqrt{\frac{t_2}{\kappa\pi}}\exp\left(-\frac{z^2}{4\kappa t_2}\right) + \sqrt{\frac{t}{\kappa\pi}}\exp\left(-\frac{z^2}{4\kappa t}\right)\right\} + f_2\left(z,t_2\right)\right] dz \quad (5.18)$$

$$= \Theta_2(z,t_2) + \frac{1}{K}\left[\left\{\tau_f a_1 t_1 - \tau_f a_2\left(t - t_2\right)\right\} \times \left\{-zerfc\left(\frac{z}{\sqrt{4\kappa t}}\right) + 2\sqrt{\frac{\kappa t}{\pi}}\exp\left(-\frac{z^2}{4\kappa t}\right) + zerfc\left(\frac{z}{\sqrt{4\kappa t_2}}\right) - 2\sqrt{\frac{\kappa t_2}{\pi}}\exp\left(-\frac{z^2}{4\kappa t_2}\right)\right\} - \tau_f a_2 \frac{1}{2\kappa}\left[-\frac{z^3}{3}erfc\left(\frac{z}{\sqrt{4\kappa t}}\right) + \frac{1}{3\sqrt{4\kappa t}}\left\{2\kappa z^2 t\exp\left(-\frac{z^2}{4\kappa t}\right) + 8\kappa^2 t^2\exp\left(-\frac{z^2}{4\kappa t}\right)\right\}\right] + \tau_f a_2 \frac{1}{2\kappa}\left[-\frac{z^3}{3}erfc\left(\frac{z}{\sqrt{4\kappa t_2}}\right) + \frac{1}{3\sqrt{4\kappa t_2}}\left\{2\kappa z^2 t_2\exp\left(-\frac{z^2}{4\kappa t_2}\right) + 8\kappa^2 t_2^{\,2}\exp\left(-\frac{z^2}{4\kappa t_2}\right)\right\}\right] - \tau_f a_2\left\{\sqrt{\frac{t_2}{\kappa\pi}}2\kappa t_2\exp\left(-\frac{z^2}{4\kappa t_2}\right) + \sqrt{\frac{t}{\kappa\pi}}2\kappa\left(t - t_2\right)\exp\left(-\frac{z^2}{4\kappa t}\right)\right\}\right] \quad (5.19)$$

5.4.5 Temperature after rupturing is stopped ($t>t_3$)

For $t > t_3$ the heat flux is not generated as there is no more movement along the fault plane, and only diffusion of heat takes place. Therefor temperature for this phase was evaluated with the source method by Carslaw and Jaeger (1959). The temperature in this region is given by

$$\Theta_4\left(z,t>t3\right)=\int_z^{\infty}\left[\Theta\left(z',t=t_3\right)\left\{e^{\frac{-(z-z')^2}{4\mathrm{K}(t-t3)}}+e^{\frac{-(z+z')^2}{4\mathrm{K}(t-t3)}}\right\}\right]dz' \tag{5.20}$$

5.4.6 Temperature profiles during faulting

The amplitude rise in case of rupture event was estimated using equations (5.14), (5.16), (5.19) and (5.20). These integrals were evaluated numerically. In general $a_1 \neq a_2$, however it is difficult to constraint this condition due to lack of information during on acceleration during nucleation phase and deceleration phase. In present case we have considered $a_1 = a_2$ which implies that time for nucleation and deceleration phase are same, also $t_1 = t_3 - t_2$. Considering the maximum slip velocity v the total slip during the rupture event is

$$\begin{aligned} L &= \frac{1}{2}v_1 t_1 + v_1\left(t_2 - t_1\right) + \frac{1}{2}v_1\left(t_3 - t_2\right) \\ &= \frac{1}{2}v_1\left(t_3 + t_2 - t_1\right) \end{aligned} \tag{5.21}$$

The temperature profiles during the faulting event were analyzed for the effect of slip velocity, pore pressure, dynamic friction coefficient and thermal conductance. We have considered that the rupture event takes place at a depth of 1km. It is observed that the rise in temperature for a pore pressure of factor 0.6 and for rock having dynamic friction coefficient 0.6 can go up to around 1300 ℃ for a total slip of 25 cm. The temperature near the fault plane decreases as the pore pressure is increased. The temperature rise for pore pressure factor 0.6 is about 500 ℃ Figure 5.5. The rise in temperature is significantly affected by the variation in the dynamic friction coefficient. When the dynamic friction coefficient is decreased the temperature at the

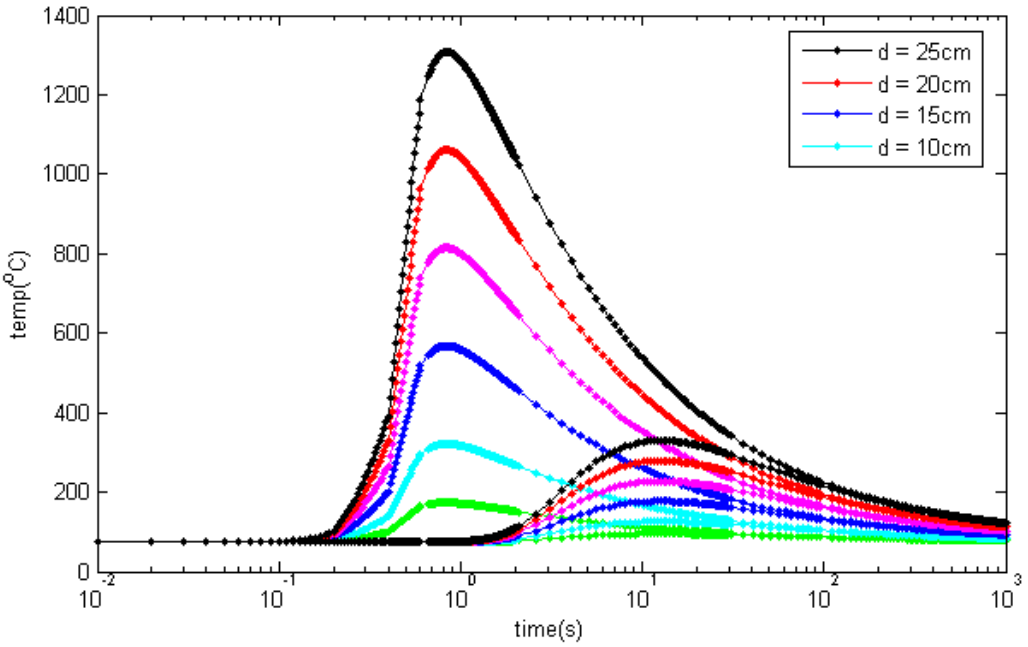

Figure 5.4: Effect of slip distance (slip velocity) on temperature rise during rupture at 1mm and 5mm away from the fault plane for depth of 1km (λ=0.6, **μ**=0.6, κ =1e-6, K=2.5 and **ρ**=2800)

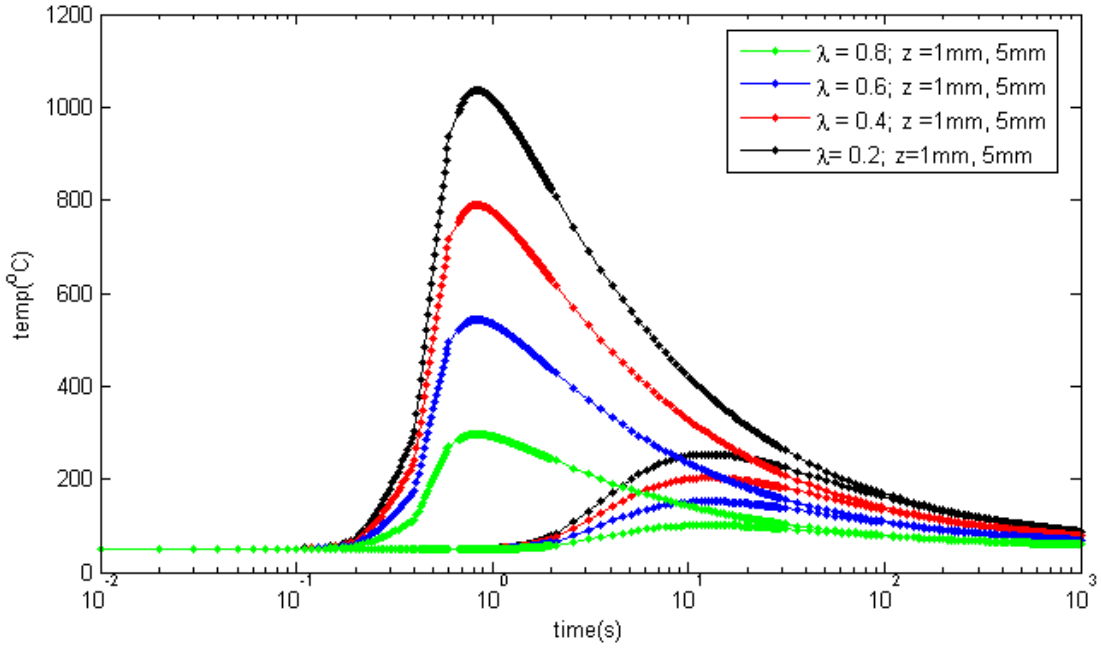

Figure 5.5: Effect of pore pressure on rise in temperature during rupture at a depth of 1km (d=10cm, μ=0.6, κ =1e-6, K=2.5 and **ρ**=2800)

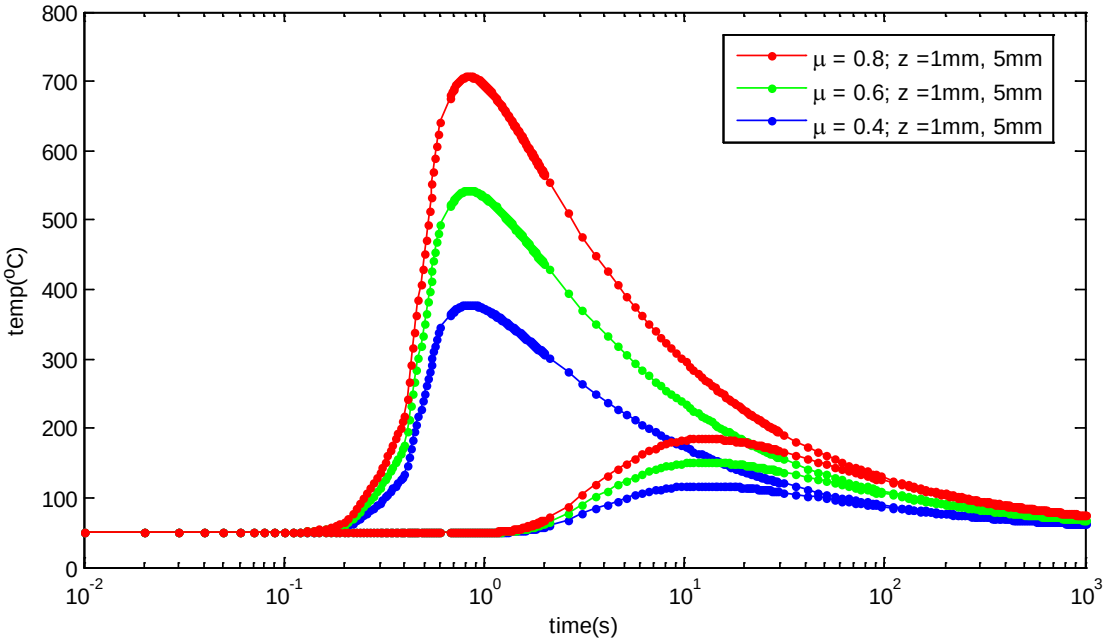

Figure 5.6: Effect of friction coefficient on rise in temperature during rupture at a depth of 1km (d=10cm, λ =0.6 κ =1e-6, K=2.5 and **ρ**=2800)

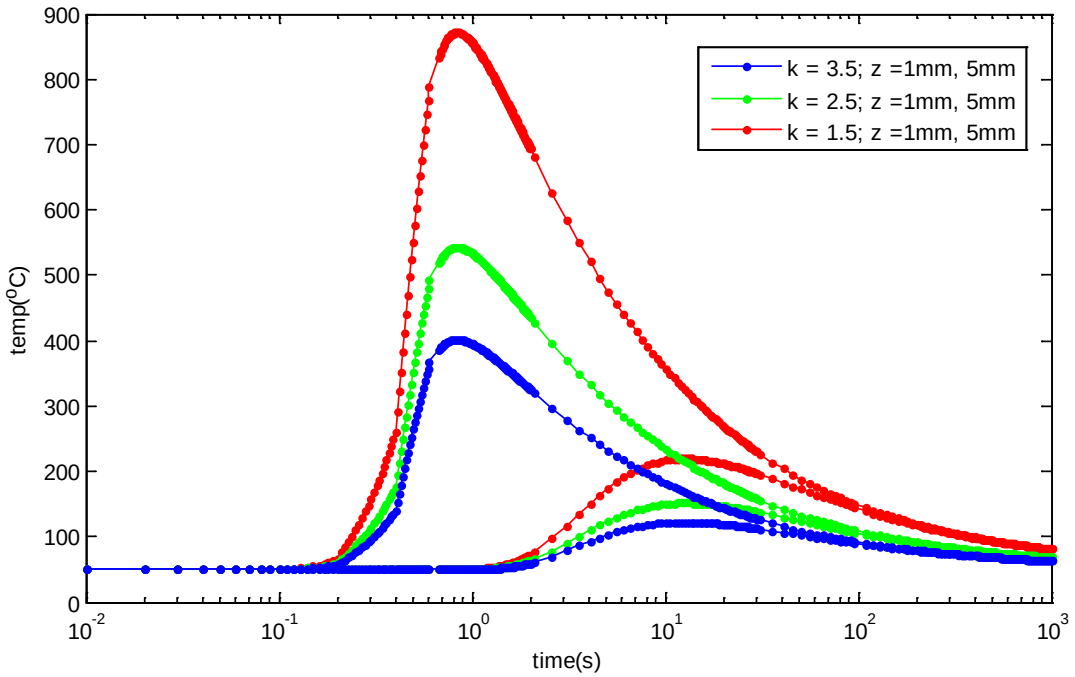

Figure 5.7: Effect of thermal conductance on rise in temperature during rupture at a depth of 1km (d=10cm, μ =0.6, λ =0.6, κ =1e-6 and **ρ**=2800)

fault plane is decreased as shown in Figure 5.6. Figure 5.7 shows the effect of thermal conductance on rise in temperature close to the fault plane.

For luminescence dating the TL peaks in range from 200-400 ℃ or the OSL signal associated with the peaks in this temperature range are being used for quartz and feldspar minerals. To reset the TL/OSL signal the mineral need to be heated to <400 ℃. From the present model study it is evident that the required temperature can be achieved for a combination of model parameters.

5.5 Luminescence Studies of Fault Gouge Samples

The resetting of luminescence signal was tested using the fault gouge samples collected from the Sikkim−Darjeeling Himalaya. The samples were analyzed using TL and IRSL of feldspar.

5.5.1 Predose effect in quartz

The quartz 110 ℃ TL peak is a prominent peak with short life time of few hours (~ 7 hrs, trap depth 0.8 eV) at room temperature. The sensitivity (luminescence per unit dose) of this peak changes after heating to 500 ℃ following the pre exposure to radiation. Since then several works (e.g. Wright, 1979; Haskell et al., 1980; Kitis et al., 2006; Koul, 2008; Koul et al., 2010; Oniya et al., 2012; Polymeris et al., 2012) have studied the characteristics of 110 ℃ quartz peak to use it for dosimetric purpose. The predose method has been used for accident dosimetry and for archaeological authenticity testing (Aitken, 1985; Bailiff, 1994). The method was used to find the thermal history (firing temperature) of fine grained quartz for pottery (David and Sunta, 1981; Koul and Chougaonkar, 2011; Polymeris et al., 2013). Zimmerman (1971b) suggested the possible mechanism based on the sensitization of deeper trap due to pre exposure to radiation and subsequent heating. The model proposed by Zimmerman (1971b) was modified to include the additional electron level to compete during heating (Chen, 1979; Chen and Leung, 1999). The experimental observation in predose method was complemented by the theoretical work (Pagonis et al., 2003; Adamiec et al., 2006; Pagonis et al., 2008).

For the explanation of predose in the model thermally disconnected electron traps, thermally unstable non-radiative recombination centers (reservoir centers) were introduced.

When dose is administered to the quartz (predose) the electrons are trapped in the thermally disconnected traps. Due to repeated cycle of heating these thermally disconnected traps are sensitized and results in increasing the TL sensitivity of the 100 ℃ peak of quartz. These traps does not show sensitization to the test dose to the pre heated temperature, and thus were of potential use in finding the firing temperature of the samples. The method was tested for natural quartz samples (David and Sunta, 1981).

5.5.2 Estimation of rise in temperature during faulting

To ascertain the last heating temperature faced by the fault gouge samples and host rock samples we used the method as suggested by (David and Sunta, 1981). The protocol used for this purpose is shown in Figure 5.8. The sample was preheated from 200 ℃ to 500 ℃ in steps of 50 ℃. The intensity ratio (S_i/S_0) is then plotted against the

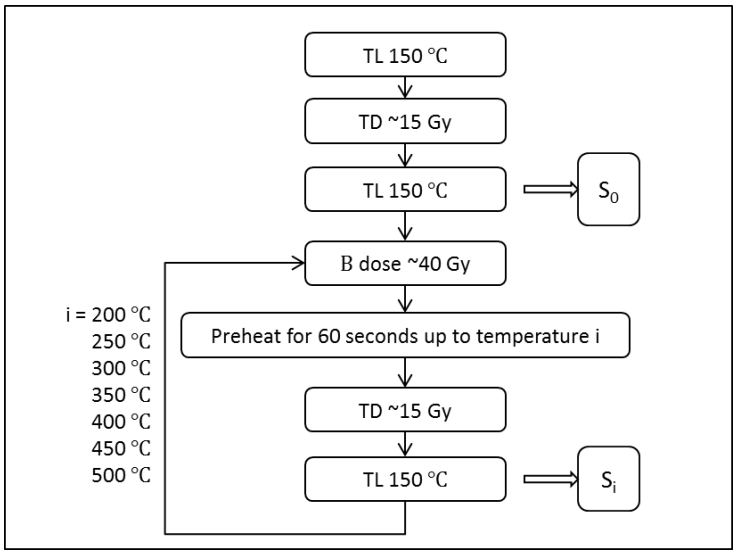

Figure 5.8: Flow chart for the measurement protocol for the monitoring of 110 ℃ TL peak of quartz

preheat temperatures. It was observed that the fault gouge samples show a sensitivity increase initially as compared to the host rock samples. In case of gouge samples it was observed that the increase in sensitivity starts in range of 250 ℃– 300 ℃, whereas for the host samples the sensitivity remains almost constant till 500 ℃ (Figure 5.11). This has been attributed to the past heating of gouge samples. The TD response of TL 110 ℃ peak of quartz after preheat of 200 ℃ gave 2390, 9929, 70322, 13906, 6221, 8089 and 83119 integrated TL intensity

(Photon counts) for samples PCMA-8, 9, 10, 11, 12, 13, and 14. The samples PCMA-8 to 10 are from fault gouge material and others are from host material. The fault gouge samples show a higher dose response as compared to the host samples with exception of PCMA-8 and PCMA-14. This higher dose response might be due to heating of the fault gouge material during the wear process.

5.5.3 Equivalent Dose and Age Estimation

The Fault gouge and host samples were analyzed using the MAAD protocol for fine grain feldspar extracted from the samples. Figure 5.9 shows the dose response of samples. For these samples the stability of the signal was observed in temperature range of 200 ℃ to 350 ℃, and the luminescence signal from within this range was used to calculate the equivalent dose (ED) of the samples. Figure 5.10 shows the ED plateau for samples PCMA-8, PCMA-10, PCMA-12 and PCMA-13. The alpha efficiency was measured for all the samples and results are listed in Table 5.1.

5.5.1 Athermal Fading

Fading is the loss of luminescence signal on storage. Athermal fading, is the loss of luminescence signal at room temperature arising due to quantum mechanical tunneling of trapped charges (Visocekas, 1985) and these cannot be explained by the standard kinetics considerations. Athermal fading was first observed in the case of volcanic feldspars by Wintle (1973). It was observed that UV blue emissions from volcanic feldspars exhibit significant fading of the luminescence signal at room temperature and hence are not suitable for dating purpose. For the measurement of the fading rates samples were irradiated and stored and after storage recorded for the faded TL signal. The ages were then corrected by the method suggested by Huntley and Lamothe (2001). The ages corrected for fading are also shown in Table 5.1.

5.6 Effect of stress on Quartz

In order to analyze the effect of stress on natural quartz, the quartz samples were stressed in laboratory and the luminescence measurements were done to characterize them and to see

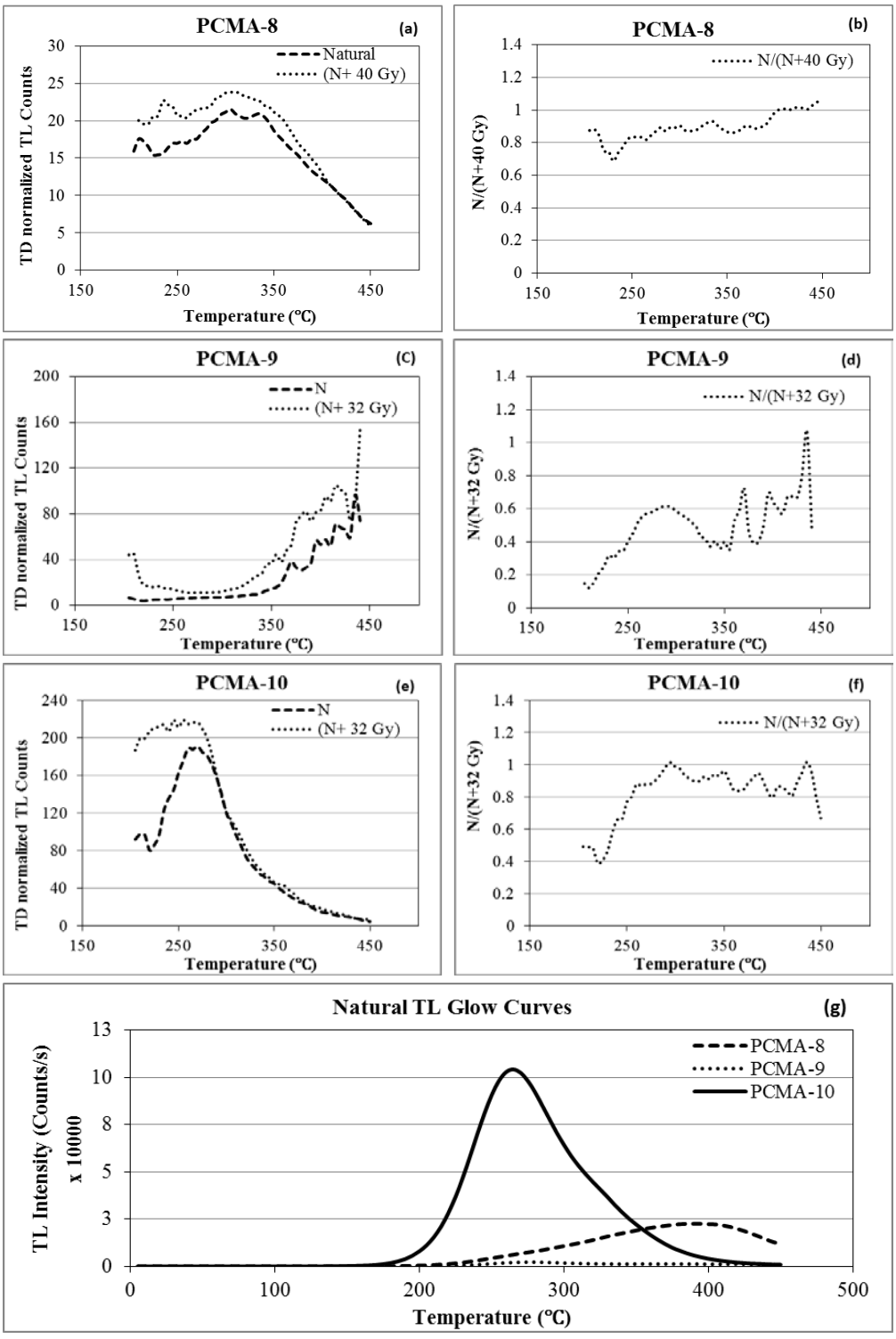

Figure 5.9: (a), (c) and (e) normalized glow curves for PCMA-8, 9 and 10; (b), (d) and (f) ratio of N/(N+β) showing the stability of the TL signal for same samples and (g) natural TL glow curves for the same samples

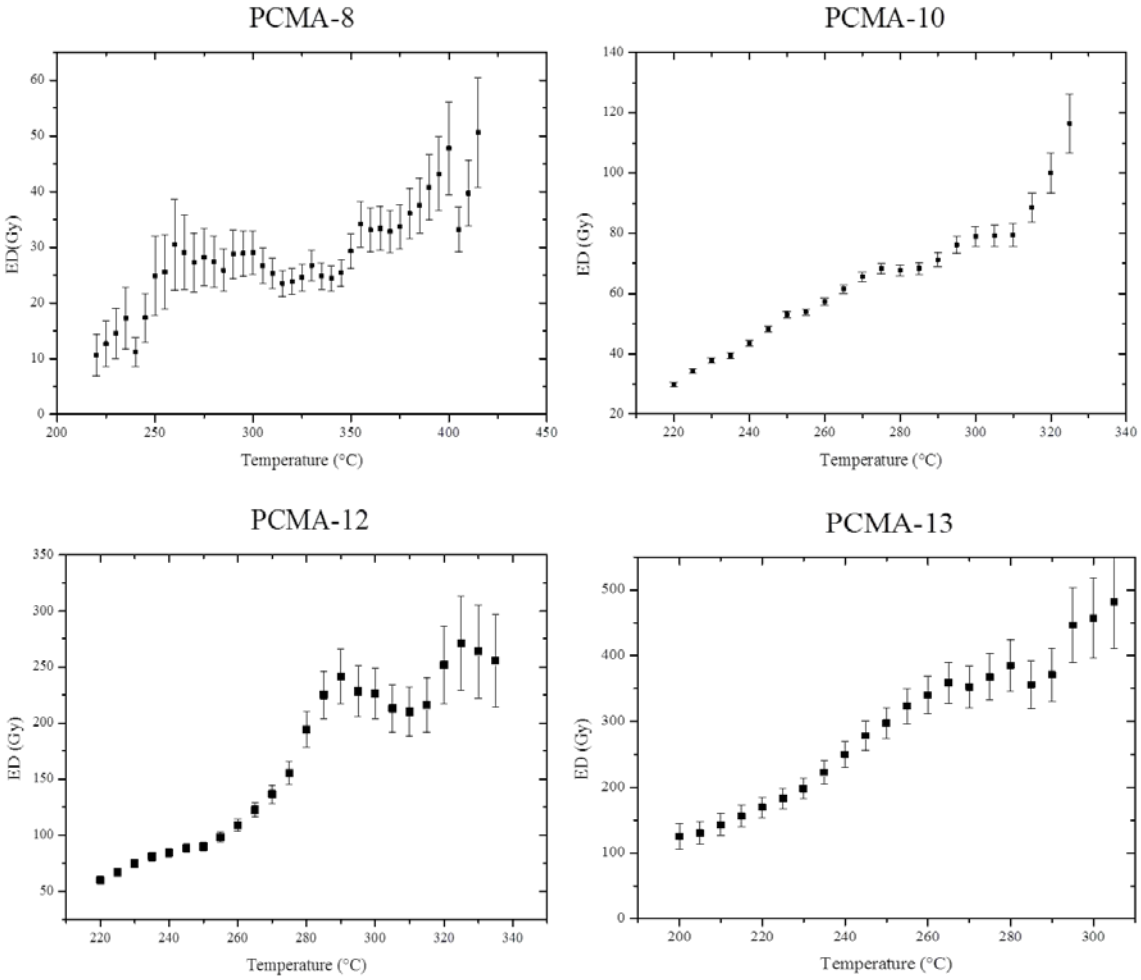

Figure 5.10: Equivalent dose plateau for samples (a) PCMA-8, (b) PCMA-10, (c) PCMA-12 and (d) PCMA-13

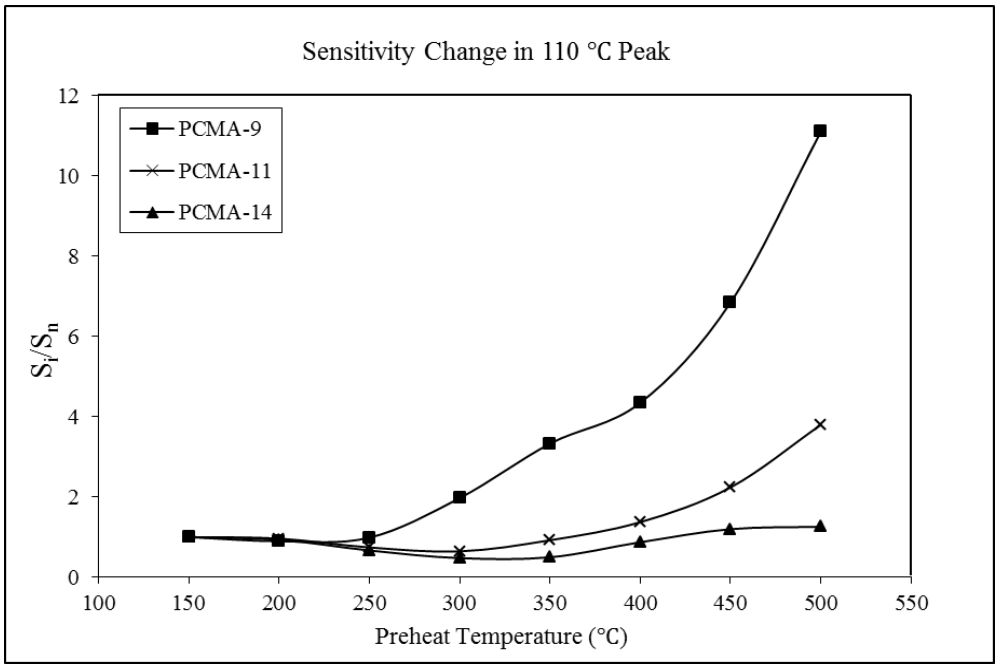

Figure 5.11: Change in sensitivity of 110 ℃ TL peak for samples PCMA-9, PCMA-11 (fault gouge) and for PCMA-14 (host)

the level of resetting of different quartz peak as well to see the change in the sensitivity of these peaks.

5.6.1 Effect of stress on OSL of quartz

In order to see the effect of stress on TL 100 °C peak, Figure 5.12 shows the measurement protocol, the measurement was performed in two steps. In first step the sample was given small test dose (6.5 Gy) to induce 110 °C TL peak and then TL and OSL of the sample were recorded. This procedure was repeated three more time to assure that there is no change in the sensitivity of 110 °C TL peak and OSL counts.

In second step after giving small test dose (6.5 Gy) the sample was stressed once (stress= 4.8 MPa), and then the TD and measurement cycles were repeated three more times. Figure 5.13 and Figure 5.14 show the response of 110 °C peak and OSL shine down curve before and after stress, as can be seen that there is reduction in the counts after stress.

To see the effect of variable and cumulative effect on TL 110°C, a protocol as shown in Figure 5.15 was used.

Table 5.1: Details of samples, measured D_e, radioactivity data, alpha efficiency fading factor, assumed water content and TL ages

Th (ppm)	**K (%)**	**CR**	**Dose Rate**	**a-value**	**Water**	**ED (Gy)**	**Age (ka)**
36.5±0.4	5.3±0.1	220±22	11.9±0.2	0.07	15±5	25.8±2.0	2.2±0.2
4.4±0.1	3.5±0.1	241±24	8.0±0.2	0.02	15±5	21.3±2.4	2.6±0.3
111±1	5.7±0.1	250±25	25.9±0.6	0.04	15±5	68.2±2.0	2.6±0.1
110±1	6.1±0.1	250±25	23.4±0.6	0.02	15±5	33.4±1.2	1.4±0.1
20.5±0.3	2.4±0.1	250±25	5.7±0.1	0.02	15±5	223.0±17.2	40.0±3.2
7.0±1.0	3.6±0.1	250±25	5.5±0.2	0.02	15±5	361.8±14.5	66.2±3.4
9.0±1.0	3.9±0.1	250±25	6.4±0.2	0.06	15±5	206.1±13.5	32.2±2.4

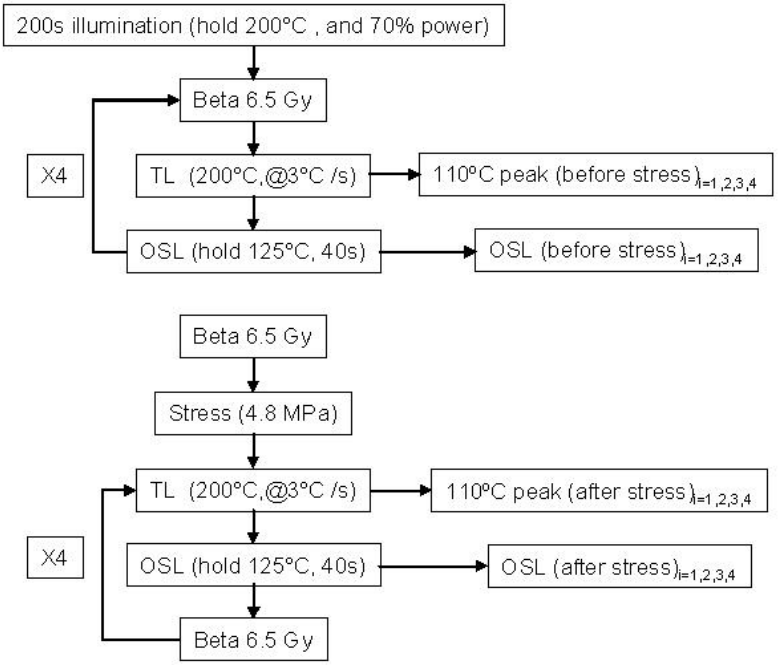

Figure 5.12: Measurement protocol to see the effect of stress on 110 °C peak and OSL

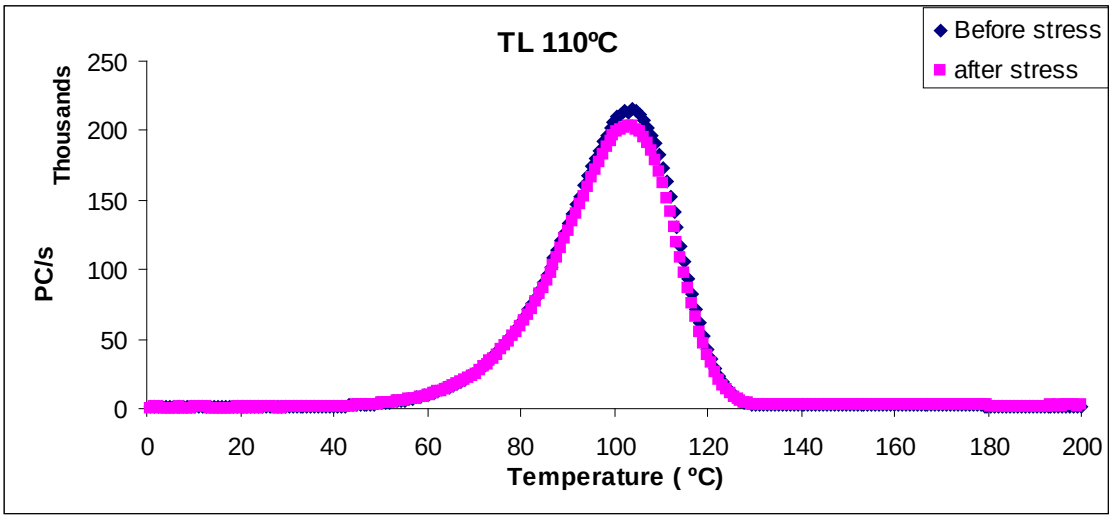

Figure 5.13: TL 110 °C response before and after stress .

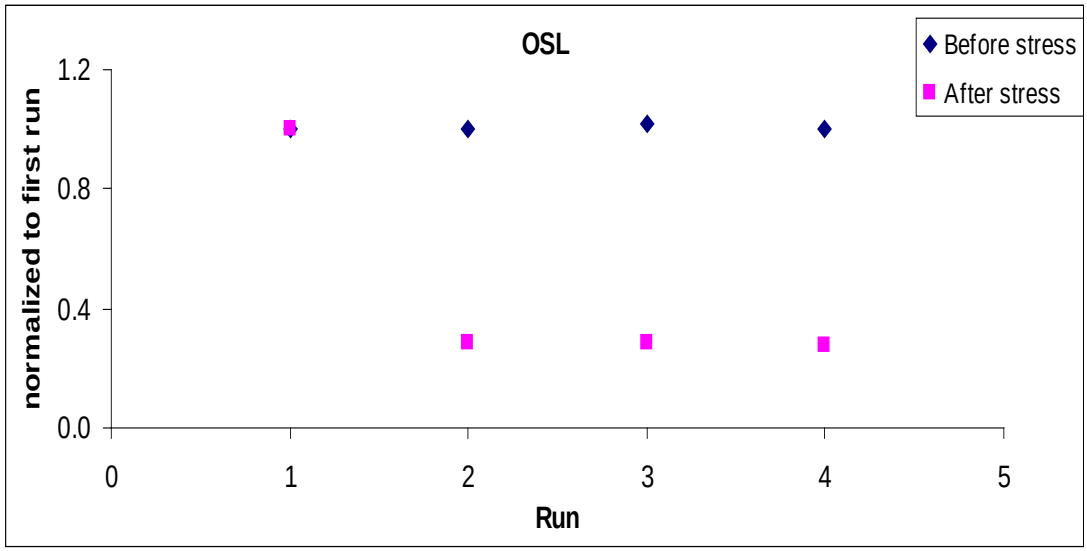

Figure 5.14: OSL normalized to first run

5.6.2 Effect of cumulative stress and variable stress on natural quartz

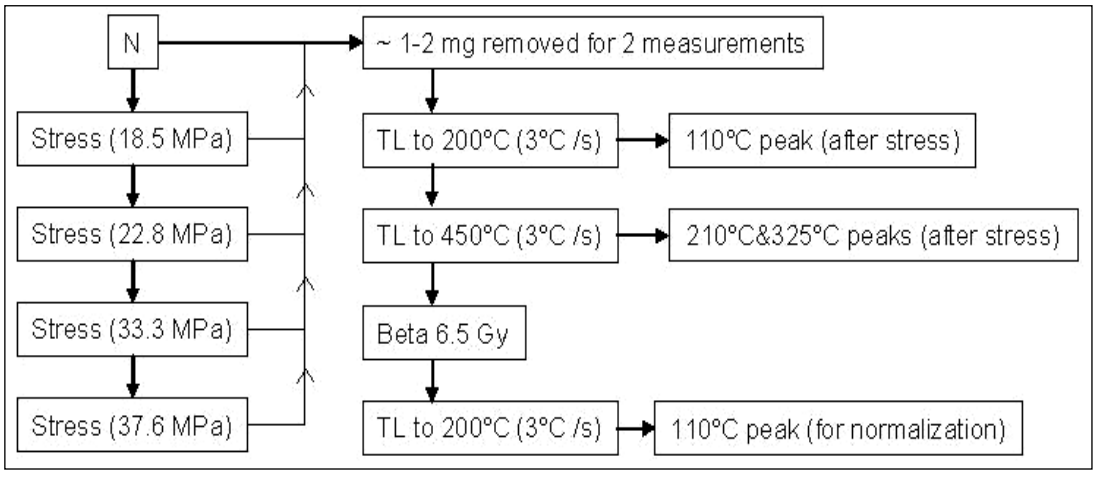

Figure 5.15:-Protocol to see the effect of cumulative and variable stress on quartz 110 °C peak

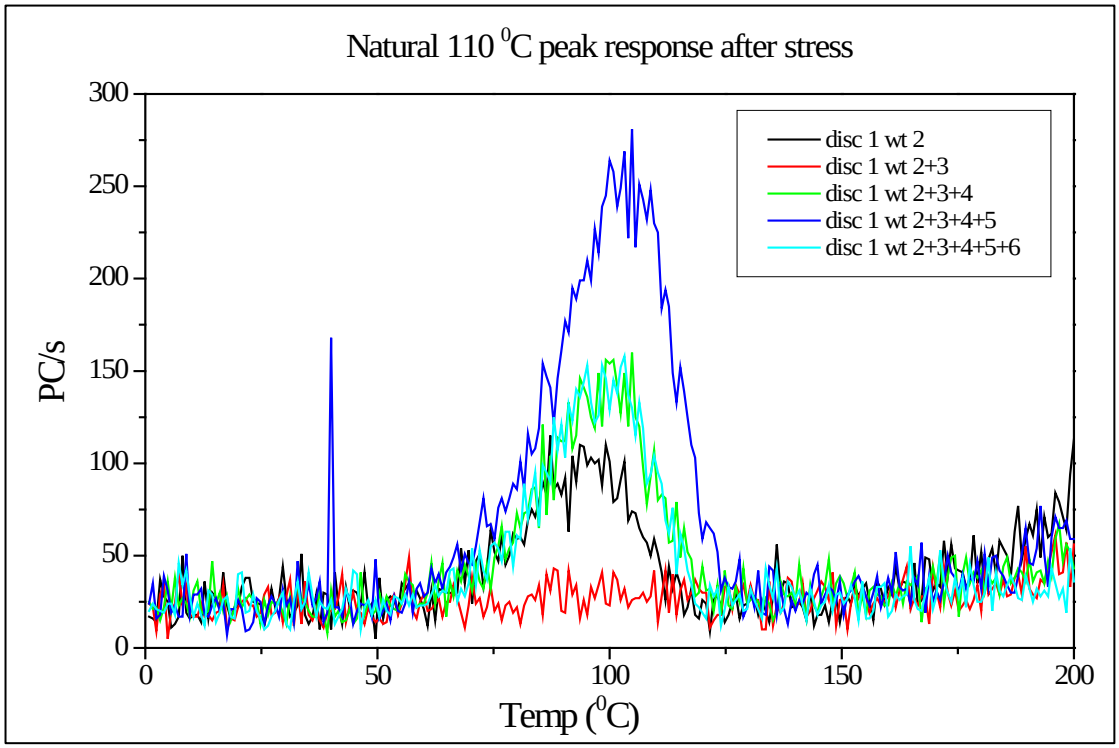

Figure 5.16: Stress induced 110 °C TL peak

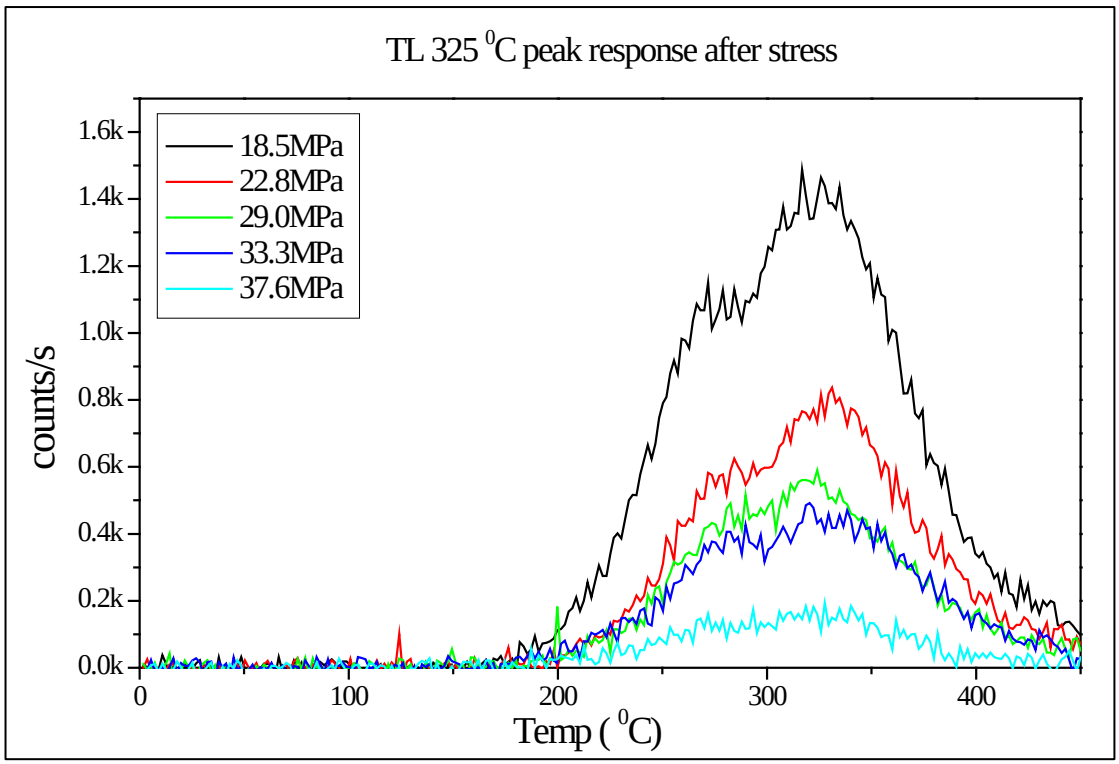

Figure 5.17: Response of 325 ºC peak after stress

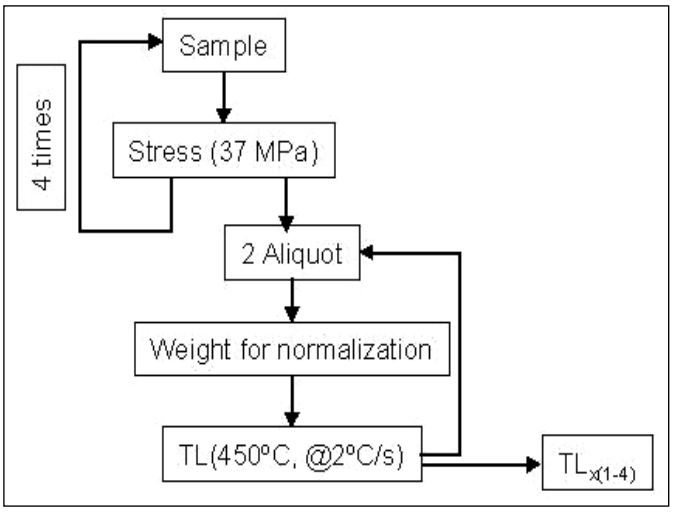

Figure 5.18: Measurement protocol to see the effect of same amount of stress due to repeated cycles.

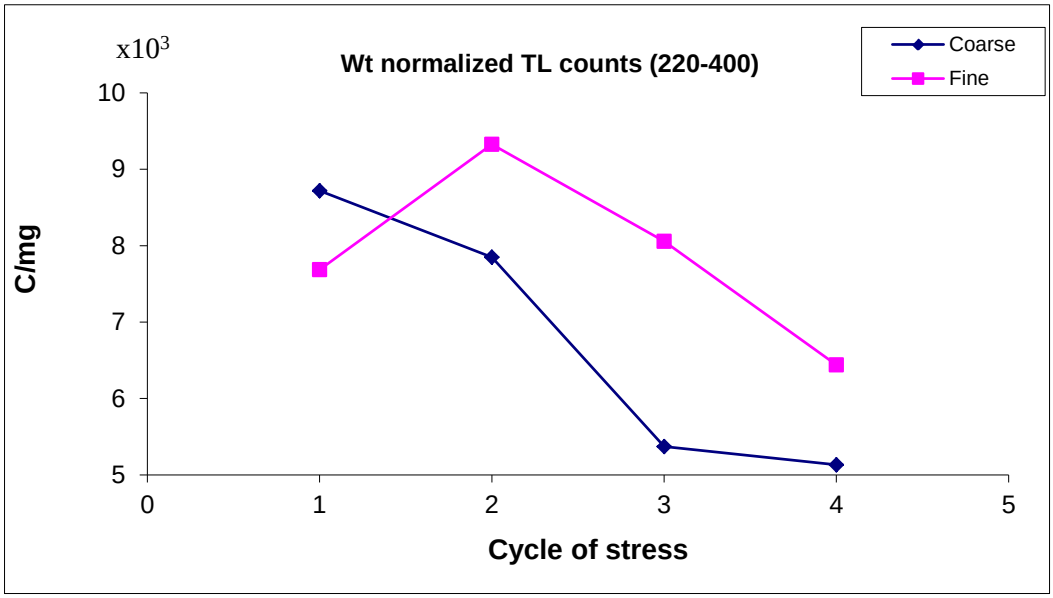

Figure 5.19: effect on grain size on TL counts integrated over temperature range 220–400°C

It was observed that samples which are not irradiated, when stressed show stress induced 110 °C TL peak. Figure–21 shows the measurement protocol. As shown the measurement was done in several steps. From the natural sample TL 200 °C and TL 450 °C was recorded and after that TL 200 °C was recorded for the normalization purpose. The remaining sample was then stressed (stress = 18.5 MPa), from the stressed sample small part was taken for the

measurement and remaining part was again stressed (stress = 22.8 MPa) and then the same process continued up to 37.6 MPa stress. Figure 5.16 shows the effect of cumulative stress, it was observed that the stress induced TL 110 °C peak. It was also observed that the height of this peak is dependent on the applied stress. When sample was stressed by dropping the increasing weight (height remains constant) a reduction of TL counts for TL 325 °C peak was also observed.

In another set of experiment the fixed amount of stress was applied to the sample the measurement protocol is shown in Figure 5.18. After the sample was stressed a small part of the sample was used for measurement of TL peak for coarser and finer part.

Figure 5.19 shows the effect of repeated stress on grain size TL counts integrated over temperature range 220–400°C were used and, the counts are weight normalized. It was expected that the resetting should be more in case of finer part but results suggest that due to the stress the resetting in coarser part is more. The reason is probably that due to the presence of coarser grains the stress is not applied effectively on finer grains.

5.7 Results and Discussion

Limited studies exist using thermoluminescence (TL) regarding the dosimetry of faulting events (Banerjee, 1996; Banerjee et al., 1999). Previous attempts to date faulting events were limited by the use of grain size plateau for EDs. It was suggested that the fine grain sample is safe to date the fault gouge samples as there is high chance of resetting of OSL signal as compare to coarse grain (Wintle and Murray, 2006). In general, fine grain dosimetry is done using infrared stimulation (IRSL) of feldspar. However, feldspar minerals face a few problems like anomalous fading and change in sensitivity during the measurements. Coarse grain quartz dating was not used earlier because of the non-availability of information on thermal history of the samples. It was thought that the resetting will be partial either due to insufficient frictional heat or due to the crushing effects.

The three phase model as discussed in section 5.3 suggested that, in case of earthquake rupture event, frictional heat generated during slip of rock ca reset the luminescence signal. To simulate the temperature conditions resulting from fault, temperature profile were generated using transient thermal modeling. Figure 5.4, Figure 5.5, Figure 5.6, and Figure

5.7 shows the T-t curve for fixed depth (1000 m) and for variable pore pressure factor with various slips up to 25 cm and for different values of vertical distances (1 and 3 mm) from fault plane. The time duration of slip was assumed to be of 0.6 for low magnitude earthquakes (De Lorenzo et al., 2001). A minimum total slip of about 10 cm is can generate temperature in the range 300−400 °C at depth of 1000m from surface. As the depth is increased, the desired temperature can be attained even for slip lesser than 10 cm.

The initial observations on the thermal profiles have shown that even for the values of the fault parameters' corresponding to weak faults, the temperatures generated at the fault plane are close to 400 °C. This indicated that the temperatures as high as 400 °C could reduce the TL signal during the faulting. The three phase model of rupturing suggested that the rise in temperature during the formation of fault gouge for shallow earthquakes can be more than 450 °C. This temperature is sufficient to reset the TL signal in quart and feldspar minerals.

Stress experiments performed on the quartz samples suggested the possibility of resetting of luminescence due to mechanical stress. In these experiments silicon oil was used to mount the grains on the stainless steel discs, which worked as the lubricant in the stress experiment. As a result of applied stress the material was crushed resulting into the finer grain sizes, which to some extent simulates the formation of fault gouge. This suggests that crushing will also contribute in the resetting of the luminescence.

The fault gouge sample study from the Sikkim-Darjeeling Himalaya gave age about 1.9 ka and 3.5 ka which are low as compared to the host rock ages of the order of 100 ka. This suggested the resetting of luminescence signal in gouge samples during the earthquake. The sensitivity measurements made on gouge and host rock samples suggested that the temperature rise during these events was above 300-350 °C which is sufficient to reset the TL peak of feldspar used for the ED measurements. The ages from the gouge samples suggested at least two earthquake events in the region at around 2 ka and 3.5 ka.

Chapter 6

Luminescence studies of Tectonic Events in western India

6.1 Introduction

The Great Rann of Kachchh (~300 km in length and 80-100 km in width) is a unique landscape in western India which gets inundated during the monsoon by wind- driven marine storm surges and continental fluvial influxes (Glennie and Evans, 1976). The Rann is bound by the Nagar Parker Fault (NPF) on the north and Kachchh Mainland Fault (KMF) on the south (Biswas, 1987) as shown in Figure 6.1a.

Western Great Rann is known for its tectonic instability. Paleoseismological investigations in the vicinity of 1819 earthquake indicate the occurrence of an older earthquake around 800–1000 years ago (Rajendran and Rajendran, 2001). According to Merh (2005) and Maurya et al. (2008), the present Rann is an uplifted floor of the former gulf. In a recent study, Chowksey et al. (2010) suggested uplift of the Rann after 2 ka based on the

occurrence of raised notches and abraded platforms. The most recent one was the 1819 Allah Bund earthquake which not only created a NE-SW trending scarp (Figure 6.1b) but was known to have significantly modified the geomorphic processes in the region (Oldham, 1926).

Sedimentation in the Great Rann has been controlled by the interplay between continental and marine processes (Glennie and Evans, 1976; Roy and Merh, 1982; Srivastava, 1971). The occurrence of clay and silt with sandy lenticles is interpreted as deposition in a low energy, protected tidal flat environment (Srivastava, 1971). Based on the limited sedimentological and geochemical studies, Glennie and Evans (1976) suggested that the Great Rann was probably occupied by shallow marine gulfs following the rise in sea level after the glacial epoch, whereas continental sediment influx dominated during the transgressive phase. According to them, clay mineral assemblages dominated by illite, kaolinite, chlorite and montmorillonite suggest the influence of the Indus River drainage system.

In present thesis an attempt was made to understand the processes responsible for terrain configuration in the vicinity of Allah Bund with an assumption that (i) presence of scarp and relict raised channels may point to tectonic and seismic activities and (ii) evidence for both continental and marine processes may be well preserved. The other objectives of the study include, to (i) ascertain the process responsible for Rann sedimentation in terms of marine and continental, assign chronology to various depositional events and environments and to reconstruct paleoseismic events. To address these issues a detailed field stratigraphy of the Rann sediments, relict and raised fluvial channels was undertaken. Due to the paucity of organic matter in fluvial sediment and the problem of the reservoir correction in marine sediments, Optical dating technique have been employed for constraining various geomorphic/climatic processes.

6.2 Study area

The present study is focused on the western part of the Great Rann between the Nara River in the west (24° 07′ 36″ N and 69° 07′ 15″E) and Shakti Bet in the east (24° 03′ 16″ N and 69° 34′ 13″E; Figure 6.1b). The rationale behind selection of the studied area was (i) the terrain was severely affected by 1819 Allah Bund earthquake, (ii) it preserves both Rann and

Bet sequences, and (iii) was drained by the Nara River in the past. Climatically the area lies in arid zone. The mean annual rainfall ranges from 200–380 mm and is contributed by the southwest summer monsoon (Pramanik, 1952). Vegetation is scant, dominated by shrubs and grows along a few linear tracts containing fine sand <1 m below the surface, which probably represent past stream courses. The shallow sedimentary sequences investigated as a part of this study are north of the Allah Bund scarp and are well above present-day tidal inundation (Figure 6.1b). The field stratigraphy and sedimentology of the sections studied are discussed below

6.2.1 Bet sequences

Karim Shahi: At Karim Shahi (24º 07′ 42″ N and 69º 30′ 73″ E), a 200 cm-thick micaceous sedimentary sequences, shows four distinct fining-upward units and overlies the clayey-silt dominated Rann sediment (Figure 6.2, Karim Shahi). From the bottom upwards, unit-1 consists of a 15 cm-thick light grey crudely laminated, fine micaceous sand overlain by a 6 cm-thick light brown silty-clay. The unit-2 is succeeded by a 35 cm- thick fine, light grey micaceous sand with dispersed clay laminae overlain by a 5 cm-thick compact light grey silty-clay. The overlying unit-3 has a 10 cm-thick light grey fine micaceous sand overlain by a 10 cm-thick light grey compact silty-clay. The uppermost unit-4 is dominated by a 30 cm-thick dark grey crudely laminated, fine micaceous sand capped by a 10 cm-thick light grey silty-clay. Finally, the succession terminates with a 25 cm-thick crudely laminated light grey medium to fine sand. The grain size analyses of unit-1 and 2 show dominance of sand (50–51%), followed by silt (46–47 %) and clay in traces (0.5–0.4%). To the west of the Bet sequence, a few archeological mounds are located in the low-lying areas overlying the Rann sediment. One such mound was excavated during the investigation in order to document the stratigraphy and to collect samples for optical and radiocarbon dating. The stratigraphy of the mound from the bottom upwards shows a 30 cm-thick crudely layered mixture of dark grey silty-clay, containing dispersed charcoal and bones. This is overlain by a 20 cm-thick light grey silty-clay with broken potsherds and finally capped by 60 cm of assorted archaeological debris containing bones, potsherds and charcoal (Figure 6.2, Archaeological mound).

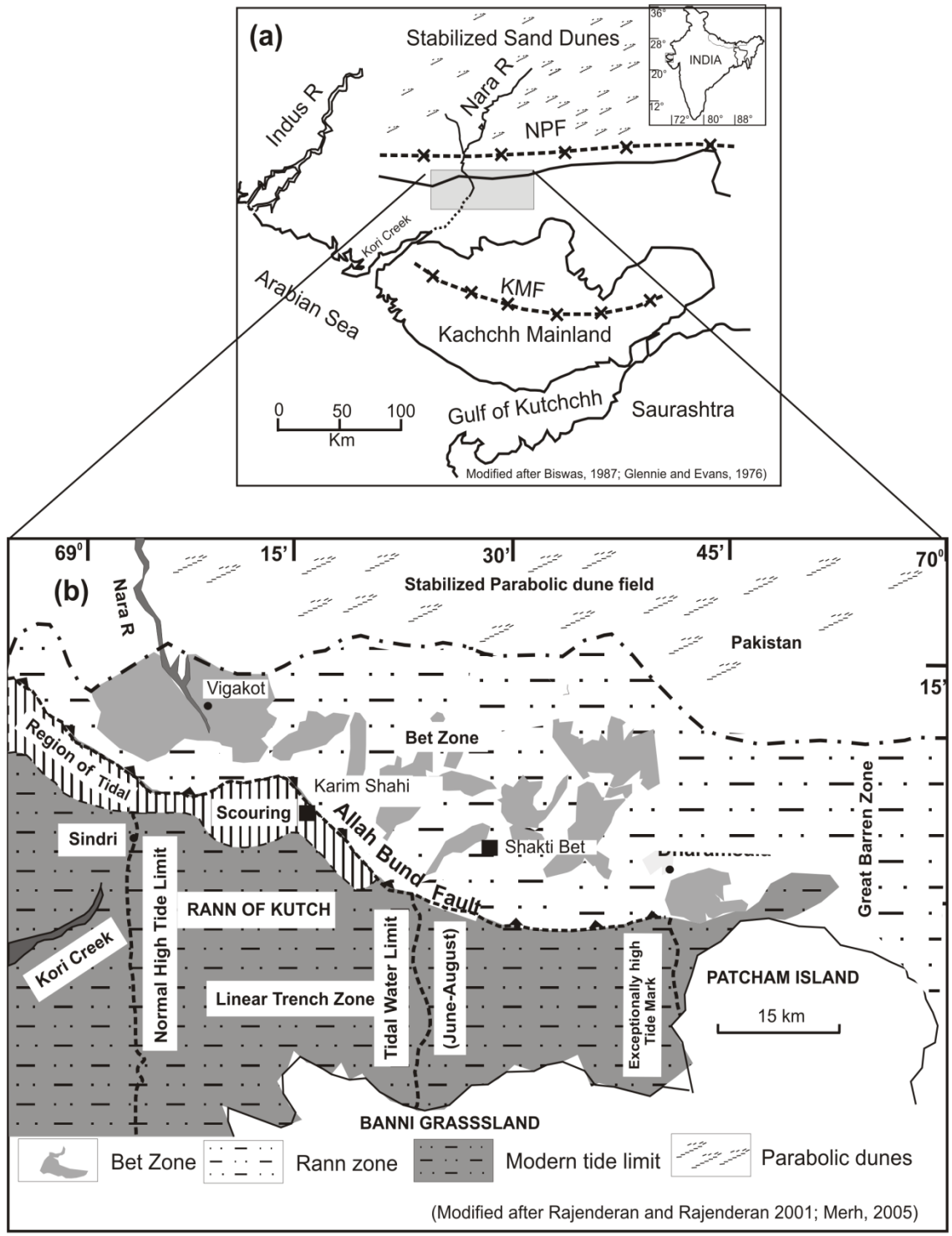

Figure 6.1: (a) Map showing the location of the study area, NPF—Nagar Parker Fault, KMF—Kachchh Mainland Fault (after Biswas, 1987). (b) Geomorphological map of the area (after Rajendran and Rajendran, 2001; Merh, 2005).

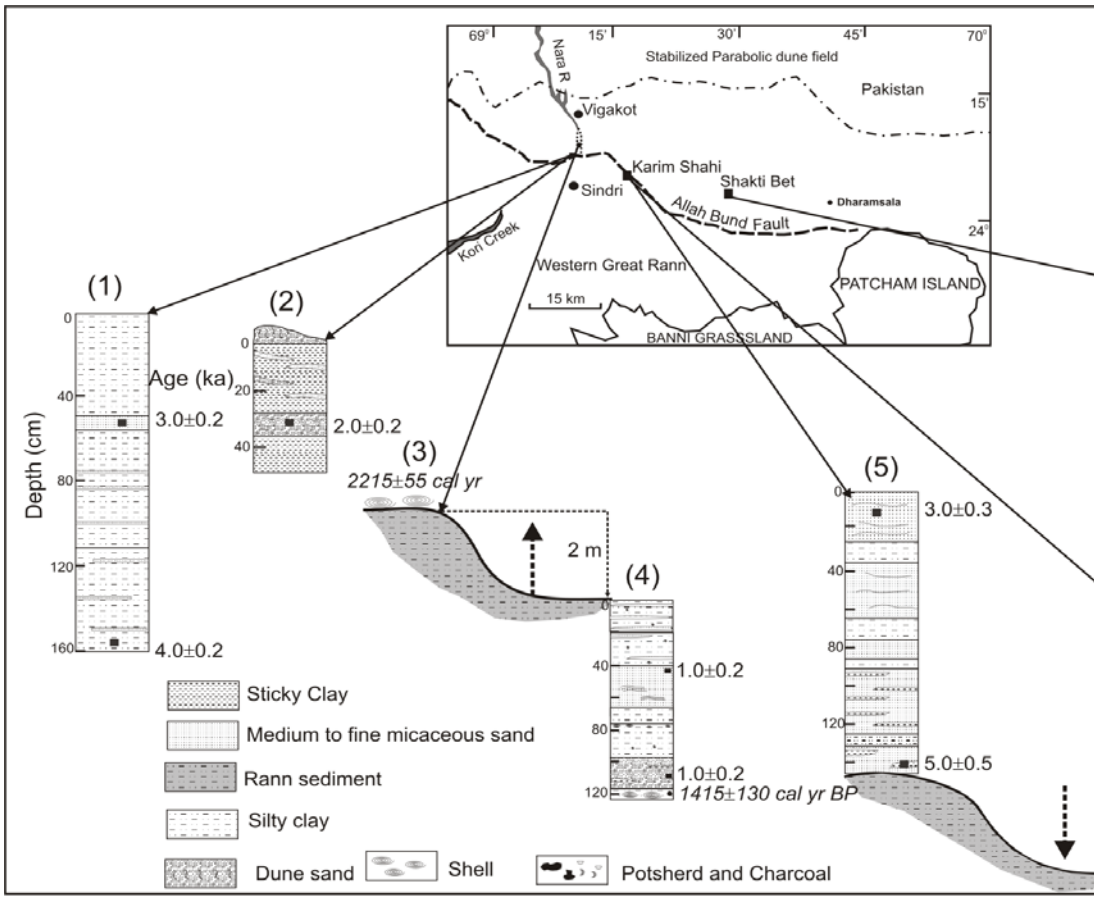

Figure 6.2: Stratigraphy and optical chronology of the shallow sedimentary sequences investigated in the present study. (1) Allah Bund (Rann sediment), (2) Rann sediment (incised channel), (3) Nara River bank, (4) Nara River Bed, (5) Karim Shahi (Bet sediment), (6) Karim Shahi (Archaeological mound) and (7) Rann sediment (at Shakti Bet). Radiocarbon ages are shown in italic bold font. Dashed upward arrow indicates land movement, whereas the downward arrow indicates river incision.

Depositional environment: The deposition of fining-upward sequence is attributed to a flood-plain environment for the following reasons; (i) sand horizons are parallel laminated (unlike the coastal fining-upward sequences which are largely cross-laminated), (ii) it overlies lenticular bedded clayey-silt (tidal flat) and (iii) it is associated with micaceous-rich elevated sandy Bets. In view of this the depositional environment is interpreted as a flood-plain adjacent to the trunk channel (Reineck and Singh, 1980). For flood-plain aggradation the channel should have a consistent flow path, well-defined channel morphology (e.g. a meandering course) and episodic over− spilling of fine sediment on to the adjacent floodplains (Juyal et al., 2000).

The Indus River sediments are rich in mica (Chauhan, 1994) because a significant contribution comes from the higher Himalayan crystalline lithologies (Alizai et al., 2011). Presently, the Indus River flows nearly 100 km west of the study area. The Nara River, an eastern branch tributary of the Indus River that once flowed into the Great Rann (Oldham, 1926), was the major source of sediment into the western Great Rann. In view of this, the presence of micaceous sand in the Bet sediment at Karim Shahi can be attributed to the contribution from the Indus alluvial plain. However, it is also likely that a part of the sand could have been reworked by the ephemeral streams from the parabolic dune fields located in the north of the study area (Figure 6.1).

Near Karim Shahi, the archaeological site is proximal to the line of present-day tidal inundation. Therefore, it is logical to assume that during the time of human occupation, the site would have been well above the tidal reach and its present elevation can be attributed to land-level changes caused due to an earthquake. That is because the historical evidence suggests that prior to the 1819 Allah Bund earthquake, a large tract of the land north-east of Kori Creek was above high tide level. After the 1819 earthquake, a terrain north of Kori Creek was subsided by about 1–5 m, which led to the creation of Sindri basin (Wynne, 1872). The archeological site is located towards the northern margin of the subsided Sindri basin; hence it is reasonable to suggest that the present elevation of the archaeological site is due to the earthquake-induced land subsidence.

6.2.2 Rann Sequences

Allah Bund Scarp: At the mouth of the dried bed of the erstwhile Nara River (24º 12′ 63″ N and 69º 11′ 84″ E), a 160 cm scarp developed on Rann sediment shows the dominance of laterally impersistent clayey-silt punctuated very fine micaceous sand laminae (Figure 6.2, Allah Bund Rann sediment).

Incised Rann sediment: A 45 cm-thick section incised by ephemeral streams was exposed along a raised NW-SE trending channel on the Allah Bund scarp (24º 07′ 39.32″ N and 69º 07′ 05.32″ E). The lower-most 15 cm-thick unit is dominated by cherry brown clayey-silt and is overlain by a 7 cm-thick ripple laminated, fine grain sand. This is succeeded by a 30 cm-thick clayey-silt with fine sand lenticles, which is capped by recent aeolian sand (Figure 6.2, Rann sediment, incised channel).

Rann sediment at Shakti Bet: In a low-lying area near Shakti Bet (24º 03′ 46″ N and 69º 29′ 54″ E), a 260 cm-thick sedimentary succession was exposed in a dried channel section (Figure 6.2, Rann sediment near Shakti Bet). The succession shows a 20 cm-thick light to dark grey clay containing discrete sand lenticles. This is overlain by a 105 cm-thick ripple-laminated dark to light brown medium to fine micaceous sand. The sand horizon is succeeded by a 60 cm-thick cherry brown laminated clayey-silt horizon punctuated by cm-thick mottled lenticular fine sand. This is overlain by a 35 cm-thick brown, sticky silty-clay alternating with light to dark grey laminated sand. The succession is terminated with a 40 cm-thick cherry brown sticky clay interspersed with sandy laminae.

Nara River bed: A 120 cm-deep pit was dug into the Nara River bed (24º 07′ 36.7″ N and 69º 07′ 15.1″ E) where it cuts through the 1819 Allah Bund fault scarp (Figure 6.2, Nara River bed). The Nara River has incised the tidal flat sediment containing bivalve shells (preserved in their living position). The lowermost 10 cm-thick clayey-silt layer has abundant unbroken Turritella shells overlain by 20 cm-thick medium to fine laminated micaceous sand with clay streaks. Overlying this is a 30 cm-thick cherry brown silty-clay with laminated fine sand intercalations in the upper part. This is overlain by a 25 cm-thick rippled and planar laminated, medium to fine sand with convolutions. Finally, a sandy-clay alteration marks the top of the river bed succession.

Depositional environment: Texturally, the fine grained nature of the Rann sediment (clayey-silt with occasional fine sand) suggests deposition in a tidal flat environment (Christiansen et al., 2006). On tidal flats, clay and fine silt is transported in suspension, whereas sand is carried by traction (Krögel and Flemming, 1998). Sand is deposited during flood and ebb tide and develops ripple bed forms with internal cross- lamination, whereas, clay is deposited during slack water condition and drapes the ripple surfaces or settles in inter-ripple troughs (Chakrabarti, 2005). The dominance of a tidal flat environment is further suggested by the occurrence of lenticular and wavy bedding with current ripple bedforms (Reineck and Singh, 1980). The presence of 105 cm-thick, current-laminated micaceous sand at Shakti Bet suggests deposition under changing tidal and wave currents. Deposition of sand occurred during the periods of moderate current activity whereas clay was deposited during calm water conditions (Le Hir et al., 2000; Yang et al., 2006). Conventionally the sand dominated areas in a tidal flat are located close to the low tide mark, which are exposed to the stronger tidal currents (Bungenstock and Schäfer, 2009), 2009). It is therefore likely that deposition of rippled-laminated 105 cm-thick sand horizons took place on low to moderate energy areas; viz. the coastline was close to the Shakti Bet. The infrequent presence of cherry brown clayey-silt suggests periodic sub-aerial exposure (Srivastava, 1971). The fossil evidence, such as the in-situ bivalve and the unbroken Turritella shells, further indicates that the Rann sedimentation occurred under intertidal-marine environment (Desai and Patel, 2008).

6.3 Evidence of Past seismic events

Truncated nature of the raised channel suggests episodic uplift of the channel bed due to seismic activity. Rajendran et al. (1998) based on the presence of truncated dry channels and absence of incipient drainage suggested existence of pre 1819 scarp. This would imply that the raised channels suggest an earthquake similar to the 1819 event. Evidence of tectonic activity is further supported by the presence of contorted horizon (flame structures) in the N-S trending raised channel sediments. Flame structures are the direct expression of the seismic activity associated with faults and are generated under the same regional or local stress field that originates in the fault slip (Rodríguez−Pascua et al., 2001). These features are generated due to liquefaction/ fluidization process (Owen, 1996) and the lowest magnitude that can

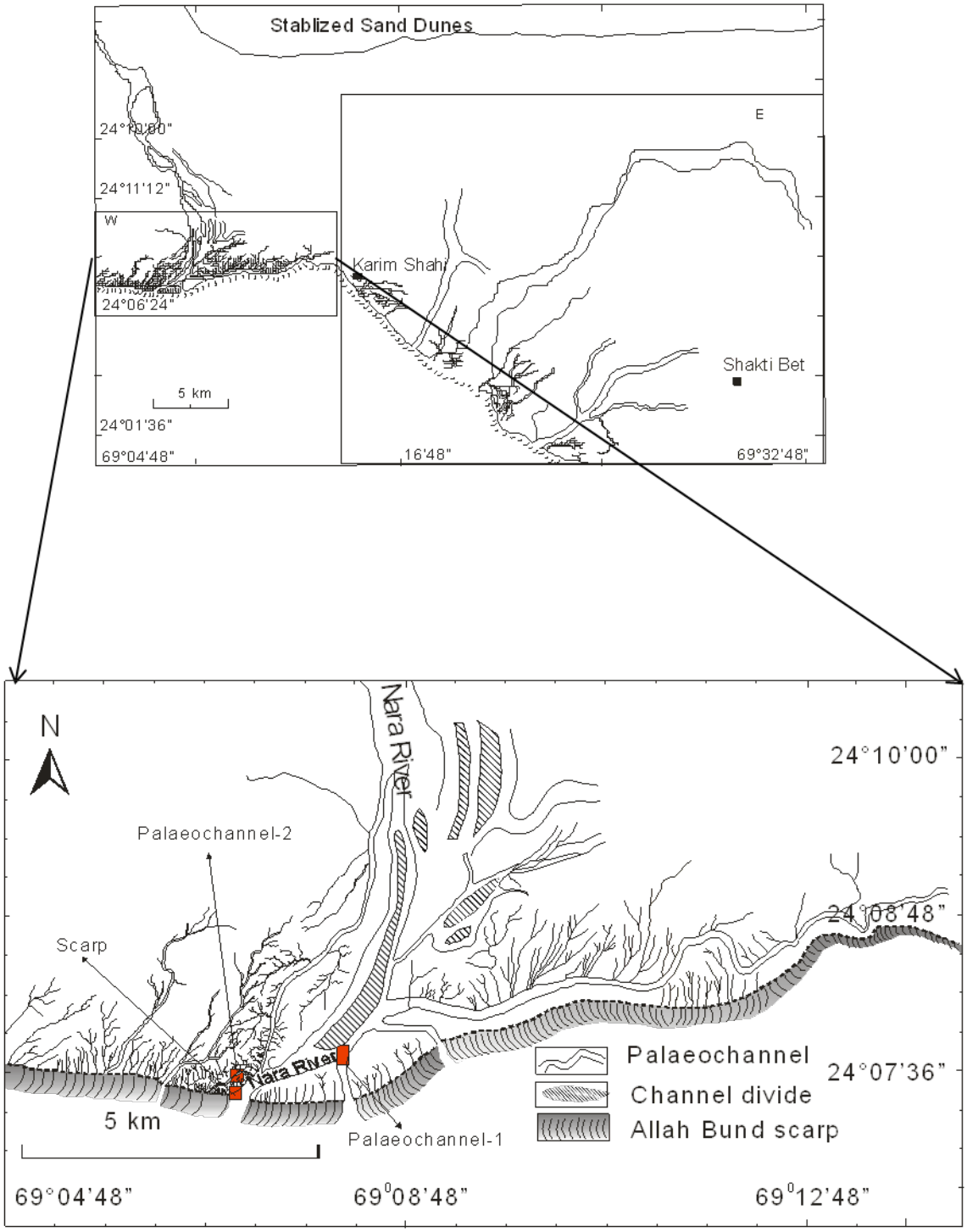

Figure 6.3: Drainage pattern in the vicinity of Allah Bund. Western segment shows higher density of embryonic streams (W) compared to the Eastern segment (E). Channels show a preferential south west side trend.

generate such features is ~M 5 (Atkinson, 1984). Maurya et al. (2006) also suggested the possibility of the type of liquefaction features based on their Ground Penetrating Radar study for 2001 earthquake in Banni region. However, the silty-clay dominated with occasional sandy lenticles in NE-SW trending raised channel suggests that it was carved on pre-existing Rann sediments that were deposited under tidal influence and was brought to the present elevation due to the past earthquake. Absence of prominent sand horizons is interpreted as reduced continental flux. Evidence for active seismicity in the study area is also suggested by the westward deviation of the streams behind the scarp Figure 6.3. Such deviations have been attributed to high rate of structural uplift relative to erosion rates in which case transverse rivers encountering a growing anticline will often be deviated rather than cutting across the structure, following the areas of structural weakness, such as transverse faults (Seeber and Gornitz, 1983; Gupta, 1997).

6.4 Luminescence Studies of Rann Samples

A suite of 13 sediment samples and one pottery sample were analyzed. The pottery sample was analyzed using the Thermoluminescence (TL) dating technique (Zimmerman, 1971a), whereas optical dating was used for sediment samples employing the Single Aliquot Regeneration (SAR) protocol. In absence of coarse grains in sample SBTL-1, the Multiple Aliquot Additive Dose (MAAD) technique on polymineral fine grained extracts was used (Singhvi et al., 2001).

Figure 6.4 shows the preheat plateau test for samples KSTL-2 and ABTl-1 for preheat temperature ranging from 180−280 ℃. It is evident from the figure that a preheat temperature from 220 to 260 ℃ can be used for D_e measurements.

Figure 6.5 (a) and (c) shows the dose recovery tests for samples KSTL-1 and KSTL-2 along with the SAR growth curves for same samples (b) and (d). The shine down curves for these samples are shown in upper right corners of (b) and (d) along with the SAR growth curves.

To visualize the dose distribution of samples radial plot as well as histograms were used Figure 6.6 (a), (c), (e) and (g) show the radial plots of samples ABTL-1, ABTL-2, KSTL-2 and ABP-1 and (b), (d), (f) and (h) shows the histograms of these samples.

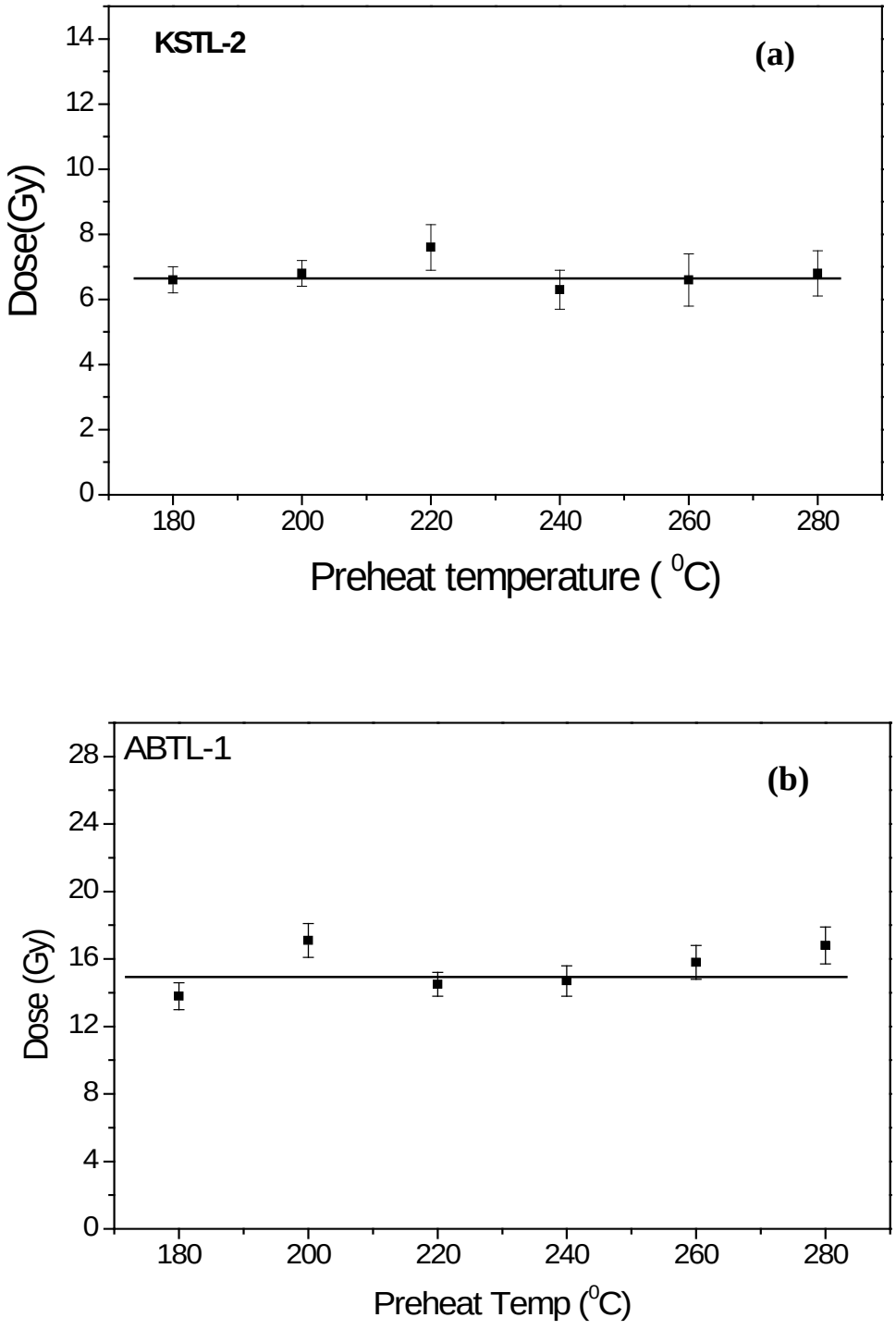

Figure 6.4: Preheat plateau test for samples (a) KSTL-2 and (b) ABTL-1

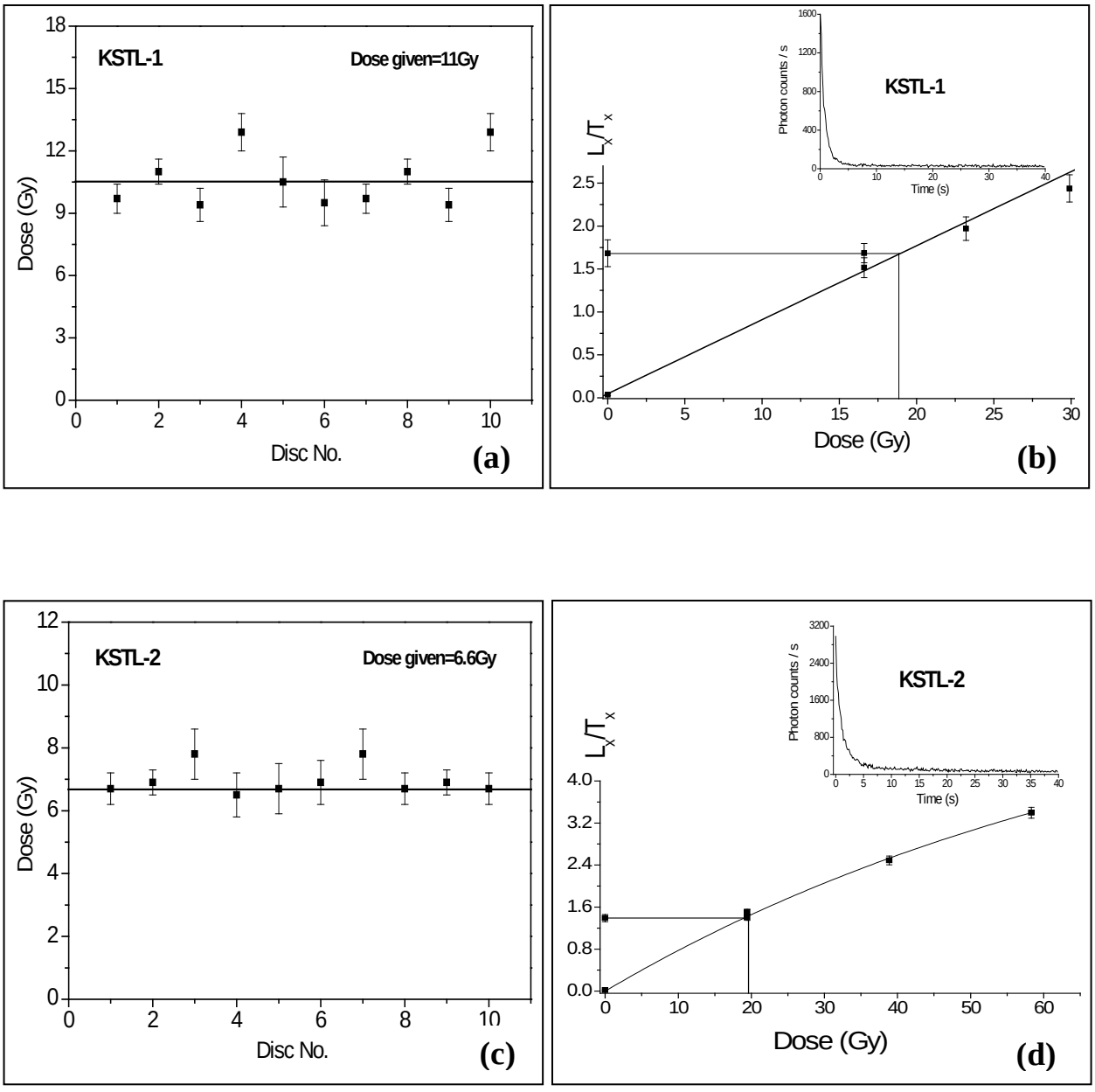

Figure 6.5: Dose Recovery test for 10 discs of sample (a) KSTL-1 and (c) KSTL-2, SAR Growth curve and Shine down curve for sample (b) KSTL-1 and (d) KSTL-2

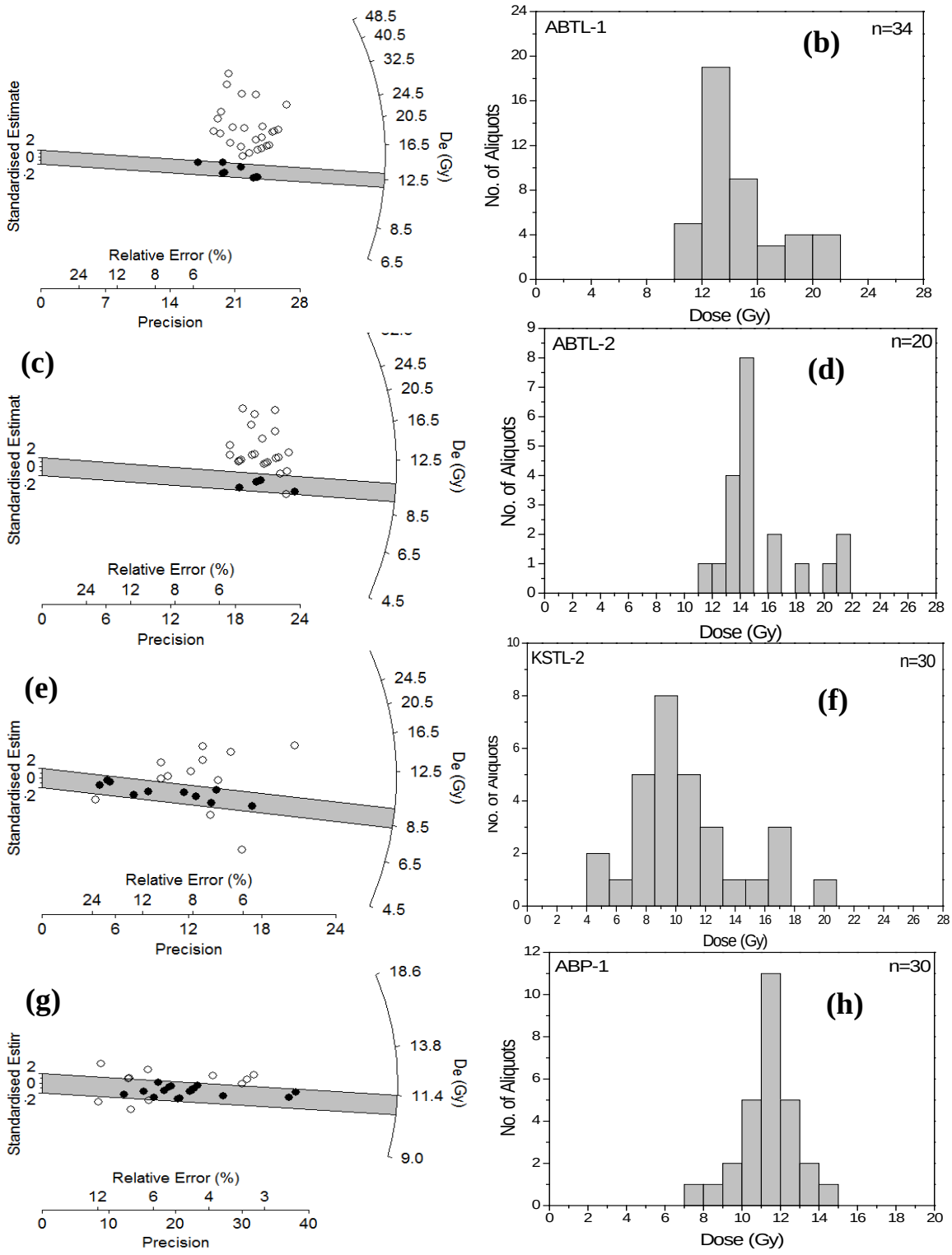

Figure 6.6: (a), (c), (e) and (g) shows radial plots for the samples ABTL-1, ABTL-2, KSTL-2 and ABP-1 and (b), (d), (f) and (h) showing the histograms of these samples. Total number of discs (n) shown on the upper right corner of the figures.

The ages obtained on Rann sediment ranged from 5.5 ± 1.0 to 1.0 ± 0.2 ka, whereas the Bet sediments were dated between 5.0 ± 0.5 and 3.0 ± 0.3 ka (Table 6.1, Figure 6.2). The pottery sample was dated to 3.0 ± 0.5 ka. The temporal changes in sedimentation rate were obtained for the Shakti Bet Rann sequence by linear interpolation between two dated depths viz. 233−133 cm (5.5 to 5 ka) and 133−50 cm (5 to 3 ka) (Fig. 5), which gives a decreasing rate from 2 to 0.4 mm/yr. Additionally, three samples were dated using the conventional radiocarbon method. These included a charcoal from the archaeological site and two shell samples, one each from the incised tidal flat terrace surface (~2 m above the Nara River bed) and one sample at 125 cm below the Nara River bed. The charcoal sample collected from 30 cm below the archaeological mound at Karim Shahi was radiocarbon dated to 3100 ± 350 cal yr BP. Within error, this age accords well with the OSL age of 3.0 ± 0.5 ka obtained on a pottery sample, suggesting that the site belongs to the late-Harappan period. The dead bivalve shells found in the living position on the river bank surface at 2 m were dated to 2220 ± 130 cal yr BP whereas the Turritella shells collected 125 cm below the present Nara River gave an age of 1420 ±1 30 cal yr BP (Figure 6.2, Nara River bank and Nara River bed).

6.5 Discussion

Field stratigraphy, sedimentology and optical dating of the shallow sedimentary sequences in the western Great Rann indicate that during the last 5.5 to 2 ka, the major part of the western Great Rann was under the influence of tidal flat sedimentation. Low energy fluvial sedimentation was limited to the north and north-eastern margins implying that compared to the tidal flat environment, fluvial activity was much more subdued during the last 5.5 ka. This negates the suggestion that Nara-Hakra Rivers were receiving waters from the Himalaya and were flowing through the Great Rann of Kachchh (Oldham, 1893; Stein, 1942; Ghose et al., 1979). The low-lying western Great Rann opens into the Arabian Sea through the macrotidal Kori Creek, which serves as a conduit for seawater to seasonally enter inland and flood the Great Rann of Kachchh during the monsoon (Roy and Merh, 1982; Inam et al., 2007; Prizomwala et al., 2010). Thus, in such a morphological setting, a marginally high sea level can inundate a large area. However, the sedimentological observations indicate marginal fluctuations in high sea level during 5.5 to 2 ka. This observation is in accordance with the suggestion of a high sea level in the western India during 6 and 2 ka (Chamyal et al.,

2003 and reference therein). There is no estimate on the height of this high sea level from the western Great Rann of Kuchchh during the mid-Holocene. However, studies carried out in the Little Rann (Gupta, 1975) and the Saurashtra coast of India (Juyal et al., 1995; Mathur et al., 2004; Gaur et al., 2006) suggested that relative to present, sea level was 2−4 m high during 6 and 2 ka. Considering the above, it is reasonable to assume that the western Great Rann was under the dominance of a marginally high sea between 5.5 and 2 ka.

The sediment distribution in the tidal flats is governed by the tidal current and wave energies. Near the level of low tide (lower part of the tidal flat), both current and wave energies are greater than the high tide area (Heineck, 1967). Dellwig et al. (2000) used the geochemical proxies, in particular the trace and heavy minerals, along with the grain size to ascertain the temporal changes in tidal current velocities The illite-dominated Indus River is the major source of suspended sediment, which is dispersed eastward towards the Gulf of Kachchh by the long shore-current (Rao and Rao, 1995; Prizomwala et al., 2010). The significant proportion of the sediments in western Great Rann was derived from the Indus River source which was transported into the tidal flat through the Kori Creek during marginally higher sea level (Glennie and Evans, 1976).

The western part of the Great Rann is known for experiencing earthquakes in the historical past (Burnes, 1835; Oldham, 1926; Rajendran and Rajendran, 2001; Rajendran et al., 2008). Thus, it is reasonable to consider the role of earthquakes in the evolution of the landforms. River course is one of the sensitive indicators of past earthquakes. For example, Rajendran et al. (1998), based on the presence of truncated dry channels and the absence of incipient drainage in the east of the Nara River bed, suggested the existence of a pre-1819 earthquake. According to Rajendran and Rajendran (2001), the Allah Bund represents a compound scarp formed by repetitive earthquakes. The above suggestion seems to be reasonable as discussed below. The bivalves (Bernea truncata and Mya sp.) dated to 2.2 ka were residing on a surface that was incised by the Nara River to a depth of ~ 2 m and below 1.25 m of the Nara River bed, where the Turritella shells are dated to 1.4 ka (Figure 6.2, Nara River bank). This implies that the Nara River occupied the present course (westward shift) after 2.2 ka and incised to a depth of 3 m before the channel aggradation began with tidal flat sedimentation.

The bivalves are filter feeders; Mya sp. makes deep burrows, while Bernea truncata is mechanical borer which prefers to colonize on the dewatered sediments/firm mud and live in

Table 6.1: Equivalent dose (De), Dose Rate and ages obtained on the western Great Rann sediments.

Sample No.	U (ppm)	Th (ppm)	K (%)	Cosmic Ray (μGy/a)	a value	De (Gy)	Dose rate Gy/ka	Age (ka)
ABP-2	3.6±0.7	10±2	2.4±0.1	205±20	-	8.7±0.4	3.8±0.3	2.0±0.2
ABP-1	4.0±1.0	10±4	1.6±0.1	200±20	-	10.3±0.2	3.1±0.4	3.3±0.4
ABTL-2	3.1±0.5	6 ±2	2.6±0.1	210±21	-	9.6±0.3	3.0±0.2	3.0±0.2
ABTL-1	3.5±0.6	8±2	2.6±0.1	194±19	-	11.7±0.2	3.3±0.2	4.0±0.2
KRM OSL-2	4.1±0.1	22±0.4	2.35±0.02	195±20		11.8±0.1	3.7±0.5	3.0±0.5
KRM OSL-1	2.7±0.05	12±0.2	1.84±0.02	214±21		10.7±0.1	2.4±0.4	4.5±1.0
KSTL-2	1.7±0.6	8±2	2.6±0.1	214±21	-	6.7±0.4	2.6±0.2	3.0±0.3
KSTL-1	1.6±0.6	8±2	1.9±0.1	195±20	-	11.0±0.4	2.2±0.2	5.0±0.5
SBTL-4	2.5±0.5	7±2	2.6±0.1	210±20	0.06	11.6±0.5	4.5±0.3	3.0±0.2
SBTL-3	2.4±0.5	5±2	2.0±0.1	198±20	-	9.4±0.8	2.0±0.3	5.0±1.0
SBTL-1	2.4±0.5	5±2	2.1±0.1	185±19	-	10.6±0.2	2.0±0.3	5.5±1.0
NRM OSL-1	4.3±0.04	19.6±0.2	1.87±0.01	205±20	-	3.1±0.1	2.9±0.4	1.0±0.2
NRM OSL-3	4.3±0.04	21.0±0.2	1.96±0.01	210±21	-	3.0±0.2	3.2±0.5	1.0±0.5
KS-ARCH	3.2±0.6	4±2	2.2±0.1	214±21	0.04	11.0±2.0	4.1±0.2	3.0±0.5

the subtidal zone (Desai and Patel, 2008). Considering this, it is logical to interpret the mortality of these bivalves in response to the withdrawal of the subtidal environment. The withdrawal of the sea after 2.2 ka could either be gradual due to the onset of regional aridity (climatically induced) in western, central and southern India (Kale, 1999; Thomas et al., 2007a; Roy et al., 2008), or abrupt due to the land-level change caused by an earthquake. At this stage, due to limited data, it is difficult to ascertain the relative contribution of either of the two factors in the withdrawal of subtidal environment from the western Great Rann.

However, the present study allow us to suggest that around 5.5 ka the low tide region was located around Shakti Bet and the high tide zone was further inland (towards east of Shakti Bet, Figure 6.7a). Based on this analogy, the decreased concentration of the trace elements and major element ratios and the dominance of clayey-silt during 5 and 3 ka can be interpreted as the westward shift in the high tide zone caused due to the relative lowering of sea level.

According to Rajendran and Rajendran (2001), the 90 km-long Allah Bund Fault Scarp (ABFS) is a compound scarp formed by more than one event, with a cumulative height of 5.3 m. Continued activity along the ABFS led to the westward migration of the Nara River. Abrupt lateral migrations of alluvial rivers in tectonically active areas are quite common (Schumm, 1986). This would imply that ABFS was in existence before the 1819 earthquake and probably prior to 2.2 ka. Until the subsurface topography is ascertained using detailed geophysical surveys, the antiquity of the ABFS as suggested in the present study (Figure 6.7c) remains preliminary and tentative. Historical evidence indicates existence of moderate fluvial activity in the Nara River until 1768 AD (Burnes, 1835). The northward tilting of the 1819 Allah Bund scarp created a natural a barrier for the river which had already lost its stream power due to the construction of dams in the upstream (Wynne, 1872). The 1819 Allah Bund earthquake of magnitude 7.5 not only uplifted the Rann sediment to variable height (3 to 6 m) to a distance of ~90 km (Rajendran and Rajendran, 2001), but also caused a coseismic subsidence of 1–5 m in the south which led to the creation of Sindri basin (Wynne, 1872; Oldham, 1926); Figure 6.7c). Based on the presence of abandoned channels, meander scrolls, shifting of stream courses, it has been estimated that around 15 km-wide zone lying north of the ABFS was affected by the 1819 earthquake (Rajendran and Rajendran, 2001). This earthquake led to the complete disruption of the Nara River channel which flowed into the Kori Creek and was used for navigation (Oldham, 1926). Thus, based on above it can be

suggested that the present day topography is an outcome of the 1819 earthquake (Figure 6.7c).

6.6 Conclusions

Sedimentation during 5.5 and 2 ka was dominated by a tidal flat environment implying a higher sea level than today. Fluvial sediment contribution in the western Great Rann sedimentation was limited, confined to the northern fringe of the study area. Thus, contrary to the earlier suggestions, our study did not find evidence for the existence of a major river draining through the western Great Rann during the last 5.5 ka. The geochemical characteristics of the Rann and Bet sediments suggest that the Indus River was a major contributor of sediment into the Western Great Rann which was largely routed through the Kori Creek. After around 2.2 ka and before 1.4 ka a combination of climate and tectonic activity probably led to the withdrawal of intertidal environment from the major part of the western Great Rann. The present-day landform and earth surface processes are largely modulated by the 1819 Allah Bund earthquake.

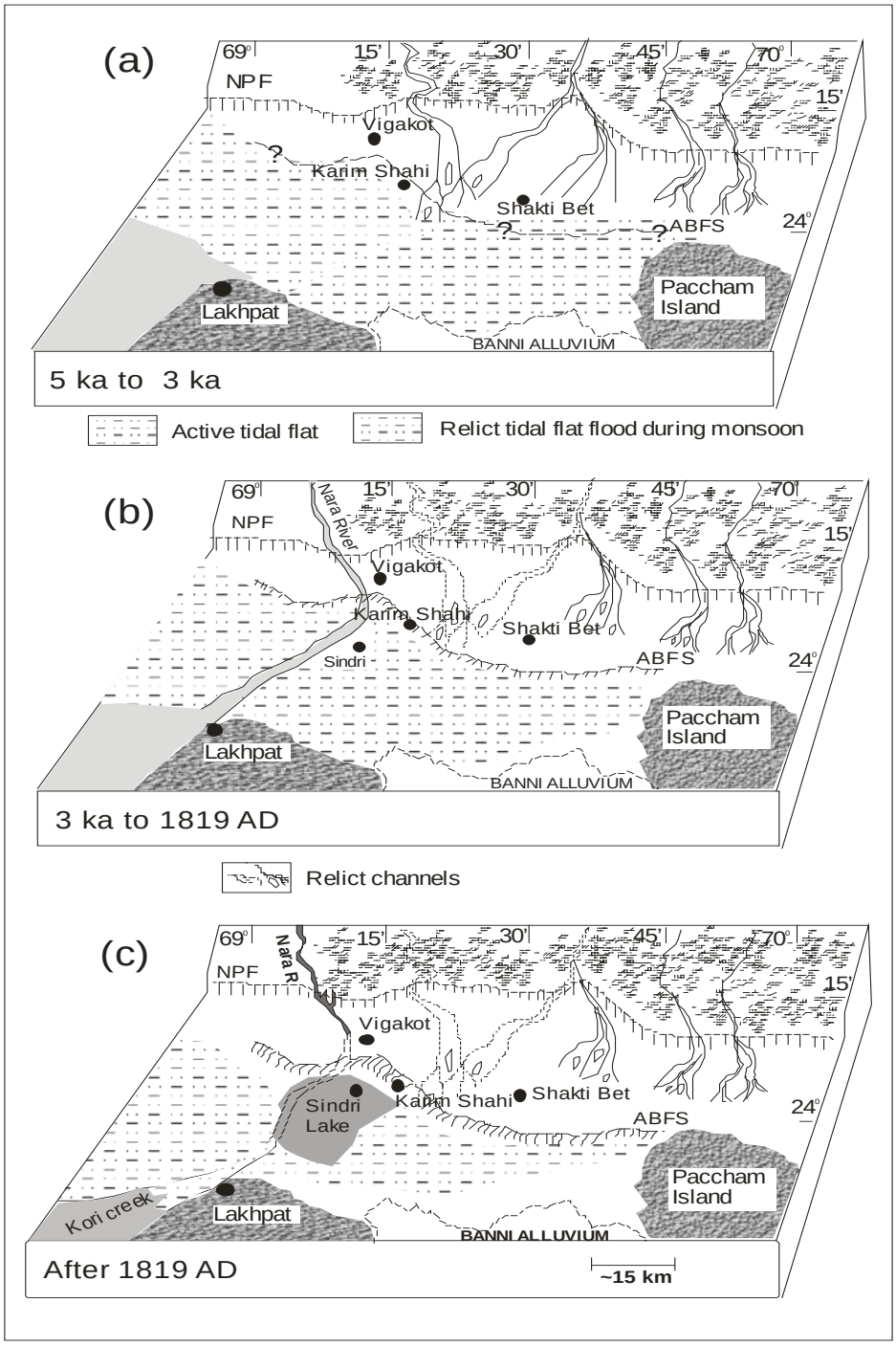

Figure 6.7: (a) Marginal lowering of the sea between 5 and 3 ka caused by low energy environment around Shakti Bet and the river activity was limited to the north-eastern fringes. Surface expression of the Allah Bund Fault Scarp (ABFS) may have appeared at this time. Human settlement probably also came around this period. (b) Fluvial system began to weaken along with withdrawal of marginally high sea; first major earthquake probably caused initiation of Allah Bund Fault during 2.2 and 1.4 ka. (c) Weakening of fluvial regime continued, development of Allah Bund scarp and submergence of Sindri after 1819 earthquake to achieve present land form.

Chapter 7

Conclusions and Future Outlook

7.1 Conclusions

This thesis examined the basic physics underlying the dating of seismic events using fault gouges, sand dikes, fault scarps, sediments of truncated river channels using luminescence dating. The general conclusions from this thesis are,

A. Luminescence dating of sand dikes

1. Calculation from first principles, suggest that during the formation of sand dike, under favourable conditions grain friction between the sediment grains injected as dikes can result in flash heating that is sufficient to erase the pre-existing luminescence at the time of injection and at the same time, the transient nature of flash heating enables a preservation of the pristine mineral composition without any thermally induced alteration. Some of the suitable conditions for such a flash

heating to occur are of kinematic viscosity of order m^2s^{-1}, minimum velocity of 30 ms^{-1} for narrow dike (~5 cm wide)

2. Luminescence studies on samples of dikes from Assam along Mora Krishna river and from Kakoti site indicated evidence of such a heating. Further experiments such as estimation of heating using predose sensitization of quartz, suggested the temperature rise at least up to 400 °C during the injection of dikes. These studies also enable dating of past earthquake during 111 years, 300 years, 500 years and 1 ka, and we anticipate a magnitude of M > 6 for Beltagat and nearby sites and M> 7 for Kakoti and Namgaon sites.

B. Luminescence Studies on Fault Gouges

1. In this case also, calculation from first principles enabled us to compute the heat generation during faulting and grain friction heating. Computation of heat conduction shows that under reasonable condition a slip of ~10 cm can result in finite heating of gouge material up to 350 °C and more, and this heat then conducts to the gouge matrix and in the process resets the luminescence of the grains constituting the gouge.

2. Studies on fault gouges from Gish fault led to evidence of heating in gouge material of about 300-350 °C. The luminescence dating of fault gouge samples suggested at least two tectonic events at ~ 2 ka and 3.5 ka.

All these sequences were a direct consequence of the seismic/tectonic events and the basic effort in the case of fault gouge and sand dikes was to validate the basic premises of the application of luminescence methodology in respect of the zeroing of luminescence signals at the time of faulting/sand dike formation. The other application was the use of standard luminescence dating procedures to an important area in western India viz. Allah Bund to reconstruct the paleoseismic history of the area.

The resetting of the luminescence signal in both cases i.e. sand dikes and fault gouge was tested by theoretical calculations and experimental methods. Based on the present study following inferences can be drawn

1. The resetting of the luminescence signal in the formation of sand dikes is possible due to viscous heating. The calculations made by using viscous heating model for sand dikes suggested that a temperature rise > 400 °C is possible.

2. The resetting of luminescence is more at the center of the dike as compared towards the edge. The temperature increase in narrow dike is higher as compared to the dike of larger width. Therefore it is suggested that the dikes of narrow width are chosen for sampling and samples from the dikes should be collected from the center of the dike.

3. The extent of heating in sand dikes was estimated experimentally based on the sensitivity of the dike samples and host samples. This suggested that the rise in temperature during the injection of the dike was 350−400 °C.

4. The samples for dating of paleoseismic events using sand dikes from North East India suggested tectonic events at 111 years, 300 years, 500 year and 1 ka. The earthquake of magnitude M >6 caused the injection of dikes in Beltaghat and nearby site areas, and M > 7 caused the injection of dikes in Kakoti and Namgaon sites.

5. The simulations made for the estimation of rise in temperature during the rupture events due to friction heating (transient heating) suggested that the temperature rise can be > 400 °C for faulting at a depth of 1 km. This temperature rise will result in the resetting of luminescence signal in fault gouge material.

6. The extent of temperature rise for fault gouge material was made by using predose method and suggested that the gouge material experienced a temperature of ~500 °C. The laboratory stress experiments on the quartz samples suggested that the transient shock events which also result in the crushing of quartz grains will also contribute to the lowering of the luminescence and higher stress may result into the full resetting on the luminescence signal.

7. The luminescence studies of fault gouge samples collected from the Sikkim−Darjeeling Himalaya suggested two earthquakes in the areas at around 2 ka and 3.5 ka.

8. Luminescence dating of samples from fault scarp, truncated channels and historical site in the proximity of Allah bund area in Great Rannn of Kuchchh suggest that the Allah bund scarp was created from at least two major earthquakes viz. the 1819 and between 2.5 and 1.4 ka respectively.

7.2 Future work

In present work while established the premises of dating of dikes and fault gouges, there is a need for further refinement, first by an extensive analysis of luminescence of fault gouges and sand dikes and their analysis in respect of the parameters such as host matrix and its physical characteristics, the slip in case of faulting, the depth of dike injection etc. Such a study will pave way or a more robust and routine application of luminescence methods for chronology. This is needed as in terms of sensitivity luminescence only provides a mean to date young historical events so that the methodology could be verified. Secondly luminescence parameters such as predose sensitization are also needed to provide additional constraints on heating and transient heating for fault gouge and sand dike respectively.

Theoretical calculations so far comprised several assumptions such as heat near the surface of the block, and away from the fault plane is zero, the velocity of the dike material during injection is less as compared to the center of the dike. For the estimation of temperature during the formation of sand dikes a linear flow of sand material is considered. However in nature the flow has to be decelerating and hence the heat generation should expectedly be nonlinear. Field observation suggests most of the sand dikes are of conical in shape (narrow at top and broad at bottom). Since the rise in temperature is affected by the width of the dike it is important to include this in the calculations. For this a detail mathematical model is needed, which takes into account the geometry of the dike and will help in considering the better position of samples for luminescence studies. In the present model we have considered the conservative value of kinematic viscosity; the model can be extended to include the effect of kinematic viscosity under confining pressure based on theoretical models for it.

Similarly for the estimation of rise in temperature we have not considered the second order effects which will also affect the temperature. For example as soon as the rupture on a fault plane takes place the dynamic frictional coefficient will change. This will have

significant effect and might cause lowering in the temperature as the recent measurement on the Great East Japan earthquake suggest a lower value of the frictional coefficient during the coseismic slip (Fulton et al., 2013; Ujiie et al., 2013). Also the effect of temperature due to the change in pore pressure as result of increase in temperature (coupling of the two as a feedback system) is not taken into account. The inclusion of this into the model will give better estimates of temperature rise during the rupture events.

The quartz can be used as a geothermometer based on the apparent age and temperature for different cooling rate (Li and Li, 2012). The detailed laboratory protocols need to be developed for this method which will be helpful in estimating the last cooling luminescence age for dikes and fault gouge samples.

In the present case dike samples from five different locations were studied to ascertain the resetting of luminescence signal. The North East area in India is seismically active and has experienced several earthquakes. However based on the sand dike studies we could identify four seismic events, and one of them was identified from the recent past (1905 earthquake). This indicated that the injection of dike was probably not there during other earthquakes, even these earthquakes were of higher magnitude M >7. This needs further investigations for the possible mechanism of the injection of the dikes in this area. Also the effect of multiple earthquakes on the resetting of luminescence in the dike material needs further experimental and theoretical work.

List of Publications

Papers in referred journal

1. **A.K. Tyagi**, A.D. Shukla, R. Bhushan, P.S. Thakker, M.G. Thakkar, N. Juyal, 2012. Mid-Holocene sedimentation and landscape evolution in the western Great Rann of Kachchh, India, Geomorphology v151–152, pp*89-98.*
2. **A. K. Tyagi**, Shipra Chaudhary, N. Rana, S. P. Sati and N. Juyal, 2009. Identifying areas of differential uplift using steepness index in the Alaknanda basin, Garhwal Himalaya, Uttarakhand, Current Science, v97(10), pp1473-1477.

Submitted

1. Rimpal Kar, Tapan Chakraborty, Chandan Chakraborty, Parthsarathi Ghosh, **Anil K. Tyagi** and Ashok K. Singhvi. Morpho-sedimentary characteristics of the Quaternary Matiali fan, Jalpaiguri, India: implications for tectonoclimatic controls, submitted to Geomorphology (under Review)

In preparation

1. Viscous heating as a possible Zeroing mechanism for OSL dating in sand dikes and results from North East India
2. Resetting of luminescence in fault gouges and luminescence dating of fault gouge from Sikkim Darjeeling Himalaya

Conference Abstracts

1. M. K. Murai, **A. K. Tyagi,** Y. C. Nagar, and A. K. Singhvi, 2006. Illumination and irradiation cross-talks in automated TL/OSL systems, APLD-2006, Hong Kong.
2. **A. K. Tyagi**, M. S. Gadhavi, P. S. Thakkar, N. Yuyal and A. K. Singhvi, 2008. Chronometry of Earthquakes Around Allah Bund, Great Rann of Kachchh, Western India, International Conference on “Terrestrial Planets: Evolution Through Time”, Gujarat (India).
3. **A. K. Tyagi**, M. Mukul and A. K. Singhvi, 2008. Luminescence Studies of Seismic Events, “ICLA-2008”, Delhi (India).
4. M. S. Gadhavi, **A.K. Tyagi**, J. N. Malik, K. Ansari, B. K. Rastogi, M. Morino, V. K. Gaur, N. Juyal, Roger Bilham, A.K. Singhvi and F. Kaneko, 2008. Palaeoseismic and Morpho-Tectonic Studies at Allah Bund in Great Rann of Kachchh, Western India, “AOGS conference 2008”, Busan (Korea).

5. **A. K. Tyagi**, M. S. Gadhavi, M. Mukul, N. Porat, N. Juyal and A. K. Singhvi, 2008. Palaeoseismic studies in India using luminescence, "Luminescence and Electrón Spin Resonance Dating conference 2008", Beijing (China).

Other Publications[2]

1. M. Himabindu, **A. K. Tyagi**, Devendra Sharma, Shishir P. Deshpande, Xavier Bonnin, 2014. Predictive 2-D SOL plasma transport modeling of Phase-I operations of tokamak SST-1 using SOLPS5, Physics of Plasmas Phys. 21(2), 022504

Conference Abstracts

1. **A.K. Tyagi**, Devendra Sharma, and Shishir Deshpande, 2012. First Implementation of 2-D Scrape-off Layer Plasma-Neutral Transport Simulation code SOLPS5.1 to a Double-Null Diverted Plasma-Magnetic Equilibrium, Plasma Science Society India Conference.
2. M. Himabindu, **A.K. Tyagi**, Ziauddin Khan, Devendra Sharma, and Shishir Deshpande, 2012. 2-D Predictive simulations of Scrape-off Layer Plasma Transport of Phase-1 Divertor Operations in Tokamak SST-1, Plasma Science Society India Conference.
3. Devendra Sharma, **A.K. Tyagi**, M. Himabindu, Shishir Deshpande and Xavier Bonnin, 2012. 2-D Scrape-off Layer Transport Modeling of First-Phase Divertor Operations in Tokamak SST-1 Using SOLPS5. Plasma Surface Interaction Conference.

[2] Not related to thesis work

References

Adamiec, G. and Aitken, M.J., 1998. Dose-rate conversion factors: update. Ancient TL, 16(2): 37-50.

Adamiec, G., Bluszcz, A., Bailey, R. and Garcia−Talavera, M., 2006. Finding model parameters: Genetic algorithms and the numerical modelling of quartz luminescence. Radiation Measurements, 41(7−8): 897−902.

Aitken, M.J., 1985. Thermoluminescence Dating. Academic Press, London, 359 pp.

Aitken, M.J. and Bowman, S.G.E., 1975. Thermoluminescent dating: assessment of alpha particle contribution. . Archaeometry, 17: 132−138.

Aitken, M.J., Bussell, G.D. and Drivver, H.S.T., 1979. Zero-glow monitoring (ZGM). Ancient TL, 6: 13-15.

Aitken, M.J., Tite, M.S. and Reid, J., 1964. Thermoluminescent dating of ancient ceramics. Nature, 202: 1032.

Aitken, M.J., Zimmerman, D.W. and Fleming, S.J., 1968. Thermoluminescent dating of ancient pottery. Nature, 219: 442.

Alizai, A., Carter, A., Clift, P.D., VanLaningham, S., Williams, J.C. and Kumar, R., 2011. Sediment provenance, reworking and transport processes in the Indus River by U–Pb dating of detrital zircon grains. Global and Planetary Change, 76: 33−55.

Allen, J.R.L., 1986. Earthquake magnitude−frequency, epicentral distance, and soft−sediment deformation in sedimentary basins. Sedimentary Geology, 46(1–2): 67−75.

Amit, R., Harrison, J.B.J., Enzel, Y. and Porat, N., 1996. Soils as a tool for estimating ages of Quaternary fault scarps in a hyperarid environment − the southern Arava valley, the Deat Sea Rift, Israel. Catena, 28: 21−45.

Andrews, D.J. and Bucknam, R.C., 1987. Fitting degradation of shoreline scarps by a nonlinear diffusion model. Journal of Geophysical Research, 92: 12857–12867.

Ariyama, T., 1985. Conditions of resetting the ESR clock during faulting. In: M. Ikeya and T. Miki (Editors), ESR dating and dosimetry. IONICS Publishing Co Limited, Tokyo, pp. 249−256.

Arrowsmith, J.R., Rhodes, D.D. and Pollard, D.D., 1998. Morphologic dating of scarps formed by repeated slip events along the San Andreas Fault, Carrizo Plain, California. Journal of Geophysical Research: Solid Earth, 103(B5): 10141−10160.

Aspler, L.B. and Donaldson, J.A., 1985. Penecontemporaneous sandstonedykes, Nonacho Basin (Early Proterozoic, Northwest Territories):Horizontal injection in vertical, tabular fissures. Canadian Journal of Earth Sciences, 23: 827-838.

Atkinson, G., 1984. Simple computation of liquefaction probability for seismic hazard applications. Earthquake Spectra, 1: 107−123.

Bailey, R.M., Smith, B.W. and Rhodes, E.J., 1997. Partial bleaching and the decay form characteristics of quartz OSL. Radiation Measurements, 27(2): 123−136.

Bailiff, I.K., 1994. The pre−dose technique. Radiation Measurements, 23(2–3): 471−479.

Banerjee, D., 1996. New Applications of Thermoluminescence, Gujarat University, 203 pp.

Banerjee, D., Singhvi, A.K., Pande, K., Gogte, V.D. and Chandra, B.P., 1999. Towards a direct dating of fault gouges using luminescence dating techniques−Methodological aspects. Current Science, 77(2): 256−268.

Berger, R. and Kaufman, S.T., 1980. Radiocarbon dating of earthquakes. Radiocarbon, 22(3): 746−756.

Bilham, R., Gaur, V.K. and Molnar, P., 2001. Himalayan seismic hazard. Indian Concrete Journal, 75(10): 615−618.

Birkeland, P.W., 1984. Soils and Geomorphology. Oxford University Press, 372 pp.

BIS, 2002. Indian Standard Criteria for Earthquake Resistant Design of Structure, Resistant Provisions and Buildings. Bureau of Indian Standards, New Delhi.

Biswas, S.K., 1987. Regional tectonics framework, structure and evolution of the western marginal basins of India. Tectonophysics, 135: 307−327.

Bluszcz, A. and Adamiec, G., 2006. Application of differential evolution to fitting OSL decay curves. Radiation Measurements, 41(7−8): 886−891.

Bortolot, V.J., 2000. New modular high capacity OSL reader system. Radiation Measurements, 32(5): 751−757.

Bortolot, V.J., Simon, N. and Siverstone, S.M., 1973. The thermoluminescence dosimetry in medicine and archeology. Bulletin of the New York Academy of Medicine, 49: 847−857.

Bøtter-Jensen, L., Andersen, C.E., Duller, G.A.T. and Murray, A.S., 2003. Developments in radiation, stimulation and observation facilities in luminescence measurements. Radiation Measurements, 37(4-5): 535-541.

Bøtter−Jensen, L., Andersen, C.E., Duller, G.A.T. and Murray, A.S., 2003a. Developments in radiation, stimulation and observation facilities in luminescence measurements. Radiation Measurements, 37(4−5): 535−541.

Bøtter−Jensen, L., Bulur, E., Duller, G.A.T. and Murray, A.S., 2000. Advances in luminescence instrument systems. Radiation Measurements, 32: 523−528.

Bøtter−Jensen, L., McKeever, S.W.S. and Wintle, A.G., 2003b. Optically Stimulated Luminescence. Elsevier Science B.V., Netherlands.

Bøtter−Jensen, L., McKeever, S.W.S. and Wintle, A.G., 2003c. Optically stimulated luminescence dosimetry. Elsevier Science: Amsterdam, Netherlands, 374 pp.

Bowman, S.G.E. and Huntley, D.J., 1984. A new proposal for the expression of alpha efficiency in TL dating. Ancient TL, 2(1): 6−8.

Bucknam, R.C. and Anderson, R.E., 1979. Estimation of fault-scarp ages from a scarp-height-slope angle relationship. Geology, 7: 11-14.

Buhay, W.M., Schwarcz, H.P. and Grün, R., 1988. ESR dating of fault gouge: The effect of grain size. Quaternary Science Reviews, 7(3–4): 515−522.

Bull, W.B., 1996. Dating San Andreas fault earthquakes with lichenometry. Geology, 24: 111−114.

Bungenstock, F. and Schäfer, A., 2009. The Holocene relative sea−level curve for the tidal basin of the barrier Langeoog, German Bight, Southern North Sea. Global and Planetary Change, 66(34−51).

Burbank, D.W. and Anderson, R.S., 2009. Tectonic geomorphology. Wiley. com.

Burg, J.P. and Gerya, T.V., 2005. The role of viscous heating in Barrovian metamorphism of collisional orogens: thermomechanical models and application to the Lepontine Dome in the Central Alps. Journal of Metamorphic Geology, 23(2): 75−95.

Burnes, A., 1835. A memoir on the eastern Branch of the river Indus giving an account of the alterations produced by it by an earthquake in 1819, also a theory of the Runn, and some conjectures on the route of Alexander the Great, drawn up in the years 1827−28. Royal Asiatic Society, 3: 550−588.

Buylaert, J.P., Jain, M., Murray, A.S., Thomsen, K.J., Thiel, C. and Sohbati, R., 2012. A robust feldspar luminescence dating method for Middle and Late Pleistocene sediments. Boreas, 41(3): 435−451.

Buylaert, J.P., Murray, A.S., Thomsen, K.J. and Jain, M., 2009. Testing the potential of an elevated temperature IRSL signal from K−feldspar. Radiation Measurements, 44(5−6): 560−565.

Caggianelli, A., de Lorenzo, S. and Prosser, G., 2005. Modelling the heat pulses generated on a fault plane during coseismic slip: Inferences from the pseudotachylites of the Copanello cliffs (Calabria, Italy). Tectonophysics, 405(1−4): 99−119.

Carslaw, H.S. and Jaeger, J.C., 1959. Conduction of Heat in Solids Clarendon Press, Oxford.

Castilla, R. and Audemard, F., 2007. Sand blows as a potential tool for magnitude estimation of pre−instrumental earthquakes. Journal of Seismology, 11(4): 473−487.

Chakrabarti, A., 2005. Sedimentary structures of tidal flats: A journey from coast to inner estuarine region of eastern India. Journal of Earth System Science, 114: 353−368.

Chamyal, L.S., Maurya, D.M. and R., R., 2003. Fluvial system of the dry lands of western India: a synthesis of Late Quaternary environmental and tectonic changes. Quaternary International, 104: 69−86.

Chandel, H.N., Patel, A.D., Vaghela, H.R. and Ubale, G.P., 2006. An effective and reusable sampling pipe for luminescence dating. Ancient TL, 24(1): 21−22.

Chauhan, N. and Singhvi, A., 2011. Distribution in SAR palaeodoses due to spatial heterogeniety of natural beta dose. Geochronometria, 38(3): 190−198.

Chauhan, O.S., 1994. Influence of macrotidal environment on self sedimentation, Gulf of Kachchh, India. Continental Shelf Research, 14: 1477−1493.

Chen, R., 1979. Saturation of sensitization of the 110 °C TL peak in quartz and its potential application in the pre−dose technique. European PACT J, 3: 325–335.

Chen, R. and Leung, P.L., 1999. Modeling the pre−dose e:ect in thermoluminescence. Radiation Protection Dosimetry, 84: 43–46.

Chen, R. and McKeever, S.W.S., 1997. Theory of Thermoluminescence and Related Phenomena. World Scientific Publishing Company, Singapore, 559 pp.

Chowksey, V., Maurya, D.M., Khonde, N. and Chamyal, L.S., 2010. Tectonic geomorphology and evidence for active tilting of the Bela, Khadir and Bhanjada islands in the seismically active Kachchh palaeorift graben, Western India. Zeitschrift für Geomorphologie, 54: 467– 490.

Christiansen, C., Gunnild VølundLund−Hansen, L.C. and Bartholdy, J., 2006. Wind influence on tidal flat sediment dynamics: Field investigations in the Ho Bugt, Danish Wadden Sea. Marine Geology, 235: 75–8.

Cosgrove, J.W., 2001. Hydraulic fracturing during the formation and deformation of a basin: a factor in the dewatering of low−permeability sediments. AAPG Bulletin, 85(4): 737−748.

Council, I.C., 2009. International Building Code, Earthquake Loads, USA.

Craig, H., 1953. The geochemistry of the stable carbon isotopes. Geochemica et Cosmocheimica Acta, 4(53−92).

Craig, H., 1957. Isotope standards for carbon and oxygen and correction factors for mass−spectrometic analysis of cargon dioxide. Geochemica et Cosmocheimica Acta, 12: 133−149.

Crone, A.J., 1987. Introduction to Directions in Paleoseismology, U.S. Geological Survey

David, M. and Sunta, C.M., 1981. Thremoluminescence of Quartz − Part VIII : Estimation of Firing Temperature in Ancient Pottery Samples. Indian Journal of Pure and Applied Physics, 19: 1054−1056.

De Lorenzo, S., Zollo, A. and Mongelli, F., 2001. Source parameters and three−dimensional attenuation structure from the inversion of microearthquake pulse width data: Qp imaging and inferences on the thermal state of the Campi Flegrei caldera (southern Italy). Journal of Geophysical Research B: Solid Earth, 106(B8): 16265−16286.

Delbecq, C.J., Toyozawa, Y. and Yuster, P.H., 1974. Tunneling recombination of trapped electrons and holes in KCl:AgCl and KCl:TlCl. Physical Review B, 9(10): 4497−4505.

Dellwig, O., Hinrichs, J., Hild, A. and Brumsack, H.J., 2000. Changing sedimentation in tidal flat sediments of the southern North Sea from Holocene to the present: a geochemical approach. Journal of Sea Research, 44: 195−208.

Desai, B.G. and Patel, S.J., 2008. Trace fossil assemblages (Ichnocoenoses) of the tectonically uplifted Holocene shorelines, Kachchh, Western India. Journal geological Society of India, 71: 527−540.

Dewey, J.F. and Bird, J.M., 1970. Mountain belts and the new global tectonics. Journal of Geophysical Research, 75(14): 2625−2647.

Eddingsaas, N.C. and Suslick, K.S., 2006. Light from sonication of crystal slurries. Nature, 444: 163.

England, P.C. and Thompson, A.B., 1984. Pressure—Temperature—Time Paths of Regional Metamorphism I. Heat Transfer during the Evolution of Regions of Thickened Continental Crust. Journal of Petrology, 25(4): 894−928.

Enzel, Y., Amit, R., Porat, N. and Zilberman, E., 1996. Estimating the ages of fault scarps in the Arava, Israel. Tectonophysics, 253: 305−317.

Fantong, E.B., Takeuchi, A. and Doke, R., 2013. Electron Spin Resonance (ESR) Dating of Calcareous Fault Gouge of the Ushikubi Fault, Central Japan. Applied Magnetic Resonance, 44: 1105−1123.

Fattahi, M., Walker, R., Hollingsworth, J., Bahroudi, A., Nazari, H., Talebian, M., Armitage, S. and Stokes, S., 2006. Holocene slip−rate on the Sabzevar thrust fault, NE Iran, determined using

optically stimulated luminescence (OSL). Earth and Planetary Science Letters, 245(3–4): 673−684.

Felix, C. and Singhvi, A.K., 1997. Study of non−linear luminescence−dose growth curves for the estimation of paleodose in luminescence dating: results of Monte Carlo simulations. Radiation Measurements, 27(4): 599−609.

Fleming, S.J., 1970. Thermoluminescence dating: refinement of the quartz inclusion method. Archaeometry, 12: 133−147.

Fleming, S.J., 1979. Thermoluminescence techniques in archaeology. The Clarendon Press, London.

Flotté, N., Plagnes, V., Sorel, D. and Benedicto, A., 2001. Attempt to date Pleistocene normal faults of the Corinth−Patras Rift (Greece) by U/Th Method, and tectonic implications. Geophysical Research Letters, 28(19): 3769−3772.

Forman, S.L., Jackson, M.E., McCalpin, J. and Maat, P., 1988. The potential of using thermoluminescence to date buried soils developed on colluvial and fluvial sediments from Utah and Colorado, U.S.A.: Preliminary results. Quaternary Science Reviews, 7(3–4): 287−293.

Forman, S.L., Machette, M.N., Jackson, M.E. and Maat, P., 1989. An evaluation of thermoluminescence dating of paleoearthquakes on the American Fork segment, Wasatch fault zone, Utah. Journal of Geophysical Research: Solid Earth, 94(B2): 1622−1630.

Forman, S.L., Nelson, A.R. and McCalpin, J.P., 1991. Thermoluminescence dating of fault−scarp−derived colluvium: Deciphering the timing of paleoearthquakes on the Weber Segment of the Wasatch Fault Zone, north central Utah. Journal of Geophysical Research: Solid Earth, 96(B1): 595−605.

Franklin, A.D., Prescott, J.R. and Scholefield, R.B., 1995. The mechanism of thermoluminescence in an Australian sedimentary quartz. Journal of Luminescence, 63(5–6): 317−326.

Freund, L.B., 1998. Dynamic Fracture Mechanics. Cambridge University Press, Cambridge, 581 pp.

Fujii, N. and Uyeda, S., 1974. Thermal instabilities during flow of magma in volcanic conduits. Journal of Geophysical Research, 79(23): 3367−3369.

Fukuchi, T., 1989. Theoretical study on frictional heat by faulting using ESR. Applied Radiation and Isotopes, 40(10−12): 1181−1193.

Fukuchi, T., 1992. ESR studies for absolute dating of fault movements. Journal − Geological Society (London), 149(2): 265−272.

Fukuchi, T. and Imai, N., 1998. Resetting experiment of E' centres by natural faulting−The case of the Nojima Earthquake Fault in Japan. Quaternary Science Reviews, 17(11): 1063−1068.

Fukuchi, T., Imai, N. and Shimokawa, K., 1985. Dating of the fault movement by various ESR signals in Quartz−Cases of the faults in the South Fossa Magna, Jpan. In: M. Ikeya and T. Miki (Editors), ESR dating and dosimetry. IONICS Publishing Co Limited, Tokyo.

Fukuchi, T., Imai, N. and Shimokawa, K., 1986. ESR dating of fault movement using various defect centres in quartz; the case in the western South Fossa Magna, Japan. Earth and Planetary Science Letters, 78(1): 121−128.

Fulton, P.M., Brodsky, E.E., Kano, Y., Mori, J., Chester, F., Ishikawa, T., Harris, R.N., Lin, W., Eguchi, N., Toczko, S., Expedition 343, T. and Scientists, K., 2013. Low Coseismic Friction on the Tohoku−Oki Fault Determined from Temperature Measurements. Science, 342(6163): 1214−1217.

Galbraith, R.F., 1988. Graphical Display of Estimates Having Differing Standard Errors. Technometrics, 30(3): 271−281.

Galbraith, R.F., 1990. Radial plots: graphical assessment of spread in ages. Nuclear Tracks and Radiation Measurements, 17(3): 207−214.

Galli, P., 2000. New empirical relationships between magnitude and distance for liquefaction. Tectonophysics, 324: 169–187.

Garlick, G.F.J. and Gibson, A.F., 1948. The electron trap mechanism of luminescence in sulphide and silicate phosphors. Proceedings of Physics society, 60: 574.

Gaur, A.S., Vora, K.H. and Sundares., 2006. Shoreline changes during the last 2000 years on the Saurashtra coast of India: study based on archaeological evidences. Current Science, 92: 103−110.

Ghose, B., Kar, A. and Husain, Z., 1979. The lost courses of the Saraswati River in the Great Indian Desert: New evidence from Landstat imagery. The Geographical Journal, 145: 446−451.

Glennie, K.W. and Evans, G., 1976. A reconnaissance of the Recent sediments of the Ranns of Kutch, India. Sedimentology, 23: 625−647.

Graham, C.M. and England, P.C., 1976. Thermal regimes and regional metamorphism in the vicinity of overthrust faults: an example of shear heating and inverted metamorphic zonation from southern California. Earth and Planetary Science Letters, 31(1): 142−152.

Grun, R., 2006. Direct dating of human fossils, Year book of physical anthropology. Wiley Inter Science, pp. 2-48.

Grun, R. and Invernati, C., 1985. Uranium accumulation in teeth and its effect on ESR dating-a detailed study of a mammoth tooth. Nuclear Tracks, 10: 869-878.

Gundu Rao, T.K., Rajendran, C.P., Mathew, G. and John, B., 2002. Electron spin resonance dating of fault gouge from Desamangalam, Kerala: Evidence for Quaternary movement in Palghat gap shear zone. Proceedings of the Indian Academy of Sciences (Earth and Planetary Sciences), 111(2): 103−113.

Gupta, S., 1997. Himalayan drainage patterns and the origin of fluvial megafans in the Ganges foreland basin. Geology, 25: 11−14.

Gupta, S.K., 1975. Silting of the Rann of Kutch during Holocene. Indian Journal of Earth Sciences, 2: 163−175.

Hanks, T.C., Bucknam, R.C., Lajoie, K.R. and Wallace, R.E., 1984. Modification of wave−cut and faulting−controlled landforms. Journal of Geophysical Research, 89: 5771–5790.

Haskell, E.H., Wrenn, M.E. and Sutton, S.R., 1980. Predose analysis of brick samples: Feasibility for fallout dosimetry. Ancient TL, 12: 9−13.

Heineck, H.E., 1967. Layered sediments of Tidal flats, beaches and shelf bottom of the North Sea. . In: H.L. George (Editor), Estuaries. American Association for the Advancement of Science, Washington DC, pp. 191−206

Huntley, D.J., 2006. An explanation of the power−law decay of luminescence. Journal of Physics Condensed Matter, 18(4): 1359−1365.

Huntley, D.J., Godfrey−Smith, D.I. and Haskell, E.H., 1991. Light−induced emission spectra from some quartz and feldspars. Nuclear Tracks and Radiation Measurements, 18(1−2): 127−131.

Huntley, D.J. and Lamothe, M., 2001. Ubiquity of anomalous fading in K−feldspars and the measurement and correction for it in optical dating. Canadian Journal of Earth Sciences, 38(7): 1093−1106.

Huntley, D.J., Short, M.A. and Dunphy, K., 1996. Deep traps in quartz and their use for optical dating. Canadian Journal of Physics, 74(3-4): 81-91.

Hütt, G., Jaek, I. and Tchonka, J., 1988. Optical dating: K−feldspars optical response stimulation spectra, . Quaternary Science Reviews, 7: 381−385.

Ichikawa, Y., 1965. Dating of ancient ceramics by thermoluminescence. Bulletin of Institute of Chemical Research, Kyoto University, 43: 1−6.

Ikeya, M., 1993. New application of electron spin resonance dating, dosimetry and microscopy. World Scientific Publishing Co. Pvt. Ltd., London.

Ikeya, M., Tani, A. and Yamanaka, C., 1995. Electron spin resonance isochrone dating of fracture age: grain size dependence for fault gouge Japanese journal of Applied Physics, 34: 334−337.

Ikeya, M., Toshikatsu, M. and Kazuhiro, T., 1982. Dating of a Fault by Electron Spin Resonance on Intrafault Materials Science, 215(4538): 1392−1393.

Inam, I., Clift, P.D., Giosan, L., Tabrez, A.R., Tahir, M., Rabbani, M.M. and Danish, M., 2007. The Geographic, Geological and Oceanographic Setting of the Indus River. In: A. Gupta (Editor), Large Rivers, Geomorphology and Management. John Wiley & Sons, Ltd., London, pp. 333−346.

Ivanovich, M. and Harmon, R.D., 1992. Uranium− series Disequilibrium: Applications to Earth, Marine, and Environmental Sciences. Oxford University Press, Oxford, 911 pp.

Ivanovich, M., Vita−Finzi, C. and Hennig, G.J., 1983. Uranium−series dating of molluscs from uplifted Holocene beaches in the Persian Gulf. Nature, 302(5907): 408−410.

Jain, M. and Ankjærgaard, C., 2011. Towards a non−fading signal in feldspar: Insight into charge transport and tunnelling from time−resolved optically stimulated luminescence. Radiation Measurements, 46(3): 292−309.

Jain, M., L., B.J. and Singhvi, A.K., 2003. Dose evaluation using multiple−aliquot quartz OSL: Test of methods and a new protocol for improved accuracy and precision. Radiation Measurements, 37(1): 67−80.

Jolly, R.J.H. and Lonergan, L., 2002. Mechanisms and controls on formation of sand intrusions. Journal of Geologiccal Society, London, 159: 605−617.

Jungner, H. and Huntley, D.J., 1991. Emission spectra of some potassium feldspars under 633 nm stimulation. Nuclear Tracks and Radiation Measurements, 18(1−2): 125−126.

Juyal, N., Pant, R.K., Bhushan, R. and Somayajulu, B.L.K., 1995. Radiometric dating of Late Quaternary sea levels of Saurashtra coast, Western India: an experiment with Oysters and Clamshell. Geological Society of India Memoirs, 32: 372−379.

Juyal, N., Raj, R., Maurya, D.M., Chamyal, L.S. and Singhvi, A.K., 2000. Chronology of late Pleistocene environmental changes in the lower Mahi basin, western India. Journal of Quaternary Science, 15(5): 501−508.

Kagan, E.J., Agnon, A., Bar−Matthews, M. and Ayalon, A., 2005. Dating large infrequent earthquakes by damaged cave deposits. Geology, 33(4): 261−264.

Kale, V.S., 1999. Late Holocene temporal patterns of palaeofloods in central and western India. Man and Environment, 24: 109−115.

Kanaori, Y., 1983. Fracturing mode analysis and relative age dating faults by surface textures of quartz grains from fault gouges. Engineering Geology, 19: 261−281.

Kanaori, Y., Miyakoshi, K., Kakuta, T. and Satake, Y., 1978. Surface Texture of quartz grains in intrafault materials.

Kawamura, J., Hattori, K. and Akagi, H., 2002. Experimental evaluation of viscid properties of liquefied sand, Proceedings of the Eighth US−Japan Workshop on Earthquake Resistant Design of Lifeline Facilities and Countermeasures Against Liquefaction, pp. 405−412.

Kitis, G., Kiyak, N., Polymeris, G.S. and Tsirliganis, N.C., 2010. The correlation of fast OSL component with the TL peak at in quartz of various origins. Journal of Luminescence, 130(2): 298−303.

Kitis, G., Liritzis, I. and Vafeiadou, A., 2002. Deconvolution of optical stimulated luminescence decay curves. Journal of Radioanalytical and Nuclear Chemistry, 254(1): 143−149.

Kitis, G., Pagonis, V., Chen, R. and Polymeris, G., 2006. A comprehensive comparative study of the predose effect for three quartz crystals of different origin. Radiation Protection Dosimetry, 119(1−4): 438−441.

Koul, D. and Chougaonkar, M., 2011. An attempt to estimate firing temperature using OSL pre−dose sensitization of quartz. Geochronometria, 38(3): 217−222.

Koul, D.K., 2008. 110 °C thermoluminescence glow peak of quartz − A brief review. Pramana − Journal of Physics, 71(6): 1209−1229.

Koul, D.K., Polymeris, G.S., Tsirliganis, N.C. and Kitis, G., 2010. Possibility of pure thermal sensitization in the pre−dose mechanism of the 110 °C TL peak of quartz. Nuclear Instruments and Methods in Physics Research, Section B: Beam Interactions with Materials and Atoms, 268(5): 493−498.

Krbetschek, M.R., Gotze, J., Dietrich, A. and Trautmann, T., 1997. Spectral information from minerals relevant for luminescence dating. Radiation Measurements, 27(5−6): 695−748.

Krögel, F. and Flemming, B.W., 1998. Evidence for temperature adjusted sediment distributions in the back−barrier tidal flats of the East Frisian Wadden Sea (southern North Sea). In: C.R. Alexander, R.A. Davis and V.J. Henry (Editors), Tidalites: Processes and products SEPM Special Publication. National Academy Press, Washington DC, pp. 31–41.

Lachenbruch, A.H., 1980. Frictional heating, fluid pressure, and the resistance to fault motion. Journal of Geophysical Research, 85(B11): 6097−6112.

lal, D. and Arnold, J.R., 1985. Tracing quartz through the environment. Proceedings of Indian Academy of Science: Earth and Planetory Science Letters, 94: 1−5.

Lamothe, M. and Auclair, M., 1999. A solution to anomalous fading and age shortfalls in optical dating of feldspar minerals. Earth and Planetary Science Letters, 171(3): 319−323.

Le Hir, P., Roberts, W., Cazaillet, O., Christie, M., Bassoullet, P. and Bacher, C., 2000. Characterization of intertidal flat hydrodynamics Continental Shelf Research, 20: 1433–1459.

Lee, H.K. and Schwarcz, H.P., 1994. Criteria for complete zeroing of ESR signals during faulting of the San Gabriel fault zone, southern California. Tectonophysics, 235(4): 317−337.

Levi, T., Weinberger, R., Eyal, Y., Lyakhovsky, V. and Heifetz, E., 2008. Velocities and driving pressures of clay−rich sediments injected into clastic dykes during earthquakes. Geophysical Journal International, 175: 1095−1107.

Levy, P.W., 1974. Physical Principles of Thermoluminescence and Recent developments in measurments, International seminar on applications of science to dating of works of art. Brookhaven National Lab., Upton, N.Y., Boston, Massachusetts.

Li, B. and Li, S.H., 2006. Comparison of De estimates using the fast component and the medium component of quartz OSL. Radiation Measurements, 41: 125−136.

Li, B. and Li, S.H., 2008. Investigations of the dose−dependent anomalous fading rate of feldspar from sediments. Journal of Physics D: Applied Physics, 41(22).

Lorenz, J.C., Teufel, L.W. and Warpinski, N.R., 1991. Regional fractures 1: A mechanism for the formation of regional fractures at depth in flat−lying reservoirs. AAPG Bulletin, 75: 1714–1737.

Lyons, J.B. and Jonathan, S., 1971. Dating Faults. Geological Society of America Bulletin, 82(6): 1749−1752.

Mahan, S.A. and Crone, A.J., 2008. Luminescence dating of paleoliquefaction features in the Wabash River valley area of Indiana. Geological Society of America Abstracts with Programs, 40(5): 78.

Mathew, G., Gundu Rao, T.K., Sohoni, P.S. and Karanth, R.V., 2004. ESR dating of intrafault gypsum from Katrol hill range, Kachchh, Gujarat: Implications for neotectonism. Current Science, 87(9): 1269−1274.

Mathur, U.B., Pandey, D.K. and Bahadur, T., 2004. Falling late Holocene sea−level along Indian coast. Current Science, 87: 439−440.

Mattson, A. and Bruhn, R.L., 2001. Fault slip rates and initiation age based on diffusion equation modeling: Wasatch Fault Zone and eastern Great Basin. Journal of Geophysical Research: Solid Earth, 106(B7): 13739−13750.

Maurya, D.M., Goyal, B., Patidar, A.K., Mulchandani, N., Thakkar, M.G. and Chamyal, L.S., 2006. Ground Penetrating Radar imaging of two large sand blow craters related to the 2001 Bhuj earthquake, Kachchh, Western India. Journal of Applied Geophysics, 60: 142–152.

Maurya, D.M., Thakkar, M.G., Patidar, A.K., Bhandari, S., Goyal, B. and Chamyal, L.S., 2008. Late Quaternary geomorphic evolution of the coastal zone of Kachchh, Western India. Journal of Coastal Research, 24: 746−758.

Mayer, L., 1984. Dating Quaternary fault scarps formed in alluvium using morphologic parameters. Quaternary Research, 22(3): 300−313.

Mayya, Y.S., Morthekai, P., Murari, M.K. and Singhvi, A.K., 2006. Towards quantifying beta microdosimetric effects in single−grain quartz dose distribution. Radiation Measurements, 41(7−8): 1032−1039.

McCalpin, J. and Forman, S.L., 1991. Late Quaternary faulting and thermoluminescence dating of the East Cache fault zone, north−central Utah. Bulletin of the Seismological Society of America, 81(1): 139−161.

McCalpin, J.P., 1996. Paleoseismology. International Geophysical Series, 62. Academic Press, San Diego.

McCalpin, J.P. and Berry, M.E., 1996. Soil catenas to estimate ages of movements on normal fault scarps, with an example from the Wasatch fault zone, Utah, USA. CATENA, 27(3–4): 265−286.

McKeever, J., 1985. Thermoluminescence of Solids. Cambridge university press, London.

McKeever, S.W.S. and Chen, R., 1997. Luminescence models. Radiation Measurements, 27(5−6): 625−661.

McKenzie, D. and Brune, J.N., 1972. Melting on Fault Planes During Large Earthquakes. Geophysical Journal International, 29(1): 65−78.

Mejdahl, V., 1987. Internal radioactivity in quartz and feldspar grains. Ancient TL, 5(2): 10−17.

Mejdahl, V., 1989. Thermoluminescence dating based on feldspar. Nuclear Tracks and Radiation Measurements, 10: 133-136.

Merh, S.S., 2005. The great Rann of Kachchh: perceptions of a field geologist. Geological Society of India, 65: 9−25.

Miki, T. and Ikeya, M., 1982. Physical basis of fault dating with ESR. Naturwissenschaften, 69(8): 390−391.

Mohindra, R. and Bagati, T.N., 1996. Seismically induced soft−sediment deformation structures (seismites) around Sumdo in the lower Spiti valley (Tethys Himalaya). Sedimentary Geology, 101(1–2): 69−83.

Molnar, P. and Tapponnier, P., 1975. Cenozoic Tectonics of Asia: Effects of a Continental Collision: Features of recent continental tectonics in Asia can be interpreted as results of the India−Eurasia collision. Science, 189(4201): 419−426.

Molnar, P. and Tapponnier, P., 1977. Relation of the tectonics of Eastern China to the India−Eurasia collision: application of slip−line field theory to large−scale control tectonics. Geology, 5(4): 212−216.

Moretti, M., 2000. Soft−sediment deformation structures interpreted as seismites in middle−late Pleistocene aeolian deposits (Apulian foreland, southern Italy). Sedimentary Geology, 135(1–4): 167−179.

Murakami, M. and Tagami, T., 2004. Dating pseudotachylyte of the Nojima fault using the zircon fission−track method. Geophysical Research Letters, 31(12): L12604.

Murari, M.K., 2008. Component specific luminescence of natural minerals and their application to dosimetry of natural radiation environment, Mohan Lal Sukhadiya University, Udaipur.

Murari, M.K., Singh, R.N. and Singhvi, A.K., 2009. Flash heating of faults and resetting of TL clocks in sahllow earthquakes, 2nd Asia Pacific Luminescence and Electron Spin Resonance Dating (APLED), abstract book, India, pp. 81.

Murray, A.S., 1996. Developments in optically stimulated luminescence and photo−transferred thermoluminescence dating of young sediments: Application to a 2000−year sequence of flood deposits. Geochimica et Cosmochimica Acta, 60(4): 565−576.

Murray, A.S. and Olley, J.M., 2002. Precision and accuracy in the optically stimulated luminescence dating of sedimentary quartz: a status review. Geochronometria, 21: 1−16.

Murray, A.S. and Roberts, R.G., 1997. Determining the burial time of single grains of quartz using optically stimulated luminescence. Earth and Planetary Science Letters, 152(1-4): 163-180.

Murray, A.S. and Wintle, A.G., 2000. Luminescence dating of quartz using an improved single−aliquot regenerative−dose protocol. Radiation Measurements, 32(1): 57−73.

Naeser, C.W., 1967. The use of apatite and sphene for fission track age determinations. Bulletin Geological Society of America, 78(12): 1523−1526.

Nash, D.B., 1984. Morphologic dating of fluvial terrace scarps and fault scarps near West Yellowstone, Montana. Geological Society of America Bulletin, 95: 1413–1424.

Noller, J.S., Sowers, J.M. and Lettis, W.R., 2000. Quaternary Geochronology: Methods and Applications. AGU Ref. Shelf, 4. AGU, Washington, DC, 582 pp.

Nuriel, P., Rosenbaum, G., Zhao, J.x., Feng, Y., Golding, S.D., Villemant, B. and Weinberger, R., 2012. U−Th dating of striated fault planes. Geology, 40(7): 647−650.

Obermeier, S.F., 1996. Use of liquefaction-induced features for paleoseismic analysis — An overview of how seismic liquefaction features can be distinguished from other features and how their regional distribution and properties of source sediment can be used to infer the location and strength of Holocene paleo-earthquakes. Engineering Geology, 44(1–4): 1-76.

Oldham, C.F., 1893. The Saraswati and the lost river of the Indian desert. Journal of the Royal Asiatic Society, 34: 49−76.

Oldham, R.D., 1899. Report on the great earthquake of 12th June 1897, Geological Survey of India, Calcutta.

Oldham, R.D., 1926. The Cutch (Kachh) earthquake of 16th June 1819 with a riviusion of the great earthquake of 12th June 1897. Memoir Geological Survey of India, 46: 71–147.

Oniya, E.O., Polymeris, G.S., Tsirliganis, N.C. and Kitis, G., 2012. On the pre−dose sensitization of the various components of the LM−OSL signal of annealed quartz; comparison with the case of 110 °C TL peak. Radiation Measurements, 47(9): 864−869.

Owen, H.G., 1996. Experimental soft−sediment deformation: structures formed by the liquefaction of unconsolidated sands and some ancient examples. Sedimentology, 43: 279−293.

Pagonis, V., Balsamo, E., Barnold, C., Duling, K. and McCole, S., 2008. Simulations of the predose technique for retrospective dosimetry and authenticity testing. Radiation Measurements, 43(8): 1343−1353.

Pagonis, V., Kitis, G. and Chen, R., 2003. Applicability of the Zimmerman predose model in the thermoluminescence of predosed and annealed synthetic quartz samples. Radiation Measurements, 37(3): 267−274.

Palumbo, L., Benedetti, L., Bourlès, D., Cinque, A. and Finkel, R., 2004. Slip history of the Magnola fault (Apennines, Central Italy) from 36Cl surface exposure dating: evidence for strong earthquakes over the Holocene. Earth and Planetary Science Letters, 225(1–2): 163−176.

Pawley, S.M., Toms, P., Armitage, S.J. and Rose, J., 2010. Quartz luminescence dating of Anglian Stage (MIS 12) fluvial sediments: Comparison of SAR age estimates to the terrace chronology of the Middle Thames valley, UK. Quaternary Geochronology, 5(5): 569−582.

Pearthree, P.A. and Calvo, S.S., 1987. The Santa Rita fault zone: Evidence for large magnitude earthquakes with very long recurrence intervals, basin and range province of southeastern Arizona. Bulletin of the Seismological Society of America, 77(1): 97−116.

Phillips, F., Ayarbe, J., Harrison and Elmore, D., 2003. Dating rupture events on alluvial fault scarps using cosmogenic nuclides and scarp morphology. Earth and Planetary Science Letters, 215(1−2): 203−218.

Polymeris, G.S., Kiyak, N.G., Koul, D.K. and Kitis, G., 2013. The Firing Temperature of Pottery from Ancient Mesopotamia, Turkey, Using Luminescence Methods: A Case Study for Different Grain−Size Fractions. Archaeometry: n/a−n/a.

Polymeris, G.S., Oniya, E.O., Jibiri, N.N., Tsirliganis, N.C. and Kitis, G., 2012. In−homogeneity in the pre−dose sensitization of the 110 °C TL peak in various quartz samples: The influence of annealing. Nuclear Instruments & Methods in Physics Research Section B−Beam Interactions with Materials and Atoms, 274: 105−110.

Pons−Branchu, E., Hamelin, B., Brulhetet, J. and Bruxelles, L., 2004. Speleothem rupture in karst: tectonic or climatic origin? U−Th dating of rupture events in Salamandre Cave (Gard, southeastern France). Bulletin de la Societe Geologique de France, 175: 473−479.

Poolton, N.R.J., Ozanyan, K.B., Wallinga, J., Murray, A.S. and Bøtter−Jensen, L., 2002a. Electrons in feldspar II: A consideration of the influence of conduction band−tail states on luminescence processes. Physics and Chemistry of Minerals, 29(3): 217−225.

Poolton, N.R.J., Wallinga, J., murray, A., Bulur, E. and Bøtter−Jensen, L., 2002b. Electrons in Feldspar I: on the wavefunction fo electrons trapped at simple lattice defects. Physics and Chemistry of Minerals, 29: 210.

Porat, N., 2006. Use of magnetic separation for purifying quartz for luminescence dating Ancient TL, 24(2): 33.

Porat, N., Levi, T. and Weinberger, R., 2007. Possible resetting of quartz OSL signals during earthquakes—Evidence from late Pleistocene injection dikes, Dead Sea basin, Israel. Quaternary Geochronology, 2(1−4): 272−277.

Porat, N., Wintle, A.G., Amit, R. and Enzel, Y., 1996. Late quaternary earthquake chronology from luminescence dating of colluvial and alluvial deposits of the Arava Valley, Israel. Quaternary Research, 46(2): 107−117.

Postpischl, D., Agostini, S., Forti, P. and Quinif, Y., 1991. Paleoseismicity from Karst sediments: the 'Grotta del Cervo' cave case study (Central Italy). Tectonophysics, 193(33−44).

Pramanik, S.K., 1952. Hydrology of the Rajasthan Desert: rainfall, humidity and evaporation, Proceedings Symposium Rajputana Desert, Natn. Inst. Sci. India, pp. 183−197.

Prescott, J.R., Huntley, D.J. and Hutton, J.T., 1993. Estimation of equivalent dose in thermoluminescence dating− the Australian slide method. Ancient TL, 11(1): 1.

Prescott, J.R. and Hutton, J.T., 1994. Cosmic ray contributions to dose rates for luminescence and ESR dating: Large depths and long−term time variations. Radiation Measurements, 23(2−3): 497−500.

Price, P.B. and Walker, R.L., 1962. Observation of fossil particle tracks in natural micas. Nature, 196: 732−734.

Price, P.B. and Walker, R.M., 1963. Fossil tracks of charged particles in mica and the age of minerals. Journal of Geophysical Research, 68

Prizomwala, S.P., Shukla, S.B. and Bhatt, N., 2010. Geomorphic assemblage of the Gulf of Kachchh coast, western India: Implications in understanding the pathways of coastal sediments. Zeitschrift für Geomorphologie, 54: 31−46.

Rajendran, C.P. and Rajendran, K., 2001. Characteristics of deformation and past seismicity associated with the 1819 Kutch earthquake, North−western India. Bulletin of the Seismological Society of America, 91: 407−426.

Rajendran, C.P., Rajendran, K. and John, B., 1998. Surface deformation related to the 1819 Kachchh earthquake: Evidence for recurrent activity. Current Science, 75: 623−626.

Rajendran, C.P., Rajendran, K., Thakkar, M. and Goyal, B., 2008. Assessing the previous activity at the source zone of the 2001 Bhuj earthquake based on the near−source and distant paleoseismological indicators. Journal of Geophysical Research, 113(B05311): 1−17.

Ranalli, G., 1995. Rheology of the earth. Chapman and Hall, London, U.K.

Randall, J.T. and Wilkins, M.H.F., 1945. Phosphorescence and electrontraps. I. The study of trap distributions. Proceedings of Royal Society of London, 184: 366.

Rao, N.P. and Kumar, M.R., 1997. Uplift and tectonics of the Shillong plateau, northeast India. Journal of Physics of the Earth, 45: 167−176.

Rao, P.V. and Rao, R., 1995. Provenance and distribution of clay minerals in the sediments of the western continental shelf and slope of India. Continental Shelf Research, 15: 1757−1771.

Reddy, D.V., Nagabhushanam, P., Kumar, D., Sukhija, B.S., Thomas, P.J., Pandey, A.K., Sahoo, R.N., Ravi Prasad, G.V. and Datta, K., 2009. The great 1950 Assam Earthquake revisited: Field evidences of liquefaction and search for paleoseismic events. Tectonophysics, 474(3−4): 463−472.

Reineck, H.E. and Singh, I.B., 1980. Depositional Sedimentary Environments. Springer−Verlag, Berlin.

Rendell, H.M., Townsend, P.D. and Wood, R.A., 1995. TL and IRSL Emission Spectra of Detrital Feldspars. New Experimental Data. physica status solidi (b), 190(1): 321−330.

Report, G., 2009. Geology and Mineral Resource of Assam, GEOLOGICAL SURVEY OF INDIA, Assam.

Rink, W.J., Toyoda, S., Rees−Jones, J. and Schwarcz, H.P., 1999. Thermal activation of OSL as a geothermometer for quartz grain heating during fault movements. Radiation Measurements, 30(1): 97−105.

Rodríguez−Pascua, M.A., Calvo, J.P., De Vicente, G. and Gómez−Gras, D., 2000. Soft−sediment deformation structures interpreted as seismites in lacustrine sediments of the Prebetic Zone, SE Spain, and their potential use as indicators of earthquake magnitudes during the Late Miocene. Sedimentary Geology, 135(1–4): 117−135.

Rodríguez−Pascua, M.A., Pérez−López, R., Garduño−Monroy, V.H., Giner−Robles, J.L., Silva, P.G., Perucha−Atienza, M.A., Hernández−Madrigal, V.M. and Bischoff, J., 2012. Paleoseismic and geomorphologic evidence of recent tectonic activity of the Pozohondo Fault (Betic Cordillera, SE Spain). Journal of Iberian Geology, 38(1): 239−251.

Rodríguez−Pascua, M.A., Vicente, G.D. and Calvo, J.P., 2001. Paleoseismological analyses of late Miocene lacustrine successions in the Prebetic Zone, SE Spain. Acta Geologicahispanica, 36: 213−232.

Rosenhead, L., 1954. The Second Coefficient of Viscosity: A Brief Review of Fundamentals. Proceedings of the Royal Society of London. Series A, Mathematical and Physical Sciences, 226(1164): 1−6.

Roy, B. and Merh, S.S., 1982. The Great Rann of Kutch: An intriguing Quaternary terrain. Recent Research in Geology, 29: 519−539.

Roy, P.D., Nagar, Y.C., Juyal, N., Smykatz−Kloss, W. and Singhvi, A.K., 2008. Geochemical signature of Late Holocene paleo−hydrological changes from Phulera and Pokharan saline playas near the eastern and western margins of the Thar Desert, India. Journal of Asian Earth Science, 34: 275−286.

Saillard, M., Riotte, J., Regard, V., Violette, A., Hérail, G., Audin, L. and Riquelme, R., 2012. Beach ridges UeTh dating in Tongoy bay and tectonic implications for a peninsulaebay system, Chile. Journal of South American Earth Sciences, 40: 77−84.

Sasseville, C., Tremblay, A., Clauer, N. and Liewig, N., 2008. K–Ar age constraints on the evolution of polydeformed fold–thrust belts: The case of the Northern Appalachians (southern Quebec). Journal of Geodynamics, 45(2–3): 99−119.

Schlagenhauf, A., Manighetti, I., Benedetti, L., Gaudemer, Y., Finkel, R., Malavieille, J. and Pou, K., 2011. Earthquake supercycles in Central Italy, inferred from ^{36}Cl exposure dating. Earth and Planetary Science Letters, 307(3–4): 487−500.

Scholz, C.H., 1987. Wear and gouge formation in brittle faulting Geology, 15(6): 493−495.

Schubert, G., Turcotte, D.L. and Olson, P., 2001. Mantle convection in the earth and planets. Cambridge University Press, United Kingdom.

Schumm, S.A., 1986. Alluvial river response to active tectonics. Active Tectonics, Geophysics Research Forum. Geophysics Study Committee. National Academy Press, Washington, DC, 80−94 pp.

Scott, J.S. and Drever, H.I., 1953. Frictional fusion along a Himalayan thrust. 65B(2): 121−141.

Seeber, L. and Gornitz, V., 1983. River profiles along the Himalayan arc as indicators of active tectonics. Tectonophysics, 92: 335−367.

Seed, H.b., 1979. Soil Liquefaction and cyclic mobility for level ground during earthquakes. Journal of Geotechnical Engineering 97: 1249−1274.

Seward, D. and Mancktelow, N.S., 1994. Neogene kinematics of the central and western Alps: Evidence from fission−track dating. Geology, 22(9): 803−806.

Sibson, R.H., 1975. Generation of Pseudotachylyte by Ancient Seismic Faulting. Geophysical .Journal of the Royal Astronomical Society, 43(775−794).

Sibson, R.H., 1977. Fault rocks and fault mechanisms. Journal of the Geological Society, 133(3): 191−213.

Silk, E.C.H. and Barnes, R.S., 1959. Examination of fission fragment tracks with an electron microscope. Philosophical Magazine, 4: 970−971.

Singh, R.N., Murari, M.K. and Singhvi, A.K., 2009. Flash heating in sand dykes: A possible zeroing mechanism for OSL dating, 2nd Asia Pacific Luminescence and Electron Spin Resonance Dating (APLED), India, pp. 109.

Singhvi, A. and Wagner, G.A., 1986. Thermoluminescence dating and its application to young sedimentary deposits. In: A.J. Hurtford, E. Jager and J.A.M. Ten Cate (Editors), Dating young sediments. Ccop Technical Publication 16. Bangkok: CCOP Technical Secretariat, United Nations, pp. 159-197.

Singhvi, A.K. and Aitken, M.J., 1978. Americum−241 for Alpha−Irradiations. Ancient TL, 3: 2−9.

Singhvi, A.K., Banerjee, D., Pande, K., Gogte, V. and Valdiya, K.S., 1994. Luminescence studies on neotectonic events in south−central Kumaun Himalaya−a feasibility study. Quaternary Science Reviews, 13(5−7): 595−600.

Singhvi, A.K., Bluszcz, A., Bateman, M.D. and Rao, M.S., 2001. Luminescence dating of loess−palaeosol sequences and coversands: Methodological aspects and palaeoclimatic implications. Earth−Science Reviews, 54(1−3): 193−211.

Singhvi, A.K., Chauhan, N. and Biswas, R.H., 2010. A survey of some new approaches in extending the maximum age limit and accuracy of luminescence application to archeological chronometry. Mediterranean Archaeology and Archaeometry, 4: 9-15.

Singhvi, A.K., Nagar, Y.C. and Jaiswal, M., 2008. Sensitivity changes during OSL read out: Implications and modified SAR protocol, ICLA, National Physical Laboratory, New Delhi.

Singhvi, A.K., Stokes, S., Chauhan, N., Nagar, Y.C. and Jaiswal, M.K., 2011. Changes in natural OSL sensitivity during single aliquot regeneration procedure and their implications for equivalent dose determination. Geochronometria, 38(3): 231−241.

Smith, B.W., Rhodes, E.J., Stokes, S. and Spooner, N.A., 1990. The optical dating of sediments using quartz. Radiation Protection Dosimetry, 34(1−4): 75−78.

Sohbati, R., Murray, A., Jain, M., Thomsen, K., Hong, S.C., Yi, K. and Choi, J.H., 2013. Na−rich feldspar as a luminescence dosimeter in infrared stimulated luminescence (IRSL) dating. Radiation Measurements, 51–52(0): 67−82.

Spooner, N.A., 1992. Optical dating: Preliminary results on the anomalous fading of luminescence from feldspars. Quaternary Science Reviews, 11(1−2): 139−145.

Spooner, N.A., 1994. The anomalous fading of infrared−stimulated luminescence from feldspars. Radiation Measurements, 23(2−3): 625−632.

Srivastava, P.K., 1971. Recent sediments in Ranns of Kutch. Journal Geological Society of India, 12: 392−395.

Stein, A., 1942. A survey of ancient sites along the lost Saraswati River. Geographical Journal, 134: 367−382.

Stevens, P.R. and Walker, T.W., 1970. The Chronosequence Concept and Soil Formation. The Quarterly Review of Biology, 45(4): 333−350.

Stokes, S., 1994. The timing of OSL sensitivity changes in a natural quartz. Radiation Measurements, 23(2−3): 601−605.

Stokes, S., Colls, A.E.L., Fattahi, M. and Rich, J., 2000. Investigations of the performance of quartz single aliquot DE determination procedures. Radiation Measurements, 32(5): 585−594.

Stoneham, D. and Stokes, S., 1991. Investigation of the relationship between the 110°C TL peak and optically stimulated luminescence in sedimentary quartz. Nuclear Tracks and Radiation Measurements, 18(1-2): 119-123.

Stricertsson, K., 1985. Thermoluminescence of potassium feldspar- glow curve characteristics and initial rise measurements. Nuclear Tracks and Radiation Measurements, 10: 613-617.

Stuiver, M. and Polach, H.A., 1977. Discussion: Reporting of 14C data. Radiocarbon, 19: 355−63.

Sukhija, B.S., Rao, M.N., Reddy, D.V., Nagabhushanam, P., Hussain, S., Chadha, R.K. and Gupta, H.K., 1999. Paleoliquefaction evidence and periodicity of large prehistoric earthquakes in Shillong Plateau, India. Earth and Planetary Science Letters, 167: 269−282.

Sukhija, B.S., Rao, M.N., Reddy, D.V., Nagabhushanam, P., Lakshmi, B.V. and Gupta, H.K., 2000. Current status of palaeoseismology in India − an overview. Journal of the Geological Society of India, 55(5): 465−480.

Suzuki, S. and Kennedy, F.E., 1991. The Detection of Flash Temperatures in a Sliding Contact by the Method of Tribo−Induced Thermoluminescence. Journal of Triboluminescence, 113: 120−127.

Swanson, M.T., 1992. Fault structure, wear mechanisms and rupture processes in pseudotachylyte generation. Tectonophysics, 204(3−4): 223−242.

Takeuchi, A., Nagahama, H. and Hashimoto, T., 2006. Surface resetting of thermoluminescence in milled quartz grains. Radiation Measurements, 41(7–8): 826−830.

Tanaka, K. and Shidahara, T., 1985. Fracturing, crushing and grinding effects on ESR signal of quartz. In: M. Ikeya and T. Miki (Editors), ESR dating and dosimetry. IONICS Publishing Co Limited, Tokyo, pp. 239−247.

Taylor, R.E., 1985. The beginnings of radiocarbon dating in American Antiquity: A historical perspective. American Antiquity, 50: 309−325.

Temiz, U., Gökten, Y.E. and Eikenberg, J., 2013. Strike−slip deformation and U/Th dating of travertine deposition: Examples from North Anatolian Fault Zone, Bolu and Yeniçag Basins, Turkey. Quaternary International, 312: 132−140.

Templer, R.H., 1986. The Localised Transition Model of Anomalous Fading. Radiation Protection Dosimetry, 17(1−4): 493−497.

Thiel, C., Buylaert, J.P., Murray, A., Terhorst, B., Hofer, I., Tsukamoto, S. and Frechen, M., 2011. Luminescence dating of the Stratzing loess profile (Austria) - Testing the potential of an elevated temperature post-IR IRSL protocol. Quaternary International, 234: 23-31.

Thomas, P.J., Juyal, N., Kale, V.S. and Singhvi, A.K., 2007a. Luminescence chronology of Late Holocene extreme hydrological events in the Penner River basin, South India Journal of Quaternary Science, 22: 747−753.

Thomas, P.J., Reddy, D.V., Kumar, D., Nagabhushanam, P., Sukhija, B.S. and Sahoo, R.N., 2007b. Optical dating of liquefaction features to constrain prehistoric earthquakes in Upper Assam, NE India−some preliminary results. Quaternary Geochronology, 2(1−4): 278−283.

Thomsen, K., Murray, A. and Jain, M., 2011. Stability of IRSL signals from sedimentary K−feldspar samples. Geochronometria, 38(1): 1−13.

Tiwari, R.P., 2002. Status of Seismicity in the Northeast India and Earthquake Disaster Mitigation. ENVIS Bulletin: Himalayan Ecology & Development, 10(1): 11-21.

Townsend, P.D., Rendell, H.M. and Luff, B.J., 1993. High sensitivity TL spectra of quartz and feldspar. Ancient TL, 11(2): 36−39.

Toyoda, S., Rink, J.W., Schwarcz, H.P. and Rees−Jones, J., 2000. Crushing effects on TL and OSL on quartz: relevance to fault dating. Radiation Measurements, 32(5/6): 667−672.

Tsukamoto, S., Denby, P.M., Murray, A.S. and Bøtter−Jensen, L., 2006. Time−resolved luminescence from feldspars: New insight into fading. Radiation Measurements, 41(7−8): 790−795.

Tu, X.B., Dai, F.C. and Pan, Y.S., 2012. Dating of faults and estimation of surface uplift and erosion rates in the northern margin of Dabie Mountains, China. Journal of Asian Earth Sciences, 56: 72−76.

Tuttle, M. and Seeber, L., 1991. Historic and prehistoric earthquake−induced liquefaction in Newbury, Massachusetts. Geology, 19: 594−597.

Tuttle, M.P., Sims, J.D., Dyer−Williams, K., Lafferty, R.H. and Schweig, E.S., 2000. Dating of Liquefaction Features in the New Madrid Seismic Zone G6903, Office of Nuclear Regulatory Research U.S. Nuclear Regulatory Commission Washington, DC, Washington DC.

Ujiie, K., Tanaka, H., Saito, T., Tsutsumi, A., Mori, J.J., Kameda, J., Brodsky, E.E., Chester, F.M., Eguchi, N., Toczko, S., 343, E. and Scientists, T., 2013. Low Coseismic Shear Stress on the Tohoku−Oki Megathrust Determined from Laboratory Experiments. Science, 342(6163): 1211−1214.

Uysal, I.T., Feng, Y., Zhao, J.x., Altunel, E., Weatherley, D., Karabacak, V., Cengiz, O., Golding, S.D., Lawrence, M.G. and Collerson, K.D., 2007. U−series dating and geochemical tracing of late Quaternary travertine in co−seismic fissures. Earth and Planetary Science Letters, 257(3–4): 450−462.

Uysal, I.T., Mutlu, H., Altunel, E., Karabacak, V. and Golding, S.D., 2006. Clay mineralogical and isotopic (K–Ar, δ18O, δD) constraints on the evolution of the North Anatolian Fault Zone, Turkey. Earth and Planetary Science Letters, 243(1–2): 181−194.

Vandenberghe, D., Kasse, C., Hossain, S.M., De Corte, F., Van Den Haute, P., Fuchs, M. and Murray, A.S., 2004. Exploring the method of optical dating and comparison of optical and ^{14}C ages of Late Weichselian coversands in the southern Netherlands. Journal of Quaternary Science, 19(1): 73−86.

Verhaert, G., Muchez, P., Sintubin, M., Similox−Tohon, D., Vanidycke, S., Keppens, F., Hodge, F.J. and Richards, D.A., 2004. Origin of palaeofluids in a normal fault setting in the Aegean region. Geofluids, 4: 300–314.

Visocekas, R., 1985. Tunnelling radiative recombination in labradorite: Its association with anomalous fading of thermoluminescence. Nuclear Tracks and Radiation Measurements (1982), 10(4–6): 521−529.

Wallinga, J., Murray, A. and Wintle, A., 2000. Single−aliquot regenerative−dose (SAR) protocol applied to coarse−grain feldspar. Radiation Measurements, 32(5): 529−533.

Wang, X.L., Wintle, A.G. and Lu, Y.C., 2007. Testing a single−aliquot protocol for recuperated OSL dating. Radiation Measurements, 42(3): 380−391.

Wintle, A.G., 1973. Anomalous fading of thermo−luminescence in mineral samples. Nature, 245(5421): 143−144.

Wintle, A.G., 1977. Detailed study of a thermoluminescent mineral exhibiting anomalous fading. Journal of Luminescence, 15(4): 385−393.

Wintle, A.G. and Murray, A.S., 2006. A review of quartz optically stimulated luminescence characteristics and their relevance in single−aliquot regeneration dating protocols. Radiation Measurements, 41(4): 369−391.

Wright, D.A., 1979. Predose Dating of a Swedish Vitrified Fort. Ancient TL, 6: 8−12.

Wynne, A.B., 1872. Memoir on the geology of the Kutch to accompany a map compiled by A.B. Wynne and F. Fedden during the seasons 1867−68 and 1868−69. Memories Geological Survey of India, 9.

Yamada, R., Matsuda, T. and Omura, K., 2007. Apatite and zircon fission−track dating from the Hirabayashi−NIED borehole, Nojima Fault, Japan: Evidence for anomalous heating in fracture zones. Tectonophysics, 443(3–4): 153−160.

Yamazaki, H., Tsukuda, E. and Mizuno, K., 1984. Trench excavation survery of active faults. Japan Engineering Society, 25: 141−145.

Yang, B.C., Dalrymple, R.W. and Chun, S.S., 2006. The Significance of Hummocky Cross−Stratification (HCS) Wavelengths: Evidence from an Open−Coast Tidal Flat, South Korea. Journal of Sedimentary Research, 76: 2−8.

Young, D.A., 1958. Etching of radiation damage in lithium fluoride. Nature, 182: 375−377.

Yurtmen, S., Guillou, H., Westaway, R., Rowbotham, G. and Tatar, O., 2002. Rate of strike−slip motion on the Amanos Fault (Karasu Valley, southern Turkey) constrained by K–Ar dating and geochemical analysis of Quaternary basalts. Tectonophysics, 344(3–4): 207−246.

Zander, A. and Hilgers, A., 2013. Potential and limits of OSL, TT−OSL, IRSL and pIRIR 290 dating methods applied on a Middle Pleistocene sediment record of Lake El'gygytgyn, Russia. Climate of the Past, 9: 719−733.

Zhao, H., Li, S.H. and Murray, A.S., 2003. Comparison of SAAD and SAR procedures for equivalent dose determination using quartz. Radiation Measurements, 37(4−5): 417−424.

Zimmerman, D.W., 1971a. Thermoluminescence dating using fine grains from pottery. Archaeometry, 13: 29−52.

Zimmerman, J., 1971b. The radiation−induced increase of the 100 ^{0}C thermoluminescence sensitivity of fired quartz. Journal of Physics C: Solid State Physics, 4(18): 3265−3276.

Zreda, M. and Noller, J.S., 1998. Ages of Prehistoric Earthquakes Revealed by Cosmogenic Chlorine−36 in a Bedrock Fault Scarp at Hebgen Lake. Science, 282(5391): 1097−1099.

Zwingmann, H. and Mancktelow, N., 2004. Timing of Alpine fault gouges. Earth and Planetary Science Letters, 223(3–4): 415−425.

Zwingmann, H., Yamada, K. and Tagami, T., 2010. Timing of brittle deformation within the Nojima fault zone, Japan. Chemical Geology, 275(3–4): 176−185.